



UNIVERSITY OF THE
WITWATERSRAND,
JOHANNESBURG

**MODELLING OF A SLURRY BUBBLE COLUMN REACTOR FOR FISCHER-
TROPSCH SYNTHESIS**

Botang Mamabolo

A dissertation submitted to the Faculty of Engineering and the Built Environment, University of the Witwatersrand, in fulfilment of the requirements for the degree of Master of Science in Engineering.

Johannesburg, 2018

Declaration

I, Botang Mamabolo, declare that this Dissertation is my own unaided work. It is being submitted for the Degree of Master of Science in Engineering to the University of the Witwatersrand, Johannesburg. It has not been submitted before for any degree or examination to any other university.

Signature

Date

Publications arising from this study

Mamabolo, B. A., Nkazi, D. Hydrodynamics in a Slurry Bubble Column Reactor for Fischer-Tropsch Synthesis: A Review. (Submitted for publication in the ACS journal)

Mamabolo, B. A., Nkazi, D. Modelling of a slurry bubble column reactor for Fischer-Tropsch synthesis. (Submitted for publication in the ACS journal)

Abstract

The slurry bubble column reactor (SBCR) is of particular interest in Fischer-Tropsch (FT) reactor modelling because of its importance to gas-to-liquids processes and the technical challenges it poses. Being one of the most important and complex Fischer-Tropsch Synthesis (FTS) systems in use today, there is a need to improve the current knowledge and understanding of the SBCR at a fundamental level, particularly the hydrodynamics of the process. Accordingly, a mathematical model of a SBCR has been developed in this work. The model is based on mass balances into which hydrodynamic, mass transfer and kinetic parameters have been incorporated. The hydrodynamic model considers two distinct phases in the SBCR, namely the gas and slurry phases with the liquid and solid phases treated as a single pseudo-homogenous phase. The gas phase in the reactor was assumed to exist in the form of distinctly large and small bubbles with each bubble class moving predominantly upwards through the center of the reactor and down near the wall respectively. Material balances were accordingly performed over three compartments including the slurry, large bubbles and small bubbles compartments. Axial dispersion was assumed in both the slurry and gas phases. The overall superficial gas velocity decrease along the axial direction was taken into account using an overall gas balance. Species material balances, hydrodynamics, kinetics and gas/liquid physicochemical property models were all coupled into a single SBCR model. The model was able to produce simulations capable of describing the fate of the reactant species, in the axial direction, in all three phases. Notably, the CO and H₂ concentrations dropped by 62.01% and 64.13% respectively in the large bubble phase. A sensitivity study revealed the negative dependence of syngas conversion on the superficial gas velocity. A positive effect on the syngas conversion was evident with an increase in reactor diameter, i.e., an increase in diameter between 6 m and 7.8 m resulted in an increase in the syngas conversion between 38.3% and 90.78%. An increase in catalyst loading (0.28 to 0.38) resulted in a decrease in the syngas conversion (93.57% to 0.704%) due mainly to the overall decrease in the bubble hold-up. The comparison of the model results with those from literature was favorable with some noticeable discrepancies resulting from the inherent differences between the models.

Acknowledgements

I would like to thank my family and friends who have shown a great deal of patience and support throughout the completion of this work.

I acknowledge my supervisor Dr. Diakanua Nkazi for his guidance throughout this work.

I also acknowledge the school of Chemical and Metallurgical Engineering for providing me with the platform and necessary resources to carry out this study successfully.

Contents

Declaration	i
Publications arising from this study	ii
Abstract	iii
Acknowledgements	iv
List of Figures	viii
List of Tables	xiii
Nomenclature	xiv
Chapter 1: Introduction	1
1.1 History of Fischer-Tropsch	1
1.2 FT overview	4
1.2.1 Product distribution	4
1.2.2 Kinetics and mechanisms of FTS	6
1.2.3 Reactors and catalysts used in FTS	7
1.3 Problem Statement	13
1.4 Research Aims and Objectives	13
Chapter 2: Literature Review	14
2.1 Hydrodynamics	14
2.1.1 Flow models	14
2.1.2 Phase characterization	15
2.1.3 Bubble size distribution	16
2.2 Kinetics	28
2.2.1 Mass transfer controlled rate	29
2.2.2 Catalysts	37
2.3 Mass transfer	38
2.3.1 Mass transfer coefficients	39
2.4 Heat transfer	41
2.5 Hydrodynamic parameters	42
2.5.1 Gas hold-up	42
2.5.2 Liquid hold-up	46
2.5.3 Superficial gas velocity	46
Chapter 3: Model development	47

3.1 Hydrodynamic model	47
3.2 Material balances	48
3.2.1 Boundary conditions	52
3.3 Model assumptions summary	54
3.4 Parameter estimation	54
3.4.1 Superficial velocity	54
3.4.2 Hold-up	55
3.4.3 Dispersion coefficients	56
3.4.4 Mass transfer coefficients	56
3.4.5 Henry's constants	57
3.4.6 Kinetic constants	58
3.5 Reactor feed conditions	59
Chapter 4: Numerical Solution in Simulink	60
4.1 Material balances	60
4.1.1 Large bubble compartment	60
4.1.2 Small bubble compartment	63
4.1.3 Liquid compartment	65
4.2 Hydrodynamics	68
4.2.1 Superficial gas velocity	68
4.2.2 Hold-up	69
4.2.3 Axial dispersion coefficient	71
4.3 Kinetics	72
4.4 Mass transfer	74
4.5 Phase properties	76
4.6 Overall Model	80
Chapter 5: Simulation results and discussion	81
5.1 Results	81
5.2 Model Discussion	84
5.2.1 Concentration gradients	84
5.2.2 Sensitivity analysis	98
Chapter 6: Model validation	119
6.1 Sehabiague et al. (2008)	119
6.2 Krishna and Sie (2000)	122
6.3 De Swart and Krishna (2002)	124
6.4 Vik et al. (2016)	126
Chapter 7: Conclusion and Recommendations	131
7.1 Conclusion	131

7.2 Recommendations	131
References	133
Appendix A: Simulink Boundary Condition Models	144
Large bubble phase	144
Small bubble phase	146
Liquid phase	147

List of Figures

Figure 1: Hydrocarbon product distribution with different chain growth probabilities	5
Figure 2: Circulating fluidised bed reactor (Dry, 2002)	9
Figure 3: Fixed Fluidised bed reactor (Dry, 2002)	9
Figure 4: A multi-tubular fixed bed reactor (Dry, 2002)	10
Figure 5: Slurry bubble column reactor (Dry, 2002)	10
Figure 6: Liquid axial dispersion coefficient as a function of superficial gas velocity	22
Figure 7: Radial liquid superficial velocity distribution	23
Figure 8: Single circulation cell spanning entire column height (Joshi, 2001)	27
Figure 9: Multiple cell structure along column height (Joshi, 2001).....	27
Figure 10: Species transport across three phases in SBCR	29
Figure 11: Adsorption, reaction and desorption of FT species around catalyst	30
Figure 12: Surface carbide mechanism	34
Figure 13: SBCR model structure.....	47
Figure 14: Illustration of the hydrodynamic model with respect to the large and small bubbles behaviour.	48
Figure 15: Discretization with respect to height of SBCR column	50
Figure 16: Simulink model for CO material balance in the large bubble compartment	61
Figure 17: Simulink model for H ₂ material balance in the large bubble compartment	61
Figure 18: Simulink boundary condition set-up for CO material balance in the large bubble compartment	62
Figure 19: Simulink boundary condition set-up for H ₂ material balance in large bubble compartment	62
Figure 20: Simulink model for CO material balance in the small bubble compartment	63
Figure 21: Boundary condition model applied to the CO material balance model in the small bubble compartment.....	64
Figure 22: Simulink model for H ₂ material balance in the small bubble compartment.....	64
Figure 23: Boundary condition model applied to the H ₂ material balance model in the small bubble compartment.....	65
Figure 24: Simulink model for CO material balance in the liquid compartment	66
Figure 25: CO liquid phase material balance boundary condition Simulink model.....	66
Figure 26: Simulink model for H ₂ material balance in the liquid compartment	67

Figure 27: H ₂ liquid phase material balance boundary condition Simulink model	67
Figure 28: Simulink model for small bubble superficial velocity	68
Figure 29: Simulink model of gas consumption in a SBCR	69
Figure 30: Simulink model of total gas concentration	69
Figure 31: Simulink model of the small bubbles hold-up.	70
Figure 32: Simulink model representing large bubbles hold-up	70
Figure 33: Liquid phase axial dispersion coefficient	71
Figure 34: Large bubble axial dispersion coefficient Simulink model	72
Figure 35: FT kinetic rate law in Simulink	73
Figure 36: FT kinetic rate constant Simulink model.....	73
Figure 37: Simulink model of the FT adsorption rate constant	74
Figure 38: CO K _{la} Simulink model for the large bubble compartment.....	74
Figure 39: CO K _{la} Simulink model for the small bubble compartment	75
Figure 40: Simulink model of H ₂ K _{la} in large bubble compartment	75
Figure 41: Simulink model of H ₂ K _{la} in small bubble compartment	75
Figure 42: CO Henry's constant Simulink model	76
Figure 43: H ₂ Henry's constant Simulink model.....	76
Figure 44: Liquid density Simulink model.....	77
Figure 45: Liquid viscosity Simulink model	77
Figure 46: Liquid surface tension Simulink model.....	78
Figure 47: Overall SBCR Simulink model.....	79
Figure 48: SBCR Simulink model with inputs and outputs only	80
Figure 49: CO concentration in large bubble phase across reactor height.	85
Figure 50: Large bubbles-liquid CO mass transfer coefficient across reactor height.....	86
Figure 51: Large bubble hold-up as a function of reactor height	86
Figure 52: Superficial gas velocity change over reactor height	87
Figure 53: Interphase concentration difference between large bubble and liquid phases.....	88
Figure 54: Axial change of CO concentration in the liquid phase.....	89
Figure 55: CO reaction rate as a function of reactor height	90
Figure 56: Large bubble phase dispersion coefficient over height of the reactor	91
Figure 57: rate of CO depletion in large bubbles over reactor height.....	92
Figure 58: CO concentration in large bubbles over extended height.....	93

Figure 59: Rate of depletion of CO in the small bubbles over reactor height	94
Figure 60: CO concentration in small bubble phase as a function of reactor column height..	95
Figure 61: Interphase CO concentration difference between small bubble and liquid phases	96
Figure 62: Rate of depletion of CO in the liquid phase over the height of the reactor	97
Figure 63: Effect of U_g on E_{LB} and E_L	100
Figure 64: Total gas hold-up as a function of superficial gas velocity	101
Figure 65: Relative sensitivities of superficial gas velocity and total gas hold-up to a change in reactor height	102
Figure 66: Effect of U_g on large bubble hold-up.....	103
Figure 67: Comparative effects of large bubble hold-up on both the gas phase dispersion coefficient and the large bubble-liquid mass transfer coefficient	104
Figure 68: Effect of increasing inlet superficial gas velocity on syngas conversion.....	105
Figure 69: Effect of reactor diameter on superficial gas velocity.....	106
Figure 70: Effect of reactor diameter on the gas and liquid axial dispersion coefficients	106
Figure 71: Effect of reactor diameter on syngas conversion	107
Figure 72: Small bubble hold-up as a function of solids concentration.....	108
Figure 73: Effect of solids concentration on small bubbles mass transfer coefficient	108
Figure 74: Effect of solid loading on reactant consumption rate.....	109
Figure 75: Effect of solids concentration on syngas conversion	110
Figure 76: Small bubble superficial velocity as a function of solids concentration	110
Figure 77: Large bubble hold-up behaviour with increasing solids concentration.....	111
Figure 78: The total superficial gas velocity as a function of solids concentration.....	112
Figure 79: Gaseous reactant concentrations as a function of solids concentration	113
Figure 80: The rate of reaction as a function of solids concentration	113
Figure 81: Effect of temperature on the reaction rate constant	114
Figure 82: Effect of temperature on the adsorption rate constant.....	114
Figure 83: Effect of temperature on the reaction rate	115
Figure 84: Liquid density as a function of temperature	115
Figure 85: Liquid surface tension as a function of temperature	116
Figure 86: Liquid viscosity as a function of temperature.....	116
Figure 87: Effect of temperature on the small bubble phase superficial velocity	117
Figure 88: Effect of temperature on large bubble hold-up.....	117

Figure 89: Effect of temperature on the gas phase dispersion coefficient	118
Figure 90: Effect of temperature on syngas conversion.....	118
Figure 91: CO conversion as a function of reactor height based on current model simulation ($U_g=0.3$ m/s, $C_v=0.3$ (v/v))	120
Figure 92: CO conversion over reactor height from Simulation based on Sehabiague et al. (2008) model ($U_g=0.3$ m/s, $C_v=0.375$ (wt%))	121
Figure 93: Syngas conversion vs superficial gas velocity results from simulation on current model ($H=30$ m, $C_v=0.3$ v/v, $D=7$ m)	123
Figure 94: Syngas conversion as a function of superficial gas velocity based on simulation from model by Krishna and Sie (2000) (Krishna and Sie, 2000) ($H=30$ m, $C_v=0.3$ (v/v), $D=$ 7 m)	124
Figure 95: Concentration of hydrogen as a function of reactor height from simulation based on the present model ($U_g=0.3$ m/s, $C_v=0.3$ (v/v), $D=7.5$ m)	125
Figure 96: Hydrogen concentration as a function of reactor height results from simulation based on model by De Swart and Krishna (2002) (Deswart and Krishna, 2002) ($U_g=0.3$ m/s, $C_v=0.25$ (v/v), $D=7.5$ m)	126
Figure 97: CO conversion as a function of reactor height based on simulation from current model ($U_g=0.3$ m/s, $C_v=0.3$ (v/v), $D=7$ m).....	128
Figure 98: Reactor height vs CO conversion from simulation based on model by Vik et al. (2016) for various feedstocks (Vik et al., 2016) ($U_g=0.26$ m/s).....	128
Figure 99: Superficial gas velocity drop over height of reactor based on simulation from current model ($C_v=0.3$ (v/v), $D=7$ m)	129
Figure 100: U_g vs height results from Vik et al. (2016) model.....	129
Appendix	
Figure A1: Large bubble CO inlet boundary condition Simulink model.....	144
Figure A2: Large bubble H ₂ inlet boundary condition Simulink model.....	144
Figure A3: Simulink model for the gas phase axial dispersion coefficient at the reactor inlet	145
Figure A4: Small bubble CO inlet boundary condition Simulink model.....	146
Figure A5: Small bubble H ₂ inlet boundary condition Simulink model.....	146
Figure A6: Simulink model for the small bubble phase axial dispersion coefficient at the reactor inlet	147

Figure A7: Liquid phase CO inlet boundary condition Simulink model	147
Figure A8: Liquid phase H ₂ inlet boundary condition Simulink model	148

List of Tables

Table 1: Industrial application of FTS technology	3
Table 2: Proposed reaction mechanisms for FTS (Chang et al., 2007).....	7
Table 3: Gas phase axial dispersion correlations	18
Table 4: Various liquid axial dispersion coefficients.....	21
Table 5: Main FTS reactions	33
Table 6: Typical SBCR operating conditions (Krishna and Sie, 2000 and Behkish et al., 2006)	35
Table 7: Various Kinetic rate laws.....	37
Table 8: Volumetric mass transfer coefficient correlations	40
Table 9: Gas hold-up correlations from literature	43
Table 10: Applicable range of conditions for Equation 7 (Behkish et al., 2006)	45
Table 11: SBCR liquid phase properties as functions of temperature	55
Table 12: Henry's constant correlations parameters (Soriano, 2005).....	58
Table 13: Reaction rate and adsorption constants for Equations 90 and 91 (Sehabiague, 2012)	59
Table 14: Input variables into Simulink model	82
Table 15: Model parameter change across reactor height	83
Table 16: Simulation results comparison between current and Sehabiague et al. (2008) SBCR model.....	120
Table 17: Syngas conversion as a function of inlet superficial gas velocity between current and Krishna and Sie's (2000) model.....	123
Table 18: Comparison between relative effects of reactor height on CO conversion between present model and that from Vik et al. (2016).....	127

Nomenclature

$C^*_{i,L}$	Equilibrium liquid side interfacial concentration of species i (mol/m ³)
k_{FT}	FT reaction rate constant (mol/g _{cat} .s)
P_{CO_2}	Partial pressure of CO ₂ (Pa)
P_{H_2}	Partial pressure of H ₂ (Pa)
P_{H_2O}	Partial pressure of H ₂ O (Pa)
P_{CO}	Partial pressure of CO (Pa)
C^*	Total equilibrium liquid side interfacial concentration of species i (mol/m ³)
C_V	Solids concentration (v/v)
$C_{i,L}$	Concentration of species i in the liquid phase (mol/m ³)
D_C	Diameter of reactor column (m)
D_{gL}	Gas-liquid diffusivity (m ² /s)
D_{ref}	Reference diffusivity (m ² /s)
E_G	Gas phase dispersion coefficient (m ² /s)
E_L	Liquid phase dispersion coefficient (m ² /s)
H_i	Henry's constant of component i (m ³ .Pa/mol)
K_A	Equilibrium adsorption constant for species A
$K_{La,LB}$	Liquid-side mass transfer coefficient in the large bubbles compartment (s ⁻¹)
$K_{La,SB}$	Liquid-side mass transfer coefficient in the small bubbles compartment (s ⁻¹)
K_d	Gas sparger type constant
MW_g	Molecular weight of gas (g/mol)
MW_i	Molecular weight of component i (g/mol)
N_0	Number of orifices on sparger
P_T, P_S	Total pressure (Pa)

P_i	Partial pressure of component i (Pa)
P_m	Specific energy dissipation rate (W/m^3)
P_{vap}	Vapour pressure (Pa)
$R_i(G_i)$	Rate of CO consumption of component i ($\text{mol}/\text{g}_{\text{cat}}\cdot\text{s}$)
$U_{g,LB}$	Large bubbles superficial liquid velocity (m/s)
$U_{g,SB}$	Small bubbles superficial velocity (m/s)
U_g, U_G	Gas superficial velocity (m/s)
X_W	Fraction of primary liquid in mixture (w/w)
Y_n	Molar fraction of hydrocarbons with carbon number 'n' in products
d_0	Sparger orifice diameter (m)
d_{LB}	Large bubble diameter (m)
d_{SB}	Small bubble diameter (m)
d_b	Bubble diameter (m)
d_p	Particle diameter (m)
k_3	Desorption rate constant (Pa^{-1})
k_L	Mass transfer coefficient (m/s)
k_{La}	Volumetric mass transfer coefficient (s^{-1})
k_{ads}	Adsorption rate constant (Pa^{-1})
r_p	Rate of carbon chain propagation
r_t	Rate of carbon chain termination
ρ_L	Liquid density (kg/m^3)
ρ_g, ρ_G	Gas density (kg/m^3)
ρ_p	Particle density (kg/m^3)
$[*]_0$	Total concentration of active sites on catalyst surface

[*]	Concentration of vacant active sites on catalyst surface
[A *]	Concentration of active catalyst sites occupied by adsorbing species A
D	Diffusivity (m^2/s)
H	Reactor bed Height (m)
J	Molar flux ($\text{mol}/\text{m}^2.\text{s}$)
K	Liquid axial dispersion proportionality constant
T	Temperature (K)
U	Superficial velocity (m/s)

Greek

ε_S	Solids hold-up (v/v)
$\varepsilon_{g,LB}$	Large bubbles hold-up (v/v)
$\varepsilon_{g,SB,ref}$	Reference small bubbles hold-up (v/v)
$\varepsilon_{g,SB}$	Small bubbles hold-up (v/v)
ε_g	Gas hold-up (v/v)
μ_L	Liquid viscosity (kg/m.s)
σ_L	Liquid surface tension (N/m)
σ_L	Liquid surface tension (N/m)
ξ	Dimensionless co-ordinate in the axial direction
α	Product distribution constant
γ	Gas sparger type
δ	Mass transfer liquid film thickness (m)
ε	Hold-up (v/v)
θ	Species coverage on catalyst surface

Subscripts

n	Carbon number of hydrocarbon molecule
L	Liquid phase
SB	Small bubbles phase
LB	Large bubbles phase
S	Solid phase
i	Arbitrary species
cat	Catalyst particle

Dimensionless numbers

Bo	Bond number
Ga	Galilei number
Fr	Froude number
Pe	Peclet number

Chapter 1: Introduction

1.1 History of Fischer-Tropsch

In this chapter, a background to Fischer-Tropsch Synthesis (FTS) will be given so that its importance to slurry bubble column reactors (SBCR) is contextualised. A brief history of FTS will be explained followed by the science underpinning this process and the various technologies that have been developed to commercialise it. This is intended to give the reader an appreciation of the importance of SBCRs in the commercialisation of the process of FTS, a chemical reaction system which is the cornerstone of this reactor type with regards to converting syngas to liquid fuels.

The Fischer-Tropsch (FT) process has found application in the petrochemical industry since its initial development in the 1920's by a team of German chemists Franz Fischer and Hans Tropsch. The two scientists realised through their experiments that long chain hydrocarbons could be derived from a CO and H₂ feedstock run over a Ni and Co catalyst (Steynberg and Dry, 2004). This discovery saw the emergence of Fischer-Tropsch Synthesis (FTS) as an important process that provided an alternative route to the production of liquid fuels. The technology was spurred on by the determination of the German Nazi government for their country to be fuel-independent. After a successful FT pilot plant study by Ruhrchemie AG, several FT plants were constructed in Germany in efforts to relieve the nation's dependence on fuel imports (Steynberg and Dry, 2004). The technology found further development in Europe, North America and Africa in the latter part of the 20th century despite a decline in the oil price in the middle of the century (Maitlis and de Klerk, 2013). The South African Coal, Oil and Gas Corporation, Ltd. (SASOL) saw an opportunity for FTS technology in the face of oil export sanctions to South Africa and a resurgent oil price in the 1970's. SASOL has since established itself as a leader in the commercial application of FTS which has come to be the main technology in its business.

SASOL as well as other international energy companies have since seen to the development of this technology to commercial benefit. In addition to the rising oil price in the latter part of the 20th century, other factors drove the interest in FTS technology well into the 21st century. These include the growing realization that the current oil reserves alone will not be able to meet the energy needs of a growing population. An alternative to crude oil as a primary source of fuel is important in this respect. FT technology, through the gas-to-liquids (GTL)

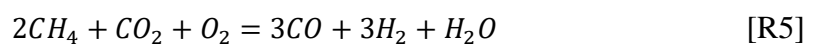
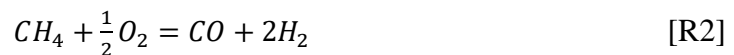
process, is ideally placed to exploit gas reserves that are in areas too remote to be economically transported to the market. The conversion of this stranded gas to liquid fuels presents an opportunity to make use of the energy from the gas reserves whilst avoiding the prohibitive costs of stranded natural gas transport (Speight, 2008; De Deugd, 2004). These factors coupled with the significant advances that have been achieved, allowing for improved economics, in FT technology have seen this process regain the popularity that it once enjoyed in the beginning and latter parts of the 20th century. A list of the various companies making use of this technology today is presented in Table 1 to show how FTS has been applied industrially since its discovery.

Table 1: Industrial application of FTS technology

Companies	Plant	Country	Reactor	Capacity (bbl/day)	Status	References
Qatar Petroleum/Sasol	GTL	Qatar	LTFT	34 000	In commercial operation	Oryx GTL (n.d)
Qatar Petroleum/ Shell	GTL	Qatar	LTFT	140 000	In commercial operation	Pearl GTL- Overview (n.d)
Sasol Chevron	GTL	Nigeria	HTFT	34 000	In commercial operation	Sasol Nigeria Operations (n.d)
Shell	GTL	Malaysia	LTFT	14 700	In commercial operation	Hoek (2005)
Sasol	GTL	South Africa(Sasolburg)	LTFT	15 600	In commercial operation	Mohammed and Datt (2013)
Sasol	CTL	South Africa (Secunda)	HTFT	160 000	In commercial operation	Mohammed and Datt (2013)
PetroSA	GTL	South Africa	HTFT	45 000	In commercial operation	PetroSA: Operations and Refinery (n.d)
Sasol	GTL	USA	HTFT	96 000	Investment decision delayed	Djakovic (2014)
Velocys	-	USA	Micro- channel	-	Production commenced in 2017	“First finished products” (2017)

1.2 FT overview

The FT process, named after the scientists that discovered it, is also commonly referred to as the Fischer-Tropsch Synthesis. It involves the conversion of synthesis gas (gaseous mixture of predominantly CO and H₂) to hydrocarbon products over a metal catalyst. The synthesis gas can be derived from coal gasification where coal is exposed to steam and/or oxygen under elevated pressures [R1] or from a methane reforming process in which methane is oxidized. Natural gas reforming can occur through partial oxidation [R2], steam reforming [R3], carbon dioxide reforming [R4] or auto-thermal reforming [R5] depending on the H₂/CO ratio required in the syngas (Steynberg and Dry, 2004).



1.2.1 Product distribution

The products from the FT process include hydrocarbons of various chain lengths and configurations that can be either straight or branched paraffins or olefins. These products are described using a probability factor because of the multiple potential products that can be formed. It is generally accepted that the formation of FT products follows a chain growth path where an initiating molecule adsorbs onto the surface of a catalyst followed by a propagation step where the molecule grows through the addition of a monomer species (Todic et al, 2014). The molecule continues to grow until the termination step whereby the molecule is released from the surface of the catalyst. In being released, this molecule either takes the form of a paraffin or olefin depending on the extent of hydrogenation. It is clear that the multiple possibilities in terms of the chain length and extent of hydrogenation make it difficult to accurately predict the quality of product and it is for this reason that a chain growth probability, α , is employed as a tool to describe the range of products formed from a FTS reaction (Steynberg and Dry, 2004). The chain growth probability gives the rate of chain propagation, r_p , relative to the sum of the rates of propagation and termination, r_t , as shown in Equation 1 (van der Laan, 1999).

$$\alpha = \frac{r_p}{(r_p + \sum r_t)} \quad [1]$$

α is applied in Equation 2 where the molar fraction of hydrocarbons in the products, Y_n , with a specific chain length or carbon number, n , can be determined. The value of α ranges between 0 and 1. A lower α value indicates a product with a higher concentration of shorter chain hydrocarbons whereas a higher α value points to a product more concentrated with longer chain hydrocarbons as illustrated in Figure 1.

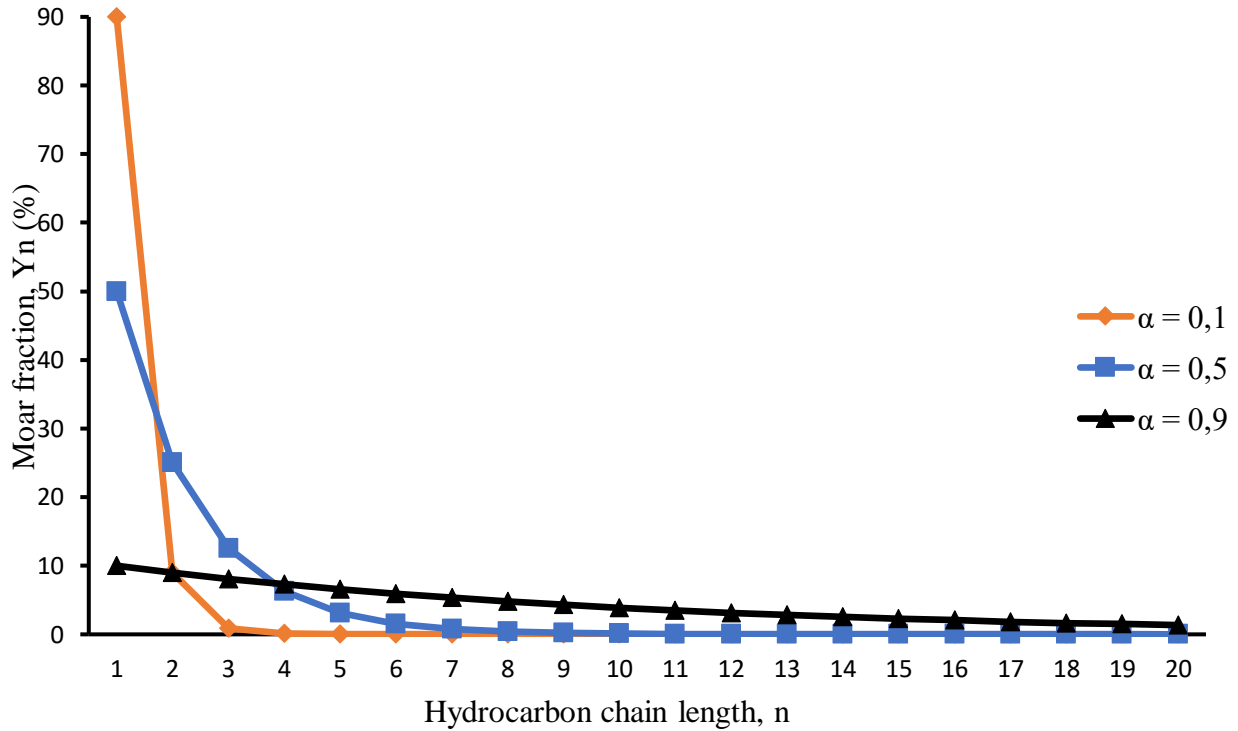


Figure 1: Hydrocarbon product distribution with different chain growth probabilities

The product distribution from a FT process follows a consistent trend for every specific value of α as suggested by the Anderson-Schulz-Flory (ASF) distribution (Steynberg and Dry, 2004). The product distribution from real systems does not always follow the ASF distribution. There have been various explanations put forward for this including the existence of more than one reaction pathway in the double- α concept (Tau et al., 1990). The two pathways are said to explain the apparent slope difference in the product distribution between the lower and higher chain length molecules. The other explanation proposed for the deviation is that product olefins undergo secondary reactions leading to an increase in the proportion of heavier hydrocarbon products (Herington, 1946).

$$Y_n = (1 - \alpha)\alpha^{n-1} \quad [2]$$

1.2.2 Kinetics and mechanisms of FTS

The kinetics in FTS rely on the reaction mechanism that is identified as the most suitable. FTS, as mentioned in an earlier paragraph, is a polymerisation reaction with hydrocarbon molecules coming together to form longer chain products. The difficulty in describing the FTS reaction lies with the mechanism by which these long chain hydrocarbon products are formed. Various mechanisms have been put forward to account for the way the hydrocarbon products are formed and depending on the mechanism chosen, the rate equation will be different. One of the mechanisms proposed is the surface carbide mechanism where methylene acts as the monomer on which the propagation of chain growth is based (Brady and Pettit, 1981; Ojeda et al., 2010; Fischer and Tropsch, 1926). In this mechanism, CO and H₂ adsorb dissociatively and the chain growth proceeds through the repeated insertion of the monomer. Various mechanisms can be differentiated based on the type of monomers present and the propagation pathways followed. Chang et al., (2007) describes six different reaction mechanisms based upon these two factors (Table 2). In Table 2, θ refers to a catalyst active site. The kinetics are also affected by the type of catalyst used with different rate equations resulting from the use of either Fe or Co catalysts.

Table 2: Proposed reaction mechanisms for FTS (Chang et al., 2007)

Alkyl propagation mechanism			Alklydiene propagation mechanism		
Model	No.	Elementary reactions of FTS	Model	No.	Elementary reactions of FTS
FT1	1	$\text{CO} + \theta \rightarrow \text{CO-}\theta$	FT4	1	$\text{CO} + \theta \rightarrow \text{CO-}\theta$
	2	$\text{CO-}\theta + \text{H}_2 \rightarrow \text{H}_2\text{CO-}\theta$		2	$\text{CO-}\theta + \text{H}_2 \rightarrow \text{H}_2\text{CO-}\theta$
	3	$\text{H}_2\text{CO-}\theta + \text{H}_2 \rightarrow \text{CH}_2\text{-}\theta + \text{H}_2\text{O}$		3	$\text{H}_2\text{CO-}\theta + \text{H}_2 \rightarrow \text{CH}_2\text{-}\theta + \text{H}_2\text{O}$
	4	$\text{H}_2 + 2\theta \rightarrow 2\text{H-}\theta$		4	$\text{H}_2 + 2\theta \rightarrow 2\text{H-}\theta$
	5	$\text{CH}_2\text{-}\theta + \text{H-}\theta \rightarrow \text{CH}_3\text{-}\theta + \theta$		5	$\text{CH}_2\text{-}\theta + \text{CH}_2\text{-}\theta \rightarrow \text{CH}_2\text{CH}_2\text{-}\theta + \theta$
		$\text{CH}_2\text{-}\theta + \text{CH}_3\text{-}\theta \rightarrow \text{CH}_3\text{CH}_2\text{-}\theta + \theta$			$\text{CH}_2\text{-}\theta + \text{C}_{n-1}\text{H}_{2n-2}\text{-}\theta \rightarrow \text{C}_n\text{H}_{2n}\text{-}\theta + \theta$
		$\text{CH}_2\text{-}\theta + \text{C}_{n-1}\text{H}_{2n-1}\text{-}\theta \rightarrow \text{C}_n\text{H}_{2n+1}\text{-}\theta + \theta$		6	$\text{CH}_2\text{-}\theta + \text{H-}\theta \rightarrow \text{CH}_3\text{-}\theta + \theta$
6	$\text{C}_n\text{H}_{2n+1}\text{-}\theta + \text{H-}\theta \rightarrow \text{C}_n\text{H}_{2n+2} + 2\theta$	7	$\text{C}_n\text{H}_{2n}\text{-}\theta + \text{H-}\theta \rightarrow \text{C}_n\text{H}_{2n+1}\text{-}\theta + \theta$		
7	$\text{C}_n\text{H}_{2n+1}\text{-}\theta \leftrightarrow \text{C}_n\text{H}_{2n} + \text{H}\theta$	7	$\text{CH}_3\text{-}\theta + \text{H-}\theta \rightarrow \text{CH}_4 + 2\theta$		
			8	$\text{C}_n\text{H}_{2n+1}\text{-}\theta + \text{H-}\theta \rightarrow \text{C}_n\text{H}_{2n+2} + 2\theta$	
			8	$\text{C}_n\text{H}_{2n}\text{-}\theta \leftrightarrow \text{C}_n\text{H}_{2n} + \theta$	
FT2	1	$\text{CO} + \theta \rightarrow \text{CO-}\theta$	FT5	1	$\text{CO} + \theta \rightarrow \text{CO-}\theta$
	2	$\text{CO-}\theta + \theta \rightarrow \text{C-}\theta + \text{O-}\theta$		2	$\text{CO-}\theta + \theta \rightarrow \text{C-}\theta + \text{O-}\theta$
	3	$\text{C-}\theta + \text{H}_2 \rightarrow \text{CH}_2\text{-}\theta$		3	$\text{C-}\theta + \text{H}_2 \rightarrow \text{CH}_2\text{-}\theta$
	4	$\text{O-}\theta + \text{H}_2 \rightarrow \text{H}_2\text{O} + \theta$		4	$\text{O-}\theta + \text{H}_2 \rightarrow \text{H}_2\text{O} + \theta$
	5	$\text{H}_2 + 2\theta \rightarrow 2\text{H-}\theta$		5	$\text{H}_2 + 2\theta \rightarrow 2\text{H-}\theta$
	6	$\text{CH}_2\text{-}\theta + \text{H-}\theta \rightarrow \text{CH}_3\text{-}\theta + \theta$		6	$\text{CH}_2\text{-}\theta + \text{CH}_2\text{-}\theta \rightarrow \text{CH}_2\text{CH}_2\text{-}\theta + \theta$
		$\text{CH}_2\text{-}\theta + \text{CH}_3\text{-}\theta \rightarrow \text{CH}_3\text{CH}_2\text{-}\theta + \theta$			$\text{CH}_2\text{-}\theta + \text{C}_{n-1}\text{H}_{2n-2}\text{-}\theta \rightarrow \text{C}_n\text{H}_{2n}\text{-}\theta + \theta$
		$\text{CH}_2\text{-}\theta + \text{C}_{n-1}\text{H}_{2n-1}\text{-}\theta \rightarrow \text{C}_n\text{H}_{2n+1}\text{-}\theta + \theta$		7	$\text{CH}_2\text{-}\theta + \text{H-}\theta \rightarrow \text{CH}_3\text{-}\theta + \theta$
7	$\text{C}_n\text{H}_{2n+1}\text{-}\theta + \text{H}_2 \rightarrow \text{C}_n\text{H}_{2n+2} + \text{H-}\theta$	8	$\text{C}_n\text{H}_{2n}\text{-}\theta + \text{H-}\theta \rightarrow \text{C}_n\text{H}_{2n+1}\text{-}\theta + \theta$		
8	$\text{C}_n\text{H}_{2n+1}\text{-}\theta \leftrightarrow \text{C}_n\text{H}_{2n} + \text{H}\theta$	8	$\text{CH}_3\text{-}\theta + \text{H}_2 \rightarrow \text{CH}_4 + \text{H-}\theta$		
			9	$\text{C}_n\text{H}_{2n+1}\text{-}\theta + \text{H}_2 \rightarrow \text{C}_n\text{H}_{2n+2} + \text{H-}\theta$	
			9	$\text{C}_n\text{H}_{2n}\text{-}\theta \leftrightarrow \text{C}_n\text{H}_{2n} + \theta$	
FT3	1	$\text{CO} + \theta \rightarrow \text{CO-}\theta$	FT6	1	$\text{CO} + \theta \rightarrow \text{CO-}\theta$
	2	$\text{CO-}\theta + \theta \rightarrow \text{C-}\theta + \text{O-}\theta$		2	$\text{CO-}\theta + \theta \rightarrow \text{C-}\theta + \text{O-}\theta$
	3	$\text{C-}\theta + \text{H-}\theta \rightarrow \text{CH-}\theta + \theta$		3	$\text{C-}\theta + \text{H-}\theta \rightarrow \text{CH-}\theta + \theta$
	4	$\text{CH-}\theta + \text{H-}\theta \rightarrow \text{CH}_2\text{-}\theta + \theta$		4	$\text{CH-}\theta + \text{H-}\theta \rightarrow \text{CH}_2\text{-}\theta + \theta$
	5	$\text{CH}_2\text{-}\theta + \text{H-}\theta \rightarrow \text{CH}_3\text{-}\theta + \theta$		5	$\text{CH}_2\text{-}\theta + \text{CH}_2\text{-}\theta \rightarrow \text{CH}_2\text{CH}_2\text{-}\theta + \theta$
		$\text{CH}_2\text{-}\theta + \text{CH}_3\text{-}\theta \rightarrow \text{CH}_3\text{CH}_2\text{-}\theta + \theta$			$\text{CH}_2\text{-}\theta + \text{C}_{n-1}\text{H}_{2n-2}\text{-}\theta \rightarrow \text{C}_n\text{H}_{2n}\text{-}\theta + \theta$
		$\text{CH}_2\text{-}\theta + \text{C}_{n-1}\text{H}_{2n-1}\text{-}\theta \rightarrow \text{C}_n\text{H}_{2n+1}\text{-}\theta + \theta$		6	$\text{H}_2 + 2\theta \rightarrow 2\text{H-}\theta$
	6	$\text{H}_2 + 2\theta \rightarrow 2\text{H-}\theta$		7	$\text{O-}\theta + \text{H-}\theta \rightarrow \text{HO-}\theta + \theta$
	7	$\text{O-}\theta + \text{H-}\theta \rightarrow \text{HO-}\theta + \theta$		8	$\text{HO-}\theta + \text{H-}\theta \rightarrow \text{H}_2\text{O} + 2\theta$
	8	$\text{HO-}\theta + \text{H-}\theta \rightarrow \text{H}_2\text{O} + 2\theta$		9	$\text{CH}_2\text{-}\theta + \text{H-}\theta \rightarrow \text{CH}_3\text{-}\theta + \theta$
9	$\text{C}_n\text{H}_{2n+1}\text{-}\theta + \text{H-}\theta \rightarrow \text{C}_n\text{H}_{2n+2} + 2\theta$	10	$\text{C}_n\text{H}_{2n}\text{-}\theta + \text{H-}\theta \rightarrow \text{C}_n\text{H}_{2n+1}\text{-}\theta + \theta$		
10	$\text{C}_n\text{H}_{2n+1}\text{-}\theta \leftrightarrow \text{C}_n\text{H}_{2n} + \text{H}\theta$	10	$\text{CH}_3\text{-}\theta + \text{H-}\theta \rightarrow \text{CH}_4 + 2\theta$		
			11	$\text{C}_n\text{H}_{2n+1}\text{-}\theta + \text{H-}\theta \rightarrow \text{C}_n\text{H}_{2n+2} + 2\theta$	
			11	$\text{C}_n\text{H}_{2n}\text{-}\theta \leftrightarrow \text{C}_n\text{H}_{2n} + \theta$	

Reaction mechanisms can also be differentiated by the way in which the reactants adsorb onto the catalyst surface. The two main adsorption paths follow the Langmuir-Hishelwood-Hougen-Watson (LHHW) and the Eley-Rideal surface reaction models. These models were formulated to describe the adsorption mechanisms of reactants in heterogeneously catalysed reactions. In the LHHW model, all the reactants adsorb onto the catalyst surface at separate active sites before reacting with one another and in the case of Eley-Rideal models only one of the reactants adsorbs onto an active catalyst site before reacting with an unadsorbed reactant (Albright, 2009).

1.2.3 Reactors and catalysts used in FTS

Thermodynamically speaking, the reaction between CO and H₂ is not favourable, i.e., it requires an external driving force to proceed. Fischer and Tropsch first discovered, in the 1920's, that a metal catalyst was able to provide the necessary thermodynamic conditions to effect what is now generally known as Fischer-Tropsch Synthesis (FTS). At the time, Ni and

Co were identified as the main catalysts and these have since changed to Fe and Co. Selection of the most appropriate catalyst is dependent on the objectives for FTS, i.e., the products that are required, the operating conditions and type of reactor used amongst other factors. Middle distillates (hydrocarbons with carbon numbers ranging between 9 and 16) may, for example, be the required products in which case the operating conditions within the selected reactor will have to be set and controlled accordingly. In selecting a reactor, two classes of FT reactors are considered; High temperature Fischer-Tropsch (HTFT) and Low Temperature Fischer-Tropsch (LTFT) reactors based on the prevailing temperature inside the reactor.

HTFT reactors operate in the temperature range from 320 – 350 °C, producing gaseous hydrocarbons mainly in the lower carbon number range. Different HTFT reactors are shown in Figures 2 and 3. These reactors operate in the fluidised bed regime where the catalyst particles are held in suspension and fluidised by the incoming gaseous reactants. The circulating fluidised bed (CFB) reactor circulates the solid catalyst between the two compartments whereas the fixed fluidised bed (FFB) reactor distinguishes itself by achieving a fluid-like motion of the catalyst bed without circulation of the catalyst.

The main catalyst used in HTFT reactors is the Fe based catalyst particularly because of its resistance to sintering under elevated pressures. Catalyst choice is also affected by the water gas shift (WGS) reaction (R8) which is predominant in Fe catalysed reactions but not in those catalysed by Co. The desirability of the WGS reaction, hence the type of catalyst used, is also dependent on the composition of the synthesis gas entering the reactor. If the aim is to produce an FT product that is more concentrated in olefins, then an H₂/CO ratio of 2 would be required as shown in R7. Should the syngas have a ratio exceeding 2, then the WGS reaction, and thus an Fe based catalyst, would be desirable.

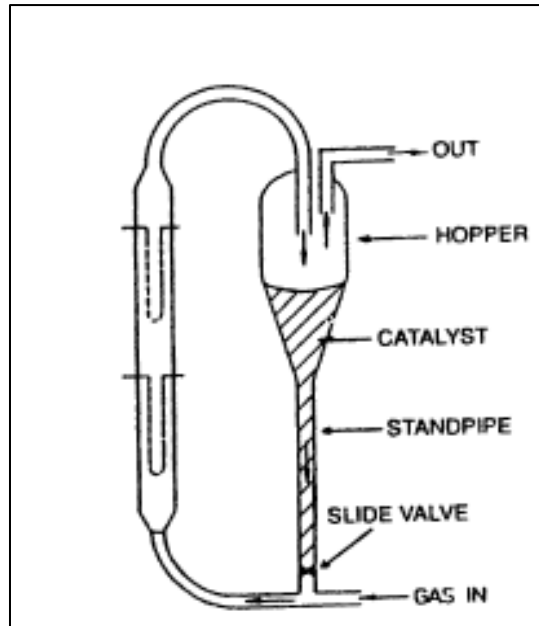


Figure 2: Circulating fluidised bed reactor (Dry, 2002)

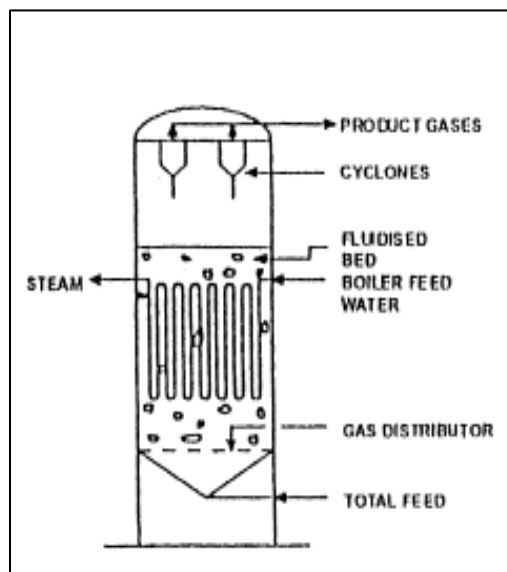


Figure 3: Fixed Fluidised bed reactor (Dry, 2002)

LTFT reactors, on the other hand, are used in the production of longer chain hydrocarbons (including wax) and they operate in the temperature range between 220 -250 °C. The reactors in this class include fixed tubular (Figure 4) and SBCRs (Figure 5). A cooling medium is passed through the inside of the reactor through tubes that allow heat exchange between the reactor and cooling tube sides to remove heat generated by the exothermic FT reactions and pass it into the cooling medium. In the multi-tubular fixed bed reactor, the reactants are passed, from top to bottom, through tubes packed with catalyst particles and the product exits

at the bottom of the reactor. The wax produced in the SBCR mixes with the catalyst to produce a slurry phase of catalyst and liquid product. The slurry makes it possible for the gaseous reactants to form bubbles as they pass through the reactor with the size of the bubbles depending on the superficial velocity of the incoming reactants. The three phases present (gas, solid, liquid) inside the reactor make modelling this type of reactor relatively more complex. Co and Fe can be utilised in LTFT reactors to achieve, to varying degrees, the production of longer chain hydrocarbons.

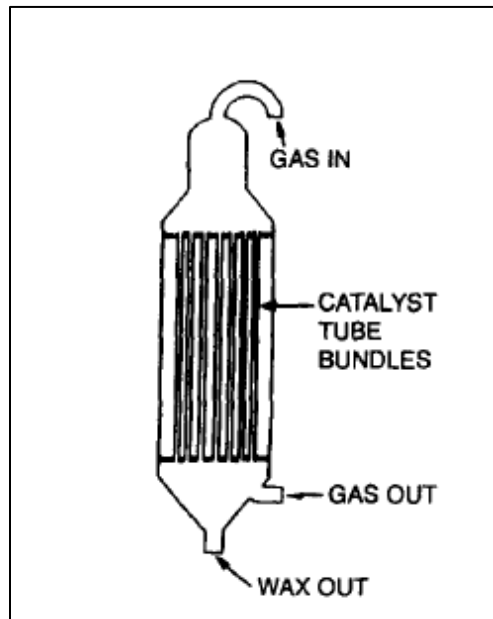


Figure 4: A multi-tubular fixed bed reactor (Dry, 2002)

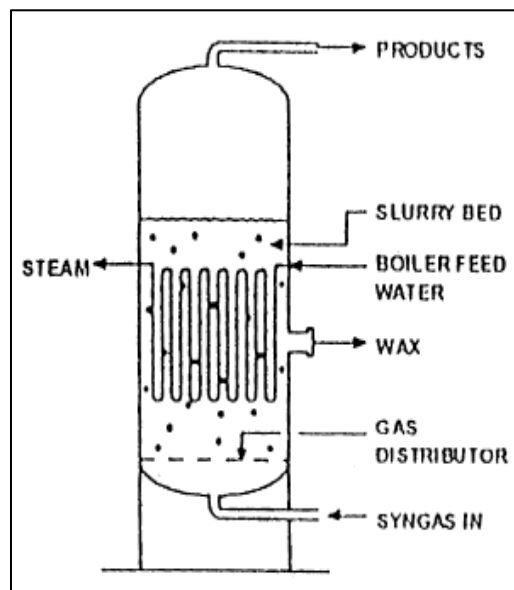


Figure 5: Slurry bubble column reactor (Dry, 2002)

The modelling of the operations inside the above-mentioned reactors is essential in providing a basis for the simulation, control and optimization with regards to FTS. Although empirical approaches to modelling FT reactor behaviour are adequate in certain circumstances, they are often applicable only under specific and limited conditions which make the resulting models limited as well. Models derived from fundamental principles are important because they can simulate FTS over a wider range of conditions with more accuracy. Such models can be time-saving in the conceptual development phase of an FT reactor design by eliminating the need to run exhaustive pilot stage tests. A 1st principle approach to the modelling of the FT process will also allow engineers to simulate various environments, in quick time, that may not be readily tested in pilot plants as a result of cost implications and time constraints.

Despite the commercial application of the FT process for the last 50 years, the fundamental principles behind FTS are still not fully understood (Maitlis and de Klerk, 2013). The complexity of FTS is such that the numerous reactions taking place and the multiple phases present (in SBCRs) make it difficult to model. This has in the past, as mentioned earlier, been overcome by empirical methods in which results from laboratory experiments were used to produce the reactor models. Also, because of the availability of well understood and reliable post FT refining processes, the FT product distribution has largely been allowed some room to deviate from expected values. This means that there is no single FTS model that can accurately predict the product environment based on the reactant and reactor environments. This problem is noted by Maitlis and de Klerk (2013) who cite the lack of a unified model which can accurately describe FT syngas consumption and product distribution. The authors attribute this to the lack of fundamental understanding of FTS.

In respect of FT reactor modelling, the SBCR is of particular interest because of its importance to FTS and the challenges it poses in terms of modelling its operations. Because of the multiple phases present in the reactor and the prevailing hydrodynamic conditions, the SBCR's complexity has hampered the development of accurate models describing its operation (Maitlis and de Klerk, 2013). SBCRs have been found to have significant mass and heat transfer advantages (Iliuta et al., 2007) over other FT reactors with the latter making it possible to achieve near isothermal conditions inside the reactor. The ability to add/remove catalysts from the reactor online, the long catalyst life and low operating costs (Kantarci et al., 2005; Degaleesan et al., 2001) have made the SBCR one of the more economical FT reactors in the market resulting in increased interest commercially and academically. In a time when alternative energy sources are becoming increasingly important, FTS has been

receiving renewed attention from academia and industry. Despite this increased attention, there are still knowledge gaps in terms of the fundamental principles governing this process. The SBCR is one of the more important and complex FTS systems in use today (Iliuta et al., 2007) and to improve its operating efficiency, the current knowledge and understanding of this process at a fundamental level, the hydrodynamics in particular, has to improve.

1.3 Problem Statement

In a time when alternative energy sources are becoming increasingly important, FTS has been receiving renewed attention from academia and industry. Despite this increased attention, there are still knowledge gaps in terms of the fundamental principles governing this process. Due to the multiple phases present and the turbulent conditions within this reactor, it has been difficult to develop a reliable model that can accurately describe the SBCR environment. The SBCR is one of the more important and complex FTS systems in use today (Iliuta et al., 2007) and to improve its operating efficiency, the current knowledge and understanding of this process at a fundamental level, the hydrodynamics in particular, has to improve. A model that can accurately describe the SBCR operations is needed. Taking due cognisance of the above-mentioned problem, the question then becomes whether the development of a SBCR mathematical model incorporating hydrodynamics can lead to;

- A better understanding of the processes inside a SBCR
- A better understanding of the FT process in general
- The design of more efficient SBCRs

1.4 Research Aims and Objectives

Given the problem statement above, the aim of this research project is the development of a comprehensive mathematical model describing the processes in SBCRs. To this end the following objectives have been set out.

- Investigation of the transport phenomena inside a SBCR
- Investigation of the reaction kinetics inside a SBCR
- Analysis of the hydrodynamics inside a SBCR
- Development and validation of a mathematical model, considering the above mentioned governing principles, to comprehensively describe the processes in FT SBCRs

Chapter 2: Literature Review

2.1 Hydrodynamics

2.1.1 Flow models

The flow of fluids in slurry bubble column reactors (SBCRs) poses a special challenge in their design primarily due to the multiphase nature of the system. The gaseous reactants move upward through the reactor in the form of bubbles. These bubbles interact with the slurry phase consisting of liquid hydrocarbon products and catalyst particles to result in hydrodynamics that are difficult to model accurately. The hydrodynamics in SBCRs are therefore difficult to model. The interaction between the separate phases is still not clearly understood and the extent of back mixing remains a point of debate. Do all the phases significantly interact chemically and/or physically or is this interaction selective? What contributes to the mixing action in the slurry phase? Considerable research effort has been undertaken to determine the actual hydrodynamics in SBCRs and a lot of progress has been made in improving the understanding of the fluid behavior in these reactors.

In beginning to conceptualize fluid behavior in a SBCR, the conditions inside it must be determined so that a physical context for the conceptual model is established. The gaseous syngas introduced to the reactor forms bubbles in the slurry bed as it makes its way upward through the height of the reactor. The bubbles will move upward due to their significantly lower density relative to that of the slurry. Several studies have found that under churn-turbulent conditions, the bubbles that form vary considerably in size (Steynberg and Dry, 2004; van der Laan, 1999; Krishna and Sie, 2000; Schumpe and Grund, 1986). This is in contrast to the bubble size distribution witnessed in bubbly flow of relatively lower superficial gas velocities in which the bubbles exhibit a narrow size distribution (Steynberg and Dry, 2004). The size distribution in churn-turbulent conditions can be simplified by assigning two bubble classes according to large and small bubbles. It has been found that the small bubbles reside mainly in the slurry phase while the large bubbles form a distinct gas phase. It is important to accurately define the bubble size distribution as the size of the bubbles is an important hydrodynamic parameter that influences the performance of the reactor as shall be discussed below.

It is widely accepted that the large bubbles move upward through the center of the SBCR while the small bubbles are immersed in the slurry phase and move downward along the wall of the column (Deckwer, 1991). The mixing in SBCRs is generally of two forms; axial

dispersion or cell circulation. Both models seek to explain the mixing inside the reactor. The axial dispersion model assigns a dispersion coefficient to the dispersive action that contributes to axial concentration and temperature gradients. The cell circulation models on the other hand attribute the mixing specifically to the circular movement of the slurry phase. This section is dedicated to reviewing these mixing models, giving attention to their advantages and disadvantages.

Axial Dispersion Model (ADM)

Axial dispersion can be described as the spatial gradient of matter and energy that exists in the direction of the theoretical axis of the reactor. In a cylindrical SBCR the axial dispersion will be along the height of the reactor. Dispersion in a SBCR is important in as far as quantifying the extent of mixing in the reactor. Greater mixing would represent conditions closer to those in CSTRs whereas less mixing would represent conditions that reflect a more plug-flow system. In an ideal plug flow reactor system, a unit volume of reactants at a point z in a column will have no interaction with a unit volume at a point $z+\Delta z$ downstream in the column (see Figure 14). This means that the unit volume that is at an advanced position will not mix with or dilute the unit volume that precedes it. The consequence of this is a less homogenous system in which the axial concentration gradients are pronounced. This should lead to a higher reactant conversion rate than can be achieved in an ideal CSTR where the perfect mixing results in no axial concentration gradients.

Use of the axial dispersion model implies the absence of dispersion in the radial direction. The exclusion of radial dispersion in slurry bubble column hydrodynamic models is justified by the relatively small radial dispersion coefficient in comparison with the axial dispersion coefficient. According to Deckwer (1991), radial dispersion coefficients have been found to be less than a tenth of the axial dispersion coefficient. This would suggest that radial dispersion is an insignificant hydrodynamic parameter whose impact on SBCR performance is unimportant. Deckwer (1991) further notes that radial dispersion will only affect reactor performance when the reaction is not 1st order and heat effects are present.

2.1.2 Phase characterization

The presence of multiple phases requires the mixing/dispersion to be understood for each individual phase. The phases in a SBCR are often reduced from three (gas-liquid-solid) to two (gas-slurry) with the slurry phase assumed to be a pseudo-homogenous phase for the purposes of simplicity. In modelling the hydrodynamics in slurry bubble column reactors in

the churn-turbulent regime, de Swart and Krishna (2002) adopted the two-phase model initially proposed by Van Deemter (1961) for gas-solid fluidized beds. Van Deemter (1961) identified dense and dilute phases as the predominant and hydrodynamically important compartments in gas-solid fluidized beds where the dilute and dense phases consisted of the fast-rising gas bubbles and solid catalyst particles respectively. de Swart and Krishna (2002) adapted the two-phase model to slurry bubble column reactors by assigning the dilute phase to the large rising bubbles and the dense phase to the small bubbles trapped in the slurry of liquid and solid suspension.

Wang et al (2008) modelled the hydrodynamics in a SBCR by considering a gaseous and liquid phase only, implicitly assuming that the liquid phase with small catalyst particles in suspension would behave as a single phase. The existence of a pseudo-homogenous slurry phase has been similarly accepted and applied in slurry bubble column models by various authors (Grevskott et al., 1996; Matos et al., 2009; Jianping and Shonglin, 1998; van der Laan, 1999; Schweitzer and Viguie, 2009). Despite the modelling convenience afforded by the pseudo-homogenous assumption in SBCRs, some authors have modelled the process by accounting for all three phases individually (Iliuta et al., 2007; Vik et al., 2016). In these three-phase models, heat and mass transport would have to be modelled for each phase which would add to the computing effort required to apply the model. The accuracy required from the SBCR model will depend on the intended use of the model and time constraints. The two-phase pseudo-homogenous model has proven to be capable of describing the hydrodynamics in SBCRs relatively accurately and will be used as the model of choice in the development of the mathematical model in this study, i.e., the axial dispersion will be defined in the pseudo-homogenous slurry phase and not in the individual liquid phase.

2.1.3 Bubble size distribution

Various researchers have modelled the processes in SBCRs using a 2-class bubble size model (Maretto and Krishna, 1999; van der Laan et al., 1999; Schumpe and Grund, 1986; Rados et al., 2003; Sehabiague et al., 2008). This effectively divides the bubbles in the reactor into two size classes; a large bubble class and a small bubble class usually assumed to be perfectly mixed in the slurry phase (Steynberg and Dry, 2004; Krishna and Sie, 2000). In the churn-turbulent regime, small bubbles coalesce to form larger bubbles and these in turn are broken up into smaller bubbles. These two processes result in a net formation of two distinct bubble sizes present as large and small bubbles ranging from a few millimetres to a few centimeters in diameter (Matsuura and Fan, 1984). It should be noted that the 2-class bubble size model is

only a qualitative approximation of the conditions inside a SBCR rather than an accurate quantitative reflection of the true nature of the bubble dynamics. In reality, a spectrum of bubble sizes exists (Kantarci et al., 2005) but for the benefit of modelling the hydrodynamic behaviour, it is sufficient to refer to relatively large and small bubbles with higher and lower rise velocities respectively.

In all cases referred to above where the 2-class bubble model was adopted, a 2-phase system with a pseudo-homogenous slurry phase is inherently implied. The 2-phase model divides the reactor contents into a predominantly gaseous, large bubble phase and a slurry phase consisting of a mixture of liquid and small bubbles holding a suspension of small solid particles. The two models are therefore inextricably linked so that use of the 2-class bubble model necessitates the application of the 2-phase model, although it does not necessarily follow that the 2-class bubble model is necessary for application of the 2-phase pseudo-homogenous model. The next concern in the hydrodynamic model then becomes the flow model applicable in each phase.

The back-mixing present in the individual phases is an important variable in determining the hydrodynamic behaviour and performance in SBCRs (Sehabiague, 2012) that must be quantified. Concerning the dilute gas phase, most authors have adopted the view that large bubbles move in a plug flow manner through the center of the reactor column, the implication being that no dispersion occurs in the gas phase (Behkish, 1997, Schweitzer and Viguie, 2009; Basha et al, 2015; Gasche et al., 1990; Krishna and Sie, 2000; Sehabiague, 2012). The upward central movement of the large bubble phase has been reported by Krishna and Sie (2000) with Iliuta et al., (2007) treating the reactor as two cylindrical sections with a core and an outer annulus with the large bubbles moving up through the core.

2.1.3.1 Gas phase dispersion

Few studies have incorporated axial mixing in the gas phase. Deckwer et al., (1980) reported on the studies by Mangartz and Pilhofer (1980) (as cited in Deckwer et al., 1980) who attributed the axial dispersion variables in the gas phase to the diameter of the column, superficial gas velocity and gas hold-up. Deckwer et al., (1980) justifies the modelling of axial dispersion in the gas phase only under conditions of high conversion in the reactor. Iliuta et al., (2007) assumed the presence of axial dispersion in the gas phase in preparing a SBCR model. Rados et al. (2005) also incorporated axial mixing in the gas phase in

developing a SBCR model. The author attributed the mixing to the interaction between bubbles of the same class.

Deckwer and Schumpe (1993) argue for the importance of gas mixing in large diameter columns where the coalescence and break-up of bubbles and different bubble rise velocities all contribute to the axial mixing. See Table 3 (Schluter et al., 1992) for a list of studies in which axial dispersion in the gas phase was modelled. The argument for the use of a plug flow model to describe the hydrodynamic behavior in the gas phase is that the dispersion in the gas phase (large bubbles) is constituted predominantly by convective transport (Shah et al., 1978). Schweitzer and Viguie (2009) found that the Peclet number (Pe), which is the ratio of transport by convection to that by diffusion, in large bubbles was over six times more than in small bubbles using a radioactive tracer test. Vermeer and Krishna (1981) report observing a swirling upward movement of large bubbles through the column with no noticeable back-mixing. Based on this evidence, the authors assumed a plug flow movement of the gas phase. Calderbank and Moo-Young (1961) (from Moo-Young et al., 1981) directly contradicts this idea, asserting that axial dispersion in the gas phase is often considerably higher than that in the liquid phase.

Table 3: Gas phase axial dispersion correlations

Correlation	Experimental conditions	Reference
$E_g = 50 D_C^{1.5} \left(\frac{U_g}{\varepsilon_g}\right)^3$		Mangartz and Pilhofer (1980) (as cited in Deckwer et al., 1980)
$E_G = 20 D_C^{1.5} U_g^{0.029}$	$0.2 < D_C < 0.5$ $H = 4.5 \text{ m}$ $0.029 < U_g < 0.45 \text{ m/s}$	Wachi and Nojima (1990)
$E_G = 0.2 D_C^2 U_g$		Towell and Ackerman (1972)
E_G $= 9.36 \times 10^{-5} D_C^{1.3} U_g^{3.56}$		Field and Davidson (1980)

The axial dispersion model appears to be a more accurate representation of the mixing in the gas phase (Rados et al., 2005; Deckwer et al., 1980) with its main drawback being that it can, in some instances, require numerous parameters to be determined which are not readily available due to the high temperature and pressure conditions required in experiments using organic liquids similar those in real FT systems (Deckwer et al., 1980). These multiple

parameters also compound the potential error that would be inherent in the model (Mponzi, 2011).

2.1.3.2 Liquid axial dispersion

The slurry phase dispersion can be attributed to various factors including liquid circulation, turbulence due to entrapment of liquid in bubble wakes and eddy formations (Groen, 2004 and Degaleesan et al., 1997). When a bubble travels up a column of liquid, a wake forms around the bubble which displaces the fluid in the immediate vicinity of the bubble. This phenomenon induces dispersion in the liquid phase through convection, i.e., through the movement of the liquid from one point in the column to another, following the path of the bubble. The movement of a bubble through a fluid also induces eddy currents behind it which create localized turbulence. This is particularly true under high velocity churn-turbulent conditions (Deckwer, 1991). These contributors to liquid phase axial dispersion are lumped together and defined by a single coefficient, the axial dispersion coefficient, E_L .

The axial dispersion coefficient is a quantitative representation of the back-mixing that occurs in fluids inside slurry bubble column reactors. As mentioned above, one of the factors contributing to dispersion in the slurry phase is the circulation of the liquid. Liquid circulation occurs as a result of a radial gas hold-up profile that is prevalent in SBCRs under churn-turbulent conditions. This point shall be discussed in more detail when the cell circulation models are discussed. It is worth pointing out that the circulation model is acknowledged in the ADM as a cause for the dispersion in the slurry phase. The main difference between the ADM and the circulation model is that the ADM does not single out any one factor but rather assigns a single parameter, the axial dispersion coefficient, to describe the overall mixing.

Liquid Axial dispersion coefficient

The liquid axial dispersion coefficient is determined through correlations and is dependent on various hydrodynamic parameters including bubble size, superficial gas velocity, liquid phase velocity, liquid circulation velocity and reactor diameter amongst others. The correlations for the liquid phase axial dispersion coefficient are abundant in literature owing to the popularity of the ADM as a result of its relative simplicity. A comprehensive summary of the various correlations is given by (Basha et al., 2015) and a recurring theme across most of the correlations is the emphasis on the contribution of reactor diameter and superficial gas velocity to the coefficient. The correlations generally assume the form shown in Equation 3:

$$E_L = K D_C^a U_g^b \quad [3]$$

Where the relative effects of D_C and U_g on the dispersion coefficient, E_L , are represented by a and b respectively. K is a proportionality constant. Equation 3 forms the basis on which most of the existing correlations are based (see Table 4). To quantify the constants in Equation 3, tracer experiments are usually conducted. These involve introducing a trace substance into a column with flowing liquid and sparged gas and measuring the distribution of the tracer. The tests can be conducted in a steady-state or non-steady-state environment. Tracer tests have been used to develop multiple correlations, by various authors, which deviate significantly from each other. This deviation is due mainly to the different gas-liquid conditions employed in the tests. Deckwer (1991) notes the geometry of the reactors and the liquid mixture used as the biggest contributors to these apparent discrepancies. The conditions under which tracer experiments are conducted in developing an axial dispersion coefficient correlation are important and should therefore be considered carefully when selecting the most appropriate correlation to use in modelling a specific reactor and in the case of the current study, a SBCR.

Table 4: Various liquid axial dispersion coefficients

Correlation	Experimental conditions	Reference
$E_l = 0,35D_c^{\frac{4}{3}}U_g^{\frac{1}{3}}$	Mechanistic model	Baird and Rice (1975)
$E_l = 1.23D_c^{1.5}U_g^{0.5}$	gas-liquid system, $0.4 < D_C < 1$ m	Towell and Ackerman (1972)
$E_l = 2.7D_c^{1.4}U_g^{0.3}$	gas-liquid system, $20 < D_C < 440$ cm	Deckwer and Robert (1991)
$E_l = [0.15 + 0.69U_g^{0.77}]D_c^{1.5}\left(\frac{1}{\mu_L}\right)^{0.12}$	gas-liquid system, $0,043 < U_g < 0,338$ m/s air and solutions of different viscosities used	Hikita and Kikukawa (1974)
$E_l = g^{0.5}D_c^{1.5}[0.06 + 0.55\left(\frac{U_g}{\sqrt{gD_c}}\right)^{0.7}]$	gas-liquid system, various liquids including <i>NaCl</i> solution and methanol gas included air, O_2 , He and CO_2	Akita and Yoshida (1973)
$E_l = 0.3D_c^2U_g^{1.2}$	air/water system $40 < D_C < 160$ mm	Ohki and Inoue (1969)

Effect of superficial gas velocity

The axial dispersion coefficient shows a positive correlation with the superficial gas velocity. All the correlations cited in Table 4, despite the different experimental conditions, imply that increasing the superficial gas velocity should increase the axial dispersion coefficient. The relationship between the two variables is exponential, with some correlations predicting a more linear relationship than others, e.g, correlations by Hikita and Kikukawa (1974) and Pilhofer et al. (1978) versus those of Baird and Rice (1975) and Deckwer et al (1974). In Figure 6, an illustration of this comparison has been plotted. As the velocity of the gas is increased, the turbulence inside the column increases leading to a greater degree of mixing in

the liquid phase. Additionally, increased superficial gas velocity positively affects the gas hold-up (Behkish et al., 2006; Kim et al., 1992; Reilly et al., 1986; Hikita et al., 1980; Schumpe et al., 1987) which in turn increases the rate of liquid circulation (Shah et al., 1978). The higher rate of liquid circulation induces more axial mixing.

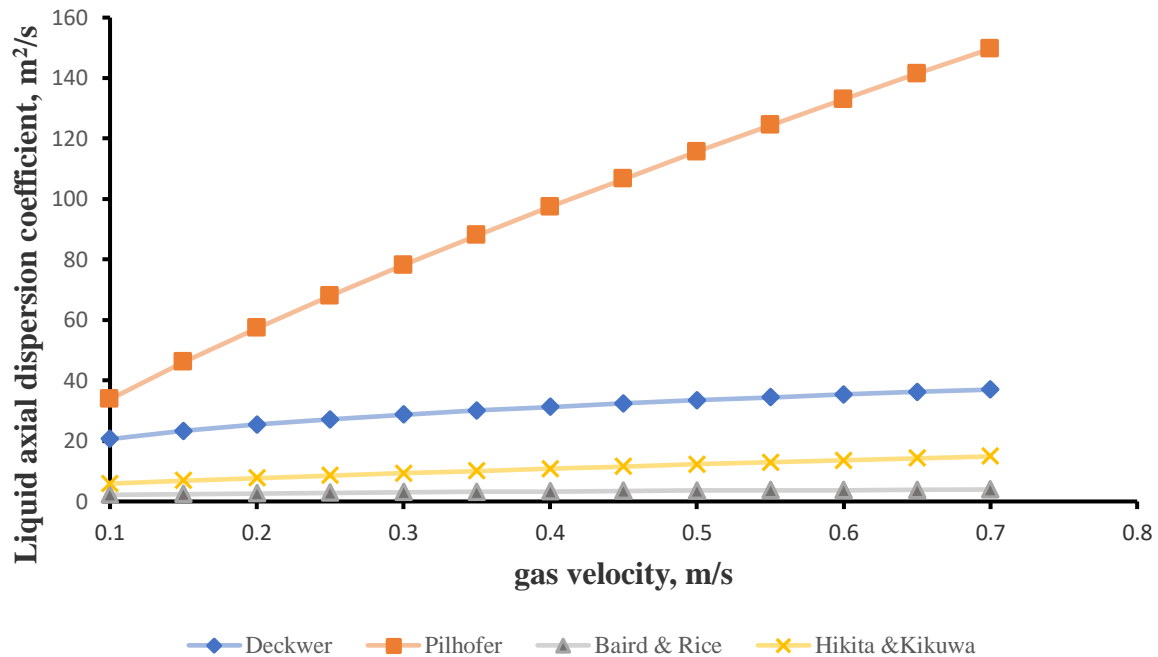


Figure 6: Liquid axial dispersion coefficient as a function of superficial gas velocity

Effect of column diameter

Similar to the superficial gas velocity effect, the column diameter is widely accepted as playing a key role in determining the liquid axial dispersion coefficient. As can be seen in Table 4, most existing correlations attribute an increasing axial dispersion to an increase in the column diameter. The dispersion coefficient is seemingly more sensitive to changes in the column diameter than to those in the superficial gas velocity (Ohki and Inoue, 1969) as evidenced by the higher exponential term associated with the diameter (1.25-1.5) compared to that associated with the superficial gas velocity (0.3-0.5) (Schweitzer and Viguie, 2009). A larger column diameter will promote turbulence in the reactor leading to greater back mixing in the liquid phase. According to (Joshi and Sharma, 1979 and Mavros, 1993), the liquid circulation velocity is higher in larger diameter columns which results in greater mixing as will be explained when the effect of liquid circulation velocity on the axial dispersion coefficient is discussed.

Effect of liquid circulation

Evidence from (Devanathan, 1991 and Degaleesan et al., 1997) suggests that two axysymmetrical liquid circulation cells, spanning the height of the reactor, form at relatively high superficial gas velocities in large diameter (>1 m) reactors. These cells form as a result of the radial gas hold-up distribution present in the column with more gas bubbles moving through the centre of the column than near the wall. The higher gas hold-up in the centre causes liquid to move up through the middle and down near the wall where the gas hold-up is lower. Figure 7 was drawn to illustrate this phenomena. This convective liquid circulation contributes to the axial mixing in the liquid phase (Degaleesan et al., 1997; Zehner, 1982(as cited in Basha et al., 2015); and Joshi and Sharma, 1979).

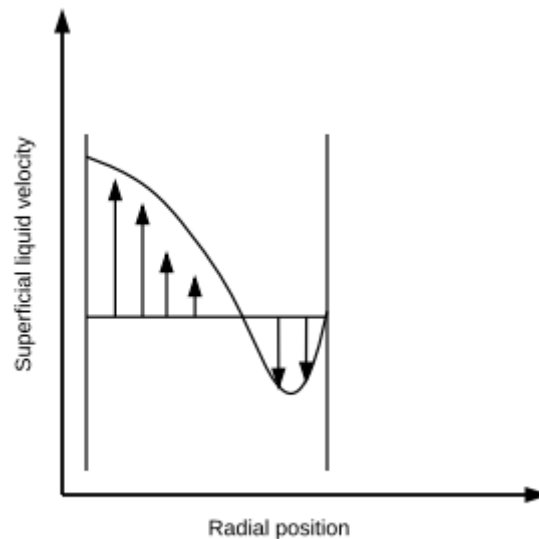


Figure 7: Radial liquid superficial velocity distribution

Other authors (Joshi and Sharma, 1979 and Joshi, 1980) have suggested the existence of multiple circulation cells in the column and used their average circulating velocity to describe their effect on liquid axial mixing. Joshi and Sharma (1979) argue that the single cell structure will not be stable in shallow ($H/D_c < 0.5$) and tall ($H/D_c > 5$) columns resulting in the formation of multiple smaller cells spanning the length or breadth of the column (see Figure 9). The multiple cell model developed by Joshi and Sharma (1979) produced favourable results in terms of predicting liquid axial dispersion. Perhaps the main disadvantage of this proposed model for the effect of liquid circulation velocity on the axial dispersion coefficient is that the existence of multiple cells in large diameter columns (>1m)

is questionable as it is not backed by experimental evidence (Basha et al., 2015). Also, the superficial gas velocity under which the model was tested was limited between 0.19 – 9.2 cm/s which falls short of the typical velocities experienced in commercial large scale SBCRs in the region of 0.2 – 0.4 m/s (Krishna, 2000). This casts doubt over the model's ability to accurately predict liquid phase axial mixing under extreme superficial gas velocity conditions.

Effect of liquid properties

Surface tension

Kim et al. (1992) studied the effects of liquid surface tension on the liquid axial dispersion coefficient and found that increasing the surface tension of the liquid phase had little and insignificant effect on the dispersion coefficient. The dispersion coefficient increased only slightly when the surface tension was increased from 32 to 72.8 mN/m. Hikita and Kikukawa (1974) found the surface tension to affect the liquid phase axial dispersion minimally when the surface tension of the liquid was varied between 38.2 and 75.5 mN/m, leading to the conclusion that the surface tension of the liquid in a bubble column is unimportant in determining the liquid phase axial dispersion. To this end, Aoyama et al. (1968) noted that the properties of the liquid phase do not have any effect on the liquid phase axial dispersion coefficient. Kelkar et al. (1984) also observed that there was a small decrease in the liquid phase axial dispersion with a decrease in the liquid surface tension. The author attributed this to the slower bubble rise velocity in liquids that have a lower surface tension leading to reduced axial mixing. This is a plausible explanation as bubbles moving through liquid with a higher surface tension can be expected to be 'pushed' out of the liquid by the more stable water surface. This can also be explained by noting that bubbles in liquid with a higher surface tension will be less prone to breaking up and forming smaller bubbles. As large bubbles rise faster, this would increase the liquid circulation and mixing resulting in a higher liquid phase axial dispersion. To this regard, Schumpe et al. (1987) refers to an increase in the proportion of small bubbles in bubble columns as the surface tension is decreased.

Viscosity

Increasing the viscosity of the continuous phase retards turbulence in the column and this has a negative effect on the axial mixing in the liquid phase. Increasing the liquid viscosity also has a positive effect on the axial mixing, i.e., the retarded turbulence slows the rate of bubble breakage thus producing a bubble size distribution that is dominated by larger bubbles (Wu et al., 2013). The net result is an insignificant change in the axial dispersion coefficient of the

liquid phase although (Kim et al., 1992) studies showed a tendency for the dispersion coefficient to slightly decrease with increasing liquid viscosity (1-72.5 mPa.s). Hikita and Kikukawa (1974) found that the axial dispersion coefficient had a proportional relationship that is to the power of -0.12 with the liquid viscosity. It should be noted though that in the study by Hikita and Kikukawa (1974), viscosity was varied between 1 and 19.2 mPa.s which is a smaller and less representative range than that used by Kim et al. (1992). The small decrease in the dispersion coefficient is also thought to be caused by large fast rising bubbles that carry less of the slurry in their wake leading to reduced mixing (Towell and Ackerman, 1972). There seems to be a general acceptance that the liquid phase viscosity has very little impact on the mixing in the slurry phase and that if it does the effect is minimally negative.

Isotropic model

Baird and Rice (1975), based on the work by Kolmogorov (1941) and Hinze (1959), determined that the isotropic turbulence model can be applied to bubble columns provided that no baffles, internals or packing is present inside the column. The work of Kolmogorov (1941) is based on the assumption of equal and uniform turbulence of a fluid in all directions. From this, the author arrived at a correlation for eddy diffusivity/dispersion as shown in Equation 4.

$$E = Kl^{4/3}P_m^{1/3} \quad [4]$$

Where E is the eddy dispersion, l is the characteristic length parameter referring to the scale of the system, P_m is the specific energy dissipation rate and K is a dimensionless constant. Baird and Rice (1975) defined the specific energy dissipation for bubble columns as:

$$P_m = U_g g \quad [5]$$

Where U_g is the superficial gas velocity and g is the gravitational acceleration constant. Furthermore, the characteristic length, l , was taken as the diameter of the column, D_C , so that Equation 4 could be re-written as:

$$E_L = KD_C^{4/3}(U_g)^{1/3} \quad [6]$$

Where K is a dimensionless constant with a value of 0.35 (Baird and Rice, 1975; Schweitzer and Viguie, 2009; Groen et al., 1996). The isotropic turbulence model, as adapted for use in bubble columns in Equation 6, compared favourably with other models used to predict the axial dispersion coefficient and can be applied under a range of conditions (Baird and Rice,

1975). Deckwer and Schumpe (1993) note that most axial dispersion coefficient models can be reduced to a form similar to the isotropic model. It is important to note the conditions under which this model is applicable, i.e, turbulent flow in the absence of internals, packing and/or baffles. Industrial slurry bubble columns are operated under turbulent conditions but they also have solid catalysts in suspension which may disqualify the use of the isotropic turbulence model. It is also important to note the theoretical nature of this model and its importance in potentially contributing to the mathematical development, from 1st principles, of the hydrodynamic models in slurry bubble column reactors. This is at this stage the most widely accepted theoretical model for the description of the axial dispersion coefficient in bubble columns. In attempting to develop a model that relies heavily on mechanistic principles, thereby ensuring the accuracy and versatility of the model, the isotropic turbulence model to describe the axial dispersion in the slurry phase will be adopted for use in the current work.

2.1.3.3 Cell Circulation models

Multiple cell circulation models (MCCM) are a different class of models to ADMs in that they seek to explain the liquid phase mixing in SBCRs through liquid entrainment and cross-flows inside the reactor. MCCMs are characterized by a circular movement of material inside the SBCR. This movement induces mixing in the slurry phase and is physically described by velocity and momentum profiles. It is generally assumed that the cause of the circulation is the radial gas hold-up profile that prevails in the column under churn-turbulent flow conditions (Ueyama and Miyauchi, 1979; Joshi et al., 2002). The gas hold-up is higher in the center of the column than near the wall and this results in momentary entrapment of the liquid in the gas phase as the gas travels up the center of the column (Ueyama and Miyauchi, 1979). It should be noted that the 2-bubble class conceptual model is implied in the circulation model. As the gas disengages at the top of the reacting bed, the liquid travels down the column near along the wall. This creates a circular motion of the liquid.

Joshi (2001) considered the presence of one circulation cell spanning the whole height of a column (see Figure 8) but this seems highly unlikely in tall columns where the circulation cell would need to maintain stability over a longer length. Joshi et al. (2002) alludes to this point and also maintains that the single cell would not be stable in shallow columns either. Zehner, (1982a) has observed the presence of multiple cells along the length of a bubble column as shown in Figure 9.

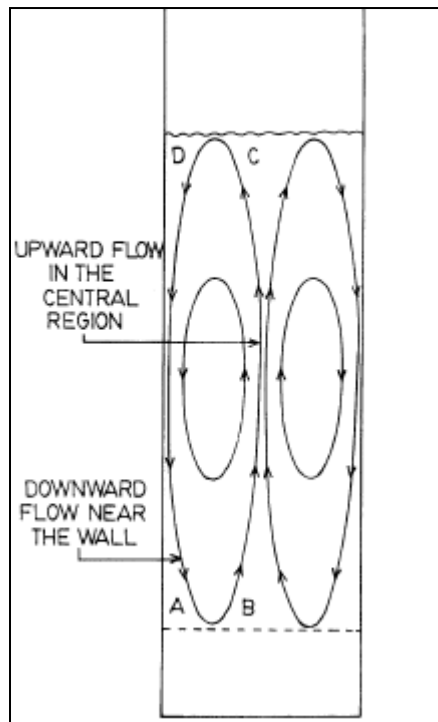


Figure 8: Single circulation cell spanning entire column height (Joshi, 2001)

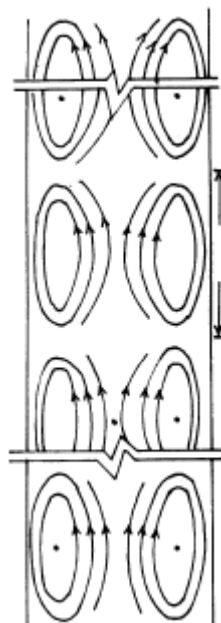


Figure 9: Multiple cell structure along column height (Joshi, 2001)

Various authors have investigated different forms of MCCM (Joshi and Sharma, 1979; Joshi, 1980; Schluter et al., 1992) with the main differences in the models arising from the boundary conditions used in solving the models and the perceived driving force of the liquid

phase circulation. Some, like Millies and Mewes (1994), attribute the circulation to the turbulence induced by the non-uniform gas hold-up in the reactor. The extent of circulation is dependent on the relative viscosities of the gas and liquid phases (De Nevers, 1968) and so it is important that the model parameters used are determined from experiments conducted with fluids similar to those in FTS and not air/water systems.

Circulation models give detailed attention to the velocity and momentum forces as the cause of axial mixing in the slurry phase. There is no dispute that the slurry phase undergoes extensive axial mixing or that circulation of the slurry phase occurs inside the SBCR. This stems from the generally accepted notion that large bubbles move in bulk through the center of the column while small bubbles are interspersed in the slurry phase. The main difference between the circulation models and the ADM is the way the mixing is conceptualized and characterized. In the circulation models, the concept is that the velocity of the circulating cells is directly involved in the mixing and so its value is determined through application of the continuity equation. The ADM on the other hand is based on the concept of a wholistic description of the causes of mixing using a single parameter. This approach seems more versatile as it attempts to describe the mixing as a sum of all possible causes. The main disadvantage of the ADM is the lack of reliable correlations available for parameter estimation. Most correlations have been derived from experiments conducted under conditions greatly dissimilar to those in industrial settings as seen in Table 4. Despite this, the ADM remains the most suitable hydrodynamic model for SBCR modelling given its ease of application and versatility. The ADM will therefore be used as the model of choice in developing the mathematical model in this work.

2.2 Kinetics

The SBCR is a heterogenous system and is thus represented kinetically by heterogenous catalysis. Reactants enter the reactor in the gas phase and diffuse through the gas-liquid interphase into the liquid phase and through the solid-liquid interphase into the solid phase where the reaction occurs (see Figure 10). The overall kinetics of this system can be driven by either of the processes shown in Figure 10. These processes can be further classified into mass transfer and kinetic factors so that the overall kinetics are determined by the rate of mass transfer or that of the surface kinetics.

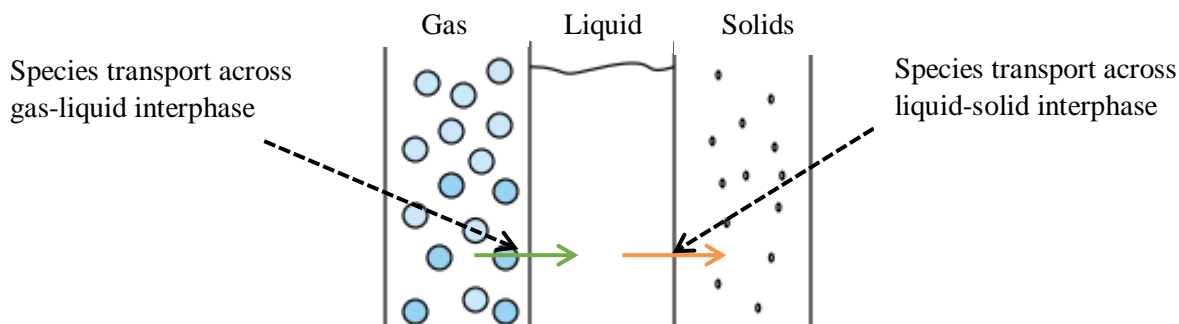


Figure 10: Species transport across three phases in SBCR

2.2.1 Mass transfer controlled rate

In a gas-solid-liquid system such as in a SBCR the reactants, namely CO and H₂, are sparged into the reactor as a gas. The reactants rise through the reactor in bubble form and have to travel to the solid catalyst surface where the reaction can take place. The reactants first need to be transported from the gas phase to the liquid phase which is made up of high molecular weight wax products. The rate at which this transfer occurs is important in the context of the overall rate of reaction and is governed by the mass transfer coefficient between the gas and liquid. Once the reactants are in the liquid phase, they are transferred to the solid catalyst surface via the solid-liquid interphase. The rate of this transfer process can also affect the rate of the overall reaction. The mass transfer processes from the gas phase to the solid phase constitute the external mass transfer phenomena because they occur outside the catalyst reactive surface area. Internal mass transfer refers to the transport of mass within the catalyst to the active sites where the reaction can take place.

The gas-side mass transfer resistance, i.e., mass transfer resistance located in the bulk gas phase, is typically ignored as its role in the overall kinetics of the system is negligible (Behkish, 1997; Deckwer and Schumpe, 1993). The liquid solid mass transfer resistance is usually negligible given the very small nature of the catalyst particles (Behkish, 1997; Gwamo et al., 2005). The small particles expose a relatively large mass transfer surface area so that the retardation of the mass transfer across the boundary as a result of the mass transfer coefficient is almost nullified. Gwamo et al. (2005) found that typical industrial SBCRs operate with catalyst particles in the range between 20 and 120 μm . The exclusion of the liquid-solid mass transfer resistance means that the only external mass transfer resistance of importance is that between the gas and liquid phases. To this effect, Inga and Morsi (1996) note that the gas-liquid mass transfer is the only important mass transport phenomena outside

of the catalyst particle. As mentioned earlier, the gas-side mass transfer resistance is usually very small so that the mass transfer across the boundary is represented through the liquid side mass transfer resistance. Internal diffusion can be safely assumed to be negligible considering the small nature of the catalyst (Gwamo et al., 2005). This makes the gas-liquid mass transfer phenomenon the only step to significantly affect the transfer of mass in the FTS.

2.2.1.1 Surface kinetics

The kinetics on the surface of a catalyst are governed by the processes of adsorption, chemical reaction and desorption as illustrated in Figure 11. Adsorption refers to the attachment of the reactant molecules to the surface of the catalyst before they can react and desorption refers to the de-attachment of the resulting products from the surface of the catalyst into the bulk liquid phase. The surface kinetics can be limited by either of the aforementioned processes and it is thus important to clearly understand each process and the underlying mechanisms therein.

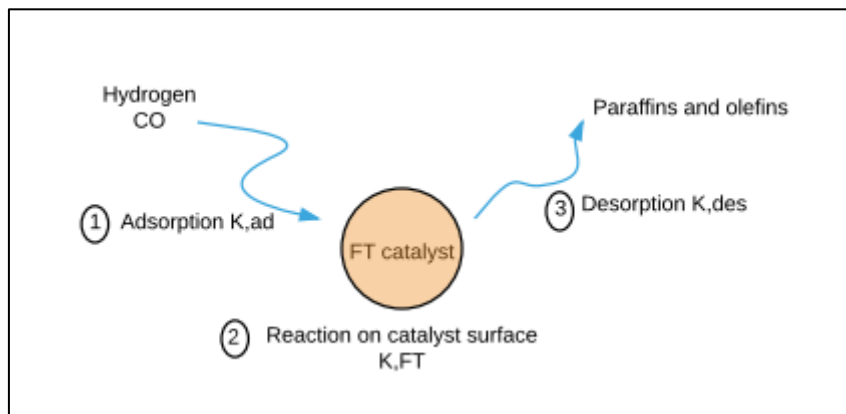


Figure 11: Adsorption, reaction and desorption of FT species around catalyst

Adsorption

When a molecule adsorbs onto a catalyst, the extent to which the molecule can cover the surface of the catalyst, referred to as the surface coverage θ , is dependent mainly on the concentration of that particular species in the bulk fluid phase. θ describes the fraction of the surface of the catalyst covered by a reactant species. A higher concentration would result in more surface coverage. Other factors including the adsorption constant affect the surface coverage as well and are an important factor to consider in modelling the adsorption process. The process of species adsorption can follow various mechanisms depending on the prevailing operating conditions.

Method of adsorption

An adsorbed reactant species will react with either another adsorbed species or with a species from the bulk fluid phase. The former and latter phenomena are referred to as dual and single site mechanisms respectively and ultimately affect the kinetics of the system. Furthermore, the reacting molecules can adsorb competitively or non-competitively. In the case of multiple reactants, the adsorbing molecules may compete for the same active site on the surface of the catalyst or the reactants may react on separate classes of active sites. The surface coverage of a reactant, which is the equivalent of concentration in homogenous reaction systems, is determined with the use of an isotherm. The Langmuir isotherm described in Equation 7 relates the concentration of the reactant in the bulk liquid phase with the surface coverage by introducing the adsorption constant. The Langmuir isotherm is predicated on a few assumptions (Levenspiel, 1999);

1. The adsorption process is in equilibrium.
2. The catalyst surface behaves ideally, i.e., all sites have equal activity.
3. The adsorbed molecules do not interact with each other.

$$\theta_A = \frac{K_A P_A}{1 + K_A P_A} \quad [7]$$

Where A is an arbitrary reactant species, K_A is the adsorption equilibrium constant and P_A is the concentration of A in the bulk fluid phase which can also be represented by C_A in the event that the fluid phase is liquid. Equation 7 is specifically for a system where A adsorbs onto the active catalyst site without competition. The surface coverage of A would be retarded if more reactants were present to compete for the same site as shown in Equation 8.

$$\theta_A = \frac{K_A P_A}{1 + K_A P_A + K_B P_B + K_C P_C + \dots + K_{m-1} P_{m-1} + K_m P_m} \quad [8]$$

If the adsorption step is rate limiting, then the rate equation will take the form:

$$R = k_{ads}[A][*] \quad [9]$$

Where $[*]$ represents the concentration/number-density of vacant active sites on the catalyst surface and k_{ads} represents the adsorption rate constant. $[*]$ can be determined through a catalyst site balance by understanding that the total available sites are shared between occupied and unoccupied sites thus:

$$[*]_0 = [*] + [A*] \quad [10]$$

Where $[*]_0$ denotes the total concentration of active sites on the catalyst surface and $[A^*]$ represents the concentration of sites occupied by a reactant molecule which can in turn be determined by understanding the definition of surface coverage as shown in Equation 11.

$$\theta_A = \frac{[A^*]}{[*]_0} \quad [11]$$

Equation 9 is possible due to the assumption of pseudo-equilibrium for the surface reaction rate and the desorption rate (Sinnot, 2005). It is common and reasonable practice to assume that the other surface processes besides the rate limiting step are in pseudo-equilibrium (Davis and Davis, 2003). Following the same logic and assuming pseudo-equilibrium for the surface reaction and the adsorption step when the desorption step is rate-limiting; the overall rate will take the form:

$$R = \frac{k_3 K_2 K_1 [*]_0 [A]}{1 + (K_1 + K_2 K_1) [A]} \quad [12]$$

Where k_3 denotes the desorption rate constant, K_1 and K_2 represent the equilibrium adsorption and reaction constants respectively.

Chemical reaction

The chemical reaction kinetics will depend on the surface coverage of the reacting species which in turn depend on the adsorption isotherm. In simple homogenous elementary single reactions, the rate law, i.e., the equation that defines the rate of reaction, is easy to determine. The reactions in FTS are multiple and non-elementary, occurring on a catalyst surface. This introduces a level of difficulty in determining a rate law that will satisfactorily model the rate and thus the reactant conversion as a function of the prevailing reactor conditions. In determining a rate law, the reaction constants of the elementary reactions must be known and consolidated to give the resulting rate law for a particular reacting system. This means that for FTS, in which multiple reactions take place and even more elementary reaction steps are present, the task of determining the rate law is made difficult. To deal with this difficulty, FT reactions are lumped together according to the products formed and the total number of reactions is reduced accordingly. In general, the important reactions in FT are those that form paraffins and olefins. The water-gas-shift (WGS) reaction is also important, along with the reactions responsible for alcohol formation and the Boudouard reaction as seen in Table 5. In SBCRs operating under the typical conditions as set out in Table 6, the FT reaction can be represented generally by [R7].

Table 5: Main FTS reactions

Name	Reaction	
Paraffin Formation	$(2n + 1)H_2 + nCO \rightarrow C_nH_{2n+2} + nH_2O$	R6
Olefin Formation	$2nH_2 + nCO \rightarrow C_nH_{2n} + nH_2O$	R7
Water Gas Shift	$H_2O + CO \rightleftharpoons H_2 + CO_2$	R8
Alcohol Formation	$2nH_2 + nCO \rightarrow C_nH_{2n+2}O + (n - 1)H_2O$	R9
Boudouard Reaction	$2CO \rightleftharpoons CO_2 + C$	R10

The next step is to determine the reaction rate constants of the elementary steps of the lumped reactions. This requires the understanding of the mechanism through which each of these reaction types occur. This is the most important step and is a point of contention among researchers. FTS is a polymerisation reaction with hydrocarbon molecules coming together to form longer chain products. The difficulty in describing the FTS reaction lies with the mechanism by which these long chain hydrocarbon products are formed. Various mechanisms have been put forward to account for the way the hydrocarbon products are formed and depending on the mechanism chosen, the rate equation will be different. One of the mechanisms proposed is the surface carbide mechanism where methylene acts as the monomer on which the propagation of chain growth is based (Brady and Pettit, 1981; Ojeda et al., 2010; Fischer and Tropsch, 1926). In this mechanism, CO and H₂ adsorb dissociatively and the chain growth proceeds through the repeated insertion of the monomer (see Figure 12). Although this mechanism has received criticism stemming from the model's inconsistency with thermodynamic data relating to the formation of hydrocarbons through hydrogenation at elevated industrial temperatures (Craxford and Rideal, 1939). Davis (2009) used tracer studies in conjunction with available characterisation data as a basis for endorsing the use of the surface carbide mechanism in Co catalysed FTS. The author further suggests use of the oxygenate mechanism for Fe catalysed FTS.

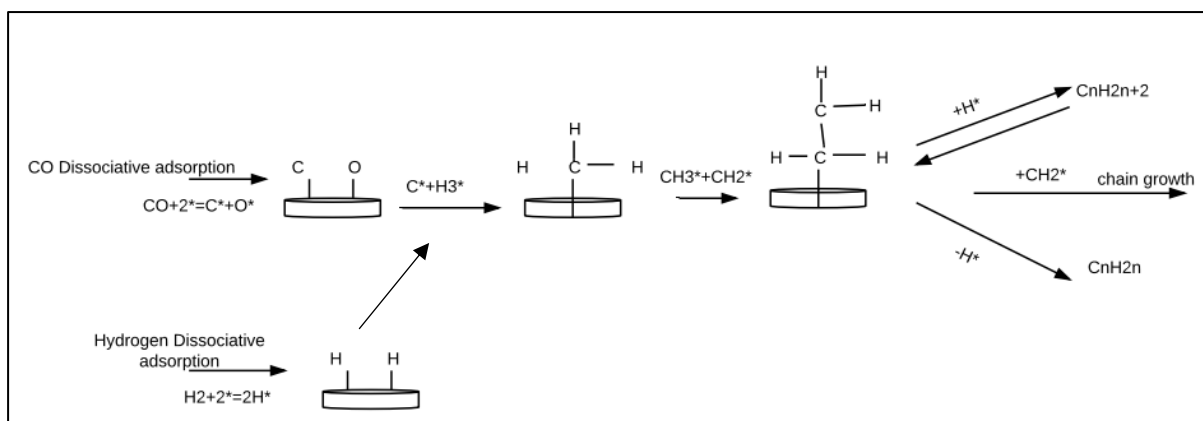


Figure 12: Surface carbide mechanism

Table 6: Typical SBCR operating conditions (Krishna and Sie, 2000 and Behkish et al., 2006)

Operating Conditions	
Reactor Temperature (K)	473 - 530
Reactor Pressure (bar)	20 - 30
Dispersion height (m)	30
Reactor diameter (m)	5 - 7
Catalyst loading (v/v)	0.05 - 0.35
Gas superficial velocity, U_G (m/s)	0.05 - 0.5
Liquid superficial velocity (m/s)	$0.1U_G$
Liquid phase properties	
Density (kg/m^3)	640 - 696
Viscosity (Pa.s)	0.00029 - 0.004
Surface tension (N/m)	0.01 - 0.018
CO diffusivity (m^2/s)	17.2×10^{-9}
H ₂ diffusivity (m^2/s)	45.5×10^{-9}
Solid phase properties (Co/MgO catalyst supported on SiO₂)	
Catalyst diameter (m)	42×10^{-6} - 50×10^{-6}
Catalyst density (kg/m^3)	647

Various mechanisms can be differentiated based on the type of monomers present and the propagation pathways followed. Chang et al., (2007) describes six different reaction mechanisms based upon these two factors (see Table 2). In the proposed mechanisms, the propagation step was assumed to be rate-limiting so that all other steps were taken to be quasi-equilibrated or in pseudo-equilibrium. The kinetics are also affected by the type of catalyst used with different rate equations resulting from the use of either Fe or Co catalysts. Reaction mechanisms can also be differentiated by the way in which the reactants adsorb onto the catalyst surface. The two main adsorption models are the Langmuir-Hishelwood-Hougen-Watson (LHHW) and the Eiley-Rideal models. These models were formulated to

describe the adsorption mechanisms of reactants in heterogeneously catalysed reactions. In the LHHW model, all the reactants adsorb onto the catalyst surface at separate active sites before reacting with one another and in the case of Eley-Rideal models only one of the reactants adsorbs onto an active catalyst site before reacting with an unadsorbed reactant (Albright, 2009). Eley-Rideal models are more important under extreme conditions, particularly in the semiconductor production field whereas LHHW models are more common in catalysed reactions (Davis and Davis, 2003).

Once a reaction mechanism is identified, the rate controlling step within that mechanism must be identified to allow for the development of the rate law, provided the surface reaction is rate limiting. Through the use of steady-state approximation, the overall rate law based on the rate limiting step can be determined (Equation 13). The steady-state approximation is based on the assumption that the concentration of an intermediate in a multiple elementary reaction system is constant, i.e., its rate of formation is equal to its rate of consumption. The steady-state approximation can greatly simplify the process of determining an overall surface reaction rate when applied to the limiting reaction step and a quasi-equilibrated step. A quasi-equilibrated step is a combination of the rest of the elementary reaction steps which are assumed to be in equilibrium. This in effect reduces a complex system of multiple elementary reactions to a simplified set of reactions on which the overall surface reaction rate can be derived (Davis and Davis, 2003).

$$R = \frac{r_i - r_{-i}}{\sigma_i} \quad [13]$$

Where R is the overall rate, r_i is the forward reaction rate, r_{-i} is the reverse reaction rate and σ_i is the stoichiometric number of the elementary reaction step. The final equation should take the form shown in Equation 14.

$$R = \frac{k_2 K_{ads} [A]}{1 + K_{ads} [A]} \quad [14]$$

Where k_2 represents the reaction rate constant. Equation 14 exemplifies a typical LHHW rate law given by:

$$Rate = \frac{(kinetic\ term)(potential\ term)}{adsorption\ term} \quad [15]$$

The overall rate law is usually determined empirically by assuming a reaction scheme and determining the reaction and adsorption constants through regression analysis. According to Levenspiel (1999), all possible reaction pathways with all possible rate-limiting steps should

be noted at which stage experiments can be used to disprove and exclude those pathways that do not fit the data. The author also cautions against the assumption that a pathway that fits the data perfectly represents the correct reaction mechanism as more than one mechanism may fit the data. It is therefore difficult to determine accurately the mechanism by which FT reactions occur. Nonetheless, several authors have put forward rate laws to describe the kinetics in FTS for both Co and Fe catalysed systems. Espinoza et al. (1999), Pratt (2012) and Sehabiague (2012) provide a summary of these rate laws (see Table 7).

Table 7: Various Kinetic rate laws

Catalyst	Rate law	Reference
Co	$R_{FT} = k_{FT} \frac{P_{H_2}^2}{P_{CO}}$	Brotz (1949)
Co	$R_{FT} = k_{FT} \frac{P_{CO}^{0.5} P_{H_2}^{0.5}}{(1+aP_{CO}^{0.5})^2}$	Sarup and Wojciechowski (1989)
Co	$R_{FT} = k_{FT} \frac{k P_{CO} P_{H_2}}{(1+aP_{CO})^2}$	Yates and Satterfield (1991)
Fe	$R_{FT} = k_{FT} \frac{P_{CO} P_{H_2}}{P_{CO} + a P_{CO_2}}$	Nettelhoff et al. (1985)
Co	$R_{FT} = k_{FT} \frac{P_{H_2}^2 P_{CO}}{P_{CO} P_{H_2} + a P_{H_2} O}$	Withers et al. (1990)
Co	$R_{FT} = k_{FT} \frac{P_{H_2}^{1.5} P_{CO}}{(a P_{CO} P_{H_2} + P_{H_2} O)^2}$	Schweich et al. (2007)
Fe	$R_{FT} = k_{FT} \frac{P_{H_2}^{0.5} P_{CO}}{(1+aP_{CO}+bP_{CO_2})^2}$	van der Laan (1999)
Fe	$R_{FT} = k_{FT} \frac{\frac{P_{H_2}^{1.5} P_{CO}}{P_{H_2} O}}{(1+a \frac{P_{CO} P_{H_2}}{P_{H_2} O})^2}$	van Steen and schulz (1999)

2.2.2 Catalysts

In general, FT processes catalysed by a Co catalyst are negligibly affected by the presence of water. This is because Co catalysis does not promote the water gas shift reaction which affects the consumption of H₂. The opposite is true for Fe catalysis (Espinoza et al., 1999). Co catalysts generally achieve a higher per pass conversion than Fe catalysts and are thus more favoured in FT systems (Espinoza et al., 1999). Being more expensive than Fe catalysts, tolerance for attrition and/or deactivation of this catalyst is typically low from an economic point of view. Compared to high temperature FT reactors whose high superficial gas

velocities and turbulence create a violent environment in which a Co catalyst would quickly degrade, SBCR conditions are less violent allowing the Co catalyst to last longer and thus justify their cost.

Yates and Satterfield (1991) developed a rate law based on Co catalysis in a continuous stirred tank reactor (CSTR). The authors modified the rate laws postulated by Sarup and Wojciechowski (1989) and Wojciekwocki (1988) and tested the resulting rate laws under 220 – 240 °C, 0.5 to 1.5 bar and H₂/CO ratios between 1.5 and 3.5. The rate law that accurately predicted the experimental results was selected (Equation 16). Equation 16 was tested against data from other sources (Wojciekwocki, 1988) and was found to be capable of producing accurate results. In Equation 25, *a* and *b* represent the kinetic and adsorption constants respectively.

$$-R_{CO} = \frac{kP_{CO}P_{H_2}}{(1+aP_{CO})^2} \quad [16]$$

With regard to the control of the overall rate between mass transfer and surface kinetics, Inga and Morsi (1996) note that the resistance to the FT process lies significantly with the kinetics so that the surface kinetics would have to improve by a great margin for the gas-solid mass transfer to be rate-limiting. Deckwer et al. (1980) also puts forth an argument to this effect. For the purposes of this research project, the rate law as proposed by Yates and Satterfield (1991) will be applied.

2.3 Mass transfer

As previously mentioned, the only significant mass transfer resistance in a SBCR is the gas to liquid mass transfer. The transfer of matter across the gas-liquid boundary is generally assumed to receive the most resistance on the liquid side of the interphase and as a result the total gas-liquid mass transfer phenomenon is based on the liquid side. Using the two-film theory, it can be shown that the mass flux from the bulk gas to liquid phase can be written thus:

$$J = k_L(C^*_L - C_L) \quad [17]$$

Where *J* represents the mass flux, *C_L* is the concentration in the bulk liquid phase, *C^{*}_L* is the liquid side interfacial concentration and *k_L* is the mass transfer coefficient. The mass transfer coefficient is a function of the gas-liquid diffusivity *D_{GL}* and liquid film *δ* thickness thus:

$$k_L = \frac{D_{GL}}{\delta} \quad [18]$$

To represent the flux in units of mass/time, the volumetric mass transfer coefficient k_{La} is often used where a denotes the interfacial area. The interfacial liquid phase concentration can be related to the partial pressure in the bulk gas phase through Henry's law with the assumption that equilibrium exists between the two phases as shown in Equation 19.

$$C_{i,L}^* = \frac{P_i}{H_i} \quad [19]$$

Where P_i is the partial pressure of species i in the gas phase and H_i is Henry's constant for species i and $C_{i,L}^*$ is the concentration of species i in the gas phase at the gas-liquid interphase under equilibrium conditions.

2.3.1 Mass transfer coefficients

Mass transfer and therefore the mass transfer coefficient depends strongly on the bubble size so that small bubbles with a greater interfacial area allow more mass transfer than larger bubbles with less area for mass transfer (Basha et al., 2015). Liquid phase dispersion can influence the volumetric mass transfer coefficient (Inga, 1997) meaning that those variables that affect dispersion will also have an impact on the mass transfer coefficient as well. These include the column size and superficial gas velocity. Various correlations for volumetric mass transfer coefficients are given in Table 8.

Table 8: Volumetric mass transfer coefficient correlations

Correlation	Experimental conditions	Reference
$K_{La} = 0.5\varepsilon_g$		Vermeer and Krishna (1981)
$K_{La, LB} = 0.5\varepsilon_{g, LB} \sqrt{\frac{D}{D_{ref}}}$ $K_{La, SB} = \varepsilon_{g, SB} \sqrt{\frac{D}{D_{ref}}}$		Vemeer and Krishna (1981)
$K_{La} = cD^{0.5} \left(\frac{\mu_L}{\rho_L}\right)^{-0.62} D_C^{0.17} g^{0.93} \varepsilon_g^{1.1}$	$D_C = 15.2 \text{ cm}$ $H = 400 \text{ cm}$	Akita and Yoshida (1973)
$K_{La} = \frac{6.14 \times 10^4 \rho_L^{0.26} \mu_L^{0.12} \varepsilon_g^{1.21} D^{0.5} \gamma^{0.11}}{\sigma^{0.52} \rho_g^{0.06} U_g^{0.12} d_b^{0.05} T^{0.68}} \left(\frac{D_C}{1+D_C}\right)^{0.4}$		Lemoine et al. (2008)
$K_{La} = 4.41 U_g^{0.338} \varepsilon_S^{0.595} \left(1 - \frac{\rho_L}{\rho_p}\right)^{0.337}$	$0.0025 < D_C < 0.05 \text{ m/s}$ $D_C = 0.06 \text{ m}$	Guo et al. (1997)
$K_{La} = 0.4 U_g^{0.625} U_L^{0.26} e^{(1.477 \times 10^{-5} H)}$	$0.02 < D < 0.04 \text{ m/s}$ $D_C = 0.05 \text{ m}$	Chen et al (2001)

Vermeer and Krishna (1981) have suggested a simple correlation for the mass transfer coefficient that relates the coefficient only to the gas hold-up (Equation 20). Steynberg and Dry (2004) recognise this correlation as a rule of thumb. Following a similar correlation, Vermeer and Krishna (1981) and Letzel et al. (1999) have provided correlations for large and small bubbles, making a clear distinction between the coefficients of the two size classes. Krishna and Sie (2000) modified the correlation put forward by Letzel et al. (1999) by introducing the liquid phase diffusive coefficient.

$$K_{La} = 0.5\varepsilon_g \quad [20]$$

Correlations by Akita and Yoshida (1973) and Calderbank and Moo-Young (1961) have garnered a lot of popularity over the years but as Maretto, and Krishna (1999) and Schweitzer and Viguie (2009) note, the correlations have limited applicability in SBCRs operating in the heterogenous regime with predominantly large bubbles. The aforementioned authors developed correlations for small bubbles in reactors operating in the homogenous regime.

This further highlights the importance of the operating conditions in experimental investigations to determine correlations to be used in industrial reactor development. It is worth pointing out then, that care must be taken in selecting the most appropriate mass transfer correlation, or any other correlation, so that the chosen correlation should be representative of real systems as much as possible. According to Akita and Yoshida (1973), factors including the kinematic viscosity, liquid phase diffusivity, liquid surface tension, liquid density, column diameter and superficial gas velocity all contribute to the volumetric mass transfer coefficient.

Sehabiague (2012), based on the work by Lemoine et al. (2008), developed a correlation (Equation 21) for the mass transfer coefficients in SBCRs using an experimental pilot plant. The author tested the validity of the correlation by comparing it to that proposed by Lemoine et al. (2008) with regard to modelling the K_{La} values from various sources (1917 in total) and found the correlation to be more accurate.

$$KLa = \frac{7.99 \times 10^{-9} \rho_L^{1.82} \rho_G^{0.27} U_G^{0.387}}{U_L^{0.25} \sigma^{0.976} MW_g^{0.02}} \left(\frac{P_T}{P_T - P_{vap}} \right)^{0.242} \left(\frac{D_c}{D_c + 0.3} \right)^{0.1} \gamma^{0.173} e^{(-0.0013 \rho_p \varepsilon_s + 0.8 \left(\frac{\rho_s \varepsilon_s}{1000} \right)^2 - \left(\frac{\rho_s \varepsilon_s}{1000} \right)^3 - 1675.7 d_p + 0.176 X_W)} \quad [21]$$

Sehabiague (2012) further provides K_{La} correlations for the individual species in each bubble class. The mass transfer coefficient for a species i in the small bubble class is given by Equation 22 and that in the large bubble class by Equation 23.

$$KLa_{i,SB} = \frac{KLa \sqrt{D_i C^*}}{\sum \sqrt{D_i C^*}_{i,SB} + 1.3548 \left(\frac{\mu_L}{\rho_L D_i} \right)^{0.167} \frac{\varepsilon_{g,LB} d_{LB}}{\varepsilon_{g,SB} d_{SB}} \sum \sqrt{D_i C^*}_{i,LB}} \quad [22]$$

$$KLa_{i,LB} = 1.3548 KLa_{i,SB} \left(\frac{\mu_L}{\rho_L D_i} \right)^{0.167} \frac{\varepsilon_{g,LB} d_{LB}}{\varepsilon_{g,SB} d_{SB}} \quad [23]$$

2.4 Heat transfer

Heat transfer in SBCRs is used to describe the exchange of energy in the form of heat between the three phases present in the reactor and between the reactor contents and cooling medium. Because of the highly exothermic nature of the FT reactions, multiple cooling tubes are normally fitted inside the reactor to remove the heat of reaction as quickly as possible. This is to avoid any formation of hot pockets or temperature accumulations resulting in temperature gradients which will impair performance. The heat transfer between the reactor contents and the cooling medium is usually very high in SBCRs, with a heat transfer

coefficient of approximately $1000 \text{ W/m}^2\cdot\text{K}$ (Krishna and Sie, 2000), mainly because of the turbulence that prevails in the reactor. This is one of the advantages of SBCRs over other FT reactors. With this in mind, various authors (Dry, 2002; Satterfield and Huff, 1980; Kuo, 1983; Calderbank et al., 1963; Krishna and Sie, 2000) have deemed it safe to assume that SBCRs operate isothermally, i.e., the heat of reaction is removed by the cooling medium as quickly as it is produced. Also, the small size of the catalyst particles used in SBCRs means temperature gradients can be assumed to be negligible in the catalyst pellets (Rahimpour et al., 2012).

2.5 Hydrodynamic parameters

2.5.1 Gas hold-up

Gas hold-up is one of the more important parameters with regard to SBCR modelling (Maretto and Krishna, 1999). It is the volume fraction of gas in the reactor at any one time. A higher gas hold-up is generally desired as this means there is more gaseous reactant available for Fischer-Tropsch Synthesis (FTS) per unit volume of the FT reactor bed. Several correlations for determining the gas hold-up are found in literature (Iliuta et al., 2007; Maretto and Krishna, 1999; Behkish, 1997). Care should be taken in selecting an appropriate correlation because not all these correlations are applicable to the same situation. Some of them are determined under experimental conditions using fluids different to those in FTS and reactor dimensions much smaller than those in real industrial cases. The use of such correlations is limited to models describing environments similar to those in the experiments and this is not useful for developing models for real situations. Typical industrial FT-SBCR conditions are shown in Table 6.

Gas hold-up is influenced by a variety of factors including operating conditions such temperature, pressure and superficial gas velocity (Maretto and Krishna, 1999). Liquid properties also affect the gas hold-up and these include density, surface tension, viscosity and vapour pressure (Basha et al., 2015). Structural properties including the column diameter and sparger type can also have an influence on gas hold-up (Behkish et al., 2006). Gas hold-up correlations as proposed by different authors are presented in Table 9. Most of these correlations were developed in experimental conditions significantly different to those in industrial settings. For example, Bach and Pilhofer (1978) conducted experiments under ambient temperature and pressure conditions with superficial gas velocities up to 0.2 m/s . Jordan and Schumpe (2001) and Fan et al. (1999) attempted to use represent real SBCR operating conditions by using pressures and temperatures in the ranges $0.1\text{-}5.32 \text{ MPa}$ and

293-351 K respectively but the superficial gas velocities and reactor column dimensions used were significantly lower than those observed in industrial reactors.

Table 9: Gas hold-up correlations from literature

Correlation	Reference
$\frac{\epsilon_g}{1-\epsilon_g} = 0.115 \left(\frac{U_g^3}{\mu_L g \frac{(\rho_L - \rho_g)}{\rho_L^2}} \right)^{0.23}$	Bach and Pilhofer (1978)
$\frac{\epsilon_g}{1-\epsilon_g} = bBo^{0.16} Ga^{0.04} Fr^{0.7} [1 + 27Fr^{0.52} \left(\frac{\rho_g}{\rho_L} \right)^{0.58}]$ $b = \text{sparger type factor (0.109 - 0.153)}$	Jordan and Schumpe (2001)
$\epsilon_g = \epsilon_{g,LB} + \epsilon_{g,SB}(1 - \epsilon_{g,LB})$ $\epsilon_{g,LB} = \frac{0.3}{D_c^{0.18} (U_g - U_{g,SB})^{0.22}} (U_g - U_{g,SB})^{0.8}$ $\epsilon_{g,SB} = \epsilon_{g,SB,ref} \left(1 - \frac{0.7}{\epsilon_{SB,ref}} \epsilon_S \right)$ $\epsilon_{g,SB,ref} = 0.27$	Maretto and Krishna (1999)
$\epsilon_g = 0.9 \left(\frac{U_g^2 d_p \rho_L}{\sigma_L} \right)^{0.11} \left(\frac{U_L}{\sqrt{g d_p}} \right)^{0.22}$	Kito et al. (1978)
$\epsilon_g = 1.61 U_g^{0.22} d_p^{0.168} D_c^{-0.125}$	Begovich and Watson (1978)
$\epsilon_G = 296 U_g^{0.44} \rho_L^{-0.98} \sigma_L^{-0.16} \rho_g^{0.19} + 0.009$	Reilly et al. (1986)
$\epsilon_g = \frac{1}{2 + \left(\frac{0.35}{U_g} \right) \left(\frac{\rho_L \sigma_L}{72} \right)^{0.3}}$	Hughmark (1967)
$\epsilon_g = 0.17283 \left(\frac{\mu_L^4 g}{\rho_L \sigma_L^3} \right)^{-0.1844} \left(\frac{P_T + P_{vap}}{P_T} \right)^{1.6105} \left(\frac{U_g \mu_L}{\sigma_L} \right)^{0.5897}$	Zou et al. (1988)

It is also important to note the nature of the gas, liquid and solids used in these experiments as they also play an important role. In the case of the liquid which is supposed to represent the wax products formed in the SBCR, organic solutions are often used including kerosene, glycol and glycerol with water and alcohols sometimes being used. While these may to some extent represent the behaviour of real FT-SBCR liquid solutions, they fall short of accurately achieving real reactor conditions which undermines the validity of the resulting correlations. Air, Nitrogen and Helium are often used in these experiments to represent the gaseous phase while glass beads and sand are the preferred medium to account for the solid particles. These

correlations should therefore be used only when their anticipated error is known and acceptable.

The gas hold-up is thought to increase with increasing superficial gas velocity (Sehabiague, 2012), temperature and pressure (Behkish et al, 2006; Wilkinson and Dlerendonck, 1990; Jiang et al., 1995; Therning and Rasmuson, 2001, Sehabiague, 2012). An increasing solids concentration has a negative effect on the gas hold-up as noted by Behkish et al. (2006), Kara et al (1982) and Gandhi et al. (1999). Sehabiague (2012) confirms this effect by attributing a drop in small bubble hold-up to an increase in solid particle concentration. The author observed from experiments that solid particle concentrations over 30 % (v/v) rendered the small bubble population virtually non-existent - citing an increase in the tendency of the small bubbles to coalesce and form larger bubbles. Since large bubbles have a higher rise velocity, they spend less time in the reactor so that for systems with a higher solids concentration the gas hold-up at any one time is lower. In respect of the liquid property influence, gas hold-up should be positively affected by an increase in liquid viscosity and surface tension (Oyevaar et al, 1989).

In an effort to develop a gas hold-up correlation that is versatile in terms of its applicability to a wide range of conditions, Behkish et al. (2006) conducted gas hold-up tests and used the results together with data from various authors to come up with a data set consisting of 3881 data points from which a correlation could be developed. The resulting correlation is given in Equation 24. The author provides a range of conditions for which the correlation is applicable (Table 10) and these fall within typical SBCR conditions given in Table 6.

$$\varepsilon_g = 4.94 \times 10^{-3} \left(\frac{\rho_L^{0.415} \rho_g^{0.177}}{\mu_L^{0.174} \sigma_L^{0.27}} \right) U_G^{0.583} \left(\frac{P_T}{P_T - P_{vap}} \right)^{0.203} \times \left(\frac{D_c}{D_c + 1} \right)^{-0.1170.1} \gamma^{0.053} \times e^{(-2.231\varepsilon_s - 0.157\rho_s\varepsilon_s - 0.242X)} \quad [24]$$

Where $\gamma = K_d N_0 d_0^{\alpha_0}$ [25]

Table 10: Applicable range of conditions for Equation 7 (Behkish et al., 2006)

Variables	Minimum value	Maximum value
P_T (MPa)	0.1	15
P_S (MPa)	0	0.7
U_G (m/s)	3.5×10^{-3}	0.574
C_v (vol.%)	0	36
X_w	0.5	1.0
T (K)	275	538
M_B (kg/kmol)	18	730
M_A (kg/kmol)	2	44
d_p ($\times 10^{-6}$ m)	5	300
ρ_P (kg/m ³)	700	4000
ρ_G (kg/m ³)	0.06	177.3
ρ_L (kg/m ³)	633.4	1583
μ_L ($\times 10^{-3}$ Pa s)	0.189	398.8
σ_L ($\times 10^{-3}$ N/m)	8.4	75
D_C (m)	0.0382	5.5

Behkish et al. (2006) determined a correlation for the hold-up of large bubbles in a similar fashion by using a total of 1426 data points to arrive a correlation shown in Equation 26.

$$\begin{aligned}\varepsilon_{g,LB} &= \varepsilon_g^{0.84} (1 - 3.04 \times 10^{-6} \frac{\rho_L^{0.97}}{\mu_L^{0.16}} e^{4.5X_w - 4.49\varepsilon_s}) \\ &= \varepsilon_g^{0.84} F\end{aligned}\quad [26]$$

The small bubble hold-up is determined from the difference between the total gas and large bubble hold-up thus:

$$\varepsilon_{g,SB} = \varepsilon_g - \varepsilon_{g,LB} \quad [27]$$

A condition of the use of Equations 26 and 27 is that $\varepsilon_g \leq F^{6.25}$, otherwise the small bubble hold-up is low enough to be negligible so that Equation 27 becomes Equation 28. A clear disadvantage of the correlations put forward by Behkish et al. (2006) is the large number of parameters that need to be determined beforehand. γ in particular poses a challenge as the parameters needed in Equation 25 are difficult to determine. Although sparger design effects on hydrodynamics have been studied in other fields, there has not been significant work done on sparger configuration effects in SBCRs presently and as a result Equation 25 should be treated with caution.

$$\varepsilon_g = \varepsilon_{g,LB} \quad [28]$$

2.5.2 Liquid hold-up

The liquid phase hold-up can be determined from a balance of the total hold-up as in Equation 29.

$$\varepsilon_l = 1 - \varepsilon_G - \varepsilon_s \quad [29]$$

2.5.3 Superficial gas velocity

The superficial gas velocity is divided between the velocities of the individual bubble classes according to Equation 30. The small bubble superficial velocity can be determined using the correlation by de Swart (1996) as in Equation 31. The large bubble superficial gas velocity can then be determined from the difference between the overall and small bubble superficial gas velocities following Equation 32.

$$U_g = U_{g,SB} + U_{g,LB} \quad [30]$$

$$U_{g,SB} = 2.25 \frac{\sigma_L}{\mu_L} \left(\frac{\sigma_L^3 \rho_L}{g \mu_L^4} \right)^{-0.273} \left(\frac{\rho_L}{\rho_g} \right)^{0.03} \quad [31]$$

$$U_{g,LB} = U_G - U_{g,SB} \quad [32]$$

Chapter 3: Model development

An illustration giving the structure of the model can be seen in Figure 13. The model is based on mass balances into which hydrodynamic, mass transfer and kinetic parameters are incorporated. The operating conditions and physical properties of the phases are included to provide a context/operating environment for the model.

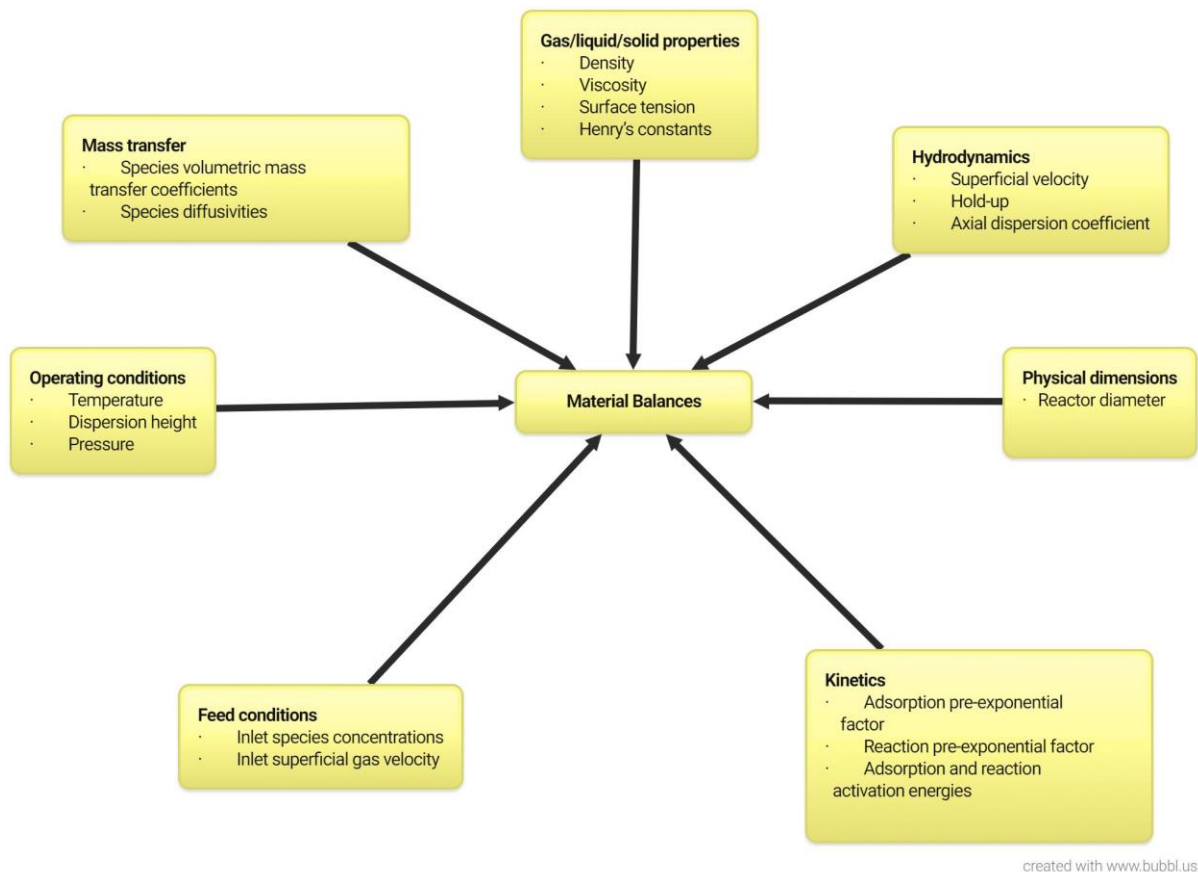


Figure 13: SBCR model structure

3.1 Hydrodynamic model

The hydrodynamic model to be used considers two distinct phases in the SBCR, namely the gas and slurry phases. The catalyst particles and the liquid FT products are treated as a single hydrodynamic phase. The model further classifies the bubbles according to size so that large and small bubbles are treated separately. Material balances will therefore be performed over three compartments including the liquid, large bubbles and small bubbles compartments. In the following model only the fate of the reactants, CO and H₂, will be investigated as the ultimate aim is to determine reactor performance with relation to reactant consumption and its relationship with various reactor parameters, particularly those influencing the hydrodynamics in the SBCR.

The hydrodynamic model considers two regions of flow; a central region where large bubbles rise through the reactor and an outer annular region where the small bubbles and the liquid phase move in a downward direction (see Figure 14). Axial dispersion is assumed in both the liquid and gas phases and this assumption is extended to the small bubbles compartment because the small bubbles are entrapped in the liquid phase.

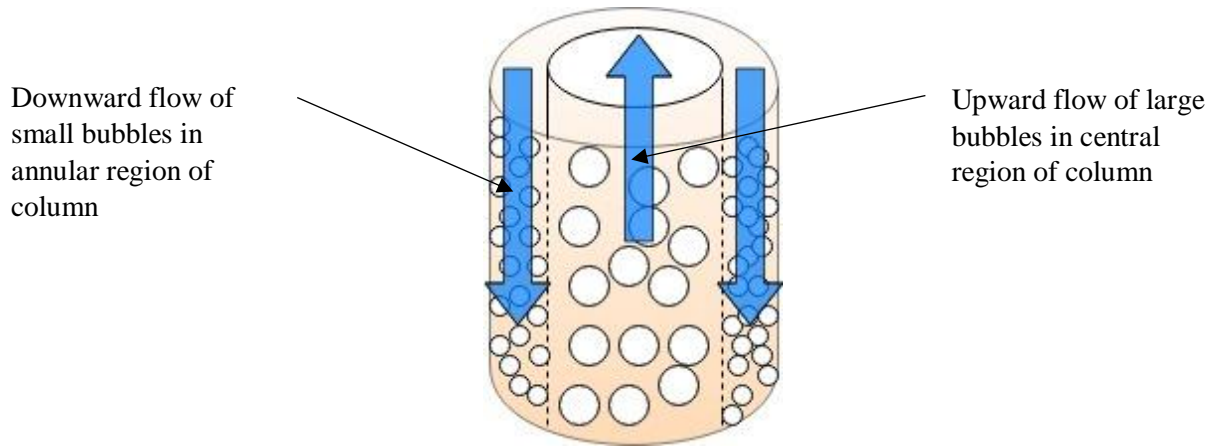


Figure 14: Illustration of the hydrodynamic model with respect to the large and small bubbles behaviour.

3.2 Material balances

The development of the SBCR mathematical model will be carried out from 1st principles based on conservation laws. Conservation laws that are typically applied to reactor systems include material, energy and momentum balances, with the exact combination of the balances dependent on the reactor type and intended application of the model. For the SBCR currently under study, only the material balance will be considered. This is because the conditions in a SBCR produce very high heat transfer between the reactor contents and the cooling medium to ensure a relatively stable temperature which can safely be assumed to be spatially constant. Also, one of the objectives identified for developing this model is to provide a platform for the study of the hydrodynamics inside a SBCR and as such the material balance should suffice.

The material balances stemming from the law of mass conservation will take the following general form:

$$\begin{aligned}
 [\textit{number of moles accumulated}] &= [\textit{number of moles transported in}] - \\
 &[\textit{number of moles transported out}] - \\
 &[\textit{number of moles consumed by reaction}]
 \end{aligned}
 \tag{33}$$

In applying the material balance, the SBCR will be discretized along its axis as shown in Figure 15. Molar fluxes will be used to represent the axial transport of material in and out of each discrete volume element ΔV . The terms in the general mole balance in Equation 33 are specified as follows:

$$[\textit{number of moles accumulated}] = (C_{i_{t+\Delta t}} - C_{i_t}) \times A_c \times \Delta z \quad [34]$$

$$[\textit{number of moles transported in}] = \textit{Flux in}_z \times A_c \times t \quad [35]$$

$$[\textit{number of moles transported out}] = \textit{Flux out}_{z+\Delta z} \times A_c \times t \quad [36]$$

$$[\textit{number of moles consumed by reaction}] = G \times A_c \times t \times \Delta z \times \rho_{cat} \times \varepsilon_s \times \varepsilon_l \quad [37]$$

The total flux is the sum of the convective and dispersive fluxes. Convective transport of material occurs along the axial direction through the bulk flow of material in and out of the volume element and is given by:

$$\textit{Convective flux} = U_i C_i \quad [38]$$

Dispersive flux is transport of material driven by, amongst other factors, molecular diffusion, turbulent mixing and eddy formations. It is described by Equation 39 thus:

$$\textit{Dispersive flux} = -E \varepsilon_n \frac{dC_{i,m}}{dz} \quad [39]$$

The total flux can then be computed as:

$$\textit{Total flux} = U_i C_i - E \varepsilon_n \frac{dC_{i,m}}{dz} \quad [40]$$

Using the specified terms in Equations 34 – 37, Equation 33 can be re-written accordingly:

$$(C_{i_{t+\Delta t}} - C_{i_t}) \times A_c \times \Delta z = (\textit{Flux in}_z \times A_c \times t) - (\textit{Flux out}_{z+\Delta z} \times A_c \times t) - (G \times A_c \times t \times \Delta z \times \rho_{cat} \times \varepsilon_s) - (\textit{Interphase mass transfer} \times A_c \times t \times \Delta z) \quad [41]$$

By dividing Equation 41 by $A_c \times t \times \Delta z$ and taking the limits as $z \rightarrow 0$ and $t \rightarrow 0$, Equation 42 is determined:

$$\frac{\partial C_i}{\partial t} = \frac{\partial \textit{Flux}_i}{\partial z} - \textit{Interphase mass transfer} - (G_i \times \rho_{cat} \times \varepsilon_s \times \varepsilon_l) \quad [42]$$

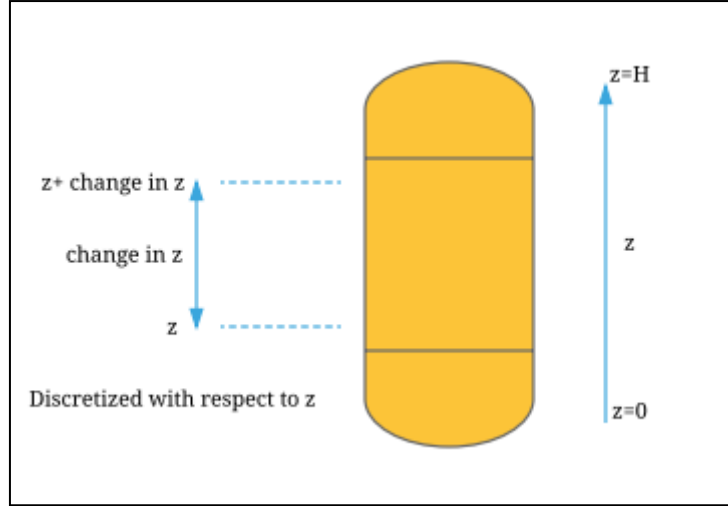


Figure 15: Discretization with respect to height of SBCR column

In Equation 42, the interphase mass transfer term refers to the transfer of material from the gas to liquid phase and is determined according to Equation 17 which is based on the two-film theory to give:

$$\text{Interphase mass transfer} = K_{La}(C_{i,L}^* - C_{i,L}) \quad [43]$$

Substituting Equation 40 into Equation 42 and taking note that a steady-state model is envisaged, a general axial dispersion ordinary differential equation (ode) for bubble column reactors can be determined as in Equation 44.

$$0 = \frac{Udc_{i,m}}{dz} - E_m \varepsilon_m \frac{d^2 c_{i,m}}{dz^2} + a^* K_{La,i,m} (C_{i,L}^* - C_{i,L}) - (G_i \times \rho_{cat} \times \varepsilon_s \times \varepsilon_l) \quad [44]$$

Where a^* is either 1 or -1 depending on whether mass is leaving the gas phase or being received by the liquid phase respectively. Using Equation 44, the large bubble compartment material balance can be written as shown in Equation 45 with the assumption that no reaction takes place in the gas phase. Accordingly, the gas phase material balances for CO and H₂ in the large bubbles compartment are given in Equations 46 and 47 respectively.

$$0 = \frac{U_{LB} dC_{i,LB}}{dz} - E_{LB} \varepsilon_{LB} \frac{d^2 C_{i,LB}}{dz^2} + K_{La,i,LB} (C_{i,L}^* - C_{i,L}) \quad [45]$$

$$\frac{U_{LB} dC_{CO,LB}}{dz} - E_{LB} \varepsilon_{LB} \frac{d^2 C_{CO,LB}}{dz^2} = -K_{La,CO,LB} (C_{CO,L}^* - C_{CO,L}) \quad [46]$$

$$\frac{U_{LB} dC_{H_2,LB}}{dz} - E_{LB} \varepsilon_{LB} \frac{d^2 C_{H_2,LB}}{dz^2} = -K_{La,H_2,LB} (C_{H_2,L}^* - C_{H_2,L}) \quad [47]$$

The small bubbles experience axial dispersion in a similar manner to the liquid phase because of the assumption previously put forward that the liquid and small bubbles compartments can be treated as a single pseudo-homogenous phase. The result of this is the inclusion of the dispersion term in the small bubble compartment material balance. Similar to the large bubble compartment, it is assumed that no reaction takes place in the small bubbles so that the balance equation can be written as shown in Equation 48. The material balances for CO and H₂ in the small bubble compartment are given in Equations 49 and 50 respectively.

$$0 = \frac{U_{SB} dC_{i,SB}}{dz} - E_{SB} \varepsilon_{SB} \frac{d^2 C_{i,SB}}{dz^2} + K_{La} (C_{i,L}^* - C_{i,L}) \quad [48]$$

$$\frac{U_{SB} dC_{CO,SB}}{dz} - E_{SB} \varepsilon_{SB} \frac{d^2 C_{CO,SB}}{dz^2} = -K_{La,CO,SB} (C_{i,L}^* - C_{i,L}) \quad [49]$$

$$\frac{U_{SB} dC_{H_2,SB}}{dz} - E_{SB} \varepsilon_{SB} \frac{d^2 C_{H_2,SB}}{dz^2} = -K_{La,H_2,SB} (C_{i,L}^* - C_{i,L}) \quad [50]$$

It is assumed that the liquid phase experiences axial dispersion and that the FT reaction takes place only in the liquid phase. Adopting R7 as a representative reaction for FT synthesis in SBCRs, the consumption rate of H₂, G_{H_2} , is twice that of CO, G_{CO} . The resulting material balance equation for the liquid phase is written in Equation 51. The CO and H₂ material balances are given in Equations 52 and 53 respectively. In Equations 51 and 52, G , which will be represented by Equation 16, is the reaction rate constant. As the gas concentration will be treated in mol/m³ instead of Pa, the partial pressure terms will be converted to concentration terms using the ideal gas law so that Equation 16 can be re-written as in Equation 54.

$$0 = \frac{U_L dC_{i,L}}{dz} - E_L \varepsilon_L \frac{d^2 C_{i,L}}{dz^2} - K_{La,i,SB} (C_{i,L}^* - C_{i,L}) - K_{La,i,LB} (C_{i,L}^* - C_{i,L}) - (G_i \times \rho_{cat} \times \varepsilon_s \times \varepsilon_l) \quad [51]$$

$$\frac{U_L dC_{CO,L}}{dz} - E_L \varepsilon_L \frac{d^2 C_{CO,L}}{dz^2} = +K_{La,CO,SB} (C_{i,L}^* - C_{i,L}) + K_{La,CO,LB} (C_{i,L}^* - C_{i,L}) + (G_{CO} \times \rho_{cat} \times \varepsilon_s \times \varepsilon_l) \quad [52]$$

$$\frac{U_L dC_{H_2,L}}{dz} - E_L \varepsilon_L \frac{d^2 C_{H_2,L}}{dz^2} = +K_{La,H_2,SB} (C_{i,L}^* - C_{i,L}) + K_{La,H_2,LB} (C_{i,L}^* - C_{i,L}) + (G_{H_2} \times \rho_{cat} \times \varepsilon_s \times \varepsilon_l) \quad [53]$$

$$R = \frac{k_{CO,G} C_{H_2,G} (RT)^2}{(1 + b_{CO,G} RT)^2} \quad [54]$$

3.2.1 Boundary conditions

The solution to the six odes in Equations 46, 47, 49, 50, 52 and 53 requires the definition of boundary conditions. Danckwerts-type boundary conditions will be used in this model. For the odes describing the large bubble compartment, the boundary conditions are applied as shown in Equations 55 – 57.

$$at\ z = 0, \quad C_{i,LB} = C_{i,G,0} \quad [55]$$

so that

$$C_{CO,LB} = C_{CO,G,0} \quad [56]$$

$$C_{H_2,LB} = C_{H_2,G,0} \quad [57]$$

Similarly, the boundary conditions applicable to the small bubble compartment are defined in Equations 58 – 60.

$$at\ z = 0, \quad C_{i,SB} = C_{i,G,0} \quad [58]$$

$$C_{CO,SB} = C_{CO,G,0} \quad [59]$$

$$C_{H_2,SB} = C_{H_2,G,0} \quad [60]$$

The ode's describing the liquid and small bubble compartments are second order, thus necessitating the use of two boundary conditions. The Danckwerts-type boundary conditions were used in this regard. For the liquid phase the boundary conditions adopted are shown in Equations 61 – 63 (Deckwer, 1991).

$$\frac{dC_{i,L}}{dz} = - \frac{HU_L C_{i,L}}{E_L \varepsilon_L} \quad [61]$$

so that

$$\frac{dC_{CO,L}}{dz} = - \frac{HU_L C_{CO,L}}{E_L \varepsilon_L} \quad [62]$$

$$\frac{dC_{H_2,L}}{dz} = -\frac{HU_L C_{H_2,L}}{E_L \varepsilon_L} \quad [63]$$

For the small bubble compartment, Danckwerts-type boundary conditions as suggested by Sehabiague (2012) were applied. These are shown in Equations 64 to 66.

$$U_{SB} C_{i,SB} - E_{SB} \varepsilon_{SB} \frac{dC_{i,SB}}{dz} = U_{SB,0} C_{i,SB,0} \quad [64]$$

For CO:

$$U_{SB} C_{CO,SB} - E_{SB} \varepsilon_{SB} \frac{dC_{CO,SB}}{dz} = U_{SB,0} C_{CO,SB,0} \quad [65]$$

For H₂:

$$U_{SB} C_{H_2,SB} - E_{SB} \varepsilon_{SB} \frac{dC_{H_2,SB}}{dz} = U_{SB,0} C_{H_2,SB,0} \quad [66]$$

Dankwerts type boundary conditions were also adopted for the large bubble compartment as shown below (Sehabiague, 2012):

$$U_{LB} C_{i,LB} - E_{LB} \varepsilon_{LB} \frac{dC_{i,LB}}{dz} = U_{LB,0} C_{i,LB,0} \quad [67]$$

For CO:

$$U_{LB} C_{CO,LB} - E_{LB} \varepsilon_{LB} \frac{dC_{CO,LB}}{dz} = U_{LB,0} C_{CO,LB,0} \quad [68]$$

For H₂:

$$U_{LB} C_{H_2,LB} - E_{LB} \varepsilon_{LB} \frac{dC_{H_2,LB}}{dz} = U_{LB,0} C_{H_2,LB,0} \quad [69]$$

3.3 Model assumptions summary

A summary of the relevant SBCR system assumptions that were adopted during the model development phase are given below:

- The system is in steady-state
- No internal/intra-particle mass transfer resistance
- External mass transfer resistance is only present across the gas-liquid interphase
- Gas-liquid mass transfer resistance is located on the liquid side of the interphase
- Only H₂ and CO are present in the feed
- No radial dispersion effects are present
- Small bubbles hold-up and velocity are independent of axial position
- System is isothermal and isobaric
- Liquid and solid phases exist as a pseudo-homogenous slurry

3.4 Parameter estimation

3.4.1 Superficial velocity

The parameters included in the material balances need to be determined first before a solution to the ode's can be found. The superficial velocity of the small bubbles was calculated based on the correlation provided by Sehabiague (2012). It is assumed that this parameter is independent of axial position. It is predominantly affected by the properties of the liquid phase as shown in Equation 31. The liquid phase in SBCRs operated under the typical conditions given in Table 6 is mainly a wax product composed of long chain hydrocarbons. Sehabiague's (2012) study on the modelling of SBCR considered the liquid properties of a Sasol wax product with an average carbon number of 80. This product was manufactured by Moore and Munger, Inc. and is supposedly closely identical to the wax that Sasol produces in their commercial FT SBCR reactors. This may be the most accurate representation of the liquid phase properties outside of using a direct liquid sample from a commercially operated FT SBCR. The surface tension, density and kinematic viscosity were measured under varying temperatures (290 -500 K). These are given as functions of temperature in Table 11. The density of the gas was taken to be 7 kg/m³ (Krishna and Sie, 2000). The large bubble superficial gas velocity is determined from the difference between the overall and small bubble velocities according to Equation 32.

Table 11: SBCR liquid phase properties as functions of temperature (Sehabiague, 2012)

Liquid Property	Correlation
Density (kg/m ³)	$\rho_L = 959.08 - 0.513T$
Viscosity (kg/m.s)	$\mu_L = e^{(-4.3284 + \frac{2319.4}{T})}$
Surface tension (N/m)	$\sigma_L = 0.001(70.57 - 0.175T + (1.04 \times 10^{-4}T^2))$

The overall superficial gas velocity will decrease along the axial direction in the reactor as a result of a decrease in the moles of total reactants due to consumption by the FT reaction. This decrease can be modelled through an overall gas phase material balance, i.e.,

$$\frac{dU_G C_G}{dz} = \frac{dU_{SB} C_{CO,SB}}{dz} + \frac{dU_{LB} C_{CO,LB}}{dz} + \frac{dU_{SB} C_{H_2,SB}}{dz} + \frac{dU_{LB} C_{H_2,LB}}{dz} \quad [70]$$

Where $U_G = U_{G,0}$ at $z = 0$ [71]

And C_G is the total gas concentration in both large and small bubble compartments:

$$C_G = C_{CO,SB} + C_{CO,LB} + C_{H_2,SB} + C_{H_2,LB} \quad [72]$$

The liquid superficial velocity describes the velocity of liquid product as it is drawn from the reactor and is generally much smaller than the superficial gas velocity, being an order of magnitude smaller (Dudukovic et al., 1999 and Boyer et al., 2016)

3.4.2 Hold-up

The small bubbles hold-up correlation given in Equation 73 as postulated by Maretto and Krishna (1999) will be used to determine the volume proportion of small bubbles relative to the total reactor bed volume. In Equation 73, $\varepsilon_{SB,ref}$ refers to the small bubble hold-up in a liquid phase void of any solid particles and is given as 0.27 for paraffin oil liquid. An $\varepsilon_{SB,ref}$ value for a wax product would be more preferable but because of the difficulty of obtaining such a value, 0.27 will be used until such time that a more representative approximation of the reference hold-up is determined. A key assumption in Equation 73 is that the small bubbles hold-up is independent of axial position. The same author put forward a correlation for the large bubble hold-up which depends on the geometry of the reactor and the velocity difference between the large and small bubbles as shown in Equation 74. As a result of its dependence on superficial gas velocity, the large bubbles hold-up will vary relative to axial position in the reactor as the gas is consumed by the FT reaction. The dependence of the large bubble hold-up on reactor diameter in Equation 74 only exists for diameters less than 1 m

(laboratory or pilot reactors), otherwise, Equation 75 is used instead. The total gas hold-up will be computed by taking into account the large and small bubble hold-ups and applying them in Equation 76 (Maretto and Krishna, 1999).

$$\varepsilon_{SB} = \varepsilon_{SB,ref} \left(1 - \frac{0.7}{\varepsilon_{SB,ref}} \varepsilon_S\right) \quad [73]$$

$$\varepsilon_{LB} = 0.3 \frac{(U_g - U_{g,SB})^{0.8}}{D_c^{0.18} (U_g - U_{g,SB})^{0.22}} \quad [74]$$

$$\varepsilon_{LB} = 0.3 \frac{(U_g - U_{g,SB})^{0.8}}{(U_g - U_{g,SB})^{0.22}} \quad [75]$$

$$\varepsilon = \varepsilon_{LB} + \varepsilon_{SB} (1 - \varepsilon_{LB}) \quad [76]$$

The liquid phase hold-up can be determined according to Equation 77.

$$\varepsilon_l = 1 - \varepsilon_g - \varepsilon_s \quad [77]$$

3.4.3 Dispersion coefficients

3.4.3.1 Liquid axial dispersion coefficient

The axial dispersion coefficient for the liquid phase is determined according to the model of isotropic turbulence developed by Baird and Rice (1975) described in Equation 6. The small bubbles dispersion coefficient is assumed to be equal to that in the liquid phase because the small bubbles are trapped in the liquid phase as a result follow the movement of the liquid phase (Steynberg and Dry, 2004). The small bubbles dispersion coefficient is given by Equation 78.

$$E_{SB} = K d_c^{4/3} (U_g g)^{1/3} \quad [78]$$

3.4.3.2 Gas phase axial dispersion coefficient

Given the importance of gas phase axial dispersion to SBCR systems exhibiting high conversion rates, the correlation put forward by Mangartz and Pilhofer (1980) was adopted in this work to represent the extent of back-mixing the large bubbles.

3.4.4 Mass transfer coefficients

The volumetric mass transfer coefficients through the large and small bubbles are determined separately and the correlations proposed by Maretto and Krishna (1999) are used in this regard. The mass transfer coefficient for the large bubbles can be determined through

Equation 79 and the coefficients for the specific CO and H₂ species can then be calculated in Equations 80 and 81 respectively.

$$K_{La,i,LB} = 0.5\varepsilon_{LB}\sqrt{\frac{D_i}{D_{ref}}} \quad [79]$$

$$K_{La,CO,LB} = 0.5\varepsilon_{LB}\sqrt{\frac{D_{CO}}{D_{ref}}} \quad [80]$$

$$K_{La,H_2,LB} = 0.5\varepsilon_{LB}\sqrt{\frac{D_{H_2}}{D_{ref}}} \quad [81]$$

For the small bubbles, Equations 82 to 84 will be used for determining the mass transfer coefficients of the reacting species. D and D_{ref} refer to the diffusion coefficient and the reference diffusion coefficient respectively. Studies by Vermeer and Krishna (1981) (from Maretti and Krishna, 1999) were able to determine a consistent relationship between the mass transfer coefficient and gas hold-up using N₂-turpentine-5 as the liquid. To extend the use of this relationship to systems using different fluids, correction factors incorporated into Equations 79 and 82 were used.

$$K_{La,i,SB} = \varepsilon_{SB}\sqrt{\frac{D_i}{D_{ref}}} \quad [82]$$

$$K_{La,CO,SB} = \varepsilon_{SB}\sqrt{\frac{D_{CO}}{D_{ref}}} \quad [83]$$

$$K_{La,H_2,SB} = \varepsilon_{SB}\sqrt{\frac{D_{H_2}}{D_{ref}}} \quad [84]$$

3.4.5 Henry's constants

In order to evaluate the mass transfer between the gas and liquid phases, $C_{i,L}^*$ must be converted to $C_{i,g}$ with the use of Henry's constants as in Equation 19. H_i For gaseous concentrations defined in moles/m³, as in the current study, H_i can be expressed in dimensionless form so that $C_{i,g}$ instead of P_i is determined from Equation 19. Consequently, Equation 19 can be re-written for $C_{i,g}$ (Equation 86) with application of the ideal gas law (Equation 85). Henry's constants are functions of temperature and Soriano's (2005) equations for CO and H₂ Henry's constants were used (see Equations 87 to 89). These equations were

developed using Sasol wax product. The parameters in Equations 88 and 89 are given in Table 12.

$$P = RT \frac{n}{V} \quad [85]$$

So that Equation 19 becomes $C_{i,L}^* = RT \frac{C_{i,g}}{H_i}$ [86]

Soriano (2005) Henry's constants correlations are given as:

$$H_i = H_{i,o} e^{(A_i(\frac{1}{T})^2 + B_i(\frac{1}{T}))} \quad [87]$$

$$H_{CO} = H_{CO,o} e^{(A_{CO}(\frac{1}{T})^2 + B_{CO}(\frac{1}{T}))} \quad [88]$$

$$H_{H_2} = H_{H_2,o} e^{(A_{H_2}(\frac{1}{T})^2 + B_{H_2}(\frac{1}{T}))} \quad [89]$$

Table 12: Henry's constant correlations parameters (Soriano, 2005)

Species	Ho	A	B
CO	22.8	-365100	1873
H ₂	42.18	-192900	1345

3.4.6 Kinetic constants

The rate law to be used in this study (Equation 16) requires knowledge of reaction rate and adsorption constants, k and a respectively. Both k and a are temperature dependent and follow the Arrhenius equation (Equation 90). For the rate constant:

$$k = A_{FT} e^{-\frac{E_{a,FT}}{RT}} \quad [90]$$

For the adsorption constant:

$$a = A_{ad} e^{-\frac{E_{a,ad}}{RT}} \quad [91]$$

The parameters in Equations 90 and 91 are given in Table 13.

Table 13: Reaction rate and adsorption constants for Equations 90 and 91 (Sehabiague, 2012)

Pre-exponential Factor		Activation Energy	
Reaction	A_{FT}	8.037×10^{-9}	$E_{a,FT}$ 37369.5
Adsorption	A_{ad}	1.243×10^{-12}	$E_{a,ad}$ -68474.1

3.5 Reactor feed conditions

The H₂/CO mole ratio of the synthesis gas fed to the SBCR will be 2 as this is the most ideal for Co catalyzed reactions that facilitate no WGS reaction (Dry, 2002). Assuming that the syngas feed contains only the reactants, the feed concentration can be determined as below:

$$\begin{aligned}
 \frac{m_{syngas,feed}}{\text{molar syngas unit}} &= 2 \text{ mol } H_2(MW_{H_2}) + 1 \text{ mol } CO(MW_{CO}) \\
 &= 4.04 + 28.01 \\
 &= 32.05 \text{ g} \qquad \qquad \qquad [92]
 \end{aligned}$$

The inlet concentrations of the reactant species can then be determined as:

$$\begin{aligned}
 C_{H_2,0} &= \frac{2}{32.05} \times \rho_G \times 10^3 \\
 &= 436.82 \frac{\text{mol } H_2}{\text{m}^3 \text{ syngas}} \qquad \qquad \qquad [93]
 \end{aligned}$$

$$\begin{aligned}
 C_{CO,0} &= \frac{1}{32.05} \times \rho_G \times 10^3 \\
 &= 218.41 \frac{\text{mol } CO}{\text{m}^3 \text{ syngas}} \qquad \qquad \qquad [94]
 \end{aligned}$$

The typical operating conditions including the physical properties of the material in the three phases given in Table 6 will be adopted in this study.

Chapter 4: Numerical Solution in Simulink

The seven odes in Equations 46, 47, 49, 50, 52, 53 and 70 together with the relevant boundary conditions and parameters can be solved by numerical methods. Simulink in MATLAB was chosen as the numerical tool to use in solving the equations. Simulink allows users to create mathematical models and solve these using built-in ode solvers in order to simulate the outcomes of various scenarios. It uses a graphical programming environment in which blocks representing the various parts of equations/models can be arranged into a pre-defined model. In the present case, the equations representing the behaviour of the components in an FT SBCR including the material balances, hydrodynamic correlations and parameters, mass transfer and kinetic parameters and the individual phase properties will be coupled in Simulink, solved and used to simulate the performance of the reactor.

4.1 Material balances

As shown in Figure 13, the material balance is the focal point of the model and it is those odes describing mass conservation that are input first into Simulink. As discussed in earlier sections, the SBCR will be divided into large and small bubble compartments so that material balances are performed for each species in each bubble compartment. In this section CO and H₂ material balance odes in large and small bubble compartments will be translated into Simulink models. In all the Simulink models, blue blocks will denote model inputs while red blocks will denote outputs from the model. Yellow blocks are used to represent the scope block which acts to produce a plot of the change in the variable of interest, in this case species concentration, over the axial position. Subsystems, which hide within them the actual model conditions, are given a grey colour.

4.1.1 Large bubble compartment

The species material balance odes in the large bubble compartment, represented by Equations 46 and 47 for CO and H₂ species respectively, have been translated into a Simulink model as shown in Figures 16 and 17. These models are set up to provide data regarding the change in CO and H₂ concentration in the large bubbles as a function of reactor axial position. The boundary conditions for the large bubble compartment material balance odes were set-up as shown in Figures 18 and 19 for both the CO and H₂ species respectively (see Appendix A for a detailed description of the boundary condition model set-up in Simulink).

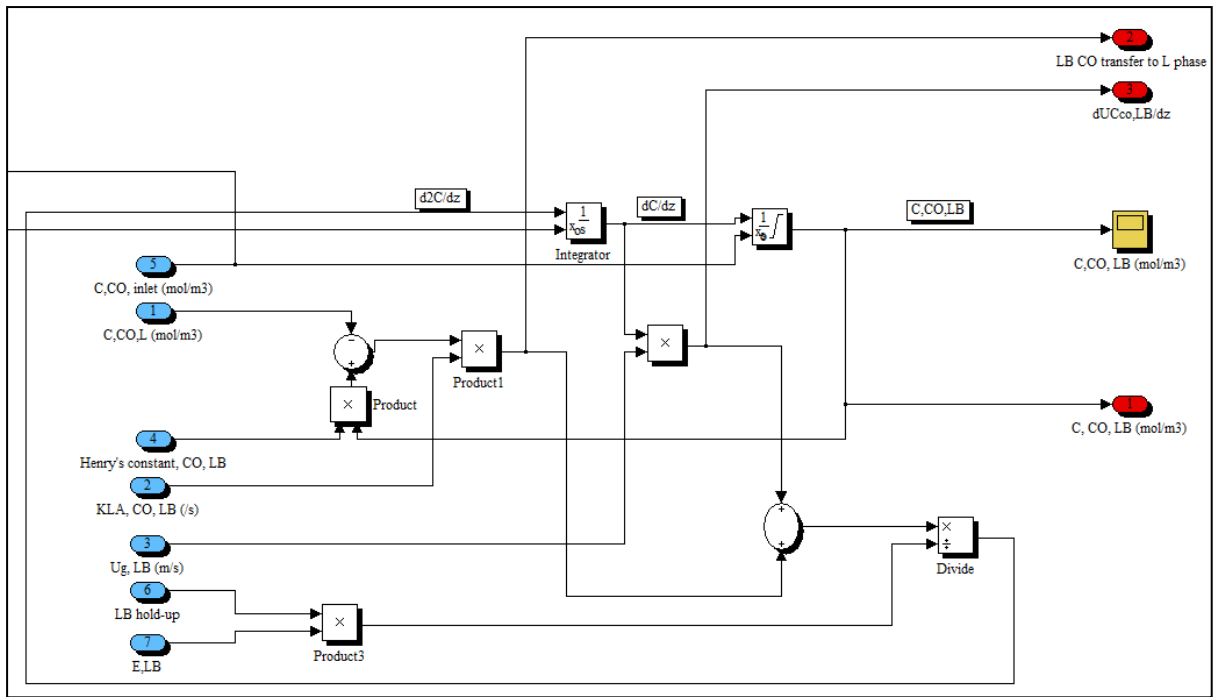


Figure 16: Simulink model for CO material balance in the large bubble compartment

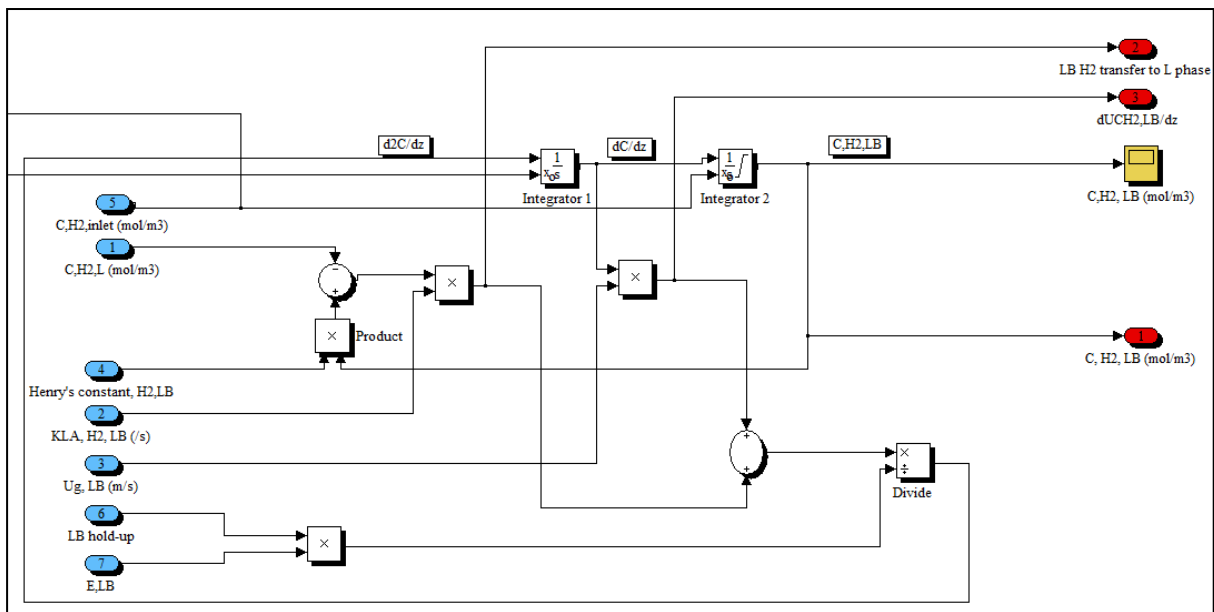


Figure 17: Simulink model for H₂ material balance in the large bubble compartment

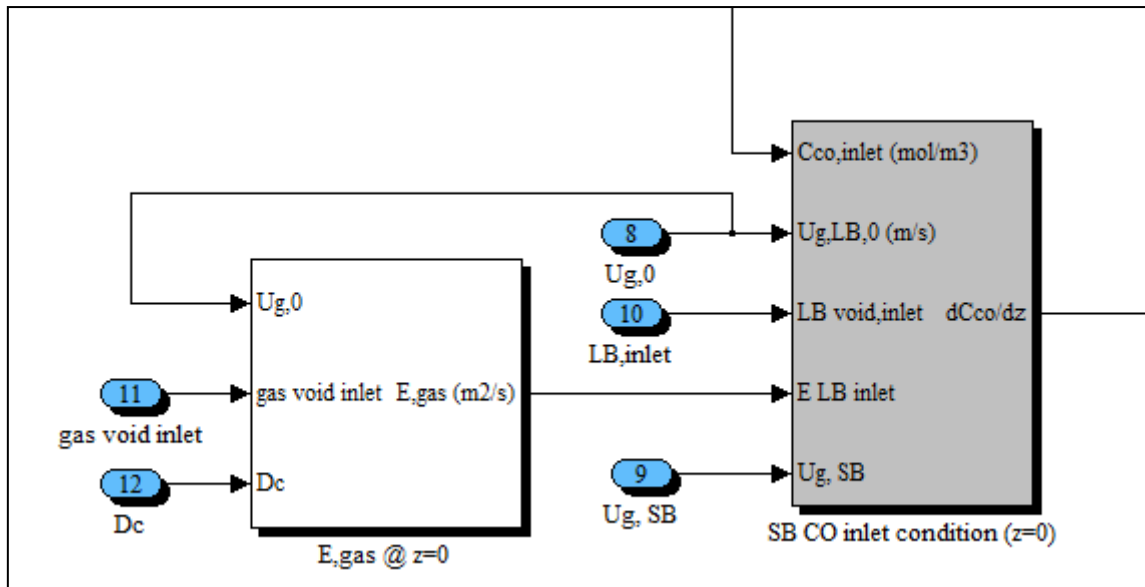


Figure 18: Simulink boundary condition set-up for CO material balance in the large bubble compartment

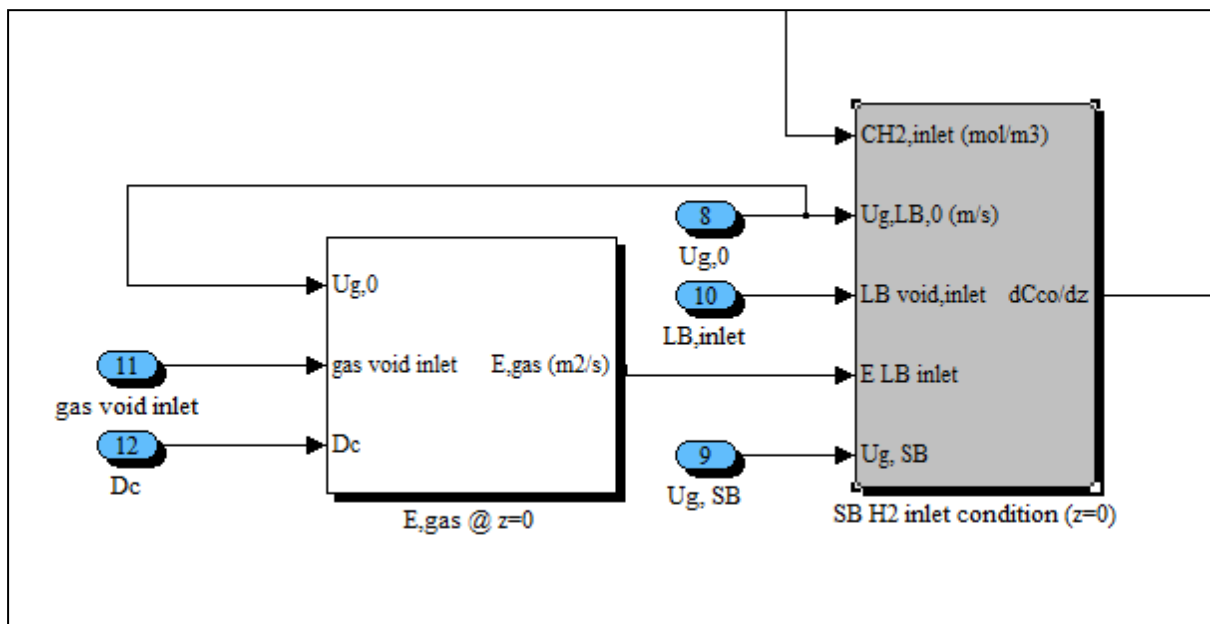


Figure 19: Simulink boundary condition set-up for H₂ material balance in large bubble compartment

4.1.2 Small bubble compartment

The odes in Equations 49 and 50 represent the CO and H₂ species mass balance odes respectively and are translated into a Simulink model with the actual block arrangement shown in Figures 20 and 22 respectively. The inlet conditions were modelled separately according to Equation 65 as shown in Figure 21. The boundary condition sub-model was then connected to the main CO material balance model. Similarly, the boundary conditions for the H₂ mass balance odes are shown in Figure 23. See Appendix A for a detailed description of the boundary condition model set-up in Simulink.

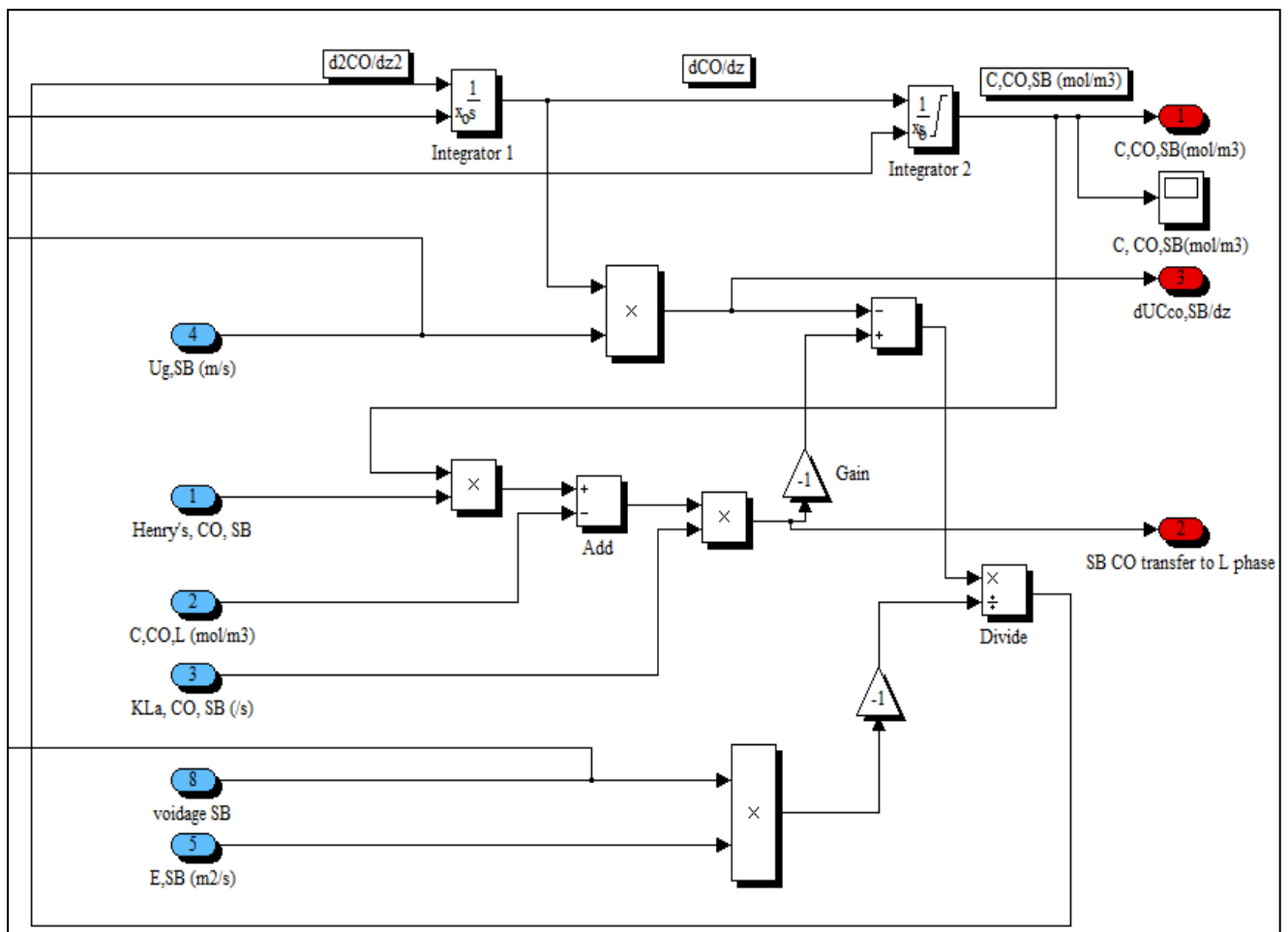


Figure 20: Simulink model for CO material balance in the small bubble compartment

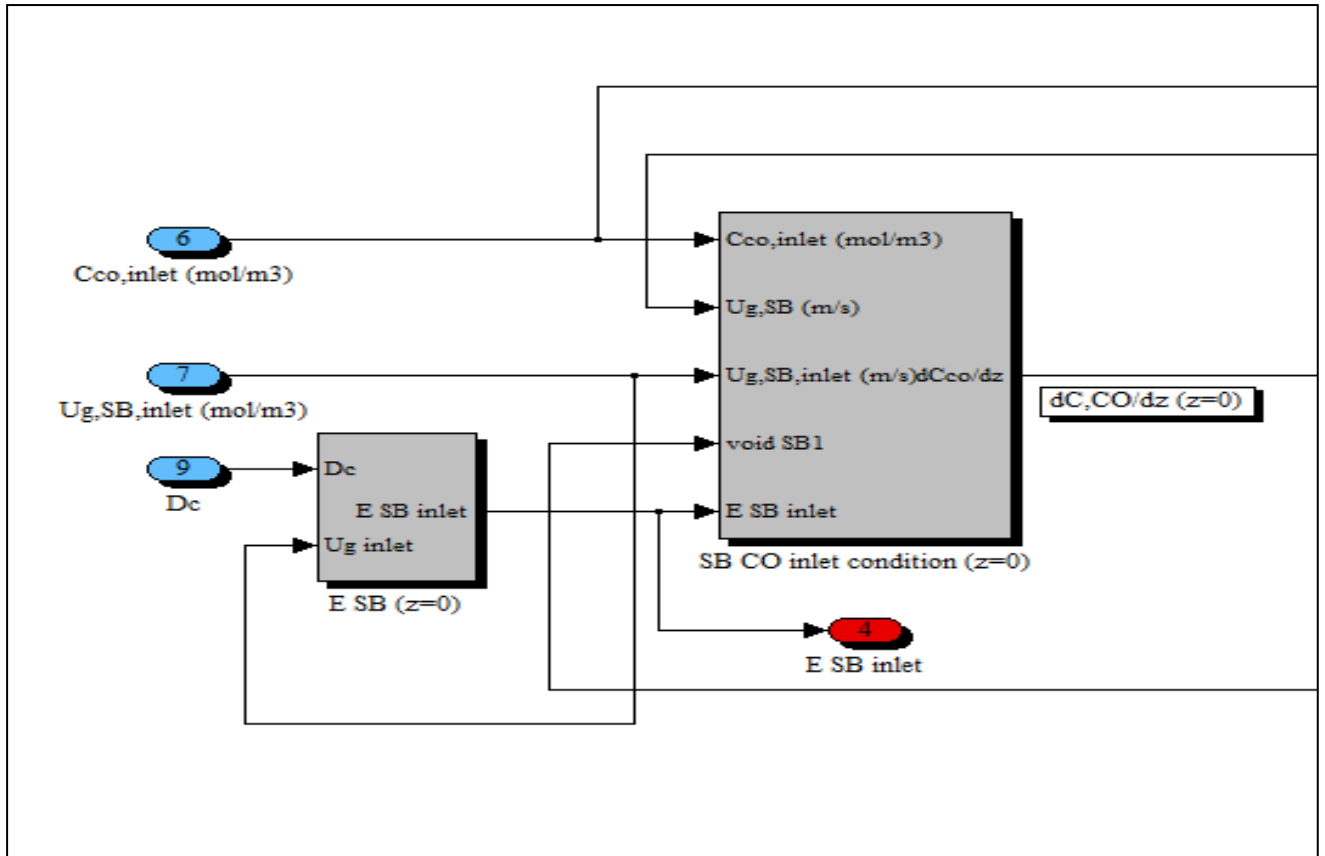


Figure 21: Boundary condition model applied to the CO material balance model in the small bubble compartment

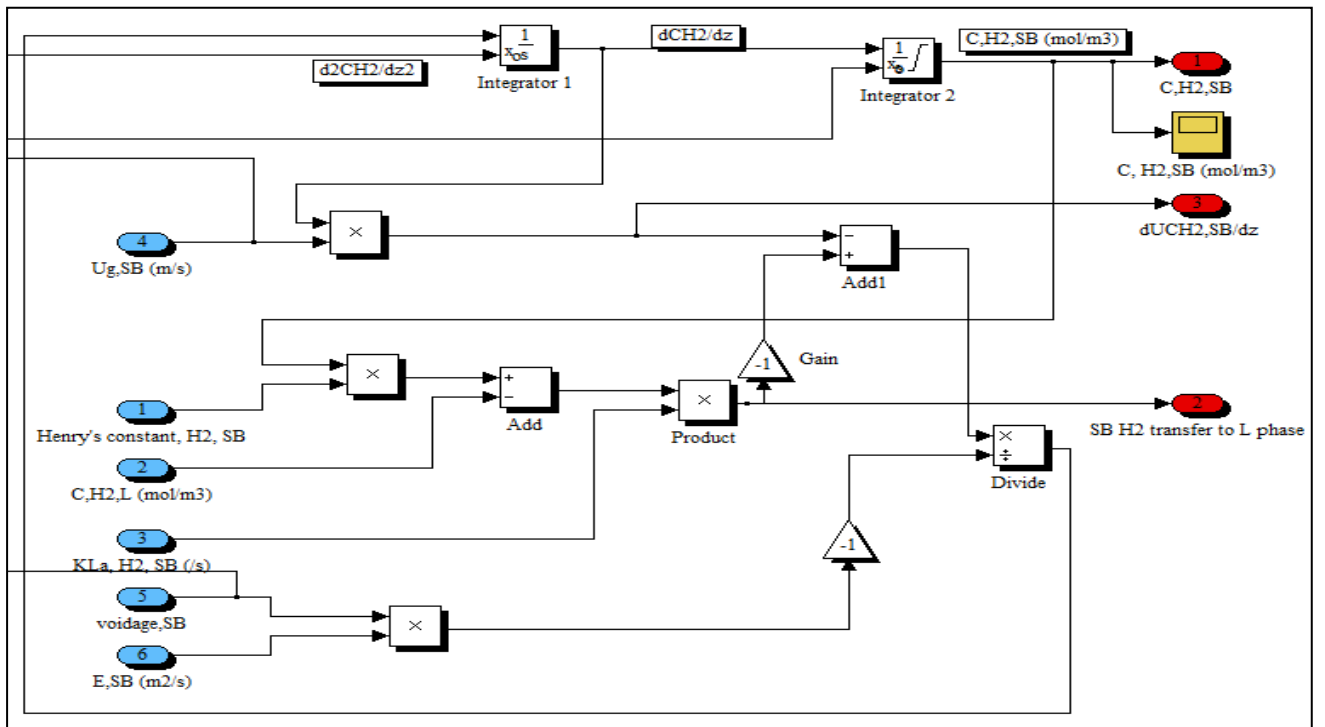


Figure 22: Simulink model for H₂ material balance in the small bubble compartment

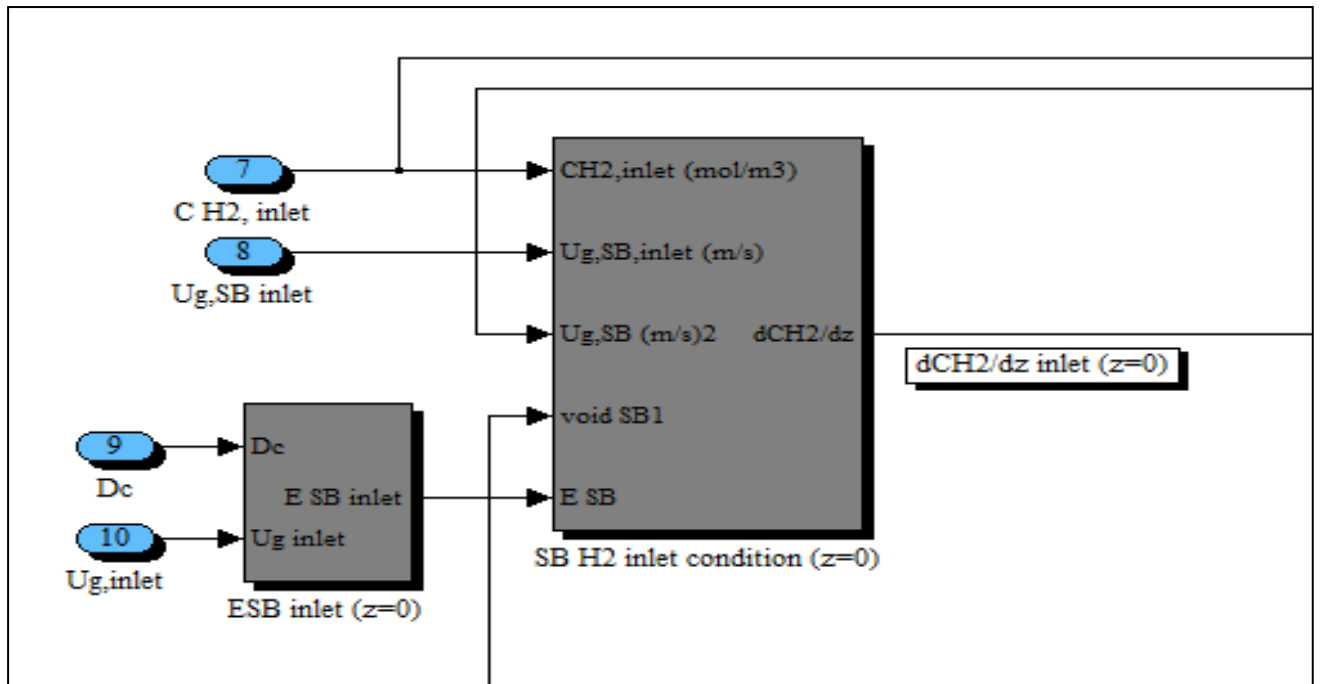


Figure 23: Boundary condition model applied to the H₂ material balance model in the small bubble compartment

4.1.3 Liquid compartment

The liquid compartment material balance is modelled using Equations 52 and 53 for the CO and H₂ species respectively in Simulink and the graphical representation is shown in Figures 24 and 26. The Simulink models for the boundary conditions of the mass balance odes for both species are given in Figure 25 for CO and Figure 27 for H₂.

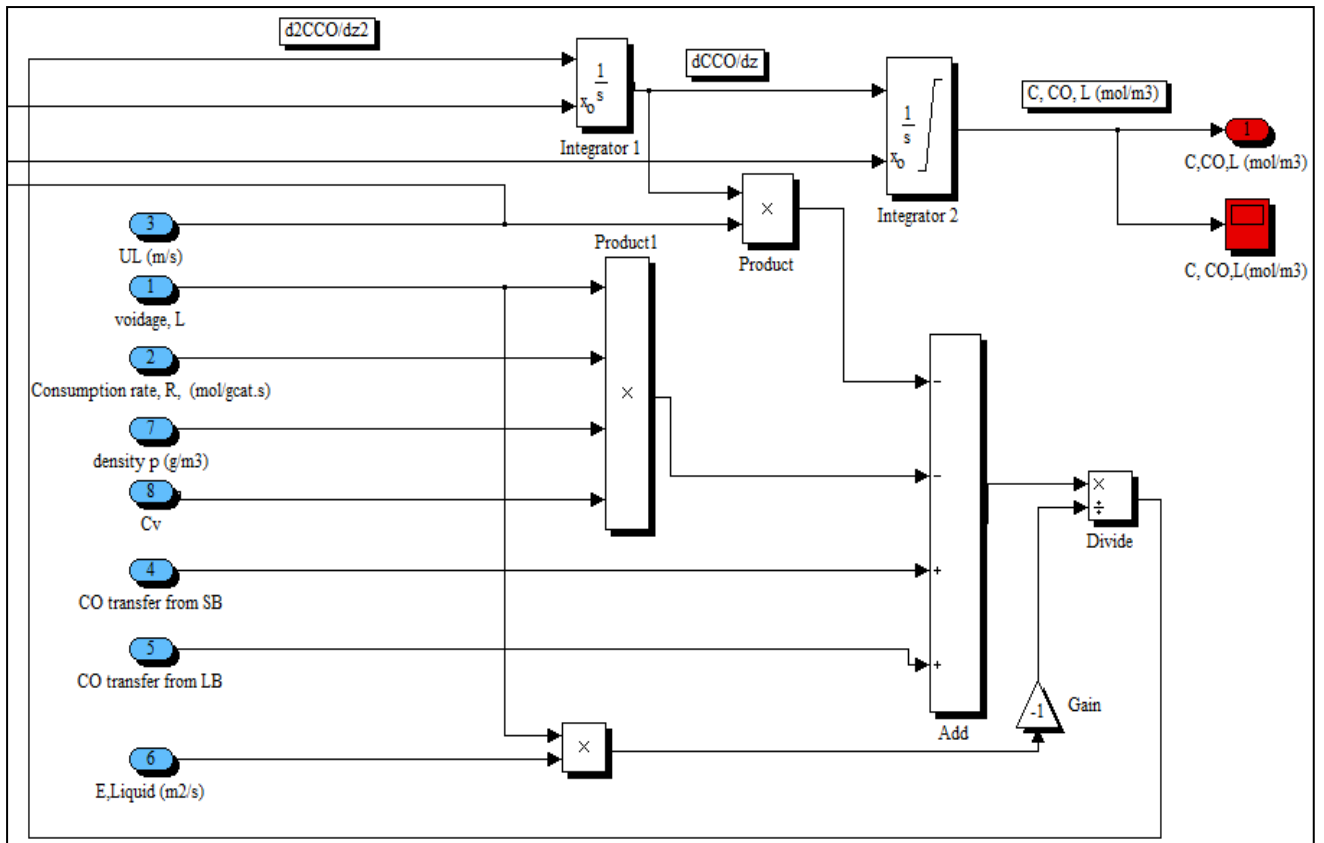


Figure 24: Simulink model for CO material balance in the liquid compartment

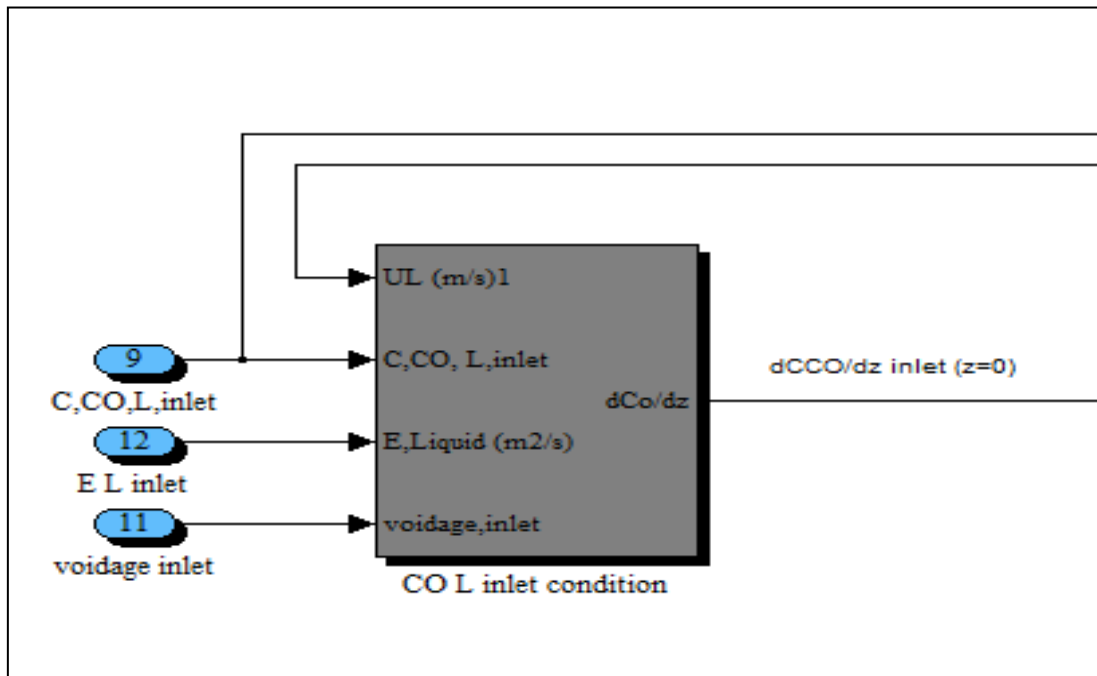


Figure 25: CO liquid phase material balance boundary condition Simulink model

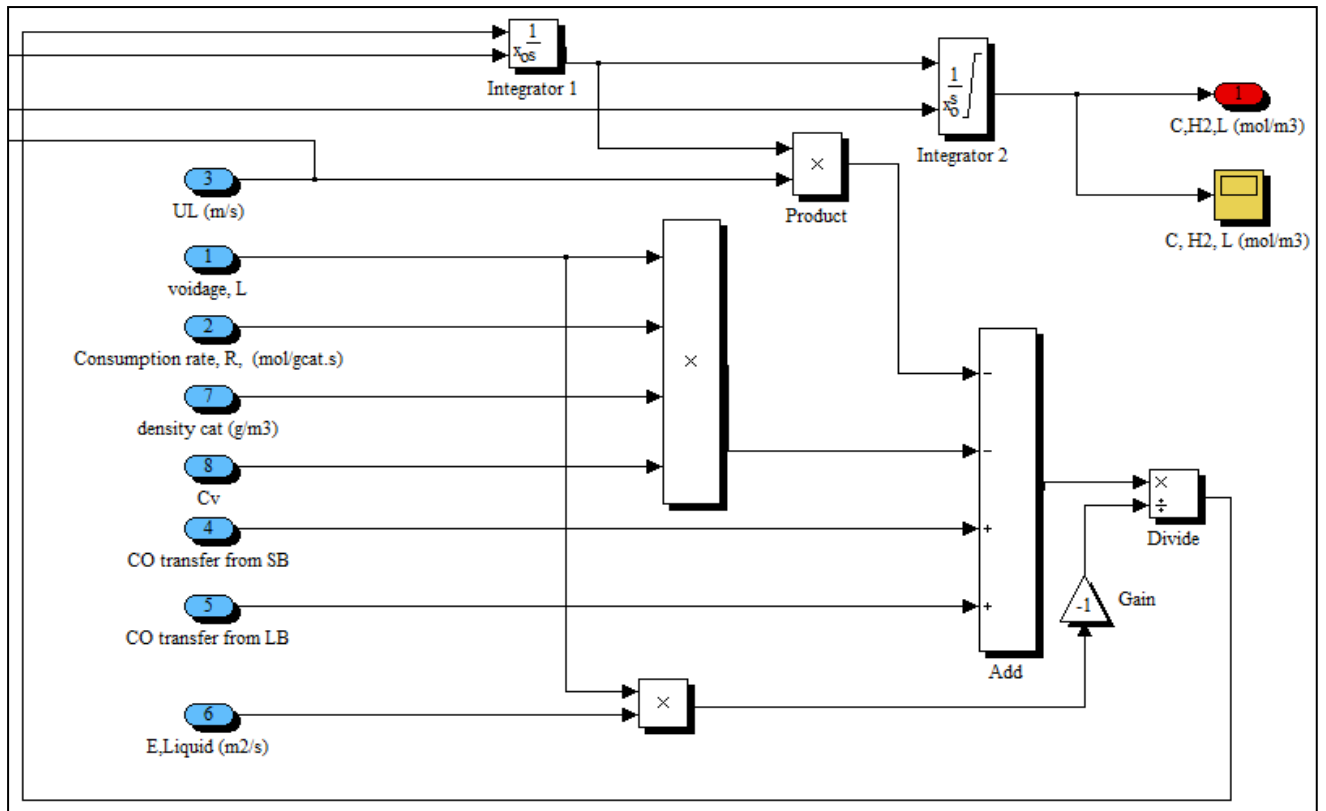


Figure 26: Simulink model for H₂ material balance in the liquid compartment

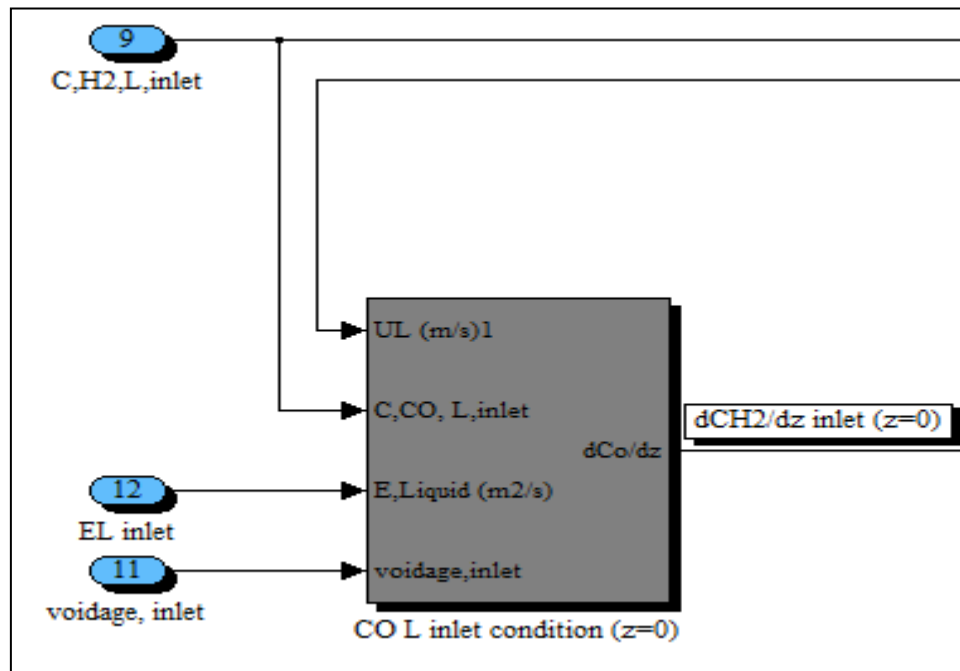


Figure 27: H₂ liquid phase material balance boundary condition Simulink model

4.2 Hydrodynamics

The equations describing the hydrodynamics are next translated into Simulink models beginning with the small bubbles superficial velocity.

4.2.1 Superficial gas velocity

The superficial velocity of the small bubbles was modelled in Simulink using Equation 31 as shown in Figure 28. The overall superficial gas velocity through the reactor was modelled using Equation 70 to show its decrease due to reaction consumption. This was modelled in Simulink as shown in Figure 29. In Figure 29, the gas concentration input refers to the sum of the concentrations of CO and H₂ in both the large and small bubble compartments, represented by Equation 72, and the relevant Simulink translation is shown in Figure 30.

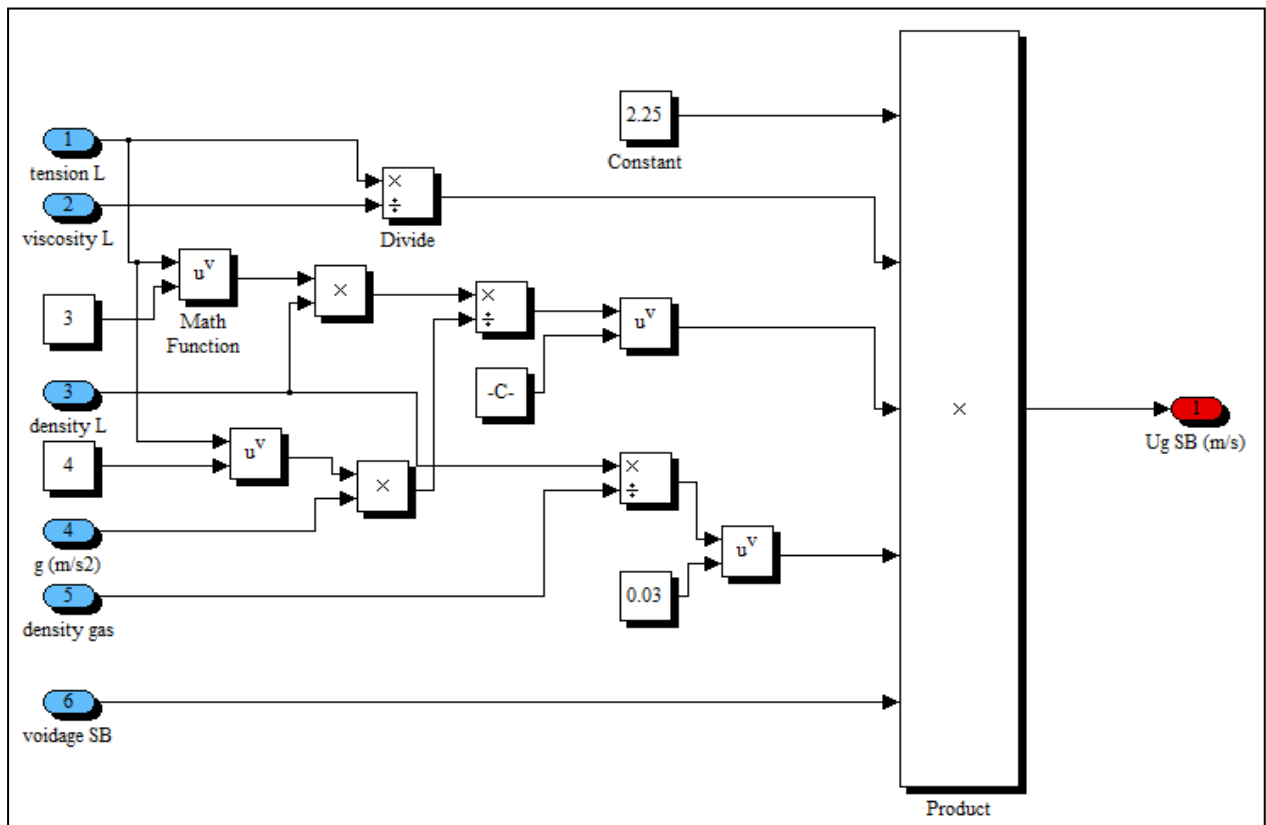


Figure 28: Simulink model for small bubble superficial velocity

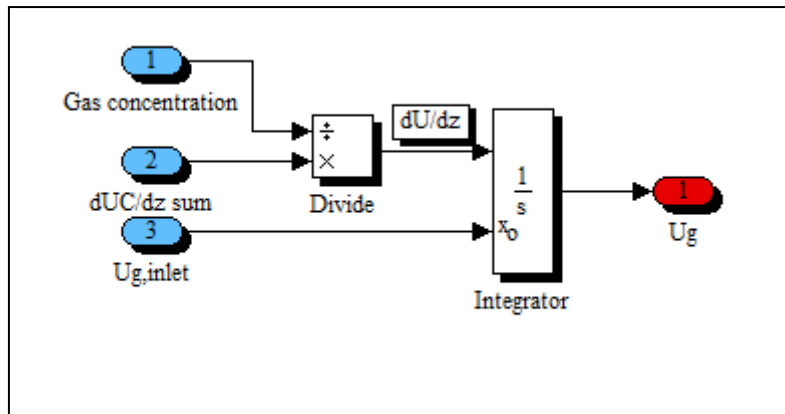


Figure 29: Simulink model of gas consumption in a SBCR

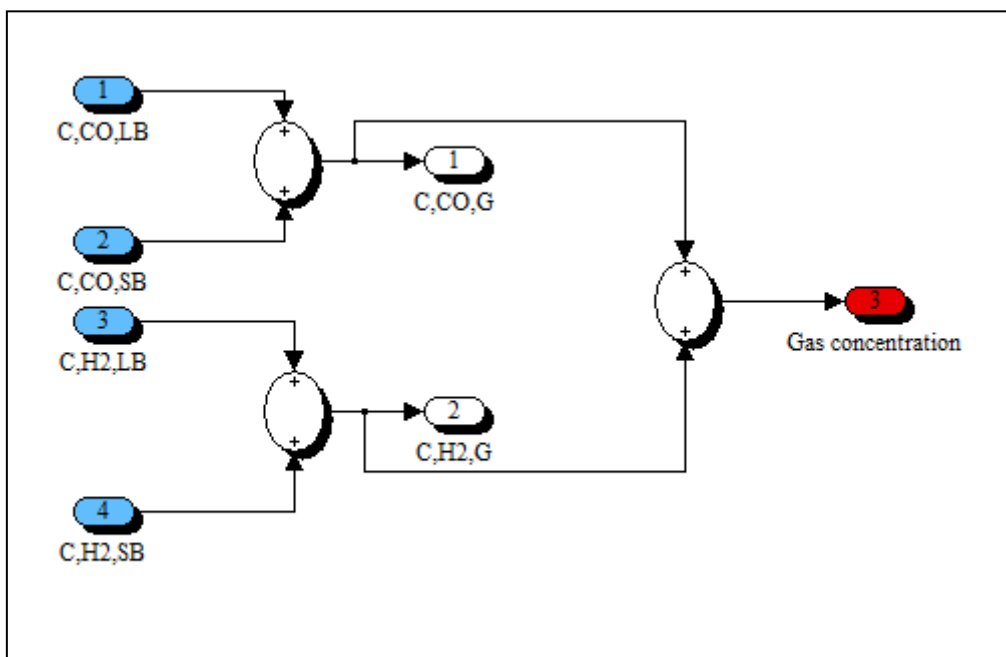


Figure 30: Simulink model of total gas concentration

4.2.2 Hold-up

The small bubbles gas hold-up was modelled in Simulink according to Equation 73 and the diagram is shown in Figure 31. The hold-up in the large bubbles compartment was modelled according to Equation 75 with the resulting Simulink model shown in Figure 32.

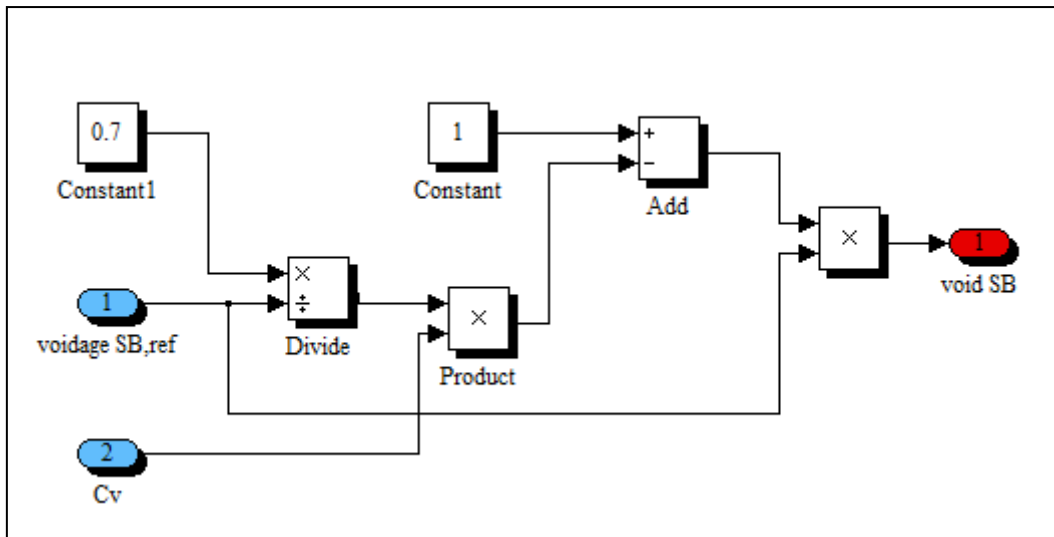


Figure 31: Simulink model of the small bubbles hold-up.

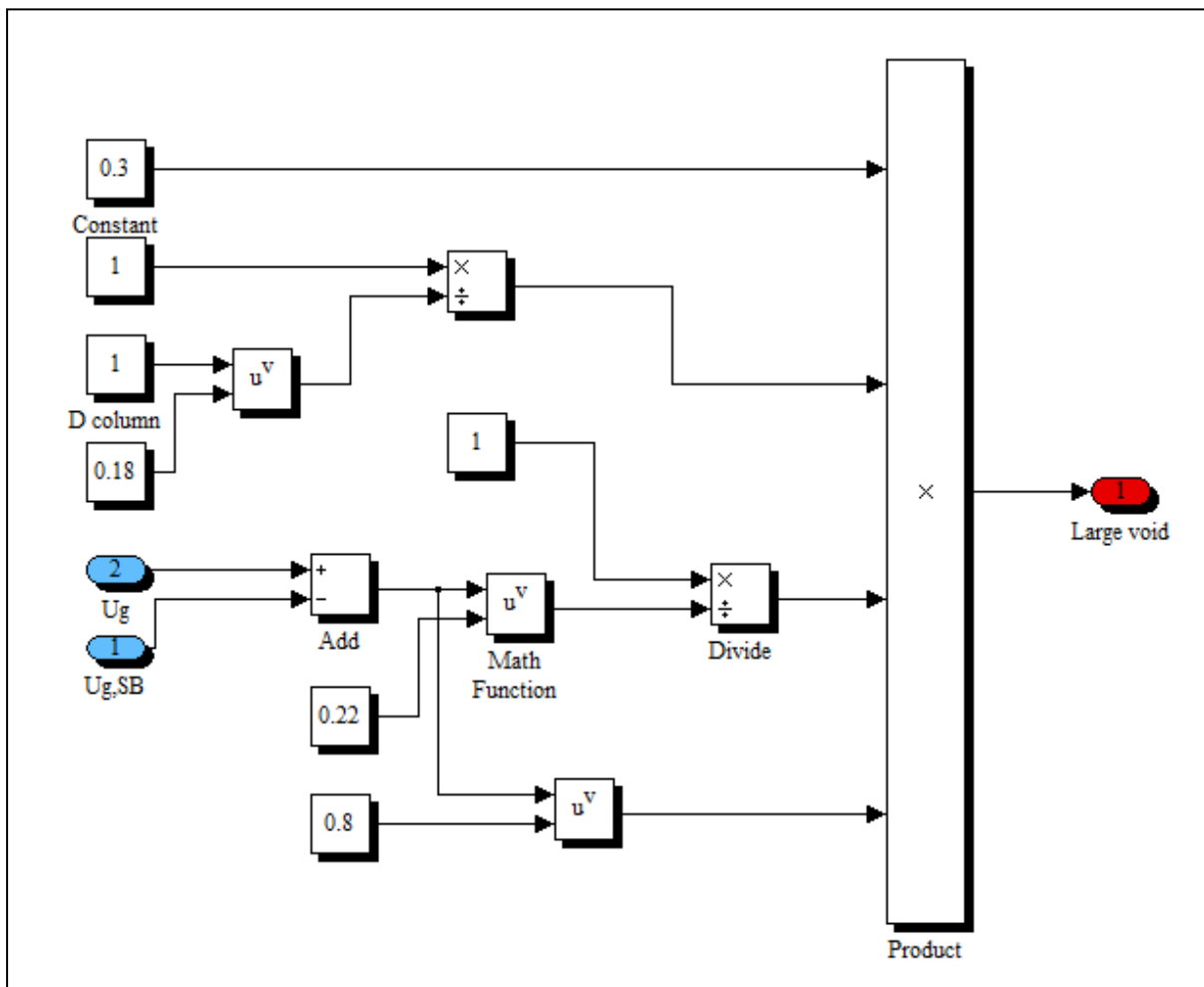


Figure 32: Simulink model representing large bubbles hold-up

4.2.3 Axial dispersion coefficient

4.2.3.1 Small bubble and liquid phase

The axial dispersion coefficient correlation (Equation 78), which is assumed to be the same in both the small bubble and liquid compartment, was built into Simulink as shown on the diagram in Figure 33.

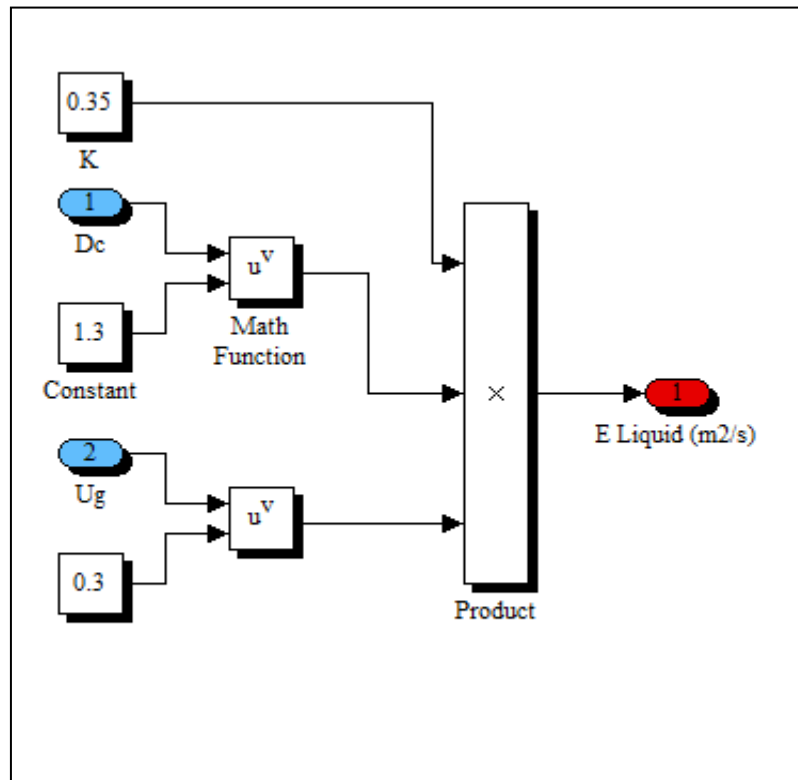


Figure 33: Liquid phase axial dispersion coefficient

4.2.3.2 Gas phase

The large bubble dispersion coefficient was modelled as shown in Figure 34 using the correlation by Mangartz and Pilhofer (1980).

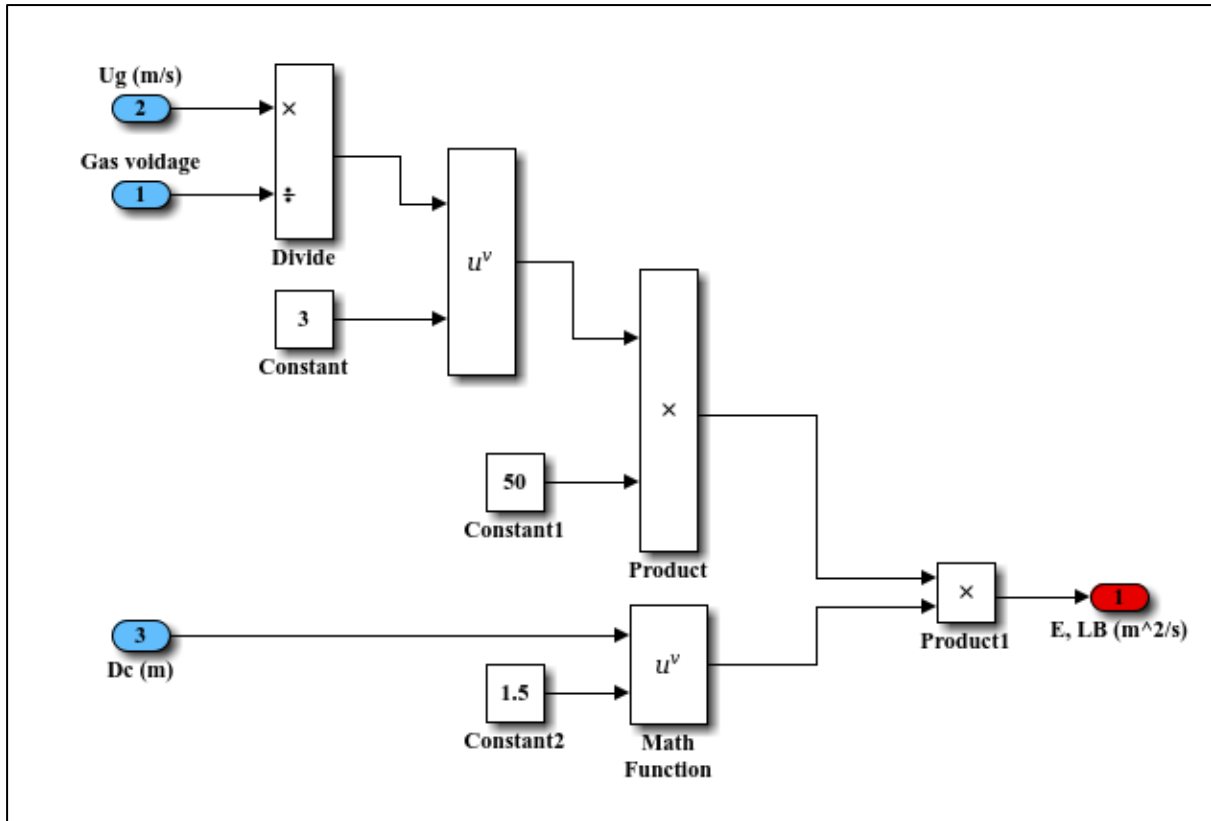


Figure 34: Large bubble axial dispersion coefficient Simulink model

4.3 Kinetics

The kinetic rate law, shown in Equation 16, was translated into a Simulink model with a block arrangement as shown in Figure 35. The rate and adsorption constant inputs in Figure 35 were determined using Equations 90 and 91 respectively with the Simulink diagrams shown in Figures 36 and 37.

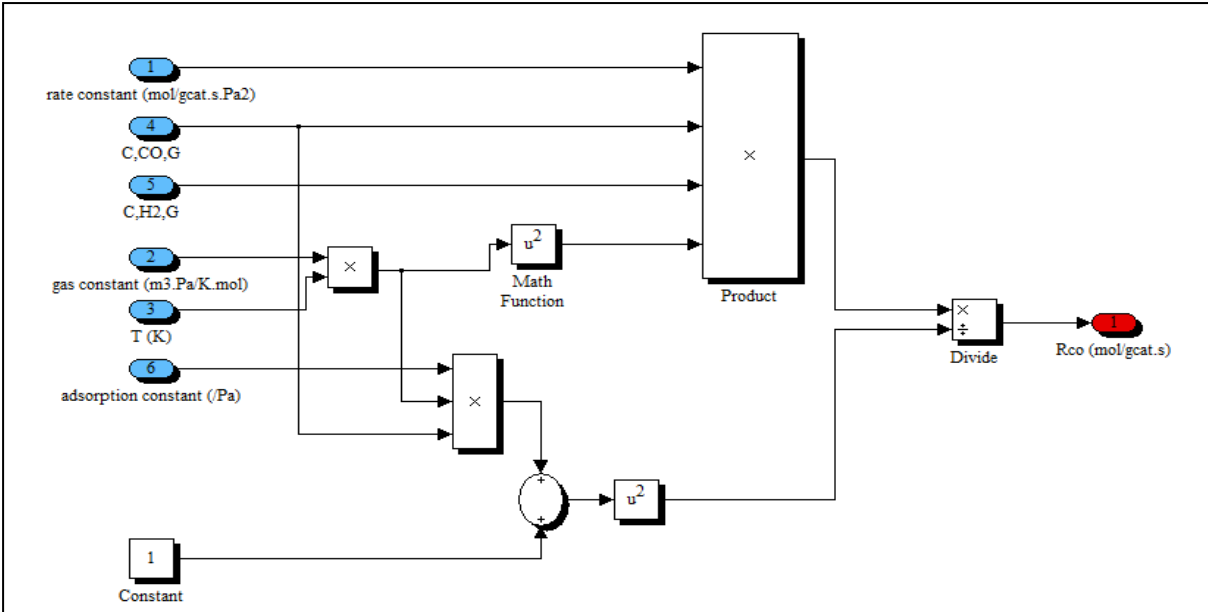


Figure 35: FT kinetic rate law in Simulink

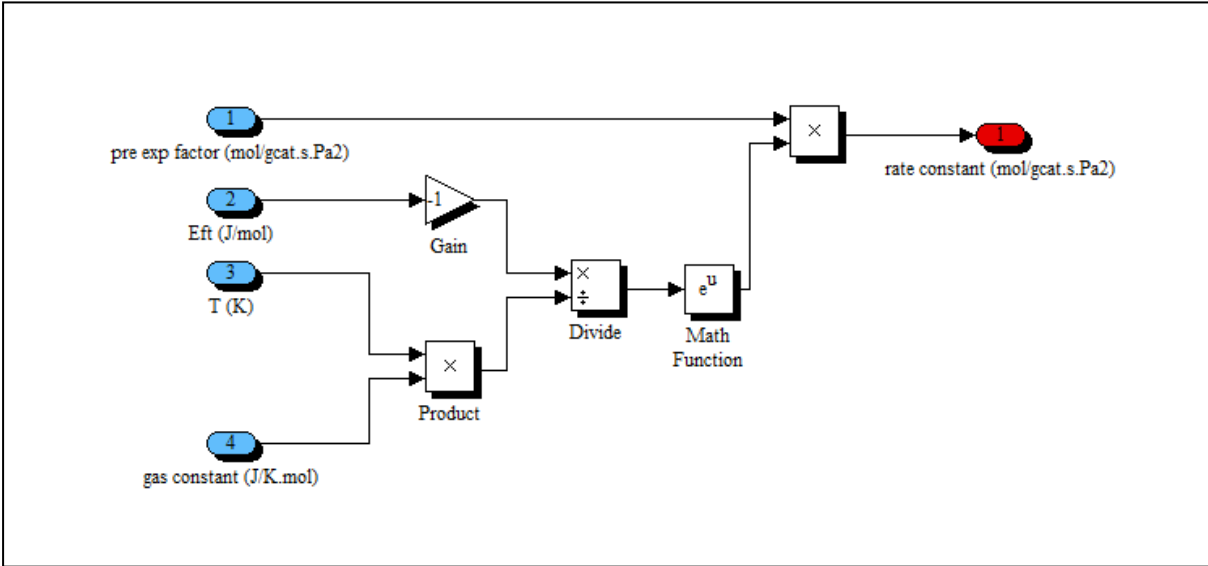


Figure 36: FT kinetic rate constant Simulink model

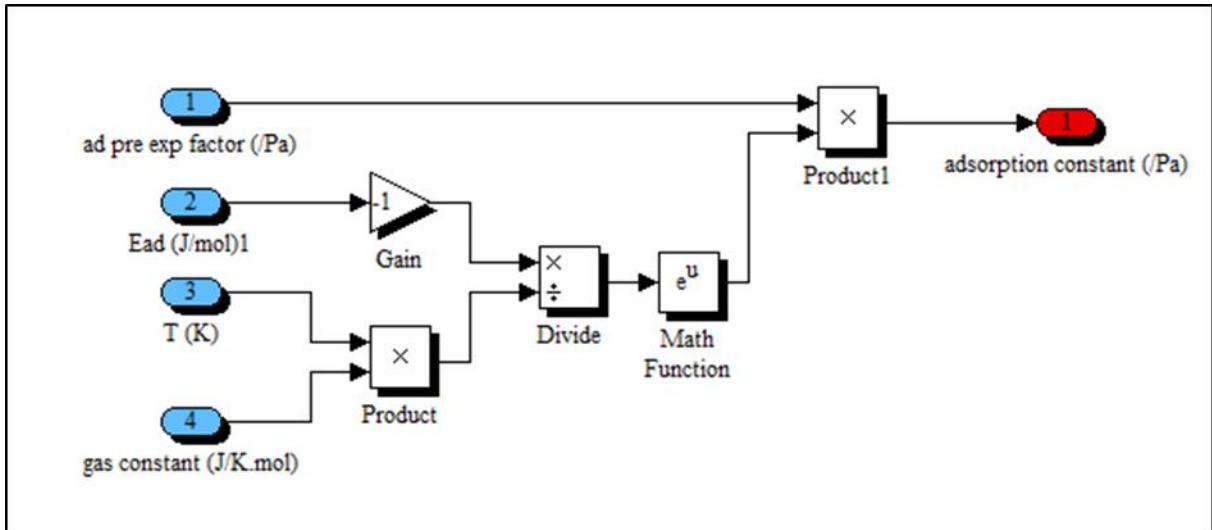


Figure 37: Simulink model of the FT adsorption rate constant

4.4 Mass transfer

The gas-liquid volumetric mass transfer coefficient correlations for CO in the large (Equation 80) and small bubble (Equation 83) compartments were translated into Simulink models as shown in Figures 38 and 39 respectively. Simulink models of the correlations for H₂ volumetric mass transfer coefficients in the large and small bubble compartments according to Equations 81 and 84 respectively, are shown in Figures 40 and 41.

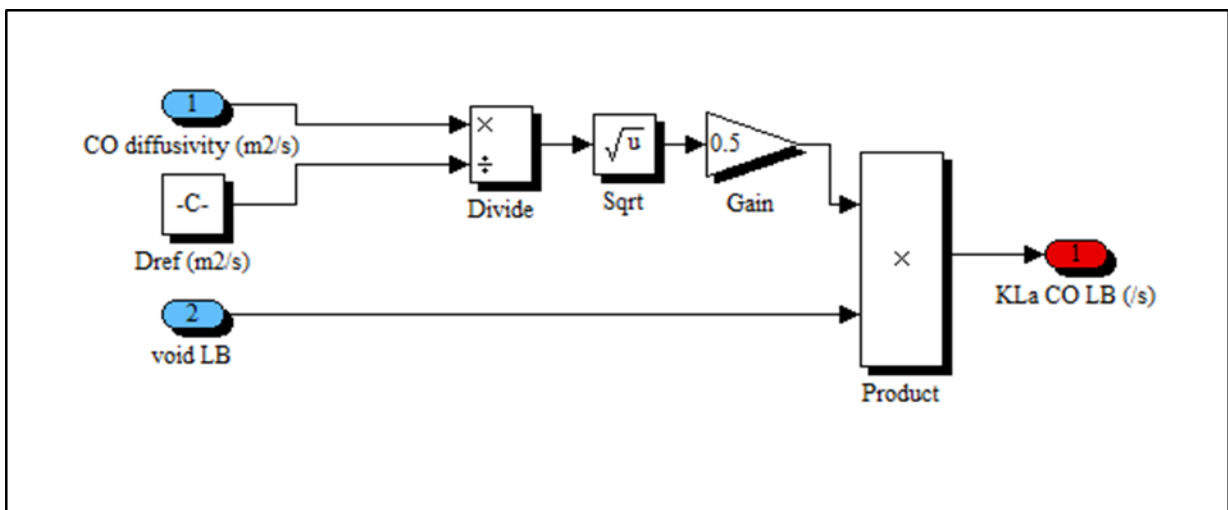


Figure 38: CO KLa Simulink model for the large bubble compartment

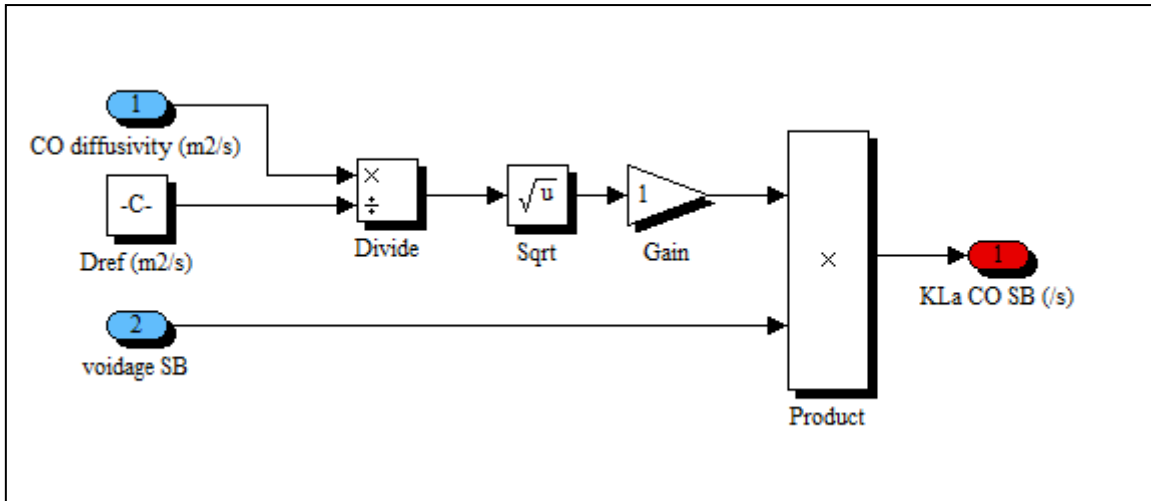


Figure 39: CO KLa Simulink model for the small bubble compartment

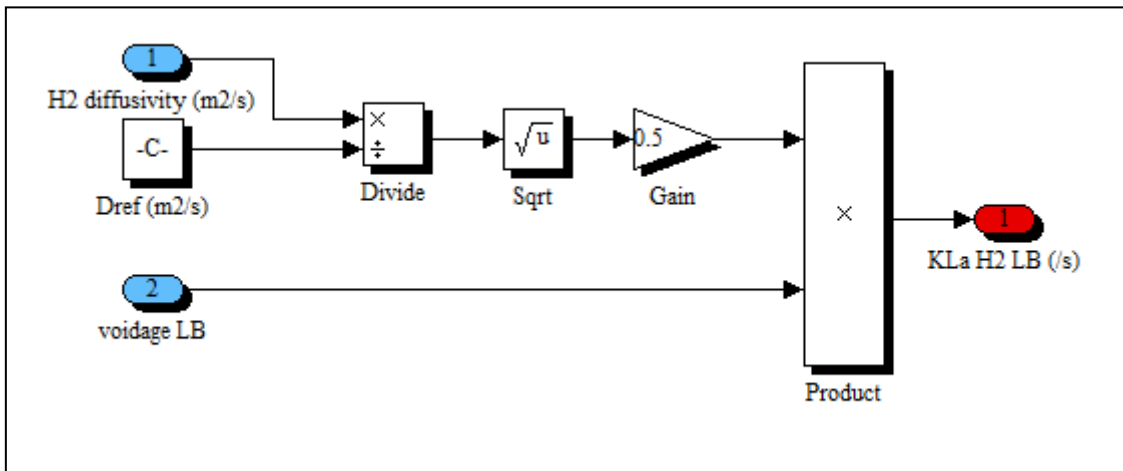


Figure 40: Simulink model of H₂ KLa in large bubble compartment

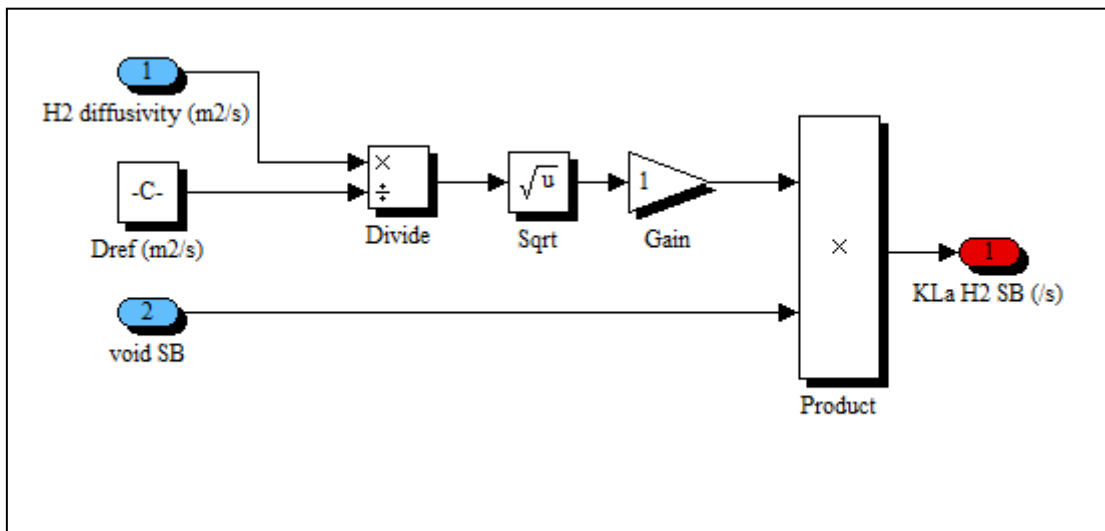


Figure 41: Simulink model of H₂ KLa in small bubble compartment

4.5 Phase properties

The gas/liquid physicochemical property correlations used were translated into Simulink models. The CO and H₂ Henry's constants from Table 12 were modelled as shown in Figures 42 and 43 respectively. The liquid density, viscosity and surface tension correlations as functions of temperature, from Table 11, were translated into Simulink models as shown in the diagrams in Figures 44, 45 and 46 respectively.

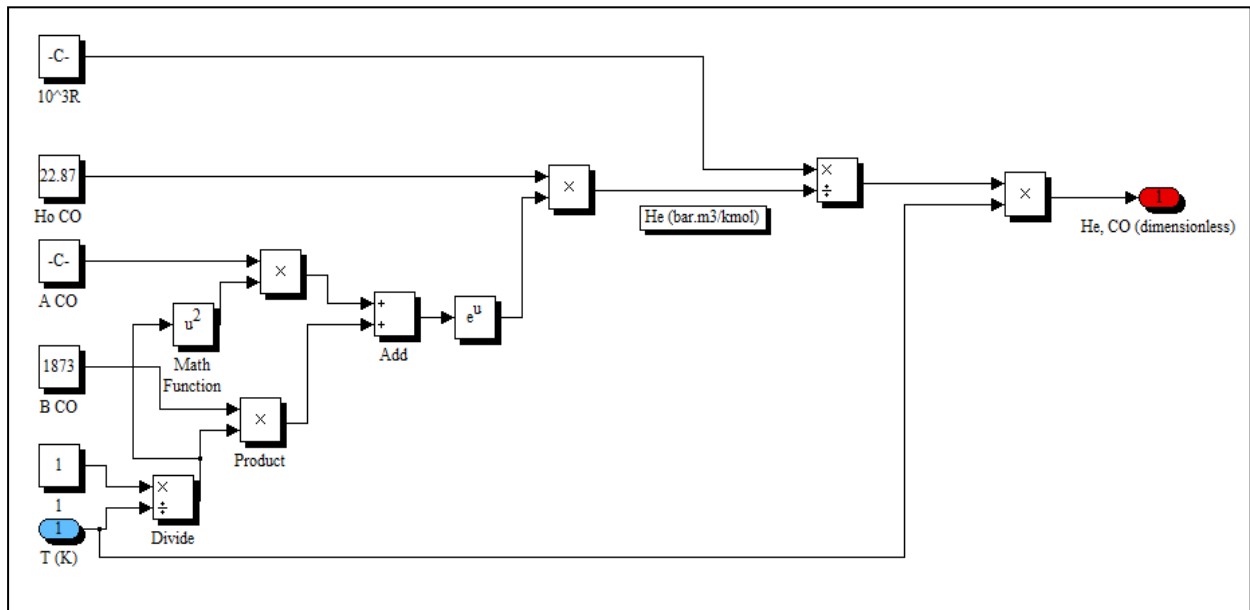


Figure 42: CO Henry's constant Simulink model

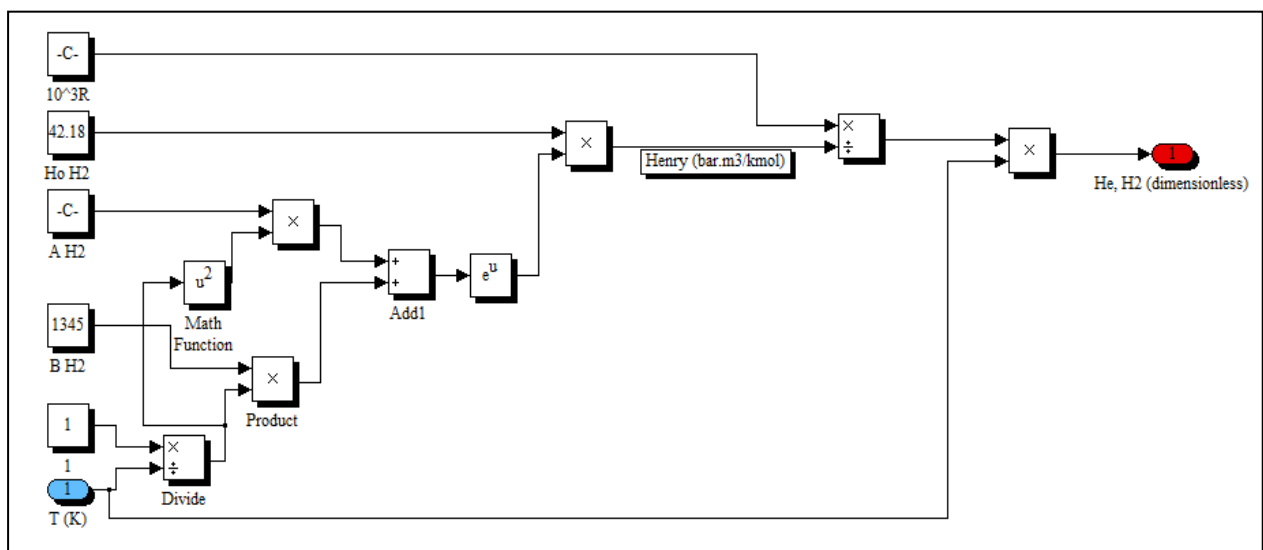


Figure 43: H₂ Henry's constant Simulink model

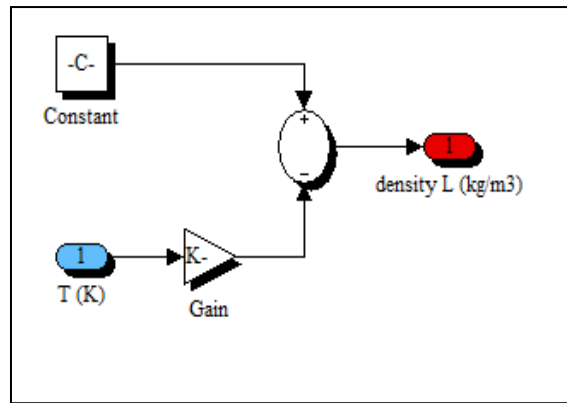


Figure 44: Liquid density Simulink model

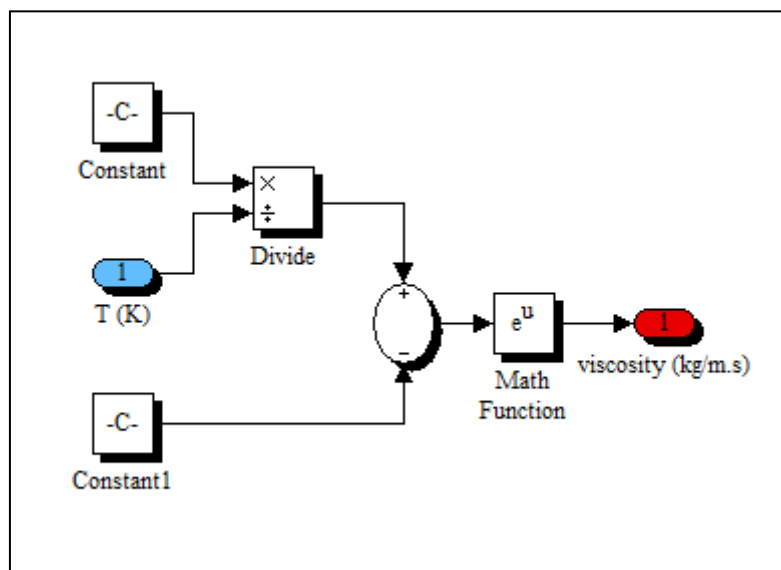


Figure 45: Liquid viscosity Simulink model

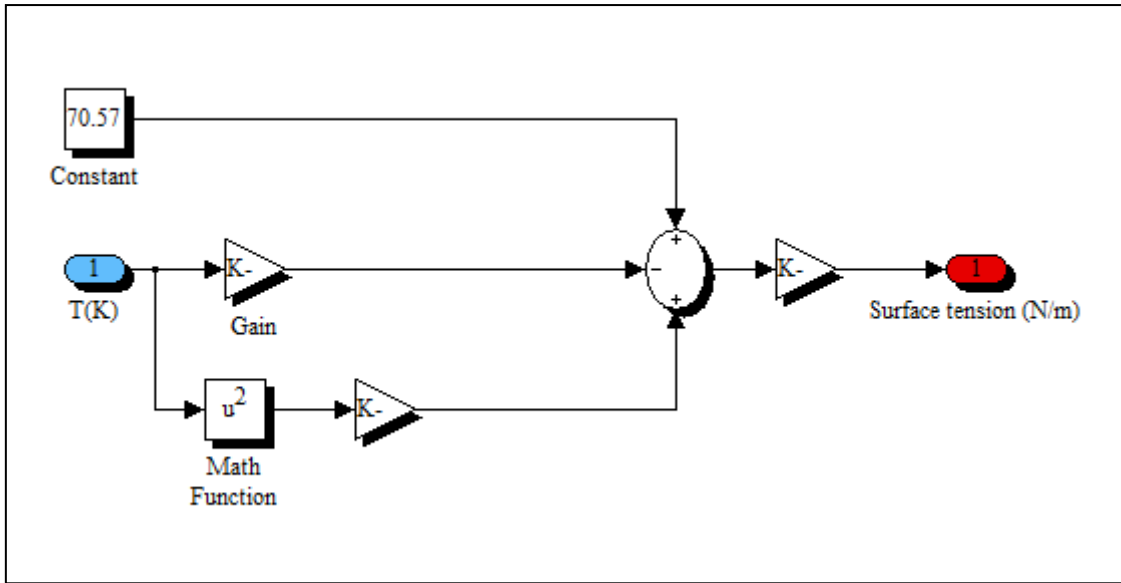
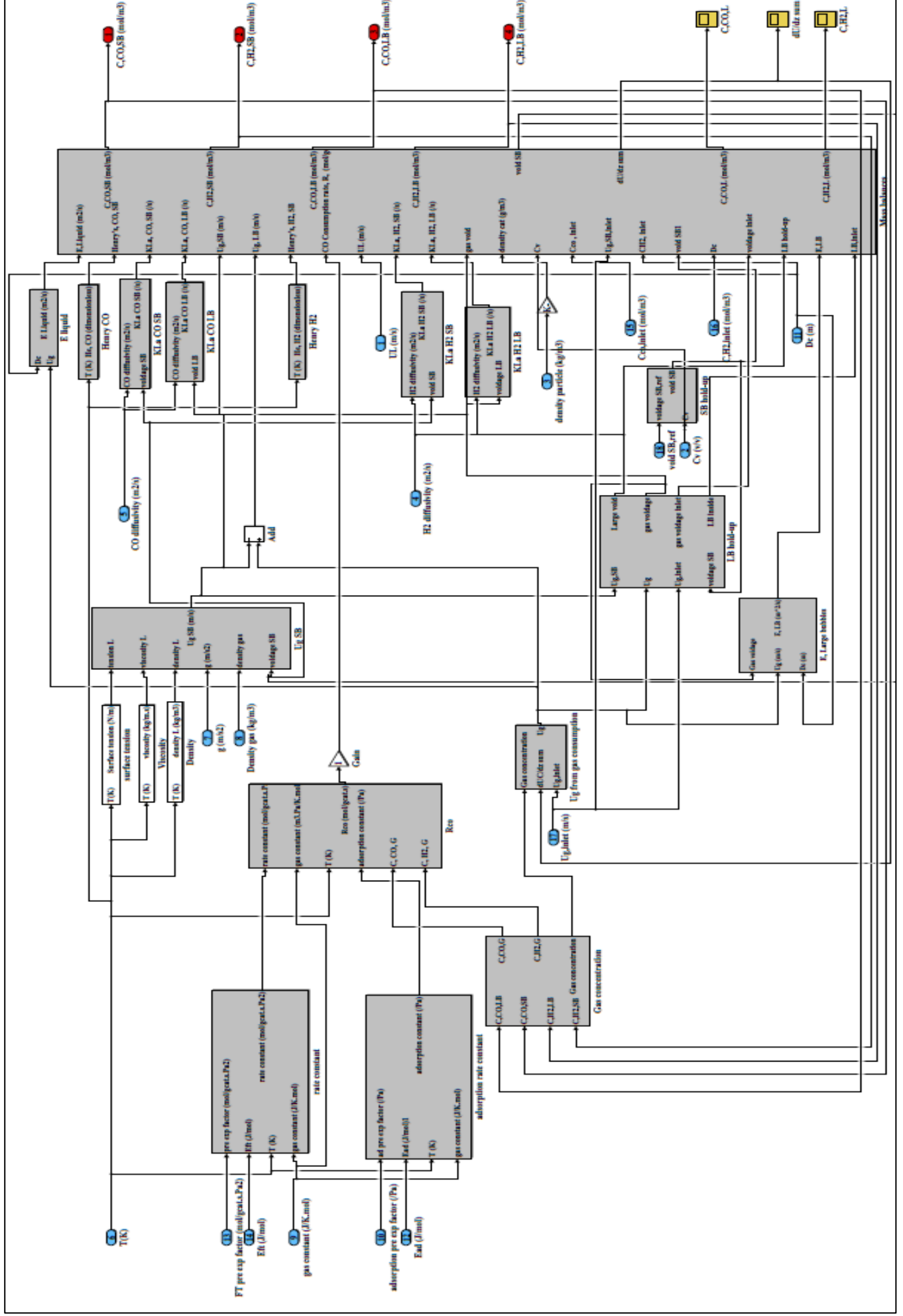


Figure 46: Liquid surface tension Simulink model

Figure 47: Overall SBCR Simulink model



4.6 Overall Model

The species material balances, hydrodynamics, kinetics and gas/liquid physicochemical property Simulink models as described above were all coupled into a single SBCR model as shown in Figure 47. A more compact view of the system in Figure 47 is shown in Figure 48. In Figure 48, only the inputs and outputs from Figure 47 are shown, allowing for easy identification of these important parameters.

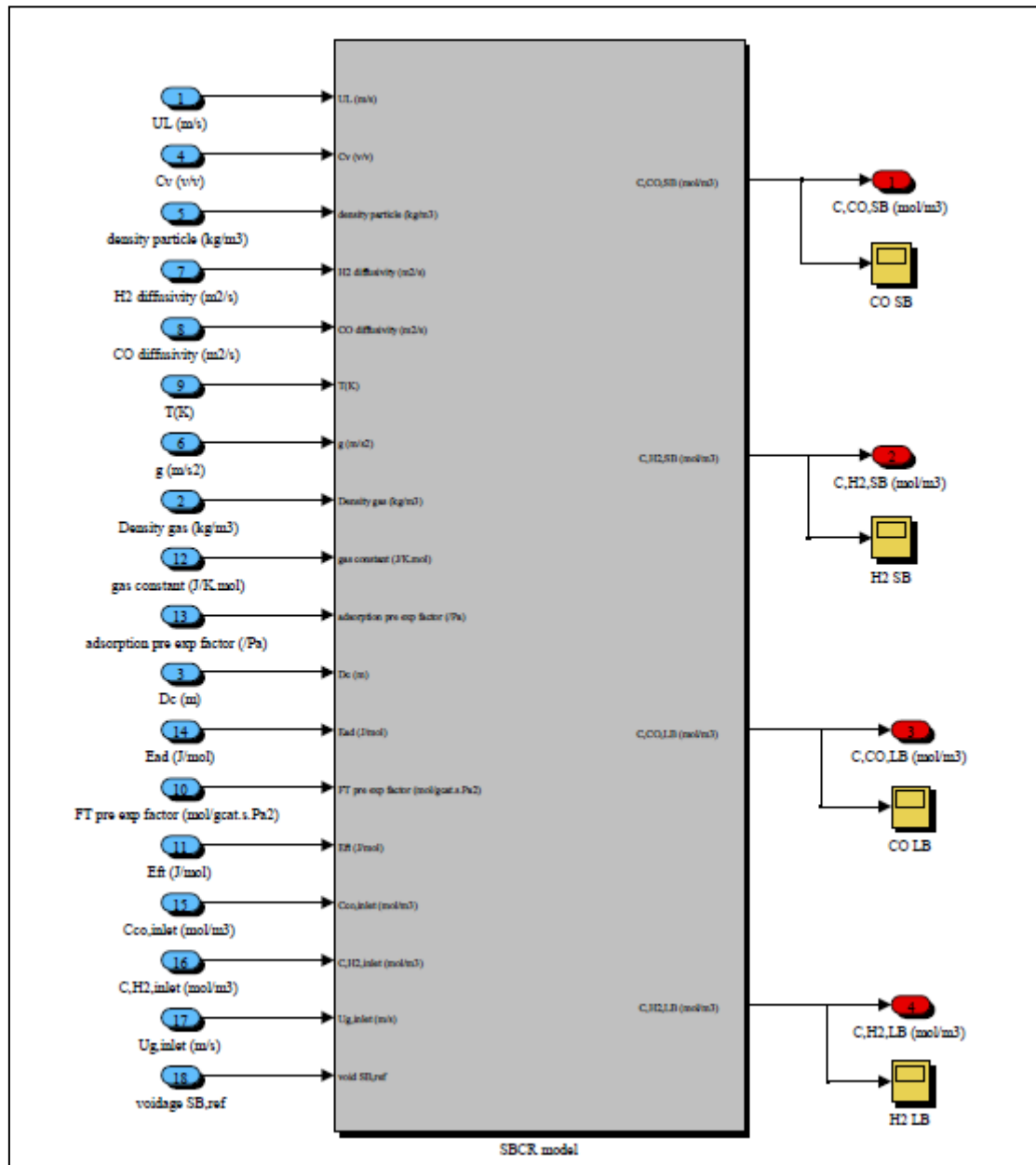


Figure 48: SBCR Simulink model with inputs and outputs only

Chapter 5: Simulation results and discussion

5.1 Results

The constructed model was simulated as per the typical SBCR conditions given in Table 6 and the feed conditions mentioned above. A detailed set of input conditions are given below in Table 14. The Simulink simulation was run between a height of 0 and 30 m, resulting in changes across the various reactor parameters. To provide a brief summary of the behaviour of the SBCR according to the simulation, the affected parameters are given at the final height of 30 m and compared to those at the inlet (H=0 m) in Table 15. A more detailed analysis of the results will follow in the discussion section. The reactant concentrations in all phases decrease over the height of the reactor as is expected, given the assumption of axial dispersion in all phases. The zero species concentrations in the small bubbles and liquid phases does not represent a total non-existence of the species in these phases but alludes to a balance between the gas/liquid mass transfer and reaction rates at these points as shall be discussed in the next section. The syngas conversion was calculated using Equation 95.

$$X_{CO+H_2} = \frac{(C_{CO}+C_{H_2})_{inlet} - (C_{CO}+C_{H_2})_{outlet}}{(C_{CO}+C_{H_2})_{inlet}} \times 100 \quad [95]$$

Table 14: Input variables into Simulink model

Input	Unit	Value
Slurry velocity, U_L	m/s	0,02
Catalyst loading, C_v	-	0,3
Catalyst density	kg/m ³	647
H ₂ diffusivity	m ² /s	45,5×10 ⁻⁹
CO diffusivity	m ² /s	17.2×10 ⁻⁹
T	K	513
g	m/s ²	9,81
Syngas density	kg/m ³	7
Ideal gas constant	J/K.mol	8,314
Adsorption pre-exponential factor	Pa ⁻¹	1.243×10 ⁻¹²
Column diameter	m	7
Adsorption activation energy	J/mol	-68474.1
Reaction pre-exponential factor	mol/g _{cat} .s.Pa ²	8.037×10 ⁻¹²
Reaction activation energy	J/mol	37369.5
CO inlet concentration	mol/m ³	218.41
H ₂ inlet concentration	mol/m ³	436.82
Inlet U_g	m/s	0,4
reference ϵ_{SB}	-	0,27

Table 15: Model parameter change across reactor height

Value				
Parameter	Unit	Inlet (z=0)	Outlet (z=30)	% decrease
C_{CO,LB}	mol/m ³	218.41	82.97	62.01
C_{H₂,LB}	mol/m ³	436.82	156.69	64.13
C_{CO,SB}	mol/m ³	218.41	0	100
C_{H₂,SB}	mol/m ³	436.82	0	100
C_{CO,L}	mol/m ³	42.3	0	100
C_{H₂,L}	mol/m ³	32.3	0	100
U_g	m/s	0.3	0.097	67.67
E_L	m ² /s	3.3	2.9	12.12
E_{LB}	m ² /s	3115.7	362.5	88.37
R_{CO}	mol/g _{cat} .s	1.69×10 ⁻⁵	1.13×10 ⁻⁵	33.14
ε_{SB}	-	0.06	0.06	0
ε_{LB}	-	0.149	0.075	49.66
ε_L	-	0.8	0.87	-8.75
K_{la,CO_{LB}}	s ⁻¹	0.22	0.11	50
K_{la,CO_{SB}}	s ⁻¹	0.18	0.18	0
K_{la,H₂,LB}	s ⁻¹	0.36	0.18	50
K_{la,H₂,SB}	s ⁻¹	0.29	0.29	0
CO conversion	%	0	62.01	-
H₂ conversion	%	0	64.13	-
Syngas conversion	%	0	63.42	-

5.2 Model Discussion

5.2.1 Concentration gradients

In this section, the reactant concentration gradients present in all applicable phases will be considered in order to provide a qualitative analysis of the behaviour and fate of the syngas fed into the reactor. In assessing the concentration change in the various phases, only the CO species will be considered. The reason is that the syngas is fed at the stoichiometrically required H₂/CO ratio of 2:1 and as the rate of reaction of the hydrogen molecules is set at twice that of the CO molecules, the behaviour of both species is expected to be similar, i.e., the overall rate of consumption of CO should be equal to that of hydrogen. The only point of difference between the two species' behaviour exists in the different mass transfer resistances experienced by these species and this is as a result of differing diffusivities. Hydrogen, as shown in Table 14, has a higher diffusivity than CO meaning more hydrogen can diffuse through the gas-liquid interphase per unit time. This is evidenced by the slightly higher hydrogen conversion in Table 15. These subtle differences in the species' behaviour can be considered small enough so that the two species can be assumed to behave the same. This assumption is certainly appropriate for the purposes of evaluating either species' behaviour as a means to study the hydrodynamics inside the SBCR which is the purpose of this work. In the following sections, the dynamics inside the SBCR shall be interpreted with regard only to the CO species.

5.2.1.1 Concentration profile in large bubbles

As can be seen in Figure 49, the concentration of CO in the large bubbles decreases linearly over the height of the reactor bed. To explain this trend, it is important to consider the rate at which the CO species is depleted. The rate of depletion of CO, $(\frac{UdC_{CO,LB}}{dz})$, depends on the rate of mass transfer from the large bubbles to the liquid phase which is in turn dependent on the gas-liquid mass transfer coefficient.

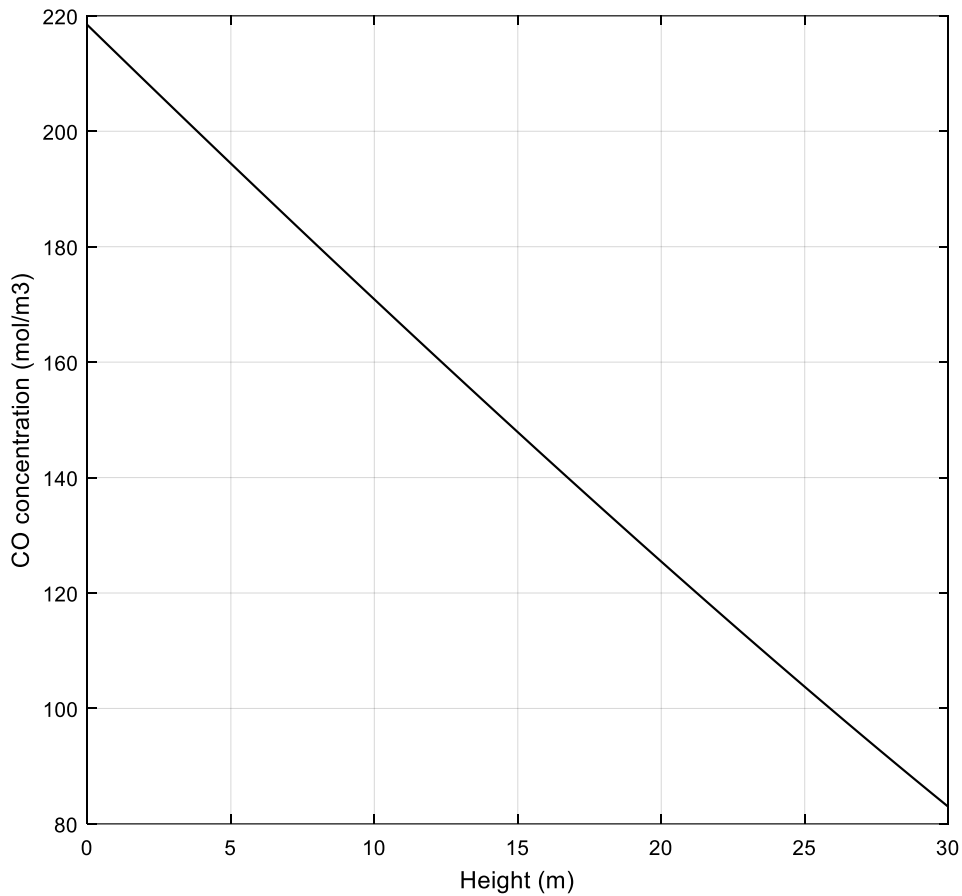


Figure 49: CO concentration in large bubble phase across reactor height.

The mass transfer coefficient between the liquid and large bubbles (Figure 50) depends on the large bubble gas hold-up according to Equation 80 (Maretto and Krishna, 1999). The large bubble hold-up (Figure 51) is proportional to the superficial gas velocity (Equation 74) which is known to decrease over the reactor bed height according to Equation 70 (Figure 52) (Bukur, 1983 and Iliuta et al., 2007). This means that the mass transfer rate across the gas-liquid interphase is proportional to the superficial gas velocity so that as it decreases, the mass transfer rate decreases as well. This will, over the reactor bed height, have the effect of reducing the rate of depletion of CO from the large bubbles.

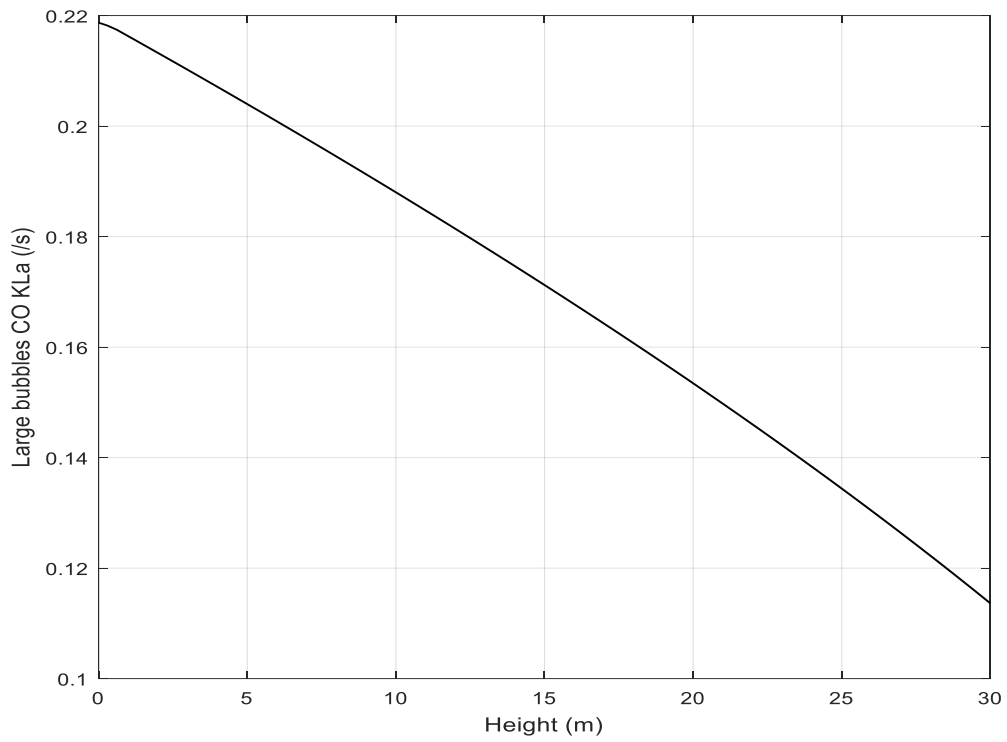


Figure 50: Large bubbles-liquid CO mass transfer coefficient across reactor height

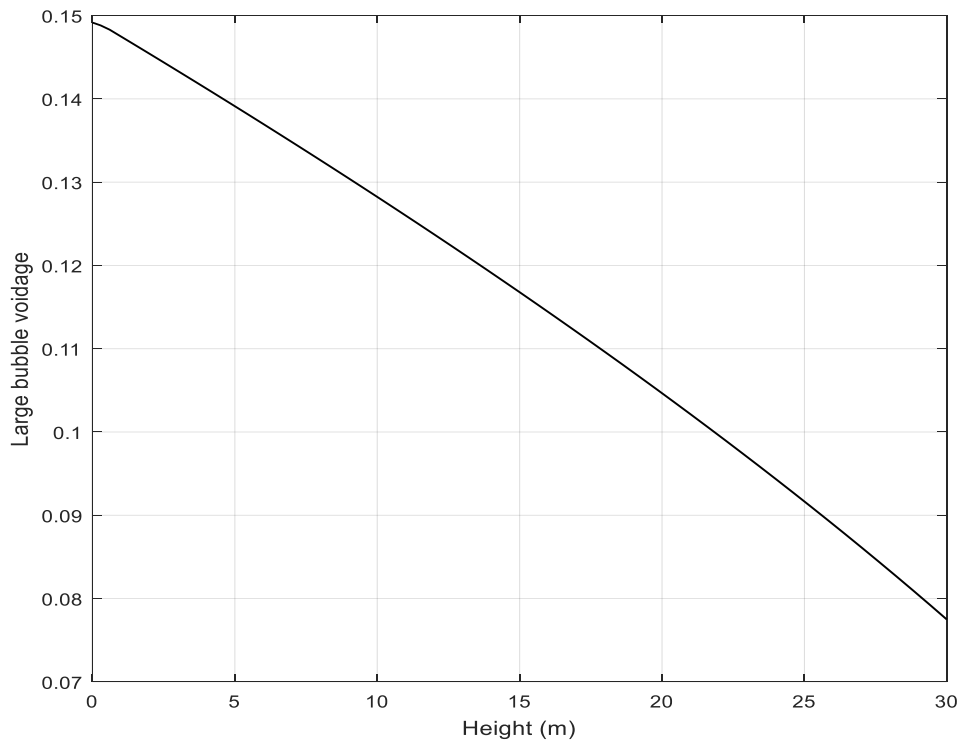


Figure 51: Large bubble hold-up as a function of reactor height

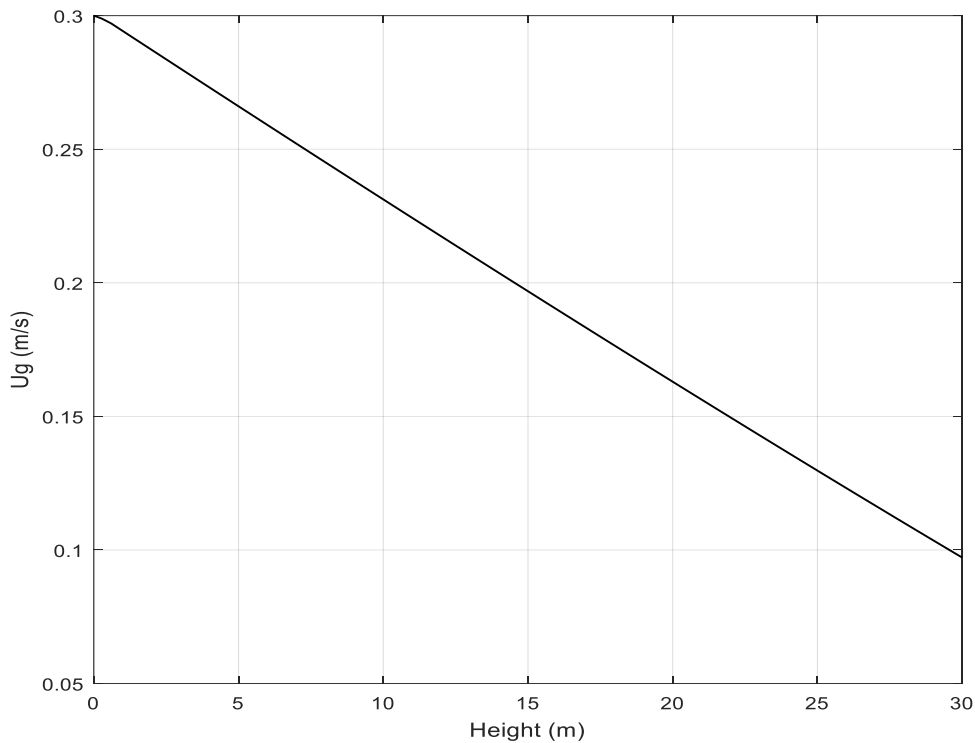


Figure 52: Superficial gas velocity change over reactor height

The rate of mass transfer is also affected by the species concentration differential that exists between the phases. As Figure 53 shows, the concentration difference, $C_{CO,LB}^* - C_{CO,L}$, changes with respect to the height of the reactor and this affects $\frac{UdC_{CO,LB}}{dz}$. The gas phase concentration of CO is dependent on the mass transfer coefficient and the concentration of the species in the liquid phase. The liquid phase concentration is dependent on the gas phase concentration and on the reaction rate. It is clear that the concentrations of CO on both sides of the gas-liquid interphase are dependent on each other but what should also be clear is that the liquid phase concentration is also dependent on R_{CO} . R_{CO} is a variable that is one of the sources, together with axial dispersion, of all the axial profiles. This means that the mass transfer rate between the large bubbles and the liquid phase is influenced by the reaction rate through the consumption of CO in both the liquid phase, through reaction itself, and the gas phase through mass transfer which depends on the superficial gas velocity (Kojima et al., 1997).

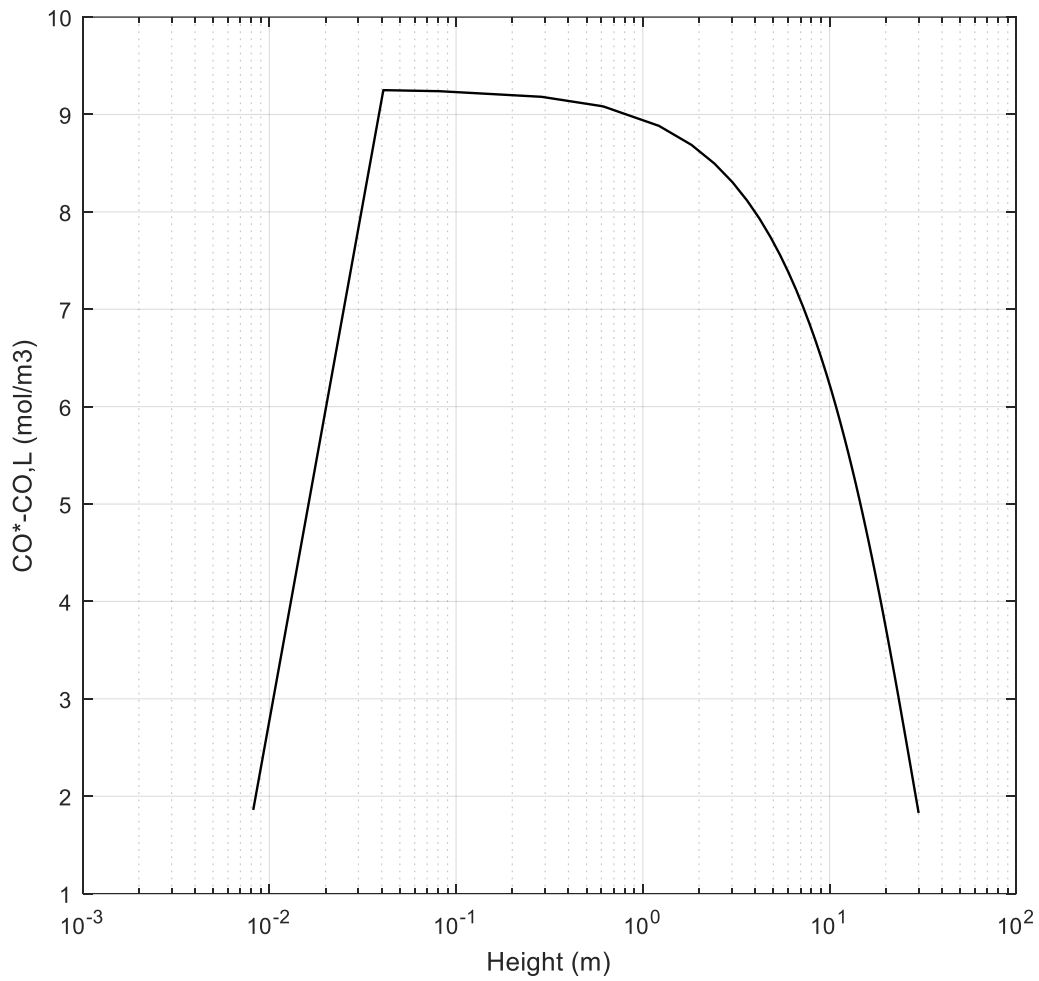


Figure 53: Interphase concentration difference between large bubble and liquid phases

Initially, $C_{CO,LB}^* - C_{CO,L}$ increases sharply and then proceeds to decrease up to the top of the reactor bed. Because of the rapid increase, a log scale was used to illustrate this change more clearly. The sharp increase is due to the rapid disappearance of CO that is initially present in the liquid phase as evidenced in Figure 54.

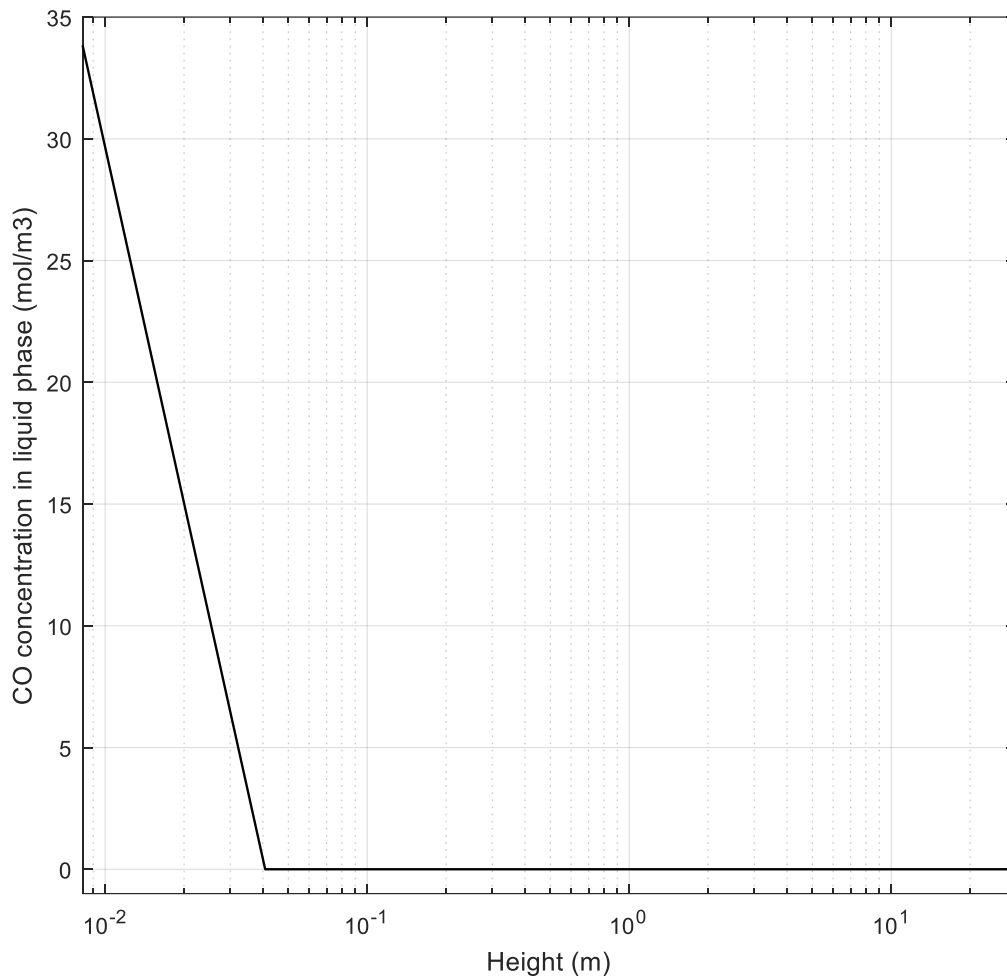


Figure 54: Axial change of CO concentration in the liquid phase

The subsequent drop in $C_{CO,LB}^* - C_{CO,L}$ over the length of the reactor indicates a constant liquid phase concentration so that the decreasing gas phase concentration becomes the dominating factor. This means that the mass transfer rate between the large bubbles and liquid phases is also proportional to the reaction rate so that as the reaction rate decreases (Figure 55), the mass transfer rate decreases as well. This will add to the retardation effect that the mass transfer coefficient has on the depletion rate of CO in the large bubbles over the height of the reactor.

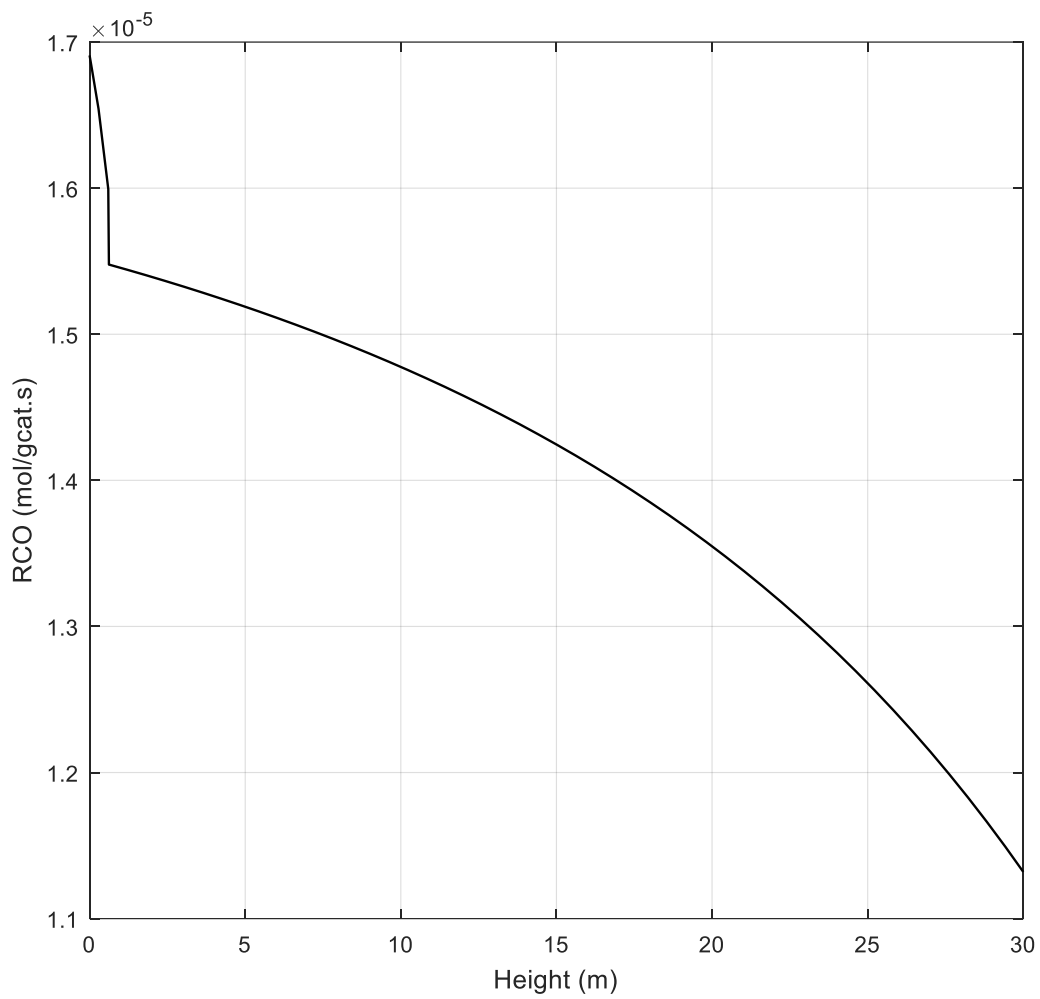


Figure 55: CO reaction rate as a function of reactor height

$\frac{UdC_{CO,LB}}{dz}$ is also affected by the extent of dispersion in the large bubbles. According to Equation 46, dispersion in the large bubble class depends on the large bubble hold-up (Figure 51) and the large bubbles dispersion coefficient (Figure 56).

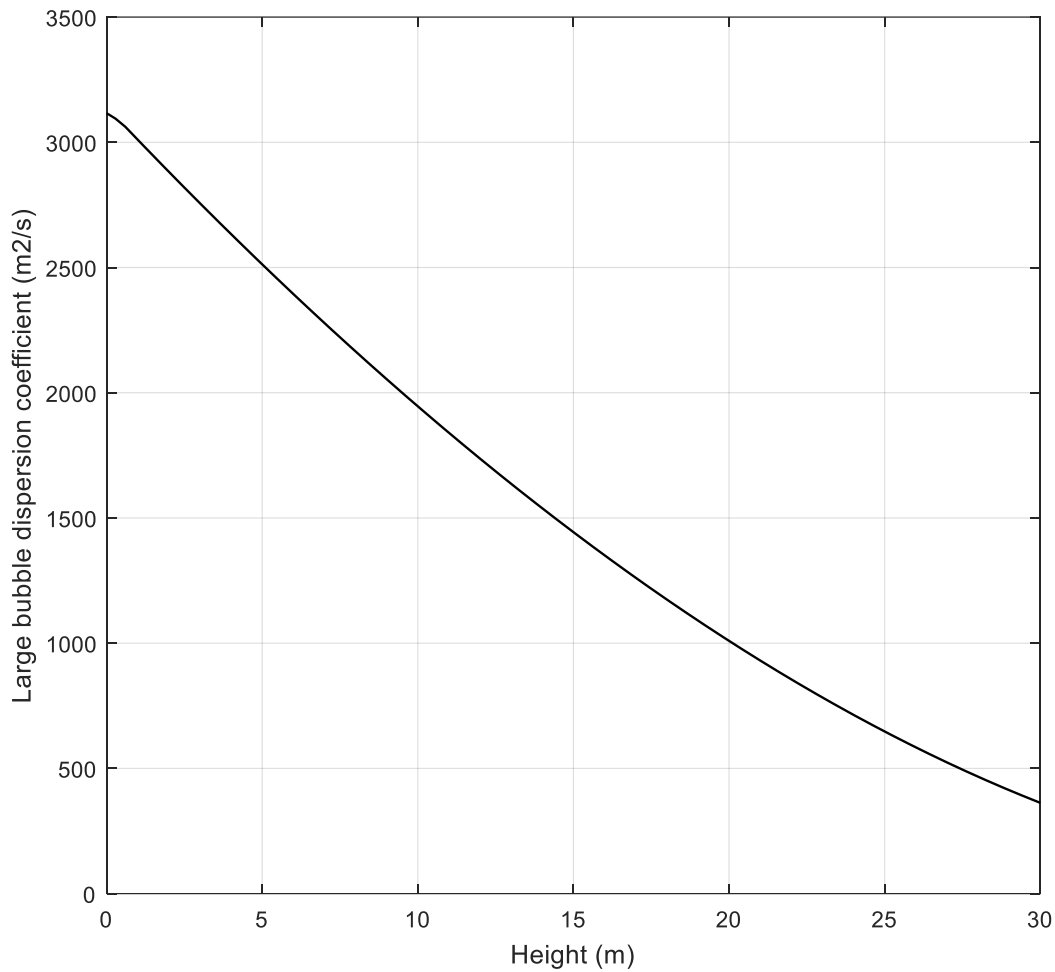


Figure 56: Large bubble phase dispersion coefficient over height of the reactor

Both these variables depend proportionally on the superficial gas velocity so that a decrease in the superficial gas velocity will result in a decrease in E_{LB} and ε_{LB} thus lowering the gas phase dispersion. A lower gas phase dispersion translates into a flow regime that is more towards plug flow and a higher rate of species depletion. The decrease of U_g across the reactor height has two opposite effects on the rate of depletion of CO in the large bubbles. On the one hand, a decreasing U_g lowers the mass transfer rate across the gas-liquid interphase resulting in a lower depletion rate of CO and on the other hand, the decreasing U_g reduces dispersion thus increasing the species' depletion rate. A decreasing U_g also reduces R_{CO} which further lowers the mass transfer rate and depletion rate of CO in the large bubbles. According to the simulation run on the model, $\frac{UdC_{CO,LB}}{dz}$ decreases (NB: $\frac{UdC_{CO,LB}}{dz}$ increases in the negative direction) over the height of the reactor (seen in Figure 57) indicating that under

the prevailing operating conditions, the effect of a decreasing mass transfer rate is dominant over that of a decreasing gas phase dispersion. The effect of this is evident in the changing gradient of the CO concentration against the axial height plot in Figure 58. The simulation was run over an extended height of 44 m to illustrate this point. As can be seen in Figure 58, the plot begins to flatten out horizontally at the greater heights where the rate of depletion is lowest.

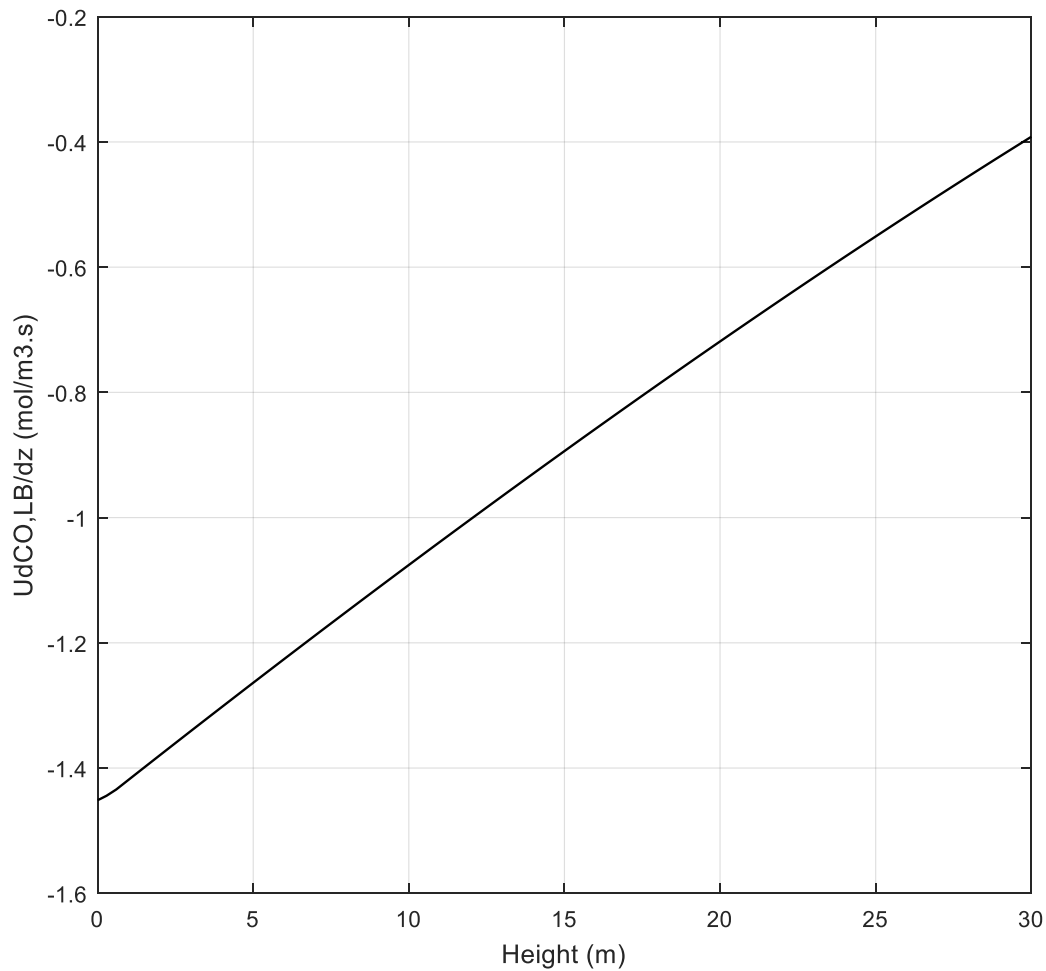


Figure 57: rate of CO depletion in large bubbles over reactor height

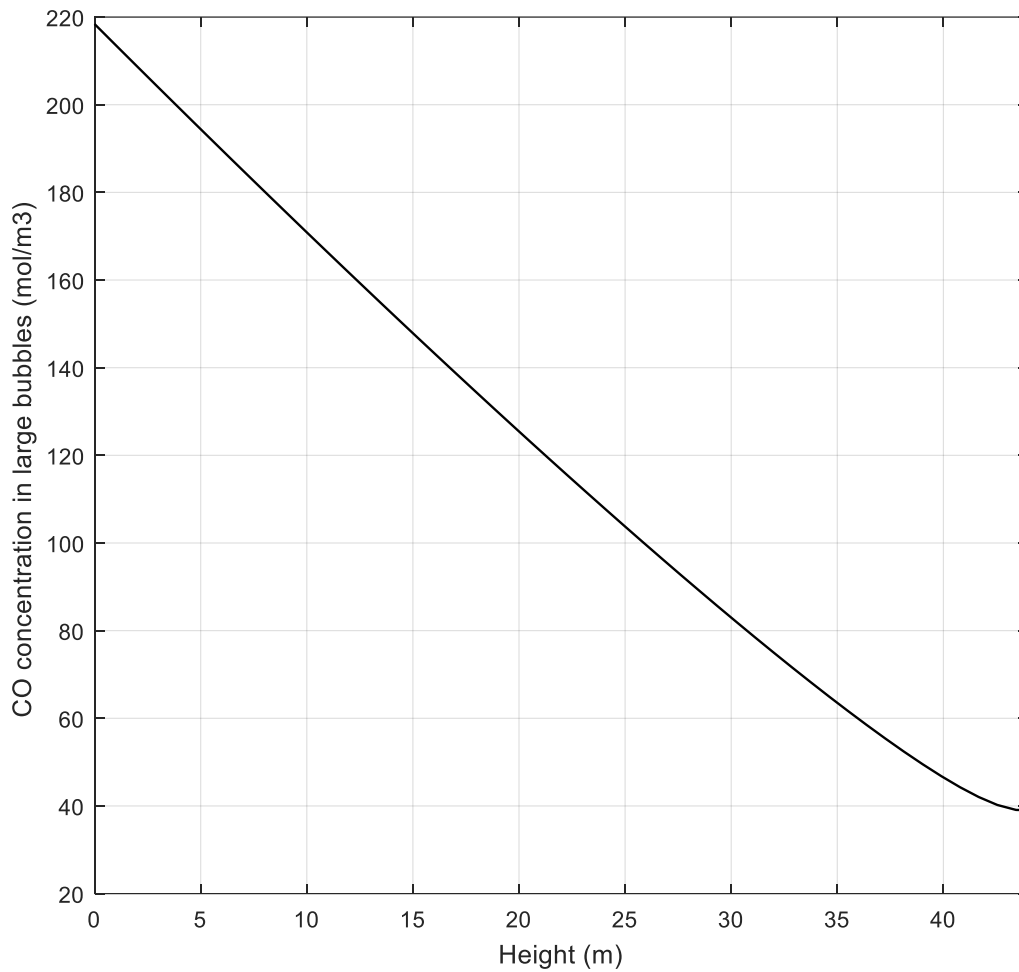


Figure 58: CO concentration in large bubbles over extended height

5.2.1.2 Concentration profile in small bubbles

The change in the rate of depletion of CO in the small bubbles is independent of the small bubble-liquid mass transfer coefficient which is constant throughout the height of the reactor. This is because ε_{SB} is constant over the reactor height as well (an assumption made in the model). This also means that the change in the small bubbles dispersion, which is dependent on the changes in ε_{SB} and E_{SB} , will depend solely on E_{SB} which is, according to Equation 78 (Baird and Rice, 1975) dependent on U_g . As U_g decreases over the reactor height, the small bubbles dispersion decreases as well resulting in an increasing $\frac{UdC_{i,SB}}{dz}$ (Figure 59).

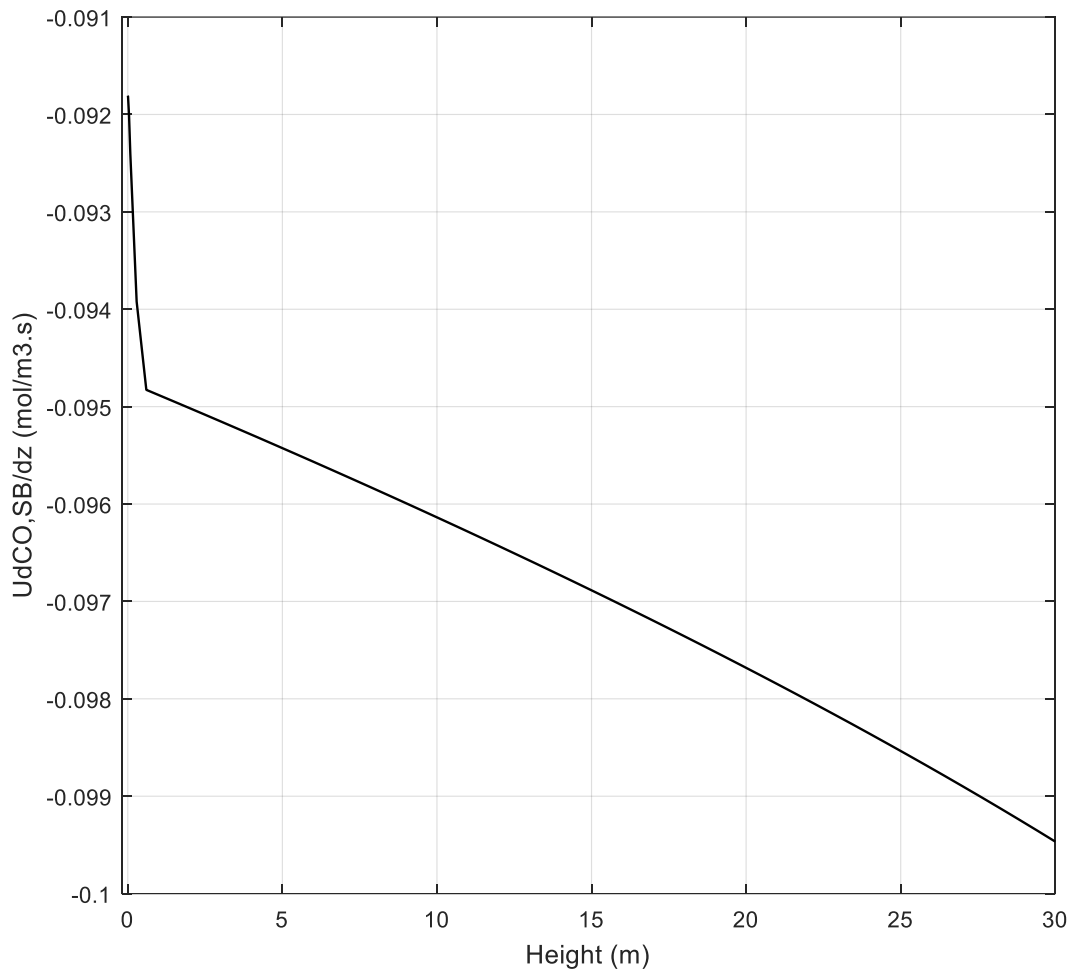


Figure 59: Rate of depletion of CO in the small bubbles over reactor height

Initially, the increase in the depletion rate of CO is rapid. This is caused by a quick drop in the concentration of CO in the small bubbles (Figure 60) owing to a relatively low extent of axial dispersion (lower than that found in the liquid phase). The lower axial dispersion means that the small bubble phase hydrodynamics reflect a more plug flow behaviour than is present in the liquid phase leading to a greater degree of axial concentration difference. This difference in the extent of axial dispersion arises because of the much lower initial small bubbles hold-up (0.06) relative to that in the liquid phase (0.8). This quick drop reduces $C_{CO,SB}^* - C_{CO,L}$ so that it is momentarily negative until CO is depleted in the small bubbles, at which point

$C_{CO,SB}^* - C_{CO,L}$ begins to increase until it reaches zero (Figure 61). At this point, the effect of a changing $C_{CO,SB}^* - C_{CO,L}$ falls away so that the only factor contributing to the increasing depletion rate is the decreasing axial dispersion.

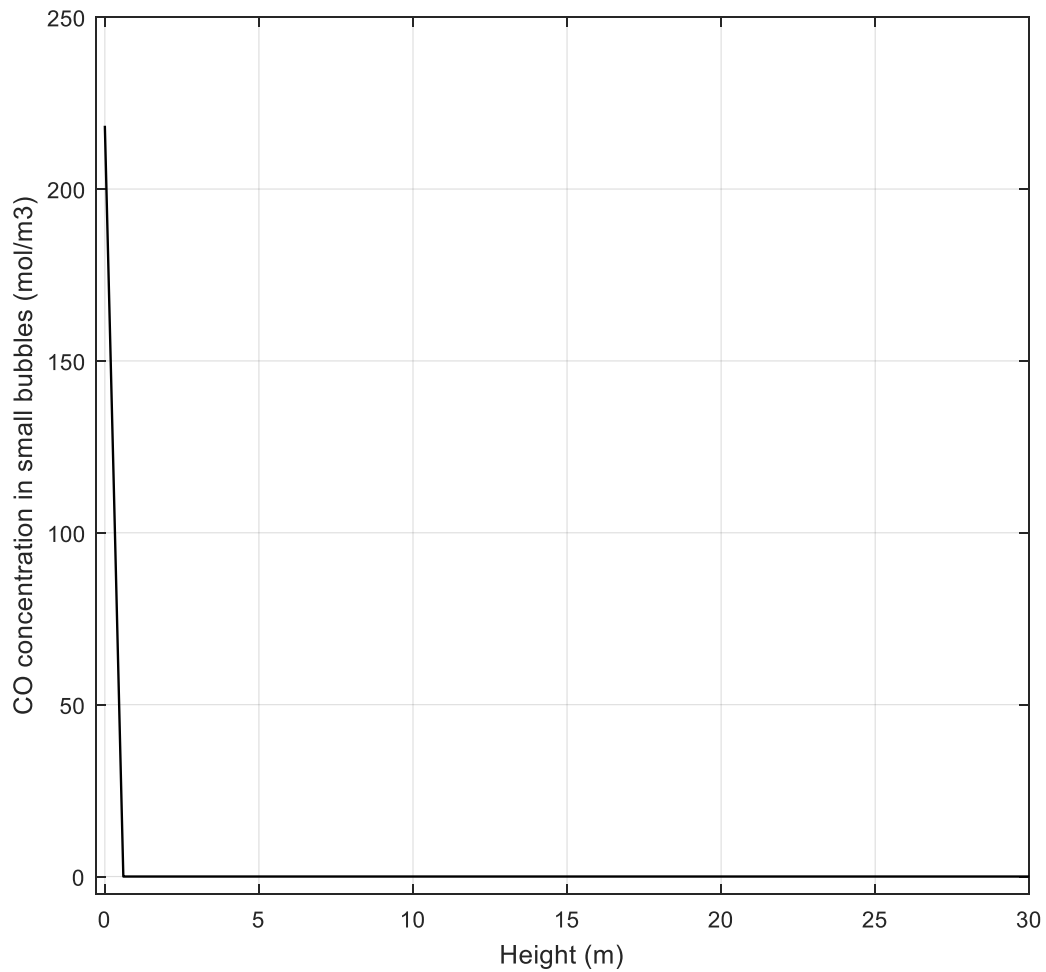


Figure 60: CO concentration in small bubble phase as a function of reactor column height

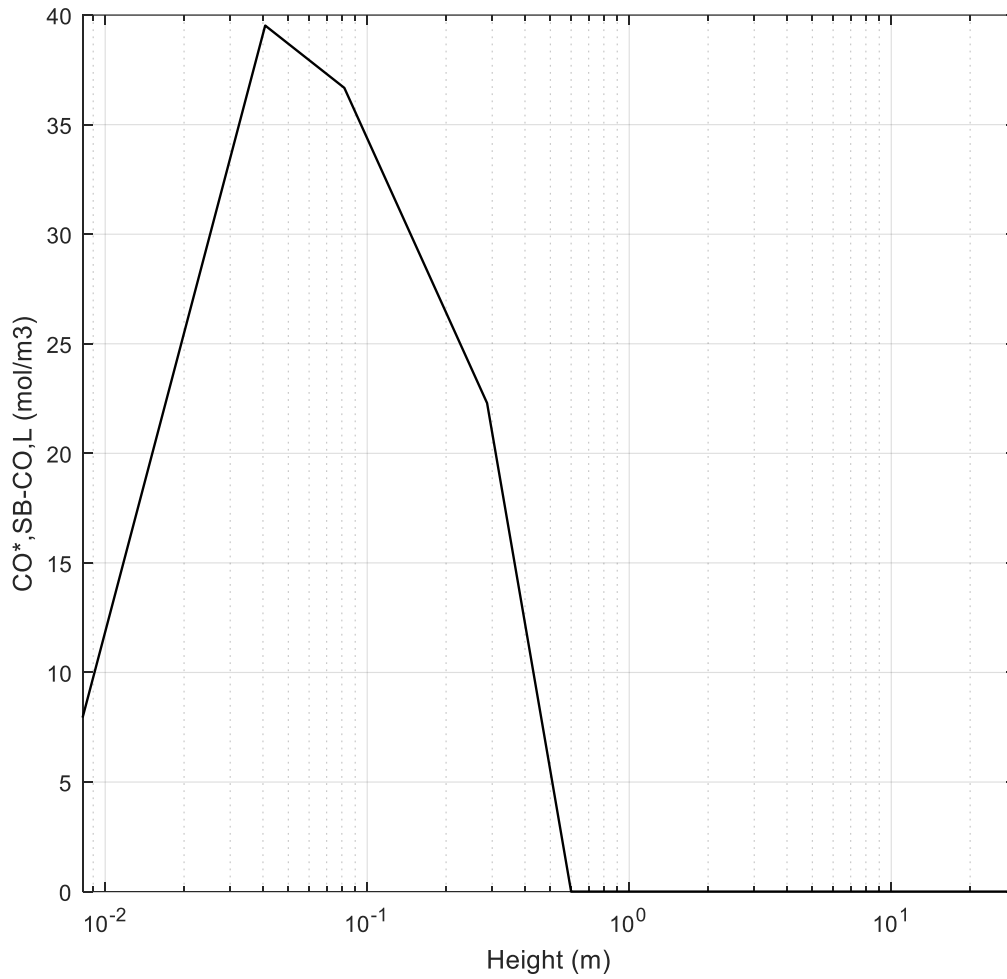


Figure 61: Interphase CO concentration difference between small bubble and liquid phases

5.2.1.3 Concentration profile in liquid phase

From Figure 62, the rate of depletion of CO in the liquid phase initially reflects a decreasing trend before showing an increase along the rest of the reactor height. The initial rapid increase of the rate of depletion of CO in the small bubbles is the cause of the momentary increase of $\frac{UdC_{CO,L}}{dz}$. As noted in Figure 61, the brief period of rapid increase is followed by one of slowed increase immediately after $C_{CO,SB}$ reaches zero. In this period, $\frac{UdC_{CO,L}}{dz}$ decreases through the height of the reactor. This period is also characterized by a decreasing $C_{CO,LB}^* - C_{CO,L}$ as shown in Figure 52 while the concentration difference across the small bubbles-liquid interphase remains constant (Figure 61). This, coupled with a decreasing large bubble mass transfer coefficient as a function of the decreasing superficial gas velocity means

that the rate of mass transfer from the large bubbles to the liquid phase decreases as a function of reactor height.

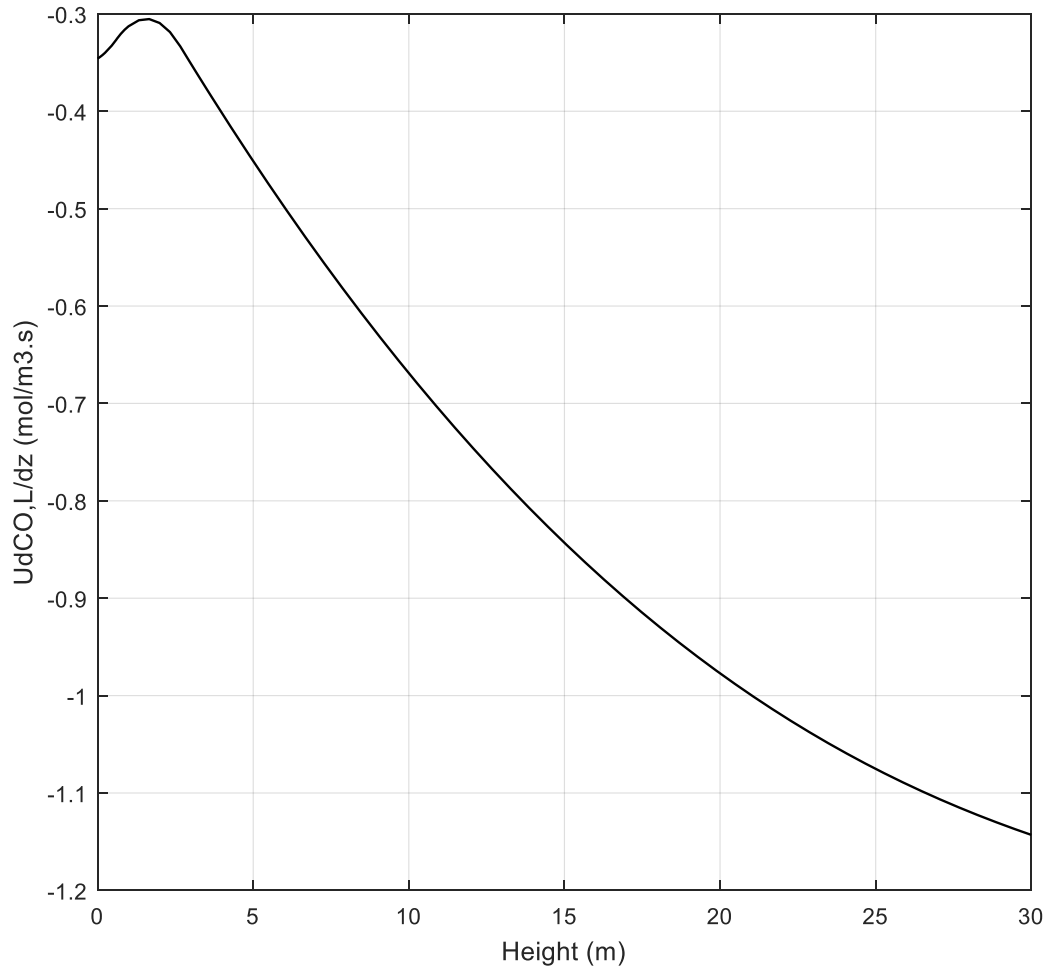


Figure 62: Rate of depletion of CO in the liquid phase over the height of the reactor

$\frac{U dC_{CO,L}}{dz}$ is also affected by the extent of dispersion in the liquid phase which has been assumed to be equal between the small bubbles and liquid phases. This means that dispersion will decrease as the superficial gas velocity decreases which in turn will increase $\frac{U dC_{CO,L}}{dz}$. The reaction rate, as discussed earlier, will decrease as a function of reactor height and this will work to reduce $\frac{U dC_{CO,L}}{dz}$. Because $\frac{U dC_{CO,L}}{dz}$ increases along the reactor height as shown in Figure 62, dispersion in the liquid phase can be said to have a greater impact on the rate of depletion of CO in the liquid phase. It is important to point out that a CO concentration of zero in the liquid phase, as shown in Figure 54, does not mean that no CO species exists in the liquid phase. The zero concentration indicates a sufficiently quick reaction rate so that the CO

species made available in the liquid phase is immediately consumed, i.e., the rate of mass transfer of CO to the liquid phase is equal to the rate of consumption of CO by reaction. This is essentially a steady-state condition in the absence of a solid-liquid interphase because of the assumption of a pseudo-homogenous slurry phase. This is similarly the case in the small bubbles. A zero concentration of CO therein, as shown in Figure 60, points to a steady-state condition where the interphase between the small bubbles and liquid phases is rendered insignificant by the high mass transfer coefficient. Had there been no initial CO species in the small bubble and liquid phases, the species concentration would have been maintained at zero in both phases.

It is clear that the decreasing superficial gas velocity, brought about by the consumption of the reactant species along the height of the reactor, is the main contributor to the axial profiles present in the SBCR. It affects the large bubble hold-up which is responsible for the mass transfer and dispersion variations in the large bubble phase. It also directly affects the large bubble dispersion in this phase. Its effect on the liquid and small bubble phase dispersion is also evident. This emphasizes the crucial role that the superficial gas velocity plays in the hydrodynamics and therefore the performance of the SBCR. The superficial gas velocity is, however, not alone in affecting the performance of the SBCR in such a manner. Other variables that are as important to the performance of the SBCR are discussed in the next section where their relative effects are studied.

5.2.2 Sensitivity analysis

In order to gain further understanding into the effects of hydrodynamics on SBCR performance, it is important to understand how various independent parameters affect the hydrodynamics and how these in turn relate to the performance of the SBCR. In an attempt to do this, a sensitivity analysis was carried out on the model to study the effects of specific parameters on the performance of the SBCR. This should give an indication as to the relative importance of such parameters in the design of SBCRs. In carrying out this task, independent parameters were manipulated so that their effect could be assessed. These included the inlet superficial gas velocity, reactor diameter, catalyst concentration and temperature. For a fair assessment of each parameter's effect on SBCR performance, only one parameter was manipulated at a time so that in any one parameter analysis, only that parameter is being varied and the rest are kept constant. The values of the parameters that are discussed in this section are those stemming from a complete simulation, i.e., the values were obtained after a

simulation was conducted from $z=0$ to $z=H$. The independent parameters are an exception as they are predetermined and are the basis of the sensitivity analysis.

5.2.2.1 Effect of superficial gas velocity

The superficial gas velocity is one of the most important determinants in the performance of SBCRs as it influences a number of conditions which directly affect the hydrodynamics in this reactor. In the first instance, U_g determines the flow regime that can be expected in a SBCR which can either be bubbly or heterogenous. Higher values of U_g promote a heterogenous flow regime so that the turbulence in the reactor is enhanced whereas a lower value of U_g will produce a mostly homogenous bubbly flow regime. These flow regimes have a real impact on the performance of a SBCR that can be characterized by their influence on the hydrodynamic parameters. A turbulent flow regime will promote back-mixing which has direct consequences for the performance of the SBCR. A higher extent of axial dispersion will negatively affect syngas conversion so that as U_g is increased, the syngas conversion will drop as well. This effect is illustrated in Figure 63 where the effects of U_g on E_L and E_G are shown respectively.

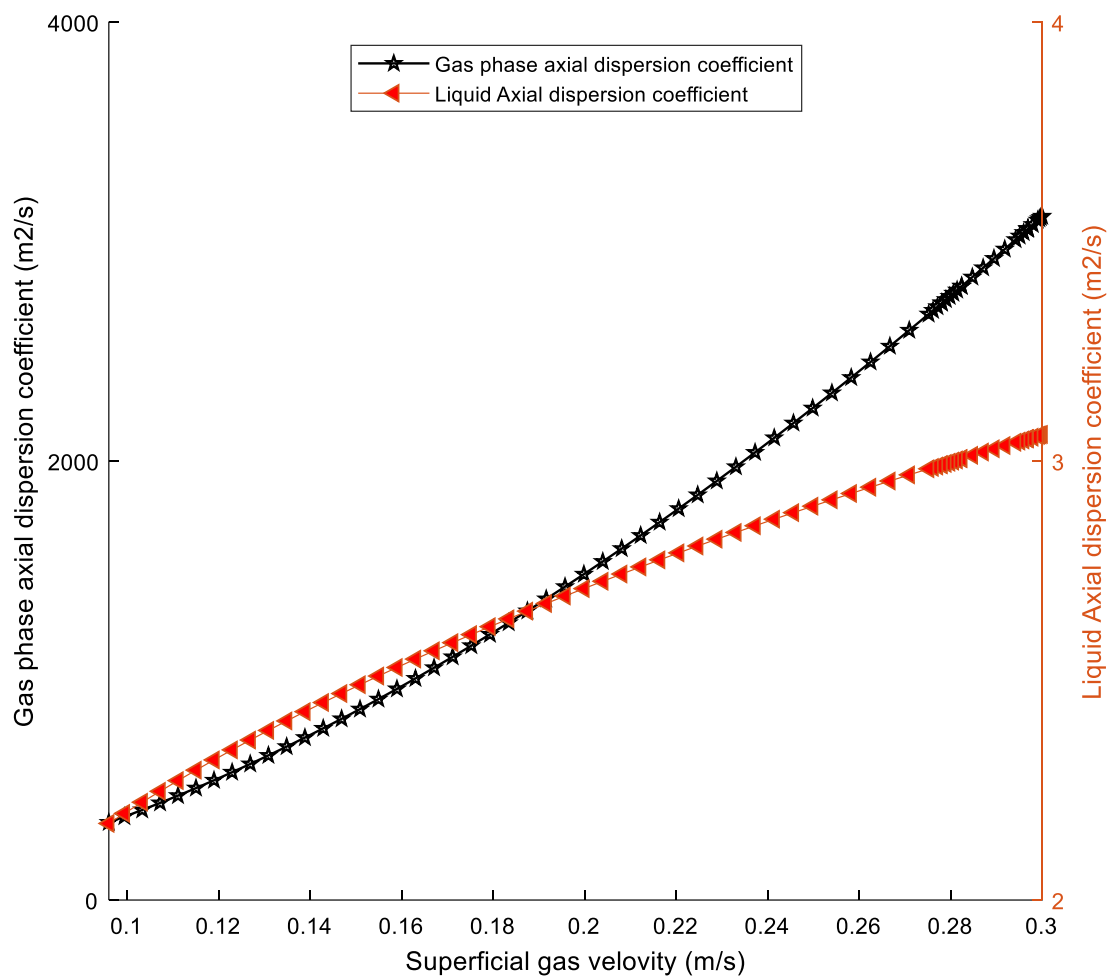


Figure 63: Effect of U_g on E_{LB} and E_L

Between a superficial gas velocity of 0.096 and 0.3 m/s, the gas phase dispersion coefficient goes up by 80% and the liquid phase dispersion coefficient similarly increases by 28%. In the case of the liquid phase dispersion coefficient, the superficial gas velocity is directly responsible for its decrease as the superficial gas velocity decreases as well. This is because the reactor diameter, which is the only other parameter upon which E_L is dependent, remains constant throughout the height of the reactor. The gas phase dispersion coefficient on the other hand, is dependent on the total gas hold-up in addition to its dependence on the superficial gas velocity. But because the total gas hold-up, through its relationship with the large bubble hold-up, is directly dependent on the superficial gas velocity such that a decrease in the superficial gas velocity results in a decrease in the total gas hold-up (Figure 64), the superficial gas velocity should be solely considered for an explanation to the apparent change in the gas phase dispersion coefficient with a change in U_g .

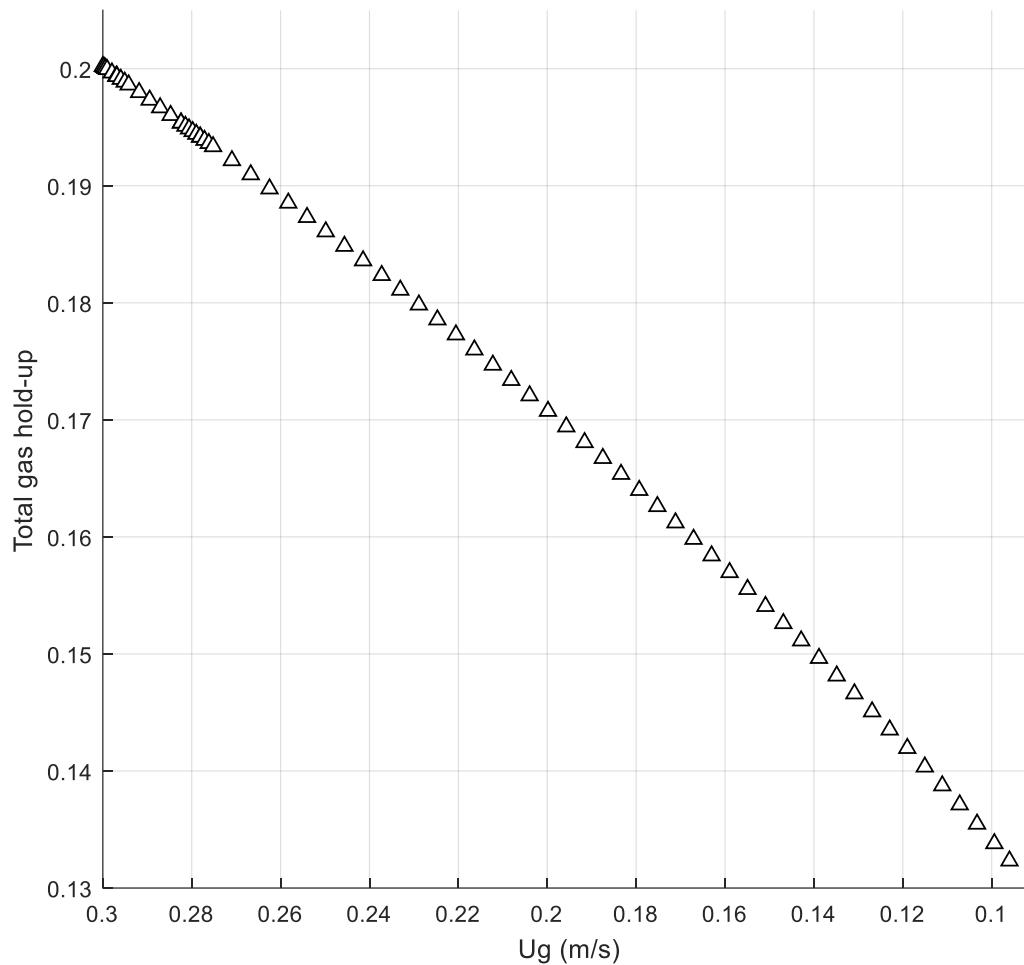


Figure 64: Total gas hold-up as a function of superficial gas velocity

Despite this, it's important to note how the superficial gas velocity ultimately affects the gas phase dispersion, i. e., directly or through its effect on the total gas hold-up. In the gas phase dispersion correlation by Mangartz and Pilhofer (1980), the relative effects of total gas hold-up and U_g are represented by $\frac{U_g}{\epsilon_g}$ and so to determine which is more significant, it is important to determine which parameter is more sensitive to a change in reactor height. It is this parameter that will be important to the gas phase dispersion coefficient. This sensitivity analysis was carried out and the results are presented in Figure 65. In Figure 65, $\frac{U_g}{\epsilon_g}$ is plotted as a function of reactor height and it shows a decreasing trend which means that the superficial gas velocity is decreasing faster than the total gas hold-up. This means that the superficial gas velocity is more sensitive to a change in reactor height than the total gas hold-

up so that its effect on the gas phase dispersion coefficient is direct and not through the total gas hold-up.

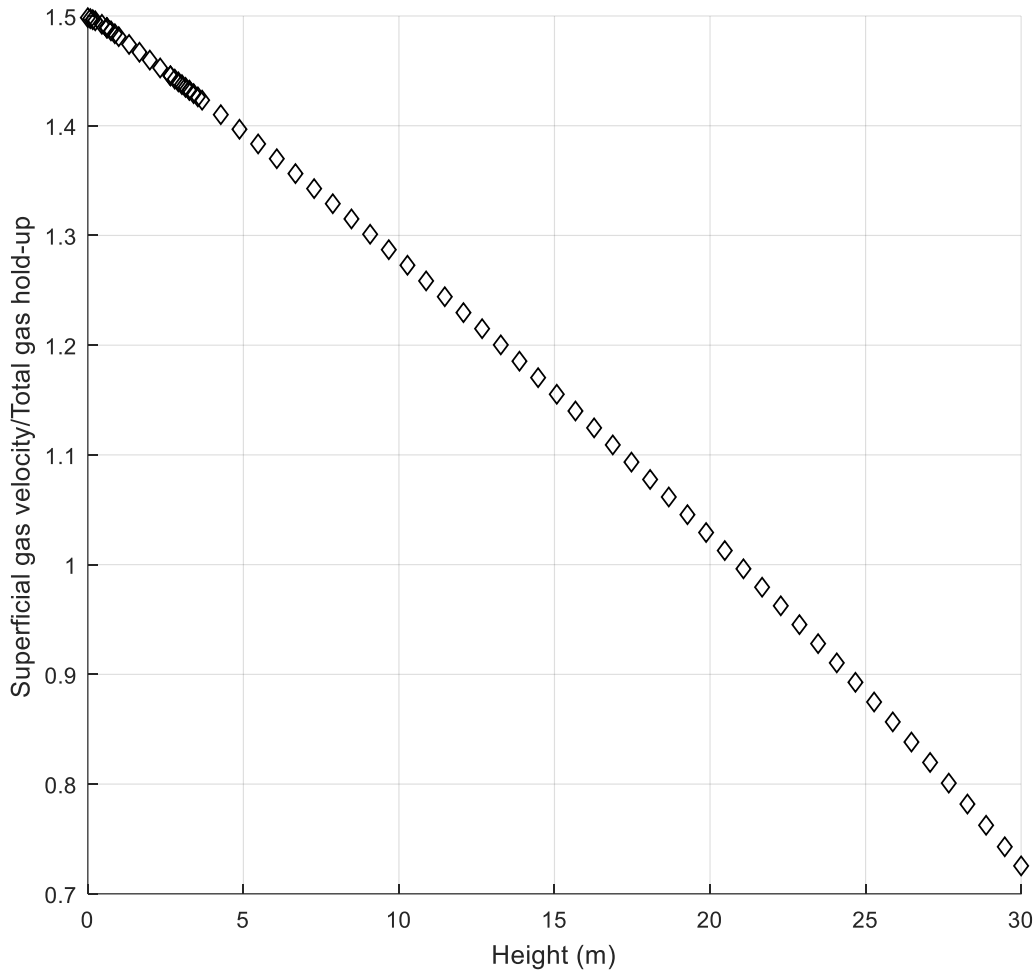


Figure 65: Relative sensitivities of superficial gas velocity and total gas hold-up to a change in reactor height

The superficial gas velocity also has a direct impact on the large bubbles hold-up which also influences the syngas conversion. From the SBCR model simulation, it is determined that an increase in the superficial gas velocity results in an increase in the large bubble hold-up (Figure 66). The large bubble hold-up affects the reactor performance in two ways; firstly, a higher large bubble hold-up will increase the large bubble-liquid mass transfer coefficient enabling more reactant to travel between the two phases and secondly, a higher large bubble hold-up will lead to a larger gas phase dispersion which directly affects performance.

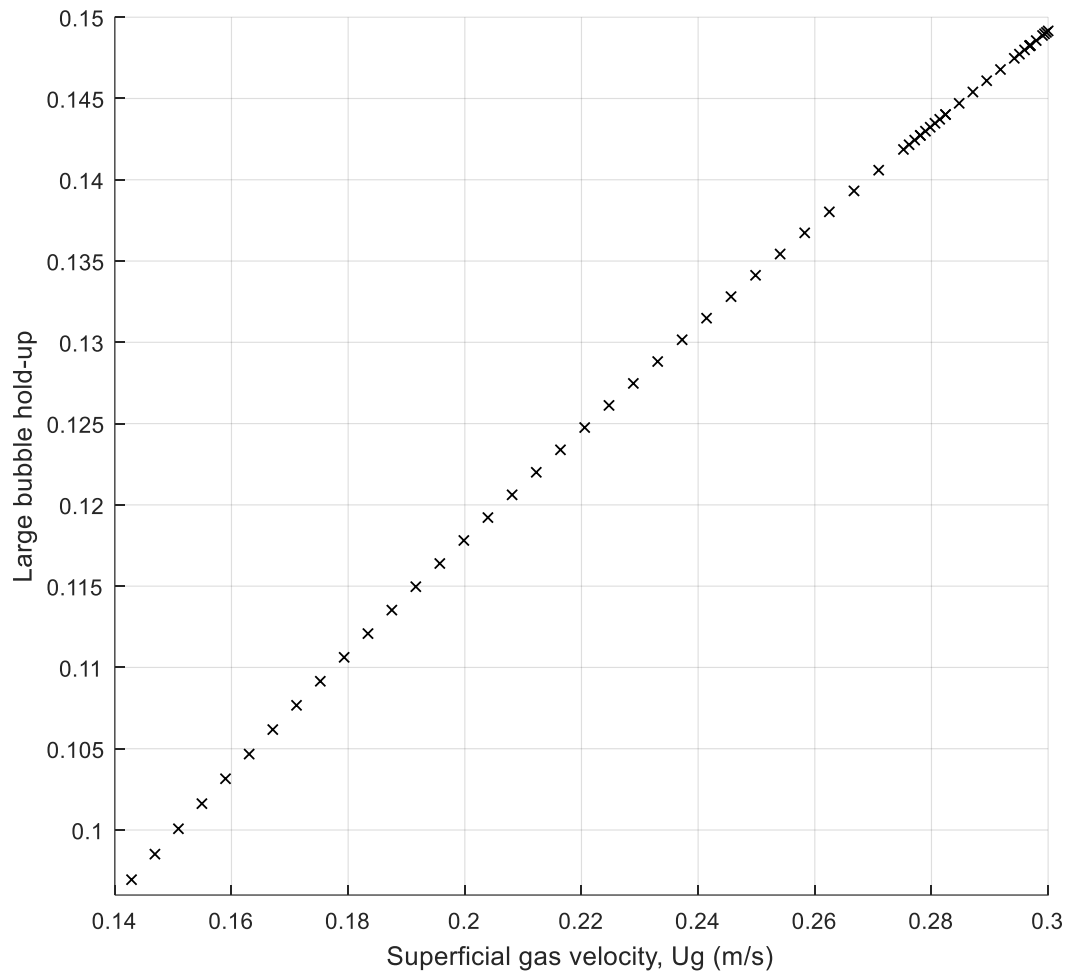


Figure 66: Effect of U_g on large bubble hold-up

Although E_G is directly affected by the total gas hold-up, the effect of large bubble hold-up on E_G still holds because of the assumption that the small bubble hold-up is constant, meaning that an increase in the large bubble hold-up is accompanied by an increase in the total gas hold-up. This means that there are two opposite effects of ε_{LB} on SBCR performance in that an increasing ε_{LB} will improve mass transfer thereby improving reactor performance but the increase will also increase the gas phase dispersion which will reduce syngas conversion. To determine which effect is dominant, a comparison between the effects of ε_{LB} on the mass transfer coefficient and the gas phase dispersion was made as shown in Figure 67. Between a large bubble hold-up of 0.1492 and 0.0769, a gas phase dispersion coefficient change of -80% is realized whereas in the same large bubble hold-up range, a large bubble CO mass transfer coefficient change of -48% is realized. This means that the main effect of gas hold-up on the SBCR performance is through its effect on the gas phase

dispersion coefficient. It is now clear that an increasing superficial gas velocity will increase the gas phase dispersion directly and indirectly through a higher large bubble hold-up. Both of these conditions result in a lower syngas conversion.

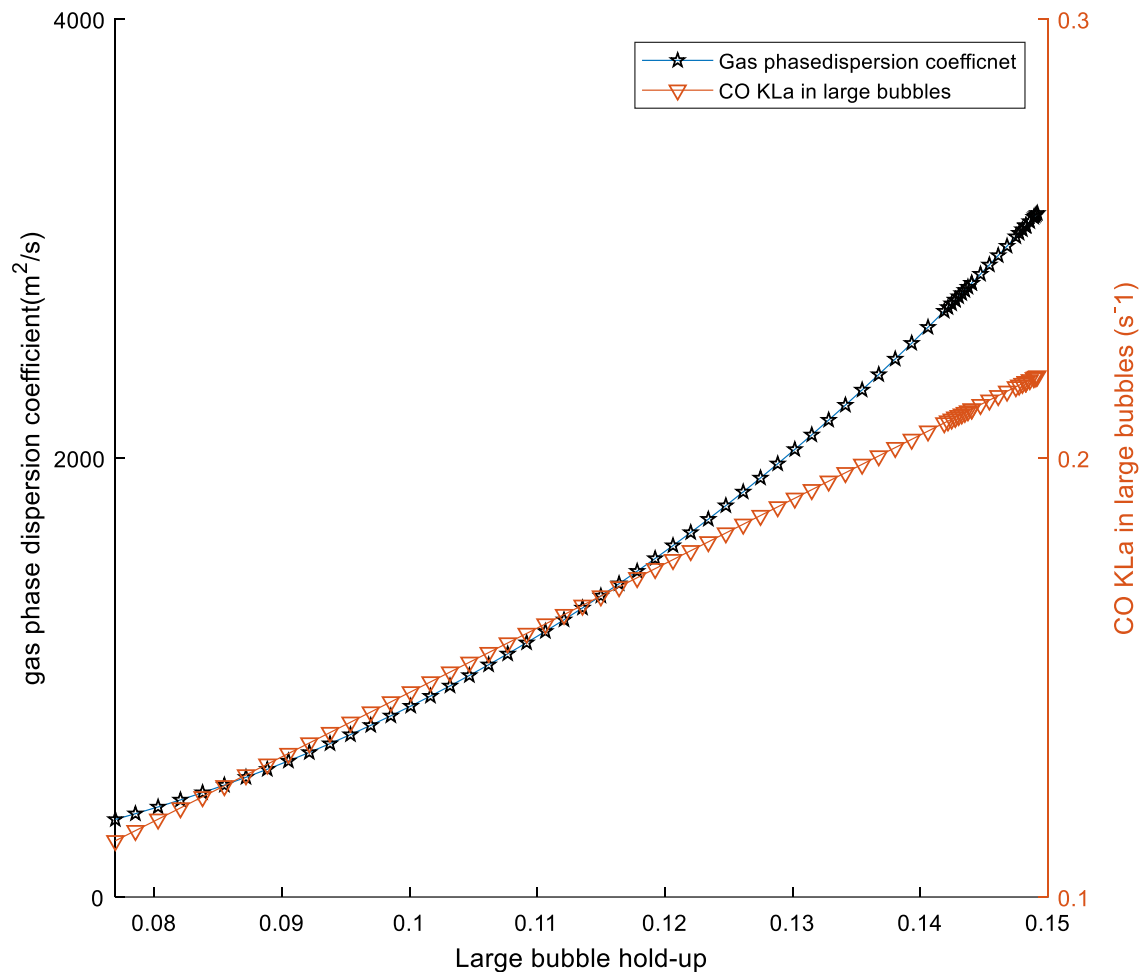


Figure 67: Comparative effects of large bubble hold-up on both the gas phase dispersion coefficient and the large bubble-liquid mass transfer coefficient

Given a constant reactor diameter, increasing the superficial gas velocity will have the effect of reducing the residence time of the reactants inside the reactor due to an increased throughput. A lower residence time will reduce the syngas conversion. The negative impacts of increased dispersion and reduced residence time have the overall impact of lowering the syngas conversion as the superficial gas velocity is increased. This is reflected in the simulation (Figure 68) where an increase in the superficial gas velocity leads to a reduction in the syngas conversion.

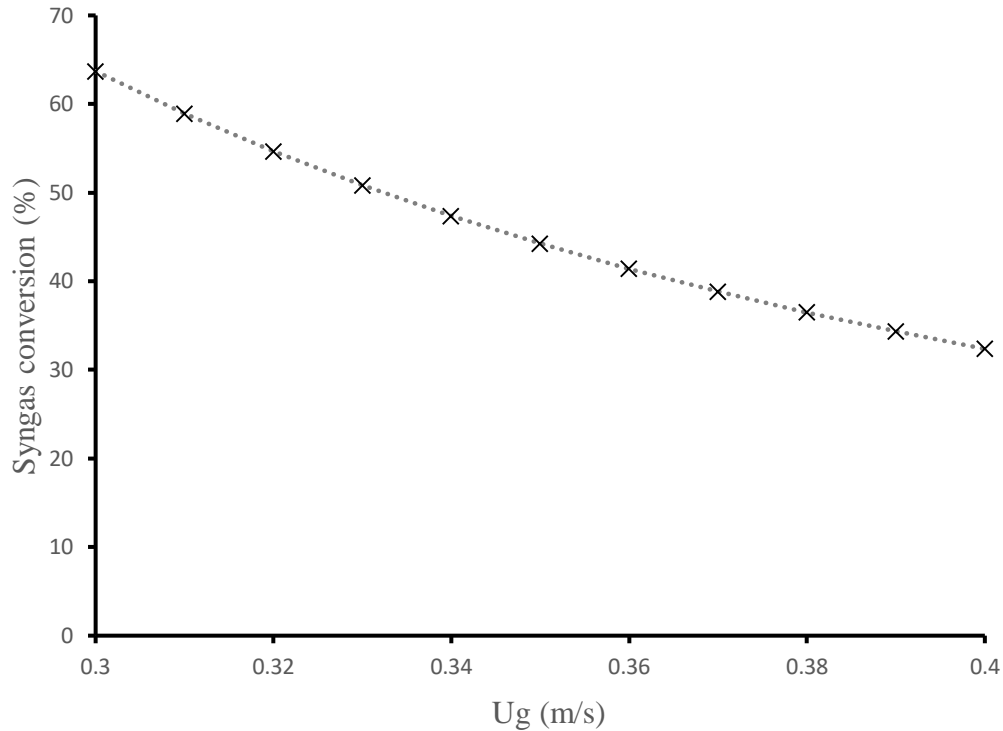


Figure 68: Effect of increasing inlet superficial gas velocity on syngas conversion

5.2.2.2 Effect of diameter

An increasing reactor diameter should directly affect the liquid and gas phase dispersion by increasing these parameters. This is however not what occurs because of the two-fold impact that a changing reactor diameter has on the gas and liquid dispersion coefficients. Increasing the diameter whilst maintaining a constant throughput would reduce the superficial gas velocity (Figure 69), whose effect on SBCR performance was discussed at length in an earlier section where it was established that a decreasing superficial gas velocity will reduce both the liquid and gas phase dispersion coefficients. This means that increasing the diameter will, at once, have the effect of directly increasing and indirectly reducing, through its effect on the superficial gas velocity, the dispersion coefficients in the two phases. But, as can be seen in Figure 70, the overall effect is that of a decrease in the respective dispersion coefficients which points to an overall sensitivity of the coefficients to a decreasing superficial gas velocity. This means that increasing the diameter of the reactor will increase the back-mixing in both phases so that the syngas conversion is impacted negatively.

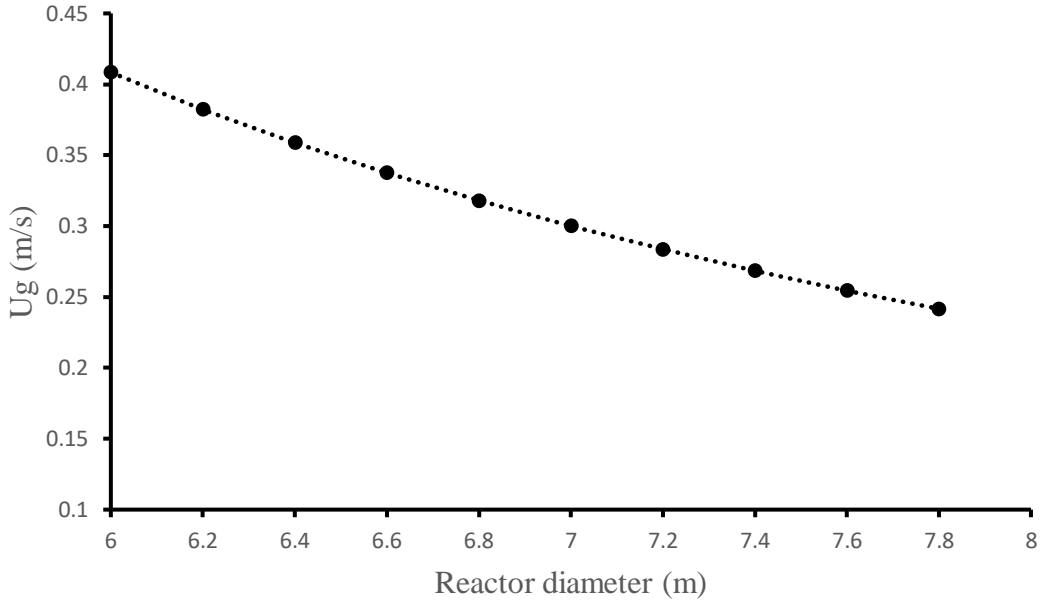


Figure 69: Effect of reactor diameter on superficial gas velocity

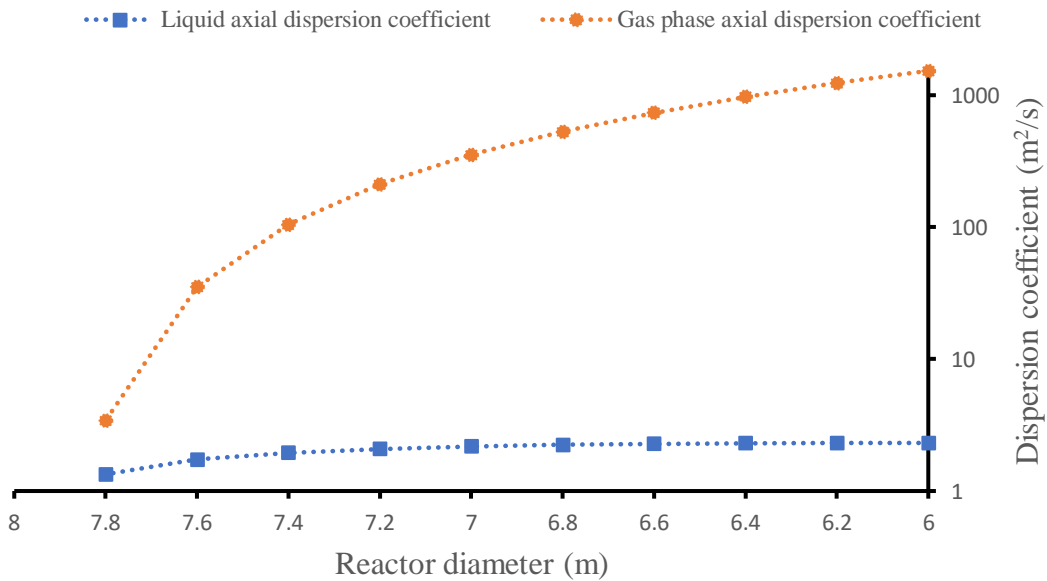


Figure 70: Effect of reactor diameter on the gas and liquid axial dispersion coefficients

Given the resulting drop in superficial gas velocity as the diameter is increased, the reactant residence time is increased which should lead to a higher syngas conversion. Overall, the effect of an increasing reactor diameter is an increased syngas conversion (Figure 71), with a diameter increase from 6 to 7.8 m resulting in a syngas conversion increase of 57%, which means the performance of the SBCR, under the prevailing conditions, is more sensitive to changes in residence time than to those in the extent of dispersion.

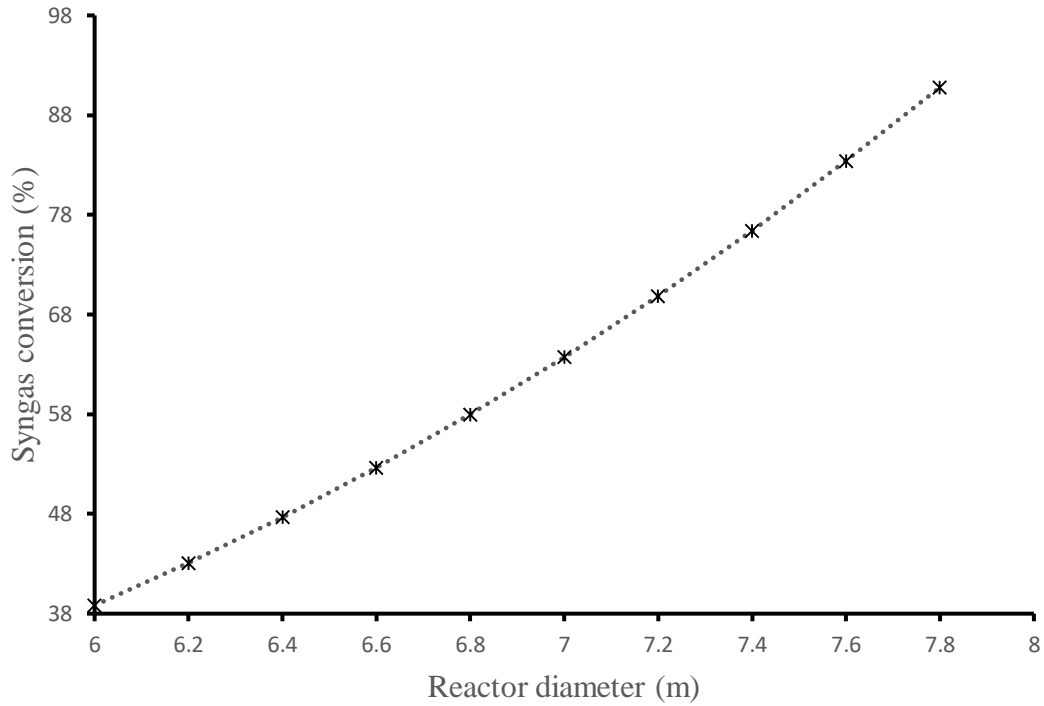


Figure 71: Effect of reactor diameter on syngas conversion

5.2.2.3 Effect of solids concentration

The solids concentration has a direct effect on the small bubble hold-up and the reactant consumption rate. Increasing the solids concentration will reduce the small bubble hold-up (Figure 72) thus reducing the small bubble mass transfer coefficient as shown in Figure 73. A higher solids loading will also increase the rate of reactant consumption as illustrated in Figure 74 produced from a simulation based on the model.

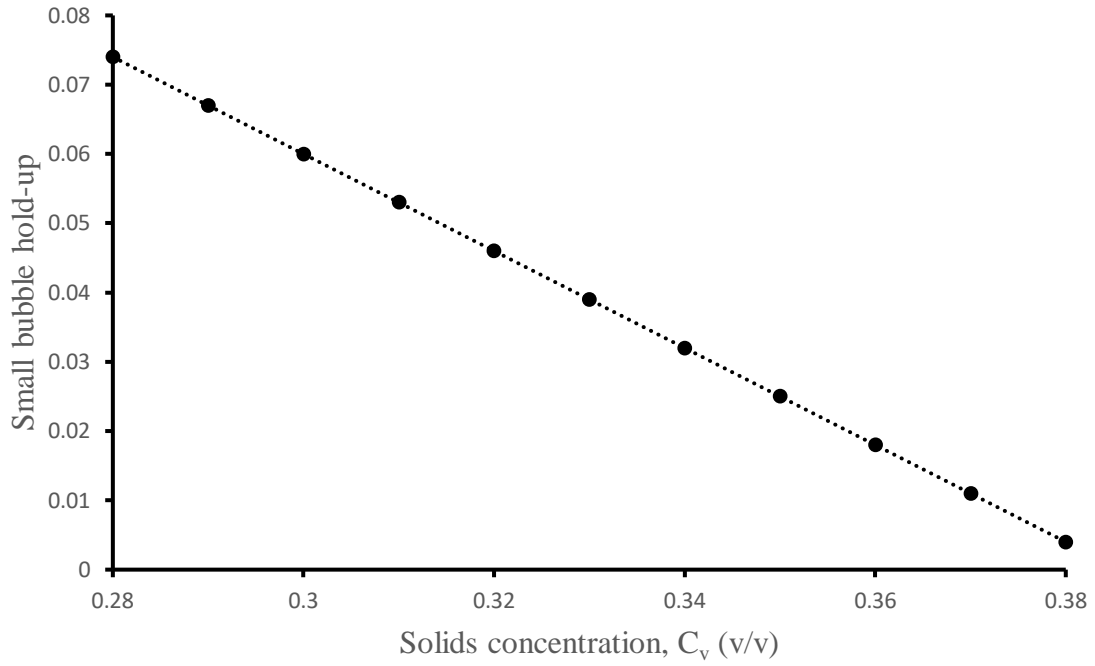


Figure 72: Small bubble hold-up as a function of solids concentration

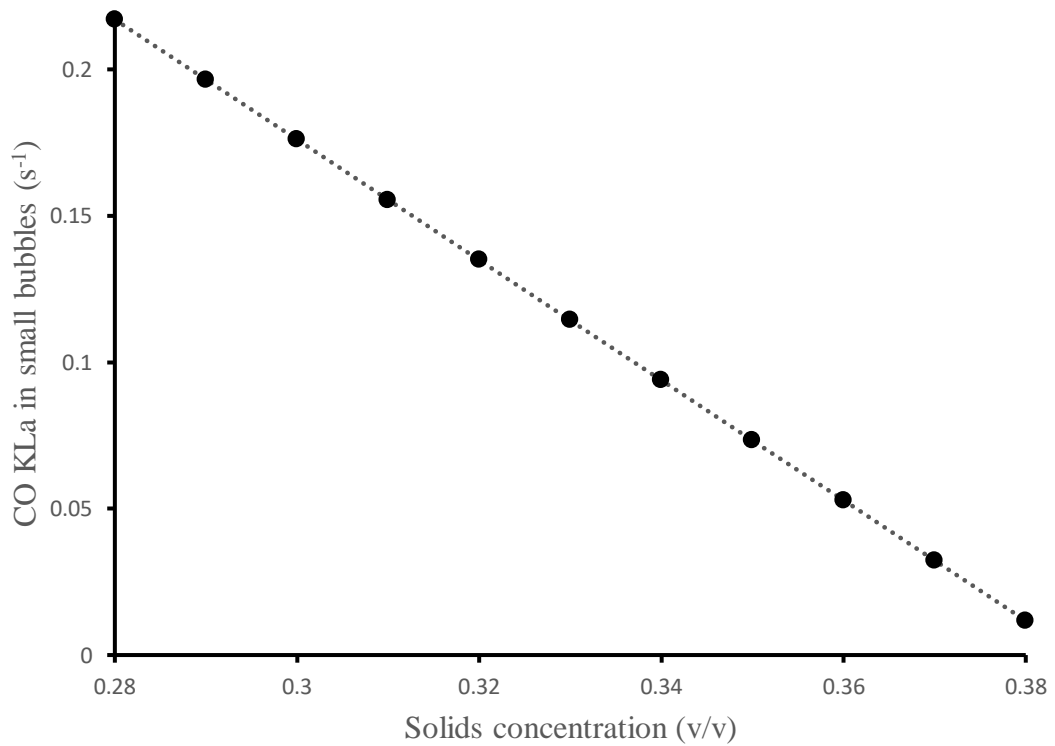


Figure 73: Effect of solids concentration on small bubbles mass transfer coefficient

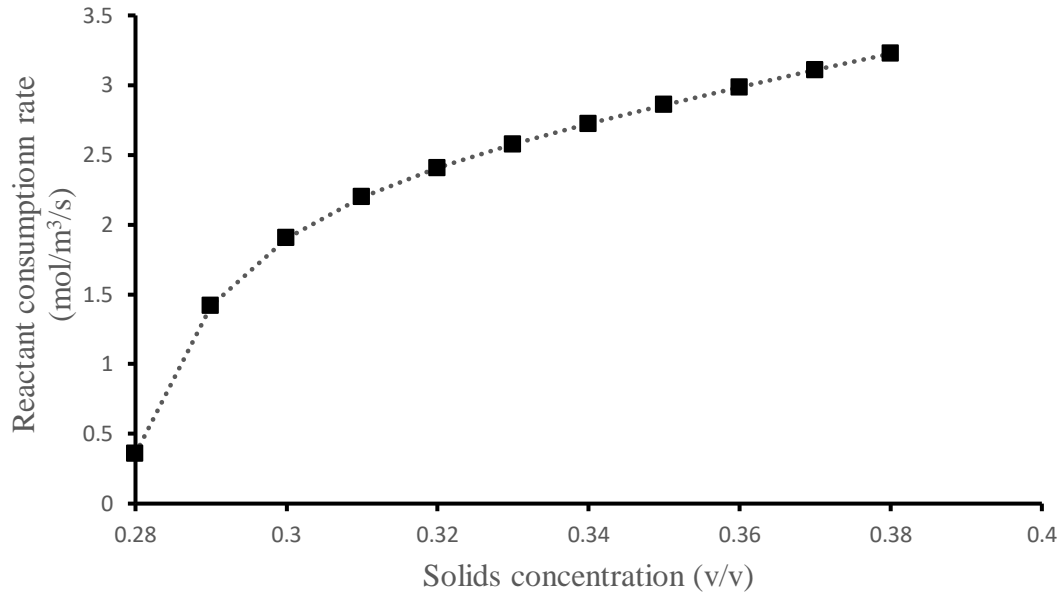


Figure 74: Effect of solid loading on reactant consumption rate

It is evident in Figure 75 that at the higher solid concentrations, the sensitivity of syngas conversion to solid concentration increases becomes weaker. This can be explained through the effect that an increasing solids concentration has on the large bubble hold-up. This is an indirect effect that an increasing C_v has on this SBCR performance. As C_v is increased and the small bubble hold-up drops, this is accompanied by a decrease in the small bubble superficial velocity as shown in Figure 76.

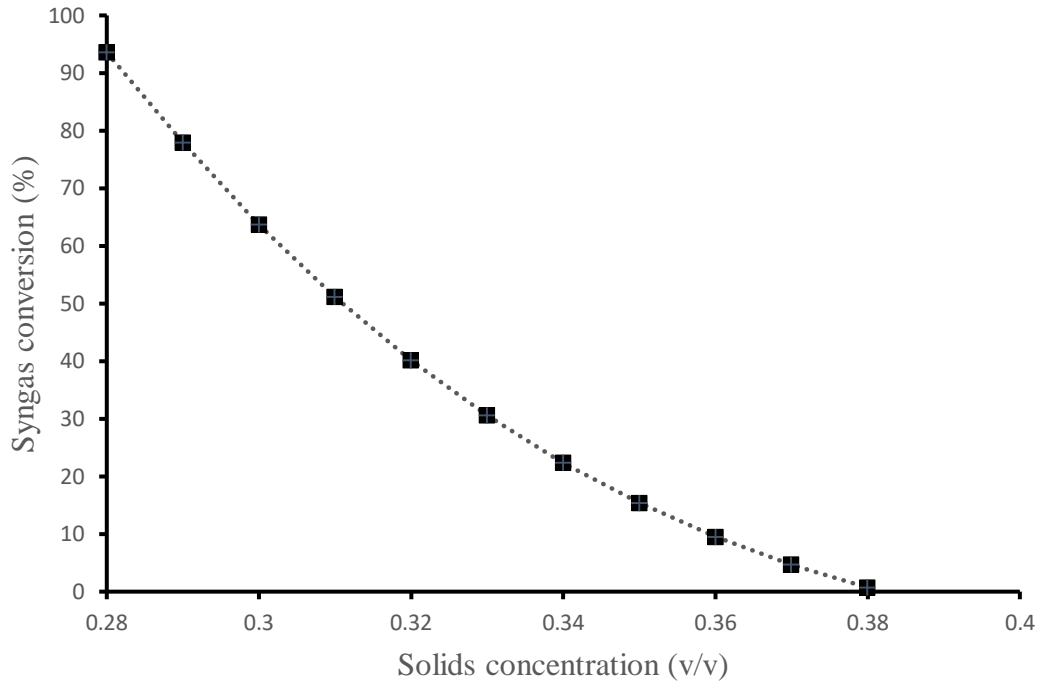


Figure 75: Effect of solids concentration on syngas conversion

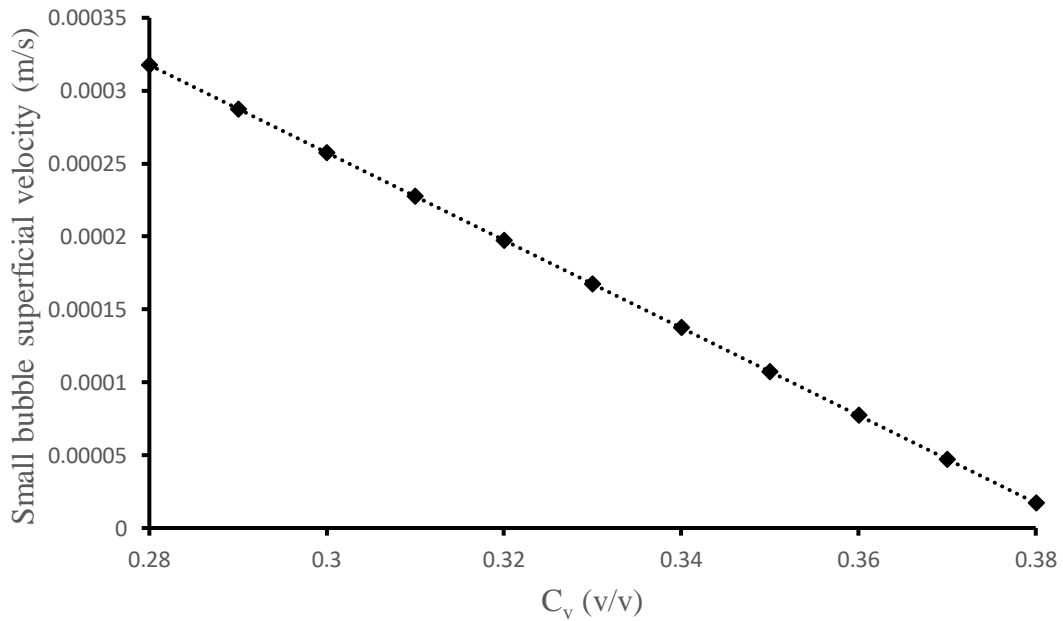


Figure 76: Small bubble superficial velocity as a function of solids concentration

The drop in small bubble superficial velocity will also cause an increase in the large bubble hold-up (Figure 77) according to Equation 75 (Maretto and Krishna, 1999). As shown in Figure 67, an increasing large bubble hold-up causes an increase in the gas phase dispersion coefficient which is detrimental to syngas conversion.

It is important to note at this point that a decreasing syngas conversion rate will result in a smaller reduction of the total superficial gas velocity across the height of the reactor so that as the solid concentration is increased, the total superficial gas velocity at the outlet of the reactor will increase (Figure 78). This increase, together with the drop in small bubble superficial gas velocity as the solids concentration is increased, work toward increasing the large bubble hold-up. This explains the drop in syngas conversion as the solids concentration is increased as shown in Figure 75. As the solids concentration is raised even further however, the small bubble population is effectively decimated (Figure 72) as is the small bubble superficial gas velocity (Figure 76) resulting in a diminishing rate of large bubble hold-up increase (see Equation 74) which subsequently causes a slower rise in the gas phase dispersion coefficient ultimately reducing the rate at which syngas conversion drops as shown in Figure 75 at the higher solid concentrations.

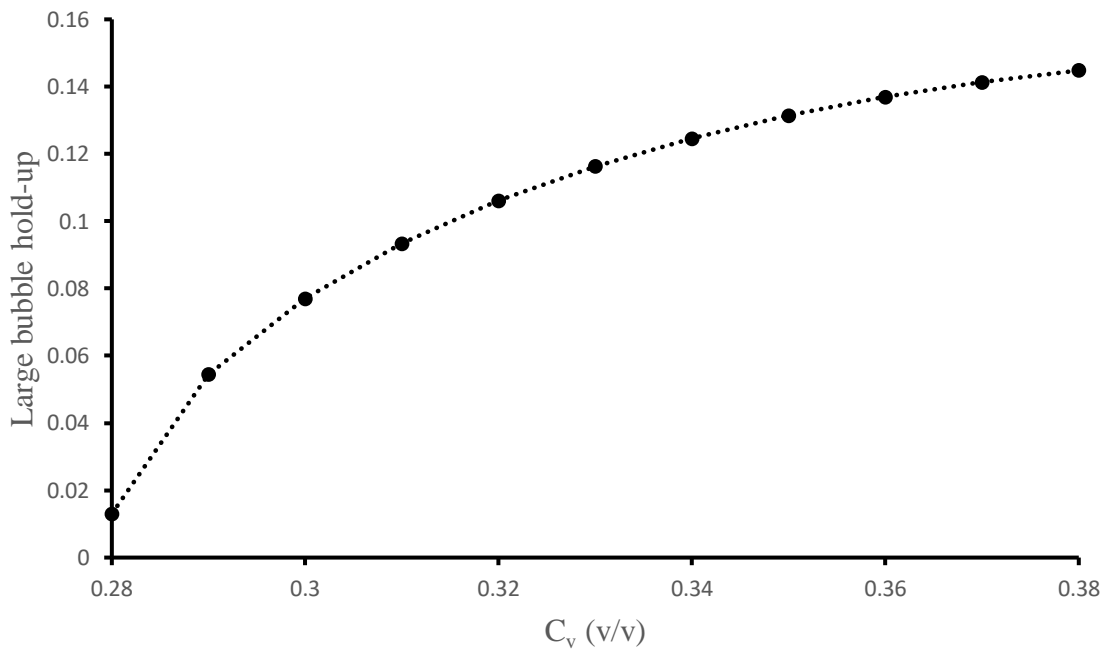


Figure 77: Large bubble hold-up behaviour with increasing solids concentration

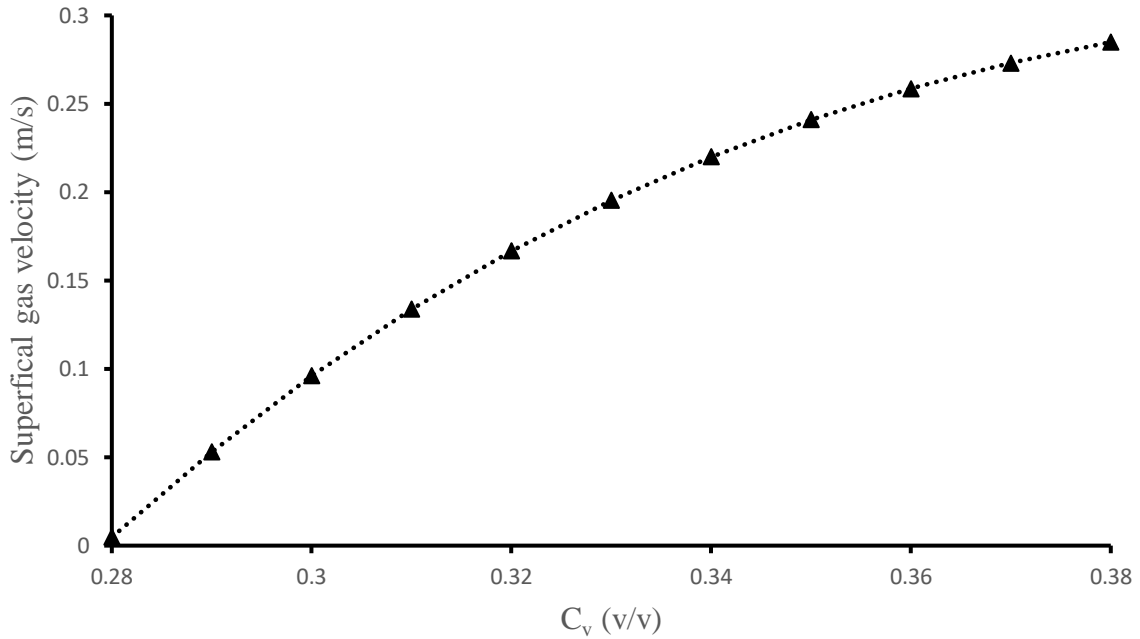


Figure 78: The total superficial gas velocity as a function of solids concentration

The diminishing syngas conversion with an increase in solids concentration means that more syngas will be available at the reactor outlet, i.e., higher concentrations of CO and H₂ (Figure 79). These higher concentrations enable a higher rate of reaction as shown in Figure 74 following the rate law in Equation 54. Because the rate at which the drop in syngas conversion declines at the higher solid concentrations, the rate at which the reactant concentrations increase also declines (Figures 79) resulting in a decrease in the rate at which the reaction rate increases. This is evident in Figure 80 at the higher solid concentrations. This trend is also apparent with respect to the consumption rate as a function of solids concentration as evidenced in Figure 74. The diminishing rate of increase of the reaction rate clearly affects the consumption rate as it can be seen from Figure 74 that the consumption rate begins to be less sensitive to the solids concentration at the higher solid loading rates.

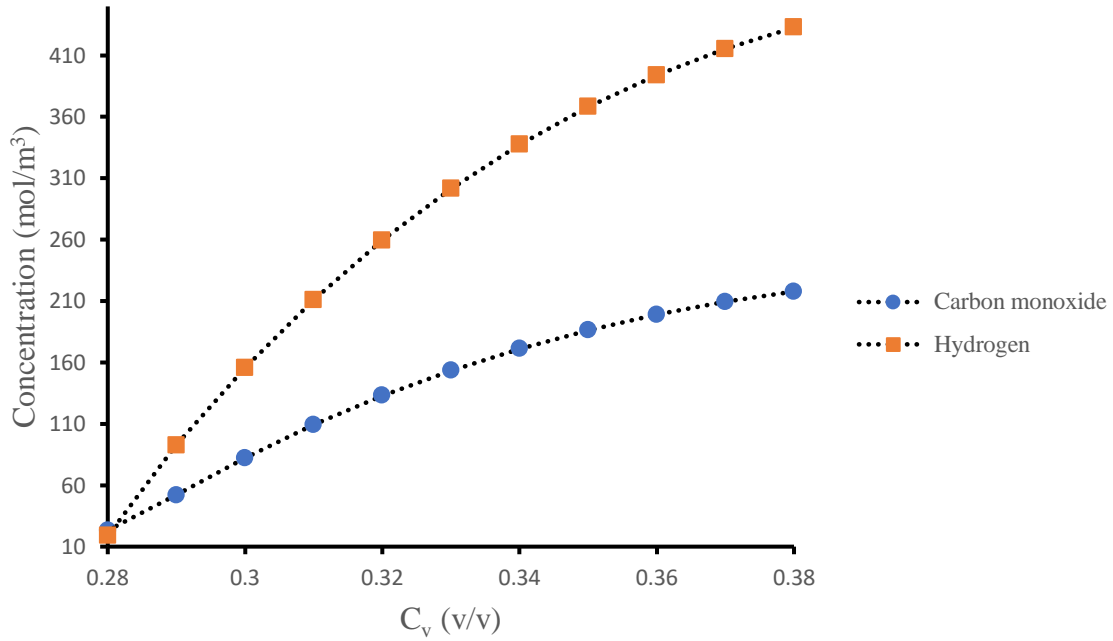


Figure 79: Gaseous reactant concentrations as a function of solids concentration

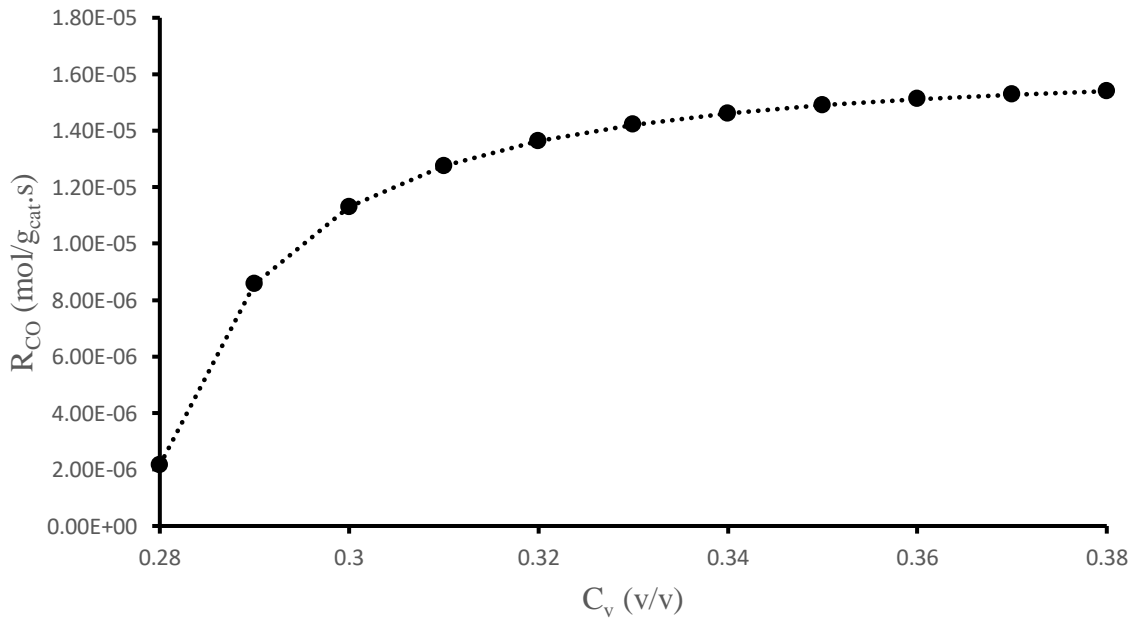


Figure 80: The rate of reaction as a function of solids concentration

5.2.2.4 Effect of temperature

The temperature has a direct effect on the reaction kinetics through its impact on the reaction rate and adsorption constants. An increase in temperature results in an increase in the reaction rate (Figure 81) constant and a drop in the adsorption rate constant (Figure 82). The drop in

the adsorption rate constant is as a result of the negative activation energy associated with this process resulting in its exothermicity so that an increase in temperature reduces the adsorption rate. The result is an overall increase in kinetics as the temperature is increased as evidenced in Figure 83. This indicates that the overall kinetics are controlled by the surface reaction as opposed to the adsorption step.

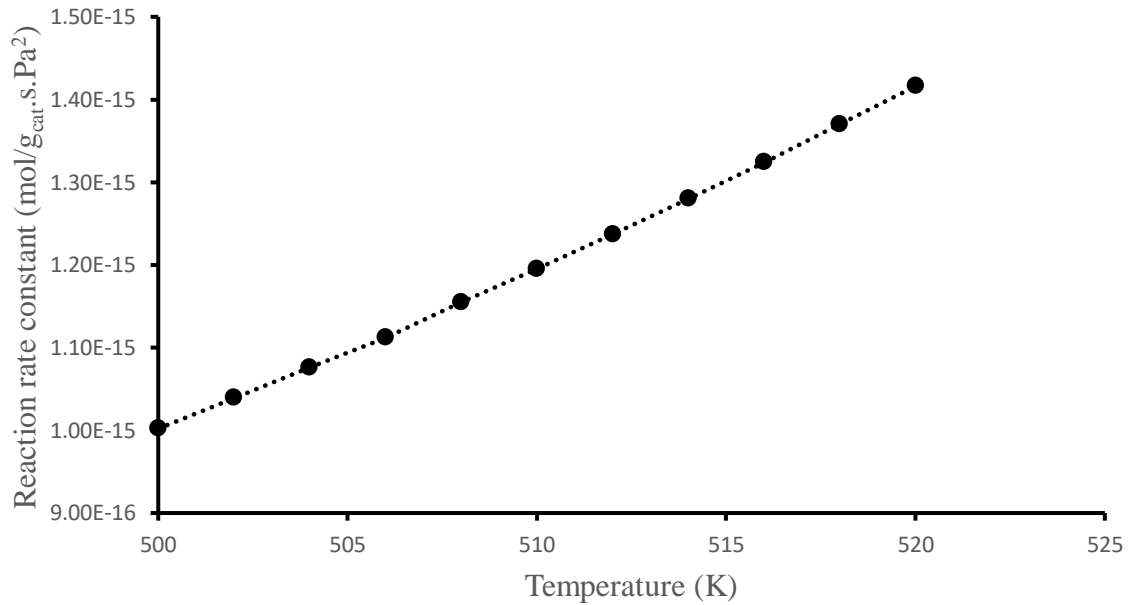


Figure 81: Effect of temperature on the reaction rate constant

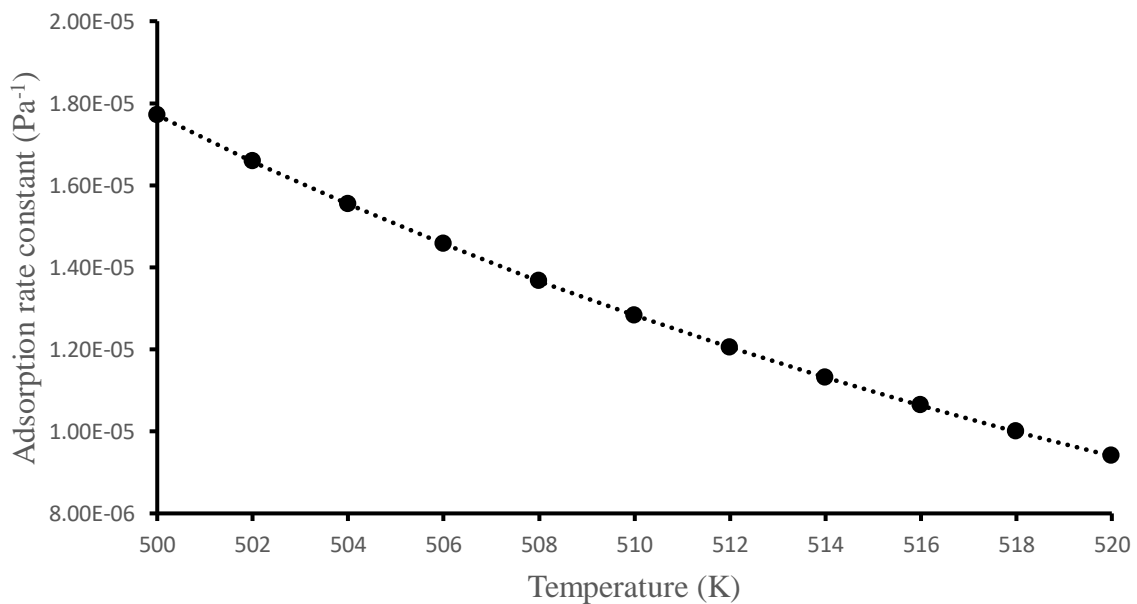


Figure 82: Effect of temperature on the adsorption rate constant

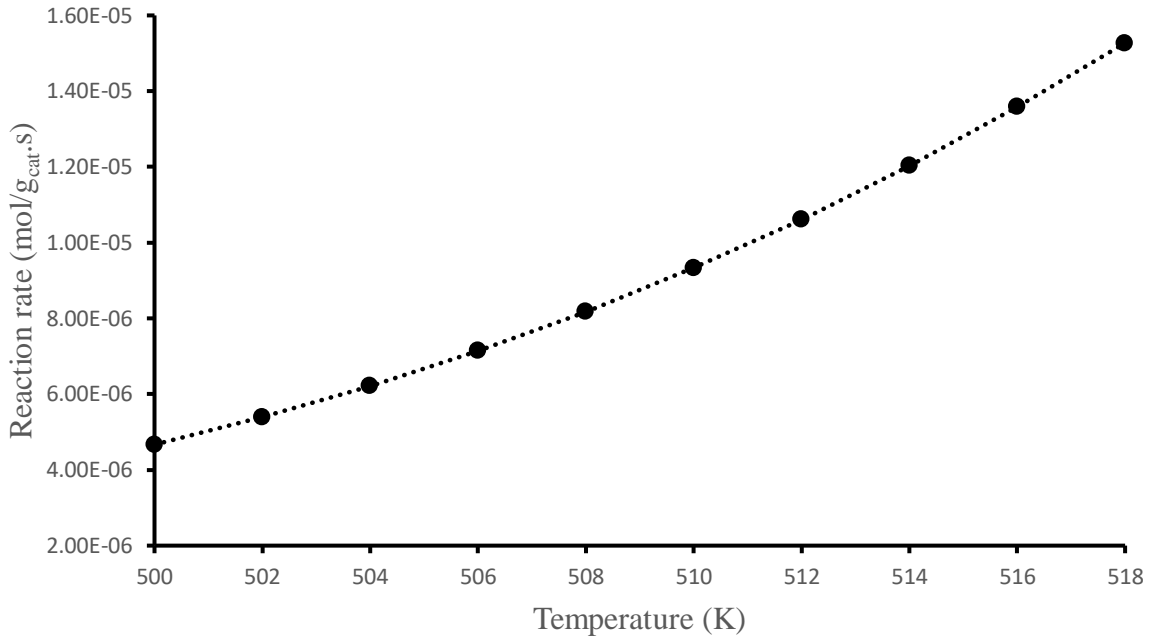


Figure 83: Effect of temperature on the reaction rate

The temperature inside the SBCR will also directly and negatively affect the liquid physical properties including the density (Figure 84), surface tension (Figure 85) and viscosity (Figure 86) which in turn directly affect the small bubble phase superficial velocity. The changes in the liquid physical properties have the net effect of increasing the small bubble superficial gas velocity.

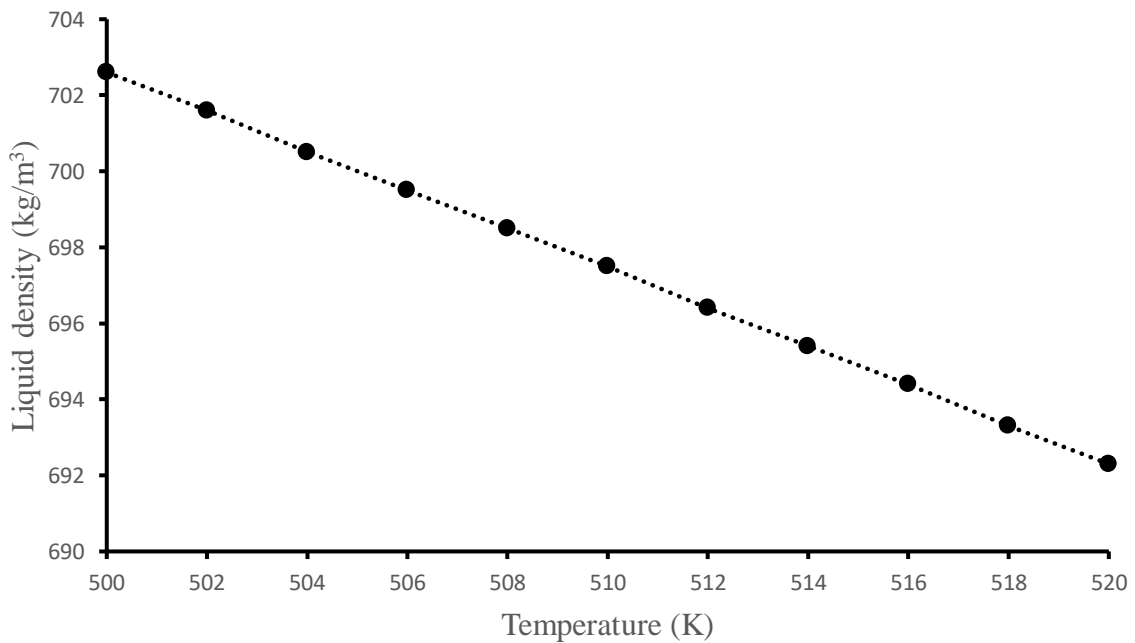


Figure 84: Liquid density as a function of temperature

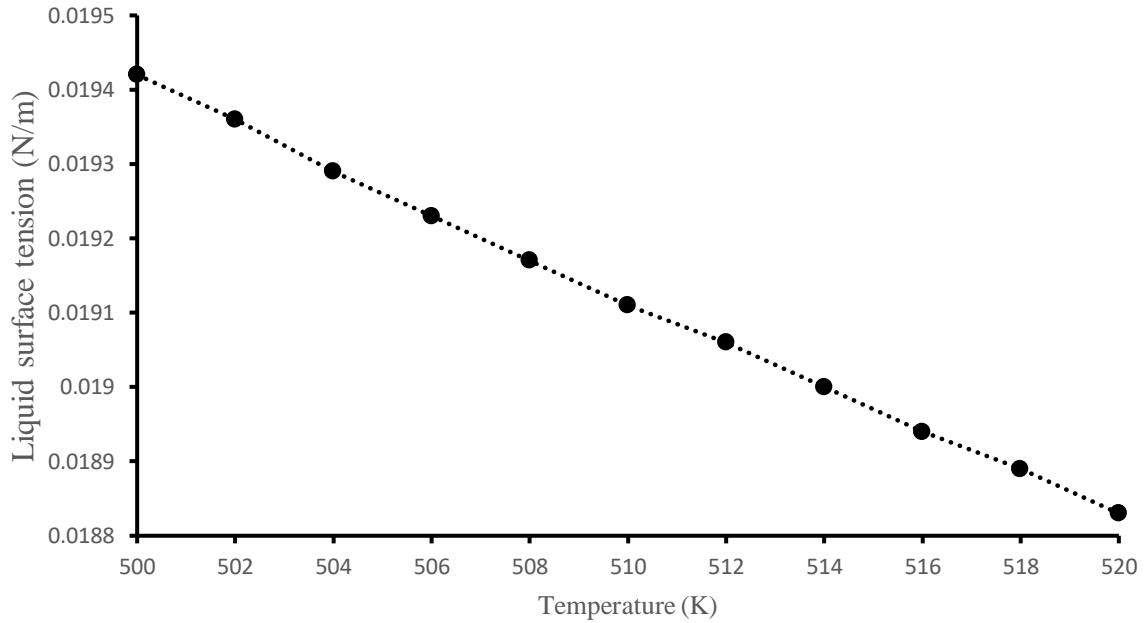


Figure 85: Liquid surface tension as a function of temperature

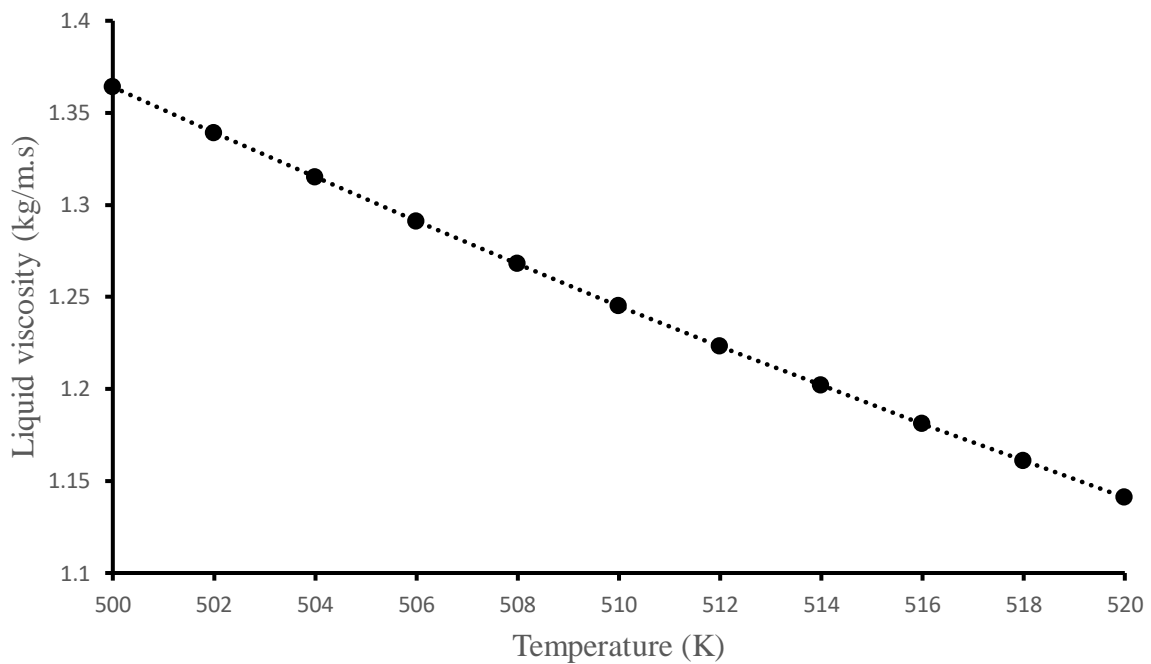


Figure 86: Liquid viscosity as a function of temperature

The indirect relationship between the temperature and the small bubble phase superficial velocity is illustrated in Figure 87. The small bubble phase superficial velocity in turn affects the large bubble hold-up which ultimately affects the gas phase dispersion as discussed earlier. The indirect relationships between the temperature and large bubble hold-up (Figure

88) and the gas phase dispersion (Figure 89) are shown below. It is evident that through its impact on liquid physical properties, the temperature in a SBCR is significant to the characterisation of the hydrodynamics inside this reactor.

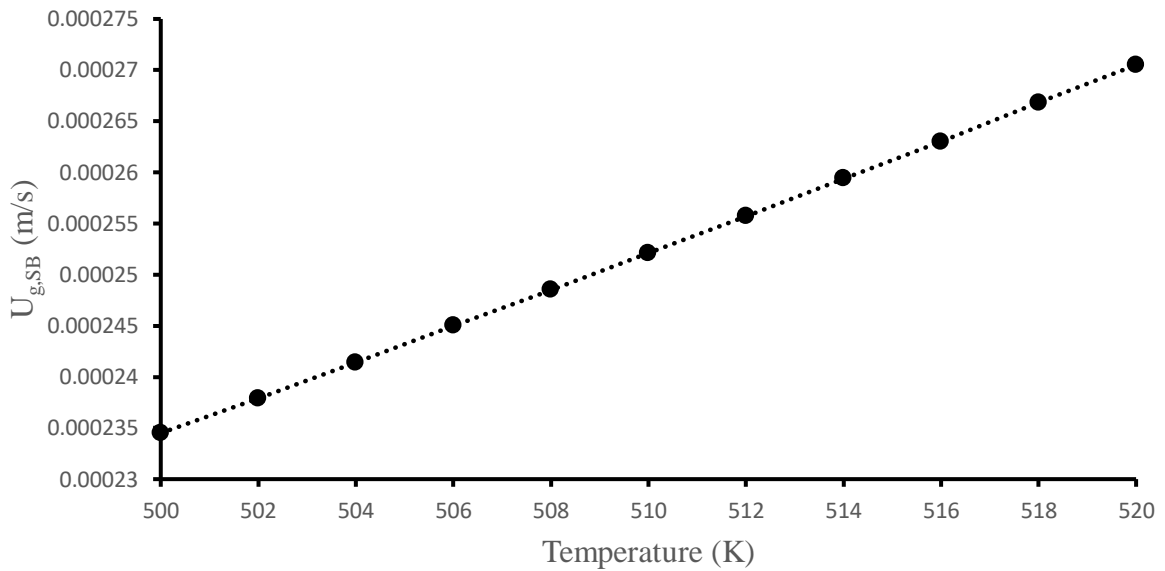


Figure 87: Effect of temperature on the small bubble phase superficial velocity

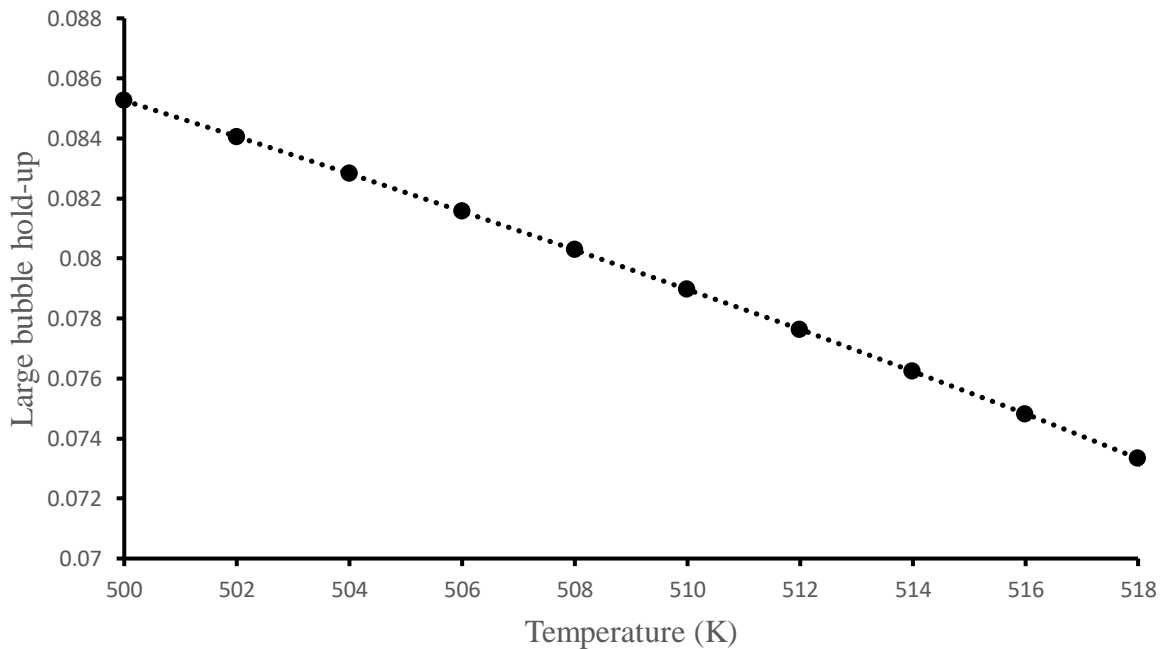


Figure 88: Effect of temperature on large bubble hold-up

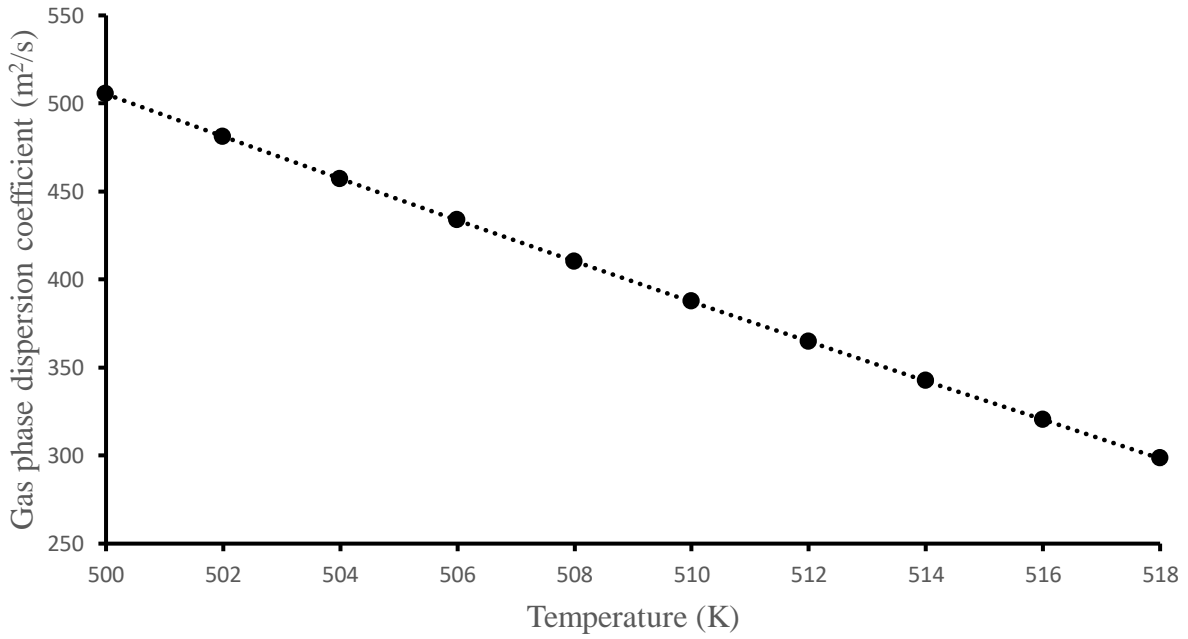


Figure 89: Effect of temperature on the gas phase dispersion coefficient

The combined effect of an increase in kinetics and a decrease in the gas phase dispersion coefficient that stems from an increase in temperature results in an increase the syngas conversion as shown in Figure 90. Between a temperature of 500 K and 518 K the syngas conversion is increased by 13.7%.

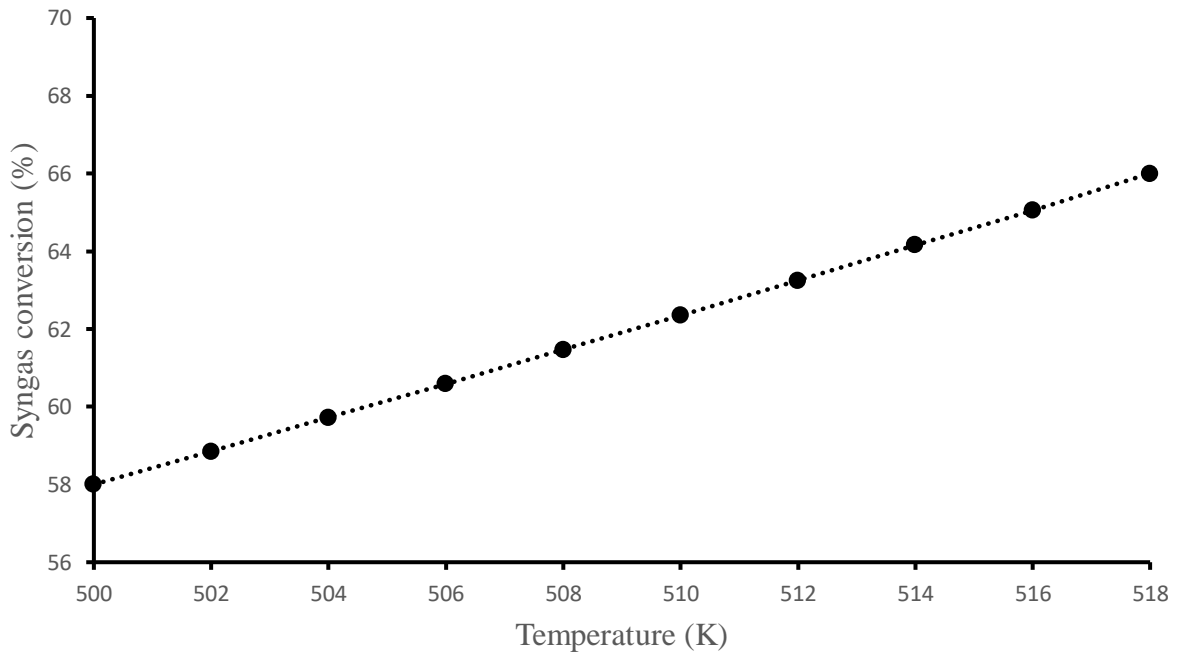


Figure 90: Effect of temperature on syngas conversion

Chapter 6: Model validation

In order to validate the presented model, data from similar reactor systems must be sourced and compared to the current simulation results. Ideally, data from a large-scale commercial SBCR would be used as a basis for the validation but this can prove to be difficult given the intellectual property protection around real plant data. As an alternative, results from the current simulation were compared with results from similar simulations on SBCR models developed by various authors. A general agreement between the current simulation results and those from the literature should serve to provide a level of confidence in the accuracy of the present model. The SBCR model, as currently presented, is different from other models from literature as it draws its constituent parts from various sources and brings them together to form a unique model. This presents a challenge in comparing the model to other models available in literature because the comparison is bound to be unfair. It is thus important to emphasise that the relevance of the comparison of the model with those from literature is that of a general indication regarding the accuracy of the model so that the model would require further validation in the form of real plant data. This is a future concern and for the purposes of the present model validation, comparison with literature models should suffice.

6.1 Sehabiague et al. (2008)

Sehabiague et al. (2008) developed a mathematical model for describing the operations in a SBCR. In the model, the authors, assume the presence of axial dispersion in all phases and include a sedimentation model to account for catalyst concentration axial gradients. A 2-class bubble model is used with large and small bubbles distinctly characterised. The kinetics are modelled using a Co catalyst. Temperature and pressure gradients are accounted for and only the gas-liquid mass transfer is considered significant. The authors measured the performance of the reactor in terms of, amongst other parameters, CO conversion and evaluated this performance as a function of both superficial gas velocity and reactor dispersion height. The results from the above-mentioned exercise have been compared to those of the current simulation as shown in Table 16. In Figures 91 and 92, the same results are compared graphically.

While the two sets of results show similar trends in that an increasing reactor height results in greater CO conversion, Sehabiague et al. (2008) results consistently reflect a lower CO conversion throughout the height of reactor. It is also worth noting the apparent slope change in both Figures 91 and 92, indicating a decrease in the sensitivity of CO conversion to an

increase in reactor height. This should be expected because of a decreasing reactant concentration with increasing height which slows down the rate of reaction (see Figure 49).

Table 16: Simulation results comparison between current and Sehabiague et al. (2008) SBCR model

CO conversion (%)				
Reactor Height (m)	Sehabiague et al. (2008)	Current study	% difference	
30	50	62,4	19,872	
35	60	71,3	15,849	
40	70	79,1	11,504	

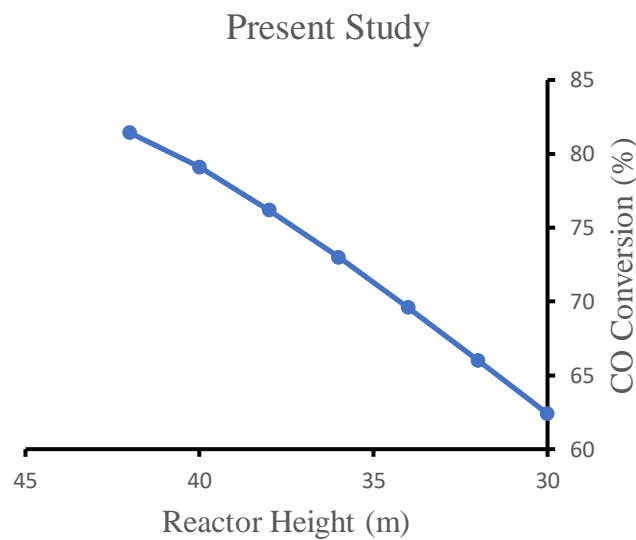


Figure 91: CO conversion as a function of reactor height based on current model simulation ($U_g=0.3$ m/s, $C_v=0.3$ (v/v))

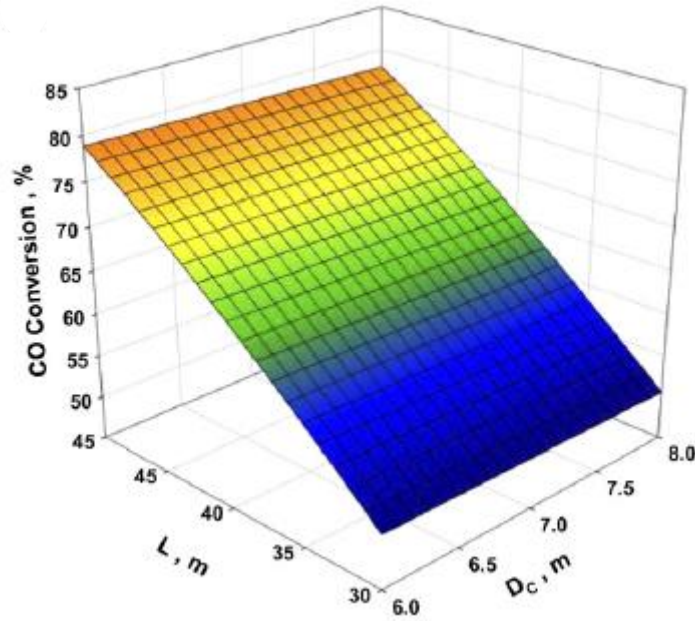


Figure 92: CO conversion over reactor height from Simulation based on Sehabiague et al. (2008) model ($U_g=0.3$ m/s, $C_v=0.375$ (wt%))

Despite the similarities between the two studies as noted below,

- Same E_L correlation used
- E_{SB} assumed to be equal to E_L
- Same Kinetic rate law, as proposed by Yates and Satterfield (1991), used
- Cobalt catalysis applied
- 2-bubble classes assumed
- ADM used to model back-mixing in small bubble, large bubble and liquid phases
- Only the gas-liquid mass transfer resistance was considered significant
- The Danckwerts type boundary conditions were used in the model numerical solution

there are significant differences to the way in which the two models were put together which can possibly explain the slightly different set of results in Table 16. These differences are outlined below:

- Different parameter correlations used
- ϵ_g correlation takes sparger design into account
- The possible total disappearance at high solids loading of the small bubble phase accounted for

- One mass transfer coefficient value used for species in both large and small bubble phases
- Reactor system assumed to be non-isothermal
- Reactor system assumed to be non-isobaric

6.2 Krishna and Sie (2000)

Krishna and Sie (2000) designed and optimised a SBCR based on a mathematical model developed using conservation laws. In this model, the liquid phase is assumed to be perfectly mixed along with the small bubbles as a 2-class bubble model is assumed. The large bubble phase is assumed to move in plug-flow through the reactor. Solid concentration gradients are assumed insignificant and duly ignored. Further similarities between the authors' model and the presently developed model are outlined below:

- Yates and Satterfield (1991) Co kinetic rate law used
- Same mass transfer coefficient correlations used
- Same ε_g , ε_{LB} , and ε_{SB} correlations used

These similarities are accompanied by a few significant differences. Firstly, the liquid and small bubbles phases are assumed to be well mixed. This assumption neglects any axial concentration profiles that may be present in these phases. Secondly, the large bubble phase is assumed to travel through the reactor in plug flow, an assumption which greatly affects the reactant conversion possible. These two differences were acknowledged when the authors' model was compared to the current model.

In comparing the two models, the models' respective responses when subjected to a changing superficial gas velocity were studied. These responses were determined in terms of the syngas conversion as defined earlier. See Table 17 for the detailed comparison. Figures 93 and 94 give a graphical representation of this comparison. In Figure 94, the plot reflecting a solids concentration of 0.3 (v/v) was used to achieve a fairer comparison between the two sets of results.

The two sets of results share a similar trend in that an increasing superficial gas velocity decreases syngas conversion. This is due to a decreasing residence time with increasing superficial gas velocity. Krishna and Sie's (2000) results show a consistently lower syngas conversion which appears to be more pronounced at the higher superficial gas velocities. The syngas conversion from Krishna and Sie's (2000) model also seems to be less sensitive to

changes in superficial gas velocities with an average change of -2.4% per 0.02 m/s step in the superficial gas velocity. The current model produces an average change of -8.15% in syngas conversion per 0.02 m/s step change in superficial gas velocity.

Table 17: Syngas conversion as a function of inlet superficial gas velocity between current and Krishna and Sie's (2000) model

Syngas conversion (%)			
Ug (m/s)	Krishna and Sie (2000)	Current study	% difference
0,26	82	89,41	8,288
0,28	80	75,05	-6,596
0,3	78	63,7	-22,449
0,32	75	54,66	-37,212
0,34	73	47,37	-54,106
0,36	70	41,41	-69,041
0,38	68	36,48	-86,404
0,4	65	32,36	-100,865

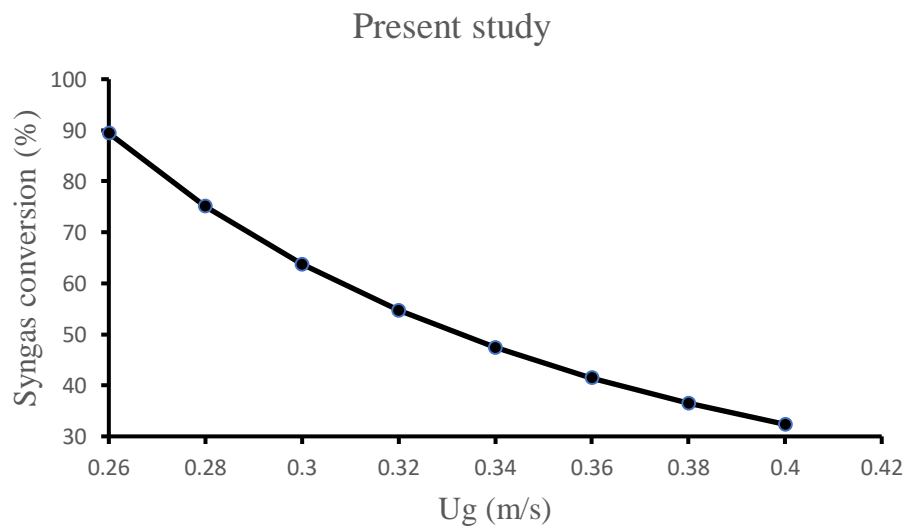


Figure 93: Syngas conversion vs superficial gas velocity results from simulation on current model (H=30 m, Cv=0.3 v/v, D=7 m)

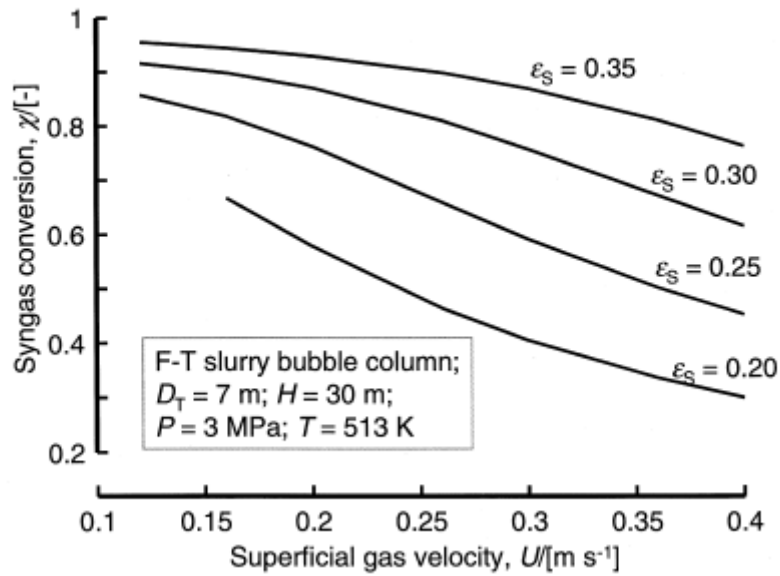


Figure 94: Syngas conversion as a function of superficial gas velocity based on simulation from model by Krishna and Sie (2000) (Krishna and Sie, 2000) (H=30 m, $C_v=0.3$ (v/v), D= 7m)

6.3 De Swart and Krishna (2002)

De Swart and Krishna (2002) carried out the development of a mathematical model to describe the SBCR and used the model to simulate the dynamic and steady-state conditions in the reactor. In the model, the gas phase was theoretically divided into small and large bubble classes. The ADM was applied in all phases of the reactor. Below is a list of the similarities followed by the differences between the model developed by the above-mentioned authors and that which was developed in the present study. The similarities are as follows:

- ADM applied to all phases
- Only gas-liquid mass transfer considered
- No intra-particle temperature and concentration gradients present
- Small bubbles velocity constant over height of reactor
- Danckwerts type boundary conditions used in model numerical solution

And the differences which contribute to the disparity between the two models are as follows:

- Catalyst distribution modelled using the sedimentation-dispersion model
- Superficial gas velocity decrease due to reaction consumption accounted for using a contraction factor

- Gas hold-up correlation by De Swart and Krishna (2002) used
- Small and large bubble mass transfer coefficient correlations from Calderbank and Moo-Young (1961) used
- ϵ_{LB} correlation from Krishna et al. (1993) used
- E_L from Deckwer et al (1982) applied
- Co Kinetic rate law used is from Post et al (1989)

A simulation, based on the model from the present study, detailing the effect of reactor height on H_2 concentration was carried out and the results compared with those from a similar simulation based on the model from the above-mentioned authors. The comparison is shown graphically in Figures 95 and 96 for the current model simulation and that from De Swart and Krishna (2002) respectively. In Figure 96, y_{large} refers to the dimensionless hydrogen concentration in the large bubble phase and ξ refers to a dimensionless co-ordinate in the axial direction. Both models show a linear relationship between the height of the reactor and the concentration of hydrogen in the gas phase.

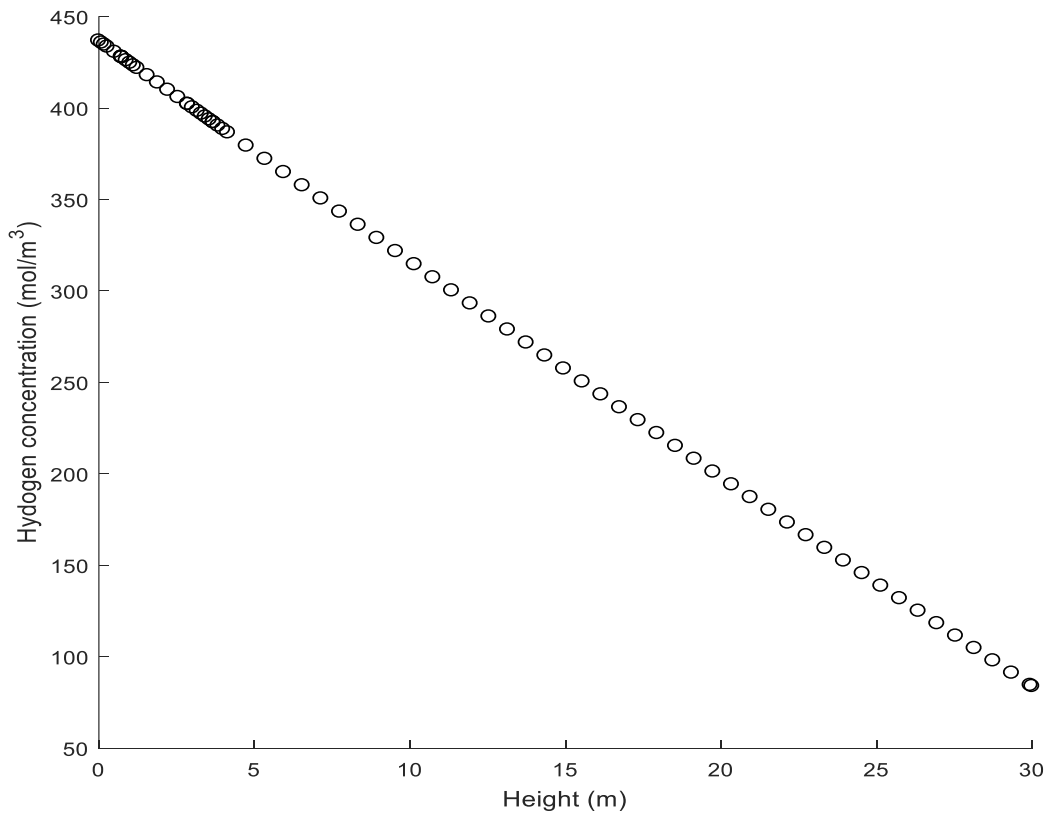


Figure 95: Concentration of hydrogen as a function of reactor height from simulation based on the present model ($U_g=0.3$ m/s, $C_v=0.3$ (v/v), $D=7.5$ m)

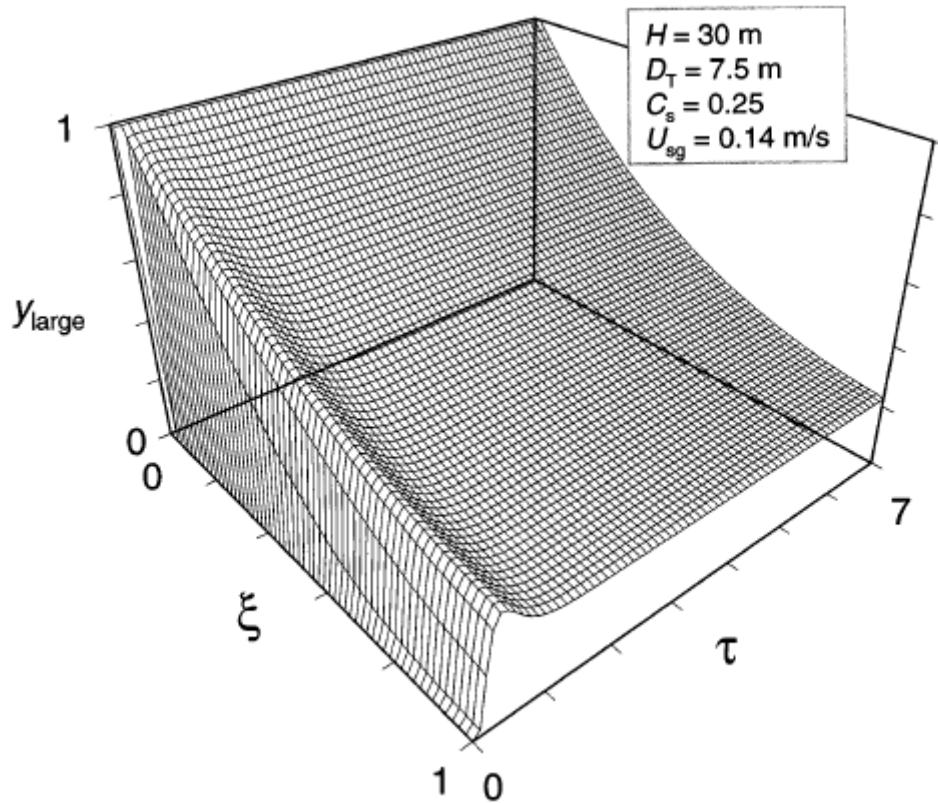


Figure 96: Hydrogen concentration as a function of reactor height results from simulation based on model by De Swart and Krishna (2002) (Deswart and Krishna, 2002) ($U_g=0.3$ m/s, $C_v=0.25$ (v/v), $D=7.5$ m)

6.4 Vik et al. (2016)

Vik et al. (2016) developed a SBCR model specifically for the conversion of biomass-derived syngas to liquid fuel. The authors used the model to simulate the effect of different feed stocks on SBCR performance. Comparisons were made between this model and that developed in the current study based on the apparent effects of reactor height on CO conversion (Table 18) (see Figures 97 and 98 for graphical comparison between results from current model and those from Vik et al. (2016) respectively) and superficial gas velocity (see Figures 99 and 100 for a graphical comparison between results from the current model and those from Vik et al. (2016) respectively). Although the model developed by the authors is starkly different from that developed in the current study, there are some similarities worth mentioning:

- No solids concentration gradients considered
- ADM used in the liquid phase
- Yates and Satterfield (1991) kinetics adopted

The differences between the models can help qualify the discrepancies noticeable between the two sets of results. These differences are outlined below:

- Population balance framework used for the gas phase to describe the concentration profile
- Calderbank and Moo-Young's (1961) mass transfer coefficient applied
- E_L correlation from Deckwer et al. (1974) used
- Liquid viscosity assumed to be independent of temperature
- Henry constants used are not temperature dependent

In terms of the effect of reactor height on CO conversion, both sets of results show an increasing CO conversion with increasing reactor height. It is also evident from both Figures 97 and 98 that the conversion of CO becomes less sensitive to an increase in reactor height at the greater heights. This is, as explained earlier, due to the lower reaction rate at these heights. The plot based on natural gas feedstock in Figure 98 was used for comparison purposes. Figures 99 and 100 show similar trends in that the superficial gas velocity is reduced linearly with respect to increasing reactor height.

Table 18: Comparison between relative effects of reactor height on CO conversion between present model and that from Vik et al. (2016)

CO conversion (%)			
Reactor height (m)	Vik et al. (2016) (Natural gas feedstock)	Current study	% difference
10	24	21,87	-9,739
15	40	32,47	-23,191
20	55	42,79	-28,535
25	65	52,78	-23,153
30	75	62,35	-20,289
35	80	71,3	-12,202
40	85	79,1	-7,459

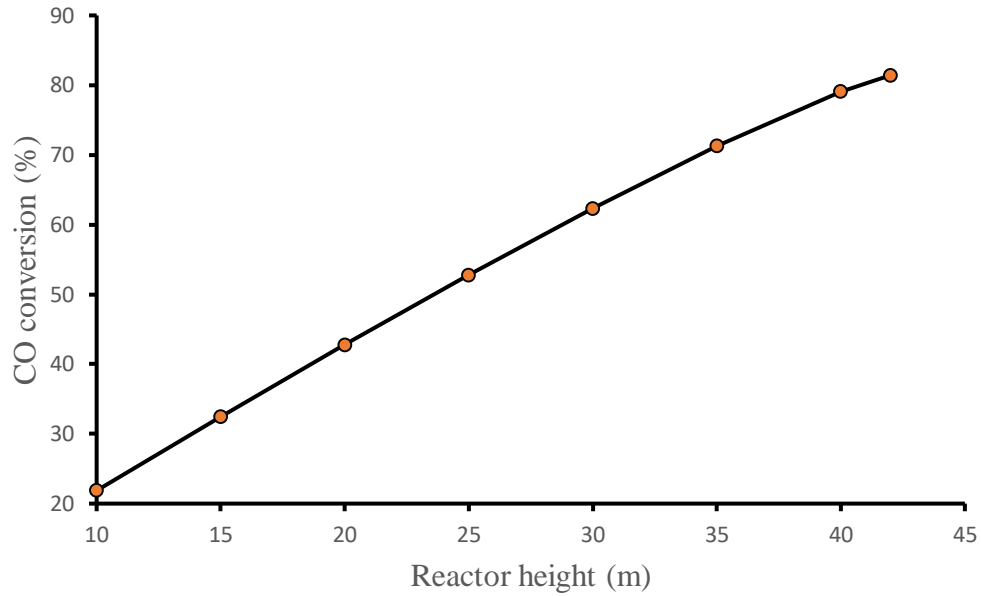


Figure 97: CO conversion as a function of reactor height based on simulation from current model ($U_g=0.3$ m/s, $C_v=0.3$ (v/v), $D=7$ m)

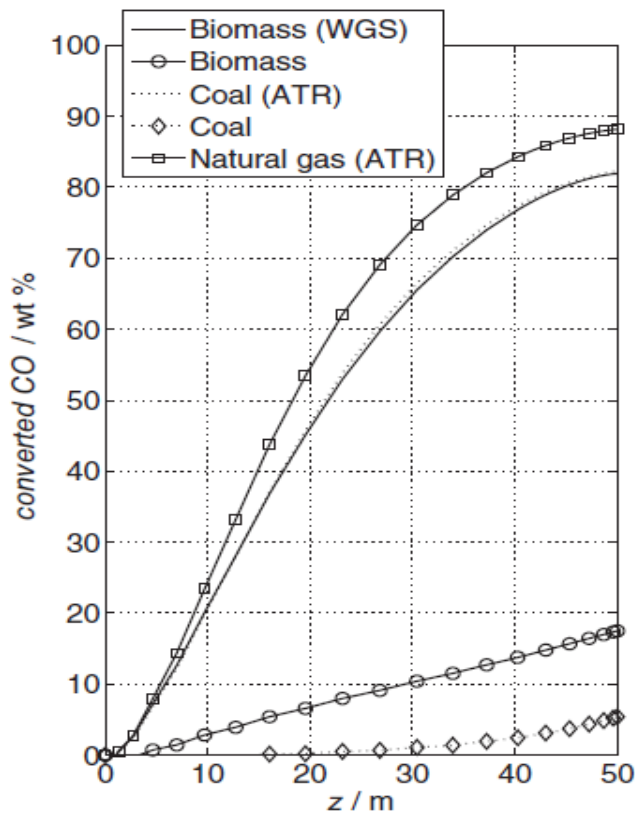


Figure 98: Reactor height vs CO conversion from simulation based on model by Vik et al. (2016) for various feedstocks (Vik et al., 2016) ($U_g=0.26$ m/s)

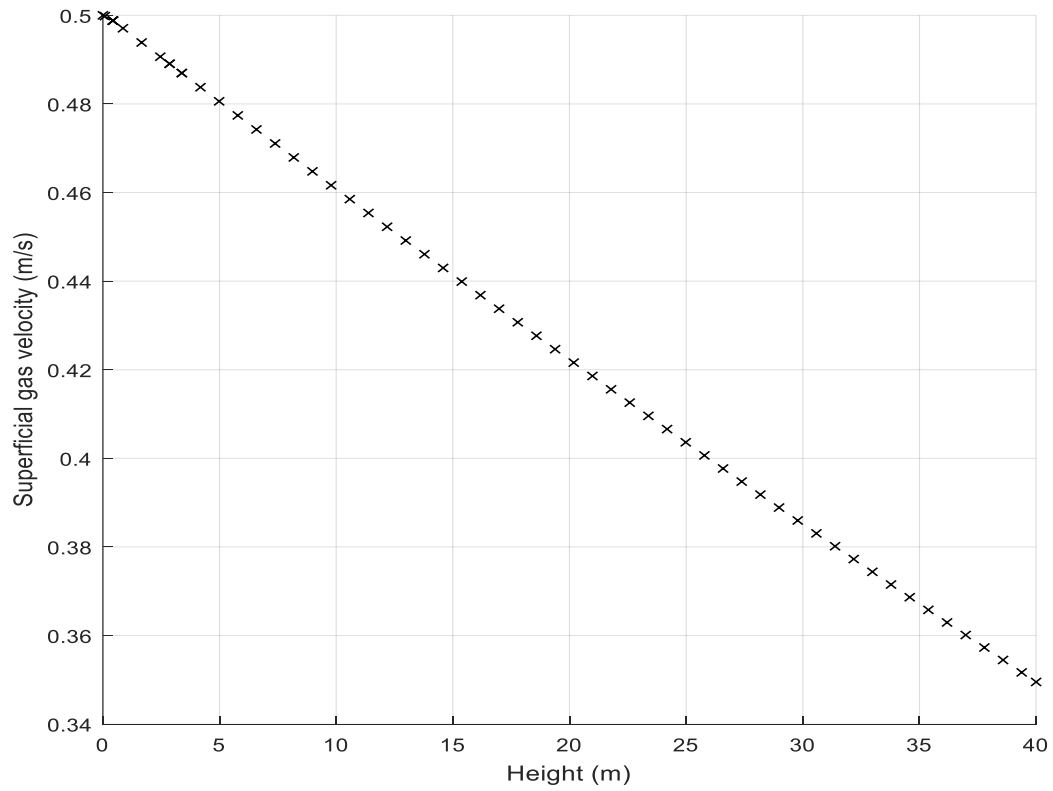


Figure 99: Superficial gas velocity drop over height of reactor based on simulation from current model ($C_v=0.3$ (v/v), $D=7$ m)

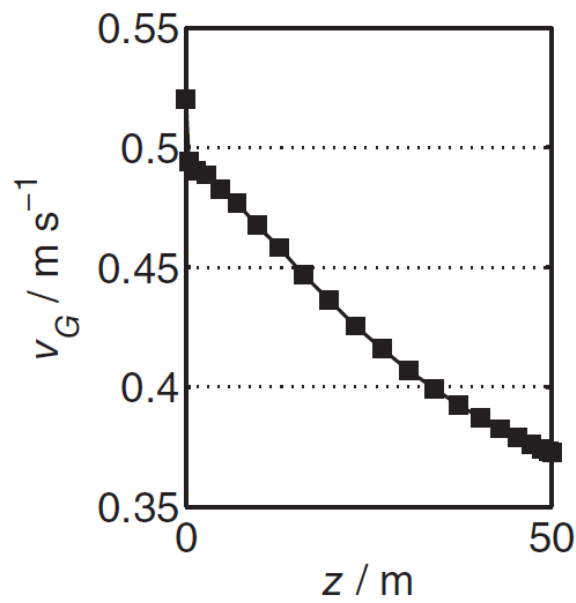


Figure 100: U_g vs height results from Vik et al. (2016) model

From the presented validation exercise, it is clear that the current model compares well with other literature models in as far as the general agreement between the models is concerned. What is also clear, however, is the presence of quantitative discrepancies noticeable between the models, i.e., the percentage deviations in simulation results between the models. This is expected, given the different sub-models that were incorporated in the proposed and literature SBCR models. Some confidence should be derived, however, from the similar trends achieved in key parameters in the models being compared because this gives an indication that the SBCR system is behaving in an expected and acceptable manner even though the exact behaviours are different from model to model. As mentioned earlier, a natural progression in the validation process should be to validate the model results against real commercial scale SBCR results or at least those from a large-scale pilot plant. In the unavailability of such data at present, the validation conducted above should be sufficient to give some indication of the correctness and accuracy of the model.

Chapter 7: Conclusion and Recommendations

7.1 Conclusion

A mathematical model describing the SBCR environment has been developed. The model is built around the principle of material conservation. Important hydrodynamic parameters along with mass transfer and kinetic parameters were sourced from various sources and incorporated into the model. The SBCR environment was conceptually divided into three distinct phases including the small bubble, large bubble and slurry phase. Material axial dispersion was accounted for in all phases to better reflect the mixing in these phases. Contrary to suggestions by various authors, axial dispersion in the large bubble phase was taken into account, occurring on a much larger scale than in the slurry phase. Simulink software from MATLAB was used to produce a numerical solution to the ode-based model formulations and the solution was used as a basis to study the dynamics inside a SBCR.

As a result of axial dispersion, the concentrations of the reactants show a gradual decrease in the large bubble phase and steep decline in the small bubble and slurry phases. The superficial gas velocity promotes axial dispersion in both the large bubble and slurry phases. It also promotes large bubble hold-up and reduces reactant residence time resulting in a net reduction in the syngas conversion. An increasing reactor diameter results in an overall increase in the conversion of syngas and an increasing solids concentration decimates the small bubble population and increases the large bubble hold-up resulting in a lower syngas conversion. The model results were compared with those from different authors and were found to show similar trends albeit with differing parameter values. This was expected as the published models were not identical to the proposed model.

A mathematical model capable of describing the hydrodynamic behaviour in a SBCR has been developed to aid in the study of this complex reactor. This model can also be used in the preliminary design stages, helping to avoid costly experiments and save time by acting as a platform on which to rule out specific design options.

7.2 Recommendations

Further work on this model including heat transfer and momentum effects can aid in making the model more complete and robust but care should be taken as to the level of detail that is incorporated as this can be difficult and time consuming. It is best to decide on the level of detail in line with the user's aims and objectives. In the present case, the objective was to

gain an understanding of the hydrodynamic behaviour in a SBCR and the factors that influence it, to this end it was deemed fit to limit the detail in the model as has been done.

References

1. Akita, K., Yoshida, F. (1973). Gas holdup and volumetric mass transfer coefficient in bubble columns. Effects of liquid properties. *Industrial and Engineering Chemistry Process Design and Development*, 12, 76–80.
2. Albright, L. F. (2009). *Albright's Chemical Engineering Handbook*. New York: CRC Press, Taylor and Francis group.
3. Aoyama, Y., Ogushi, K., Koide, K., Kubota, H. (1968). Liquid Mixing in Concurrent Bubble Columns. *Journal of Chemical Engineering Japan*, 1(2), 158-163.
4. Bach, H. F, Pilhofer, T. (1978). Variations of gas hold-up in bubble columns with physical properties of liquids and operating parameters of column. *German Chemical Engineering*, 1, 270–275.
5. Baird, M. H. I., Rice, R. G. (1975). Axial dispersion in large unbaffled columns. *The Chemical Engineering Journal*, 9, 171-174.
6. Basha, O. M., Sehabiague, L., Abdel-Wahab, A., Morsi, B. I. (2015). Fischer–Tropsch Synthesis in Slurry Bubble Column Reactors: Experimental Investigations and Modeling – A Review. *International Journal of Chemical Reactor Engineering*, 13(3), 201–288.
7. Begovich, J. M., Watson, J. (1978). *Hydrodynamic characteristics of three-phase fluidized beds*. Cambridge: Cambridge University Press.
8. Behkish, A. (1997). *Hydrodynamic and Mass Transfer Parameters in Large-Scale Slurry Bubble Column Reactors* (Doctoral thesis, University of Pittsburg, USA).
9. Behkish, A., Lemoine, R., Oukaci, R., Morsi, I. B. (2006). Novel correlations for gas holdup in large-scale slurry bubble column reactors operating under elevated pressures and temperatures. *Chemical Engineering Journal*, 115, 157–171.
10. Boyer, C., Gazarian, J., Lecocq, V., Maury, S., Forret, A., Schweitzer, J., Souchon, V. (2016). Development of the Fischer-Tropsch Process: From the Reaction Concept to the Process Book. *Oil and Gas Science and Technology - Revue d'IFP Energies nouvelles, Institut Francais du Petrole*, 71(44).
11. Brady, R. C. III, Pettit, R. (1981). Mechanism of the Fischer-Tropsch reaction. The chain propagation step. *Journal of the American Chemical Society*, 103(5), 1287–1289.
12. Brotz, W. Z. (1949). Zur Systematik der Fischer-Tropsch-Katalyse. *Zeitschrift für Elektrochemie*, 5, 301-306.

13. Bukur, D. B. (1983). Some Comments on Models for Fischer-Tropsch Reaction in Slurry Bubble Column Reactors. *Chemical Engineering Science*, 38(3),441-446.
14. Calderbank, P. H., Moo-Young, M. B. (1961). The continuous phase heat and mass transfer properties of dispersions. *Chemical Engineering Science*, 16, 39-54.
15. Calderbank, P.H., Evans, F., Farley, R., Jepson, G., Poll, A. (1963). Rate processes in the catalyst-slurry Fischer-Tropsch reaction. *Catalysis in Practice*, 66–74.
16. Chang, J., Bai, L., Teng, B. T., Zhang, R. L., Yang, J., Xu, Y. Y., Xiang, H. W., Li, Y. W. (2007). Kinetic modeling of Fischer–Tropsch synthesis over Fe.Cu.K.SiO₂ catalyst in slurry phase reactor. *Chemical Engineering Science*, 62, 4983 – 4991.
17. Chen, C. M., Leu, L. P. (2001). Hydrodynamics and mass transfer in threephase magnetic fluidized beds. *Powder Technology*, 117, 198–206.
18. Craxford, S. R., Rideal, E. K. (1939). The mechanism of the synthesis of hydrocarbons from water-gas. *Journal of the Chemical Society*, 1604-1614.
19. Davis, B. H. (2009). Fischer–Tropsch Synthesis: Reaction mechanisms for iron catalysts. *Catalysis Today*, 141, 25–33.
20. Davis, M. E., Davis, R. J. (2003). *Fundamentals of Chemical Reaction Engineering*. New York: McGraw Hill.
21. De Deugd, R. M. (2004). *Fischer-Tropsch Synthesis Revisited; Efficiency and Selectivity Benefits from Imposing Temporal and/or Spatial Structure in the Reactor* (Doctoral thesis, Technische Universiteit Delft, Netherlands).
22. De Nevers, N. (1968). Bubble driven fluid circulations. *AIChE Journal*, 14(2), 222–226.
23. de Swart, J. W. A. (1996). *Scale-Up of a Fischer-Tropsch Slurry Reactor* (Doctoral thesis, University of Amsterdam, Netherlands).
24. de Swart, J. W. A., Krishna, R. (2002). Simulation of the transient and steady state behaviour of a bubble column slurry reactor for Fischer–Tropsch synthesis. *Chemical Engineering and Processing*, 41, 35–47.
25. Deckwer, W. D., Robert, W. F (Ed). (1991). *Bubble Column Reactors*. New York: John Wiley and Sons.
26. Deckwer, W. D., Burckhart, R., Zoll, G. (1974). Mixing and Mass Transfer in Tall Bubble Columns. *Chemical Engineering Science*, 29, 2177-2188.
27. Deckwer, W. D., Louisi, Y., Zaidi, A., Ralek, M. (1980). Hydrodynamic Properties of the Fischer-Tropsch Slurry Process. *Industrial and Engineering Chemistry Process Design and Development*, 19, 699-708.

28. Deckwer, W. D., Schumpe, A. (1993). Improved Tools for Bubble Column Reactor Design and Scale-up. *Chemical Engineering Science*, 48(5), 889-911.
29. Deckwer, W. D., Serpemen, Y., Ralek, M., Schmidt, B. (1982). Modeling the Fischer–Tropsch synthesis in the slurry phase. *Ind. Eng. Chem. Process Des. Dev.* 21, 231–241.
30. Degaleesan, S., Dudukovic, M. P., Toseland, B. A., Bhatt, B. L. (1997). A Two-Compartment Convective-Diffusion Model for Slurry Bubble Column Reactors. *Industrial and Engineering Chemistry Research*, 36, 4670-4680.
31. Degaleesan, S., Dudukovic, M., Pan, Y. (2001). Experimental study of gas-induced liquid-flow structures in bubble columns. *AIChE Journal*, 47(9), 1913–1931.
32. Devanathan, N. (1991). *Investigation of Liquid Hydrodynamics in Bubble Columns via Computer Automated Radioactive Particle Tracking (CARPT)* (Doctoral thesis, Washington University, USA).
33. Djakovic, D. (2014). Gas to Liquids: Unlocking Value From Natural Gas. Texas A&M Gas and Fuels Research Initiative. Retrieved from <http://gfrc.tamu.edu/wp-content/uploads/2015/04/Djakovic.pdf>
34. Dry, M. E. (2002). The Fischer–Tropsch process: 1950–2000. *Catalysis Today*, 71, 227–241.
35. Dudukovic, M. P., Larachi, F., Mills, P., L. (1999). Multiphase reactors – revisited. *Chemical Engineering Science*, 54, 1975-1995.
36. Espinoza, R. L., Steynberg, A. P., Jager, B., Vosloo, A. C. (1999). Low temperature Fischer–Tropsch synthesis from a Sasol perspective. *Applied Catalysis A: General*, 186, 13–26.
37. Fan, L. S., Yang, G. Q., Lee, D. J., Tsuchiya, K., Luo, X. (1999). Some aspects of high-pressure phenomena of bubbles in liquid and liquid–solid suspensions. *Chemical Engineering Science*, 54, 4681–4709.
38. Field, R. W., Davidson J. F. (1980). Axial dispersion in bubble columns. *Transactions of the Institution of Chemical Engineers*, 58, 228–236.
39. First finished products at ENVIA Energy's GTL plant. (2017). Retrieved from <http://www.velocys.com/press/nr/nr170630.php>
40. Fischer, F., and Tropsch, H. (1926). The Synthesis of Petroleum at Atmospheric Pressures from Gasification Products of Coal. *Brennstoff-Chemie*, 7, 97-104.
41. Gandhi, B., Prakash, A., Bergougnou, M. A. (1999). Hydrodynamic behaviour of slurry bubble column at high solids concentrations. *Powder Technology*, 103, 80–94.

42. Gasche, H., Edinger, E., Kompel, H., Hofmann, H. (1990). A Fluid-dynamically Based Model of Bubble Column Reactors. *Chemical Engineering Technology*, 13, 341-349.
43. Grevskott S., Sannaes, B. H., Dudukovic, M. P., Hjarbo, K. W., Svendsen, H. F. (1996). Liquid circulation, bubble size distributions, and solids movement in two- and three-phase bubble columns. *Chemical Engineering Science*, 51, 1703–13.
44. Groen, J. S., Oldeman, R. G. C., Mudde, R. F., Van den Akker, H. E. A. (1996). Coherent Structures and Axial Dispersion in Bubble Column Reactors. *Chemical Engineering Science*, 51(10), 2511-2520.
45. Groen, J.S. (2004). *Scales and Structures in Bubbly Flows: Experimental analysis of the flow in bubble columns and in bubbling fluidized beds* (Doctoral thesis, Delft University of Technology, Netherlands)
46. Guo, Y. X., Rathor, M. N., Ti. H. C. (1997). Hydrodynamics and mass transfer studies in a novel external-loop airlift reactor. *Chemical Engineering Journal*, 67, 205–14.
47. Gwamo, K. I., Gidaspow, D., Jung, J. (2005). Optimum Catalyst Size for Slurry Bubble Column Reactors. *Industrial and Engineering Chemistry Research*, 44, 6393-6402.
48. Herington, E. F. G. (1946). The Fischer-Tropsch synthesis considered as a polymerization reaction. *Chemistry and Industry*, 65, 346-347.
49. Hikita, A., Kikukawa, H. (1974). Liquid-Phase Mixing in Bubble Columns: Effect of Liquid Properties. *The Chemical Engineering Journal*, 8, 191-197.
50. Hikita, H., Asai, S., Tanigawa, K., Segawa, K., Kitao, M. (1980). Gas hold-up in bubble columns, *Chemical Engineering Journal*, 20, 59–67.
51. Hinze, J. O. (1959). *Turbulence*. New York: McGraw Hill.
52. Hoek, A. (2005). The Shell GTL process: towards a world scale project in qatar. *Chemie Ingenieur Technik*, 77(8), 1172-1172.
53. Hughmark, G. A. (1967). Holdup and mass transfer in bubble columns. *Industrial and Engineering Chemistry Process Design and Development*, 6, 218–220.
54. Iliuta, I., Larachi, F., Anfray, J., Dromard, N., Schweic D. (2007). Multicomponent Multicompartment Model for Fischer–Tropsch SCBR. *AIChE Journal*, 53(8), 2062–2083.
55. Inga, J. R. (1997). *Scale-up and scale-down of slurry reactors: A new methodology* (Doctoral thesis, University of Pittsburgh, USA).

56. Inga, J. R., Morsi, B. I. (1996). A Novel Approach for the Assessment of the Rate-Limiting Step in Fischer-Tropsch Slurry Process. *Energy and Fuels*, 10, 566-572.
57. Jiang, P., Lin, T. J., Luo, X., Fan L. S. (1995). Flow visualization of high pressure (21 MPa) bubble column: bubble characteristics. *Chemical Engineering Research and Design*, 73, 269–74.
58. Jianping, W., Shonglin, X. (1998). Local hydrodynamics in a gas-liquid-solid three-phase bubble column reactor. *Chemical Engineering Journal*, 70, 81-4.
59. Jordan, U., Schumpe, A. (2001). The gas density effect on mass transfer in bubble columns with organic liquids. *Chemical Engineering Science*, 56, 6267–6272.
60. Joshi, J. B. (1980). Axial mixing in multiphase Contactors—A unified correlation. *Transactions of Institution of Chemical Engineers*, 58, 155–165.
61. Joshi, J. B. (2001). Computational flow modelling and design of bubble column reactors. *Chemical Engineering Science*, 56, 5893–5933.
62. Joshi, J. B., Vitankar, V. S., Kulkarni, A. A., Dhotre, M. T., Ekambara, K. (2002). Coherent flow structures in bubble column reactors. *Chemical Engineering Science*, 57, 3157–3183.
63. Joshi, J., Sharma, M. (1979). A circulation cell model for bubble columns. *Chemical Engineering Research and Design*, 57, 244–51.
64. Kantarci, N., Borak, F., Ulgen, K. O. (2005). Bubble column reactors. *Process Biochemistry*, 40, 2263–2283.
65. Kara, S., Kelkar, G. B., Shah, Y. T., Carr, N. L. (1982). Hydrodynamics and Axial Mixing in a Three-phase Bubble Column. *Industrial and Engineering Chemistry Process Design and Development*, 21, 584-594.
66. Kelkar, B. O., Shah, Y. T., Carr, N. L. (1984). *Industrial and Engineering Chemistry Process Design and Development*, 23, 308-313.
67. Kim, S. D., Kim, H. S., Han, J. H. (1992). Axial Dispersion Characteristics in Three-phase Fluidised Beds. *Chemical Engineering Science*, 47(13/14), 3419-3426.
68. Kito, M., Tabei, K., Murata, K. (1978). Gas and liquid holdups in mobile beds under the counter-current flow of air and liquid.). *Industrial and Engineering Chemistry Process Design and Development*, 17, 568–71.
69. Kojima, H., Sawai, J., Suzuki, H. (1997). Effect of pressure on volumetric mass transfer coefficient and gas holdup in bubble column. *Chemical Engineering Science*, 52(21-22), 4111-4116.

70. Kolmogorov, A. (1941). The Local Structure of Turbulence in Incompressible Viscous Fluid for Very Large Reynolds Numbers. *Doklady Akademiia Nauk SSSR*, 30, 301-305.
71. Krishna, R. (2000). A Scale-up Strategy for a Commercial Scale Bubble Column Slurry Reactor for Fischer-Tropsch Synthesis. *Oil and Gas Science and Technology*, 55(4), 359-393.
72. Krishna, R., Ellenberger, J., Hennephof, D. E. (1993). Analogous description of gas–solid fluidized beds and bubble columns. *Chem. Engng. J.*, 53, 89–101.
73. Krishna, R., Sie, S. T. (2000). Design and scale-up of the Fischer–Tropsch bubble column slurry reactor. *Fuel Processing Technology*, 64, 73–105.
74. Kuo, J. C. W. (1983). Slurry Fischer-Tropsch/Mobil two stage process of converting syngas to high octane gasoline, Final report DOE-PC-3022-10, DOE 1983.
75. Lemoine, R., Behkish, A., Sehabiague, L., Heintz, Y. J., Oukaci, R., Morsi, B. I. (2008). An Algorithm for Predicting the Hydrodynamic and Mass Transfer Parameters in Bubble Column and Slurry Bubble Column Reactors. *Fuel Processing Technology*, 89(4), 322-343.
76. Letzel, H. M., Schouten, J. C., Krishna, R., van den Bleek, C. M. (1999). Gas holdup and mass transfer in bubble column reactors operated at elevated pressure. *Chemical Engineering Science*, 54(13-14), 2237-2246.
77. Levenspiel, O. (1999). *Chemical Reaction Engineering (3rd edition)*. New York: Wiley.
78. Maitlis, P. M., and de Klerk, A (Eds.). (2013). *Greener Fischer-Tropsch Processes for Fuels and Feedstocks*. Weinheim: 2013 Wiley-VCH Verlag and Co. KGaA.
79. Mangartz K. H., Pilhofer, T. H. (1980). Untersuchungen zur Gasphasendispersion in Blasensaulenreaktoren. *Verfahrenstechnik (Mainz)*.
80. Maretto, C., and Krishna, R. (1999). Modelling of a bubble column slurry reactor for Fischer-Tropsch synthesis. *Catalysis Today*, 52, 279-289.
81. Matos, E. M., Guirardello, R., Mori, M., Nunhez, J. R. (2009). Modeling and simulation of a pseudo-three-phase slurry bubble column reactor applied to the process of petroleum hydrodesulfurization. *Computer Chemical Engineering*, 33, 1115–22.
82. Matsuura, A., Fan, L. S. (1984). Distribution of bubble properties in a gas–liquid–solid fluidized bed. *AIChE Journal*, 30, 894–903.

83. Mavros, P. (1993). Mixing in Flotation Columns: Axial Dispersion Modelling. *Minerals Engineering*, 6(5), 465-478.
84. Millies, M., Mewes, D. (1994). Zirkulationsströmungen und die Vermischung der kontinuierlichen Phase in Blasensäulen. *Chemie Ingenieur Technik*, 66(3), 332–342.
85. Mohammed, S., Datt, M. (2013). Sasol: an industrial perspective. Retrieved from http://cheminnerweb.ukzn.ac.za/Libraries/APCH221_Notes/Sasol_Slides.sflb.ashx
86. Moo-Young, M., Robinson, C. W., Vezina, C. (Eds). 1981. *Advances in Biotechnology: Scientific and Engineering Principles*. New York: Pergamon Press.
87. Mponzi, P. (2011). *Production of Biofuels by Fischer-Tropsch Synthesis* (Doctoral thesis, Lappeenranta University of Technology, Finland).
88. Nettelhoff, H., Ledakowics, S., Kokuun, R., Deckwer, W. D. (1985). Kinetics of the Fischer-Tropsch Synthesis in the Slurry Phase on a Pottasium Promoted Iron catalyst. *Industrial and Engineering Chemistry Process Design and Development* 24(4), 1043-1049.
89. Ohki, Y., Inoue, H. (1969). Longitudinal mixing of the liquid phase in bubble columns. *Chemical Engineering Science*, 25, 1-16.
90. Ojeda, M., Nabar, R., Nilekar, A. U., Ishikawa, A., Mavrikakis, M., Iglesia, E. (2010). CO activation pathways and the mechanism of Fischer–Tropsch synthesis. *Journal of catalysis*, 272(5), 287–297.
91. Oryx GTL. Retrieved from <https://www.qp.com.qa/en/QPActivities/Pages/SubsidiariesAndJointVenturesDetails.aspx?aid=37>
92. Oyevaar, M., De La Rie, T., Van der Sluijs, C., Westerterp, K. (1989). Interfacial areas and gas hold-ups in bubble columns and packed bubble columns at elevated pressures. *Chemical Engineering and Processing: Process Intensification*, 26, 1–14.
93. Pearl GTL Overview. Retrieved from <http://www.shell.com/about-us/major-projects/pearl-gtl/pearl-gtl-an-overview.html>
94. PetroSA: Operations and Refinery. Retrieved from http://www.petrosa.co.za/innovation_in_action/Pages/Operations-and-Refinery.aspx
95. Pilhofer, T. H., Bach, H. F., Mangartz, K. H. (1978). Determination of Fluid Dynamic Parameters in Bubble Column Design. Fifth International Symposium on Chemical Reaction Engineering, Houston, 31, 372–383.
96. Post, M. F., Van't Hoog, A. C., Minderhout, J. K., Sie, S. T. (1989). Diffusion limitations in Fischer–Tropsch catalysts. *A.I.Ch.E.J.* 35, 1107–1114.

97. Pratt, J. W. (2012). A Fischer-Tropsch Synthesis Reactor Model Framework for Liquid Biofuels Production. SANDIA Report: SAND2012-7848.
98. Rados, N., Al-Dahhan, M. H., Dudukovic, M. P. (2003). Modelling of the Fischer-Tropsch synthesis in slurry bubble column reactors. *Catalysis Today*, 79–80,211–18.
99. Rados, N., Al-Dahhan, M. H., Dudukovic, M. P. (2005). Dynamic Modeling of Slurry Bubble Column Reactors. *Industrial and Engineering Chemistry Research*, 44, 6086-6094.
100. Rahimpour, M. R., Jokar, S. M., Jamshidnejad, J. (2012). A novel slurry bubble column membrane reactor concept for Fischer–Tropsch synthesis in GTL technology. *Chemical Engineering Research and Design*, 90, 383–396.
101. Reilly, I. G., Scott, D. S., De Bruijn, T., Jain, A., Piskorz, J. (1986). A correlation for gas holdup in turbulent coalescing bubble columns. *Canadian Journal of Chemical Engineering*, 64, 705–717.
102. Sarup, B., Wojciechowski, B. W. (1989). Studies of the fischer-tropsch synthesis on a cobalt catalyst II. Kinetics of carbon monoxide conversion to methane and to higher hydrocarbons. *The Canadian Journal of Chemical Engineering*, 67(1), 62-74.
103. Sasol Nigeria Operations. Retrieved from <http://www.sasol.com/nigeria>
104. Satterfield, C. N., Huff, G. A. (1980). Effects of mass transfer on Fischer-Tropsch synthesis in slurry reactors. *Chemical Engineering Science*, 35, 195–202.
105. Schluter, S., Weinspach, P. M., Steiff, A. (1992). Modeling and simulation of bubble column reactors. *Chemical Engineering and Processing*, 31(2), 97-117.
106. Schumpe, A., Grund, G. (1986). The gas disengagement technique for studying gas holdup structure in bubble columns. *Canadian Journal of Chemical Engineering*, 64, 891–896.
107. Schumpe, A., Saxena, A. K., Fang, L. K. (1987). Gas/liquid mass transfer in a slurry bubble column. *Chemical Engineering Science*, 42, 1787–1796.
108. Schweich, D., Fongarland, P., Anfray, J. (2007). Kinetic study and modeling of Fischer-Tropsch reaction over a Co/Al₂O₃ catalyst in a slurry reactor. *Chemical Engineering Science*, 62, 5353-5356.
109. Schweitzer, J. M., Viguie, J. C. (2009). Reactor Modeling of a Slurry Bubble Column for Fischer-Tropsch Synthesis. *Oil and Gas Science and Technology*, 64(1), 63-77.

110. Sehabiague, L., Lemoine, R., Behkish, A., Heintz, Y. J., Sanoja, M., Oukaci, R., Morsi, I. (2008) Modeling and optimization of a large-scale slurry bubble column reactor for producing 10,000 bbl/day of Fischer–Tropsch liquid hydrocarbons. *Journal of the Chinese Institute of Chemical Engineers*, 39, 169–179.
111. Sehabiague, L. (2012). *Modeling, Scale-up and Optimization of Slurry Bubble Column Reactors for Fischer-Tropsch Synthesis* (Doctoral thesis, University of Pittsburgh, USA).
112. Shah, Y. T., Stiegel, G. J., Sharma, M. M. (1978). Backmixing in Gas-Liquid Reactors. *AIChE Journal*, 24(3), 369-400.
113. Sinnott, R. K. (2005). *Chemical Engineering Design (Vol 6, 4th edition)*. Ney York: Elsevier.
114. Soriano, J. P., (2005). *Mass Transfer Characteristics in an Agitated Slurry Reactor Operating Under Fischer-Tropsch Conditions* (M.S. Thesis, University of Pittsburgh, USA).
115. Speight, J. G. (2008). *Synthetic Fuels Handbook: Properties, Process and Performance*. New York: The McGraw-Hill Companies.
116. Steynberg, A. P., and Dry, M. E (Eds.). (2004). *Fischer-Tropsch Technology*. Elsevier Science and Technology Books.
117. Tau, L., Dabbagh, H., Bao, S., Davis, B. H. (1990). Fischer-Tropsch synthesis. Evidence for two chain growth mechanisms. *Catalysis Letters*, 7, 127-140.
118. Therning, P., Rasmuson, A. (2001). Liquid dispersion, gas holdup and frictional pressure drop in a packed bubble column at elevated pressures. *Chemical Engineering Journal*, 81, 331–335.
119. Todic, B., Ma, W., Jacobs, G., Davis, B. H., Bukur, D. B. (2014). Effect of process conditions on the product distribution of Fischer–Tropsch synthesis over a Re-promoted cobalt-alumina catalyst using a stirred tank slurry reactor. *Journal of Catalysis*, 311, 325–338.
120. Towell, G. D., Ackermann, G. H. (1972). Axial mixing of liquid and gas in large bubble reactors. In: *Proceedings of the Fifth European-Second International Symposium on Chemical Reaction Engineering*. Vol. B3-1. Elsevier, Amsterdam, the Netherlands.
121. Ueyama, K. Miyauchi, T. (1979). Properties of Recirculating Turbulent Two Phase Flow in Gas Bubble Columns. *AIChE Journal*, 25(2), 258-266.

122. Van Deemter, J. J. (1961). Mixing and contacting in gas–solid fluidized beds. *Chemical Engineering Science*, 13, 143–165.
123. van der Laan, G. P. (1999). Kinetics, Selectivity and Scale Up of the Fischer-Tropsch Synthesis (Doctoral thesis, University of Groningen, Netherlands).
124. van der Laan, G. P., Beenackers, A. A. C. M., Krishna, R. (1999). Multicomponent reaction engineering model for Fe-catalyzed Fischer-Tropsch synthesis in commercial scale slurry bubble column reactors. *Chemical Engineering Science*, 54, 5013-5019.
125. van Steen, E., Schulz, H. (1999). Polymerisation kinetics of the Fischer-Tropsch CO hydrogenation using iron and cobalt based catalysts. *Applied Catalysis A: General*, 186, 309-320.
126. Vermeer, D. J., Krishna, R. (1981). Hydrodynamics and Mass Transfer in Bubble Columns Operating in the Churn-Turbulent Regime. *Industrial and Engineering Chemistry Process Design and Development*, 20, 475-482.
127. Vik, B. C., Solsvik, J., Hillestad, M., Jakobsen, H. A. (2016). Modelling of a Slurry Bubble Column Reactor for the Production of Biofuels via the Fischer-Tropsch Synthesis. *Chemical Engineering Technology*, 38(4), 690–700.
128. Wachi, S., Nojima, Y. (1990). Gas-phase dispersion in bubble columns. *Chemical Engineering Science*, 45, 901-905.
129. Wang, J. (1987). *Physical, chemical and catalytic properties of borided cobalt Fischer-Tropsch catalysts* (Doctoral thesis, Brigham Young University, USA).
130. Wang, Y., Fan, W., Liu, Y., Zeng, Z., Hao, X., Ming, C., Zhang, C., Xu, Y., Xiang, H., Li, Y. (2008). Modeling of the Fischer–Tropsch synthesis in slurry bubble column reactors. *Chemical Engineering and Processing*, 47, 222-228.
131. Wilkinson, P. M., Dierendonck L. V. (1990). Pressure and gas density effects on bubble break-up and gas hold-up in bubble columns. *Chemical Engineering Science*, 45, 2309–2315.
132. Withers, H. P., Jr., Eliezer, K. F., Mitchell, J. W. (1990). Slurry-Phase Fischer-Tropsch Synthesis and Kinetic Studies over Supported Cobalt Carbonyl Derived Catalysts. *Industrial and Engineering Chemistry Research*, 29(9), 1807-1814.
133. Wojciekowski, B. W. (1988). The Kinetics of the Fischer-Tropsch Synthesis.
134. Wu, Q., Wang, X., Wang, T., Han, M., Sha Z., Wang, J. (2013). Effect of Liquid Viscosity on Hydrodynamics and Bubble Behaviour of an External-loop Airlift Reactor. *Canadian Journal of Chemical Engineering*, 91, 1957-1963.

135. Yates, I. C., Satterfield, C. N. (1991). Intrinsic Kinetics of the Fischer-Tropsch Synthesis on a Cobalt Catalyst. *Energy and Fuels*, 5, 168-173.
136. Zehner, P. (1982). Impuls-, stoff- und wärmetransport in blasensäulen. *Chemie Ingenieur Technik*, 54, 248–51.
137. Zehner, P. (1982)a. Momentum, mass and heat transfer in bubble columns. *International Chemical Engineers*, 26, 22–35.
138. Zou, R., Jiang, X., Li, B., Zu, Y., Zhang, L. (1988). Studies on gas holdup in a bubble column operated at elevated temperature. *Industrial and Engineering Chemistry Research*, 27, 1910–1916.

Appendix A: Simulink Boundary Condition Models

Large bubble phase

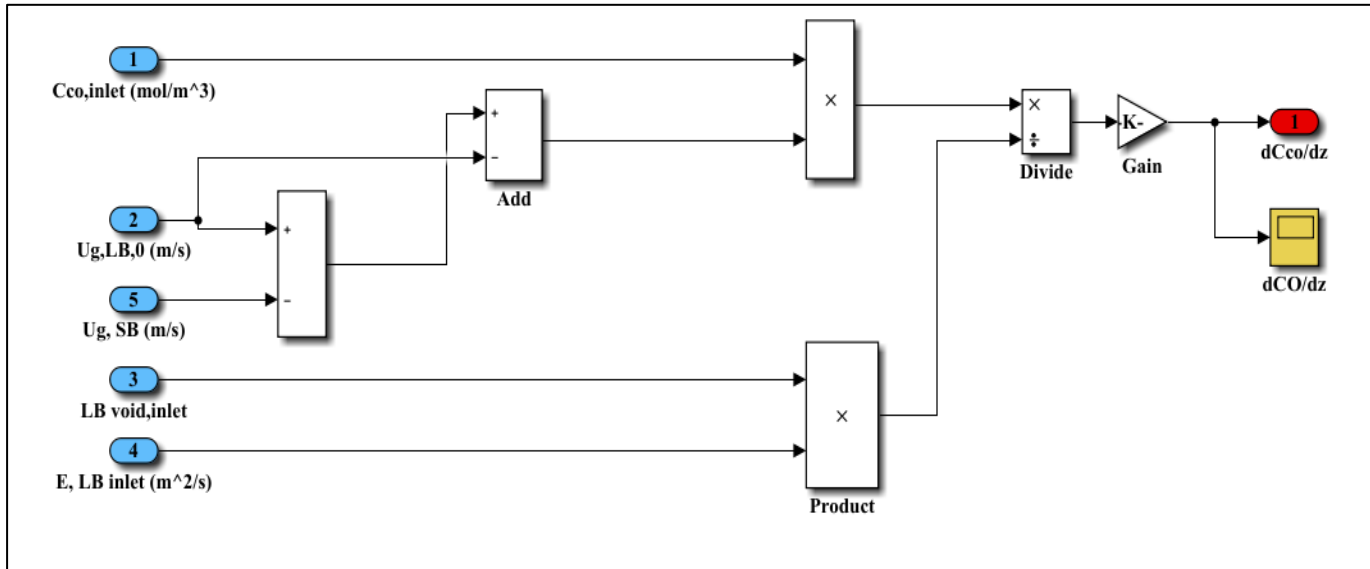


Figure A1: Large bubble CO inlet boundary condition Simulink model

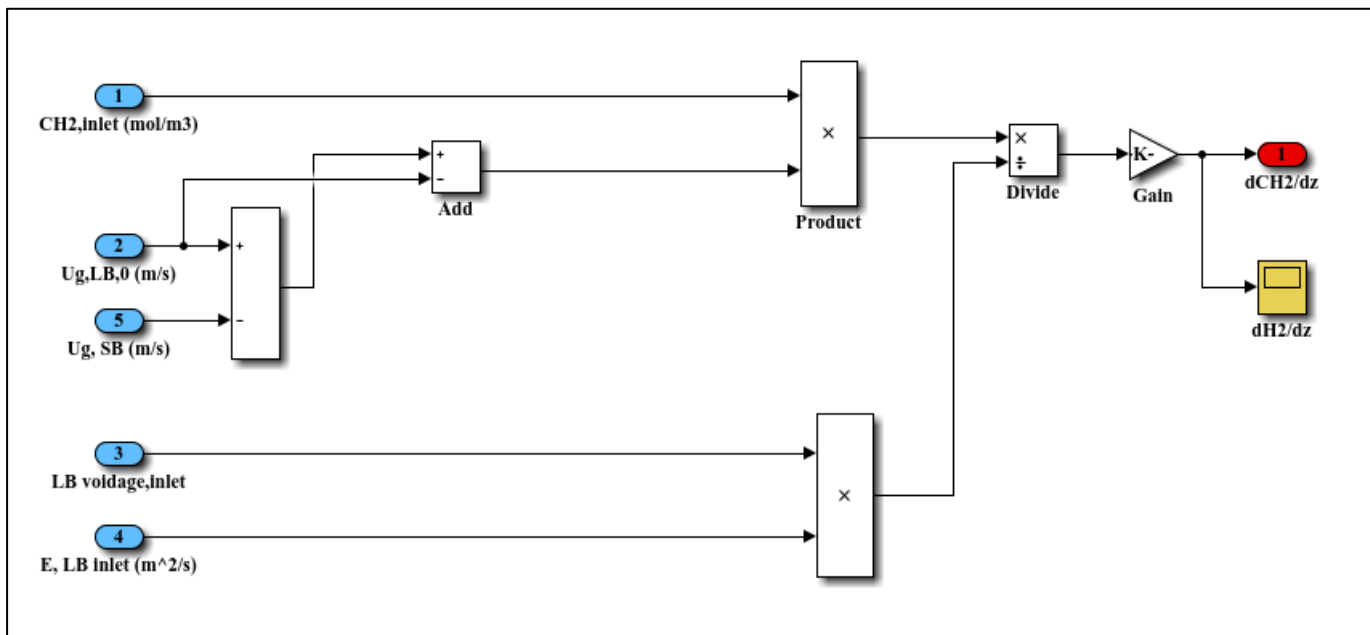


Figure A2: Large bubble H₂ inlet boundary condition Simulink model

The inlet large bubble dispersion coefficient used in both the CO and H₂ boundary condition models was determined using inlet values of the superficial gas velocity and the large bubble

voidage in the large bubble dispersion coefficient correlation suggested by Mangartz and Pilhofer (1980) in Table 3. The Simulink model is shown in Figure 103.

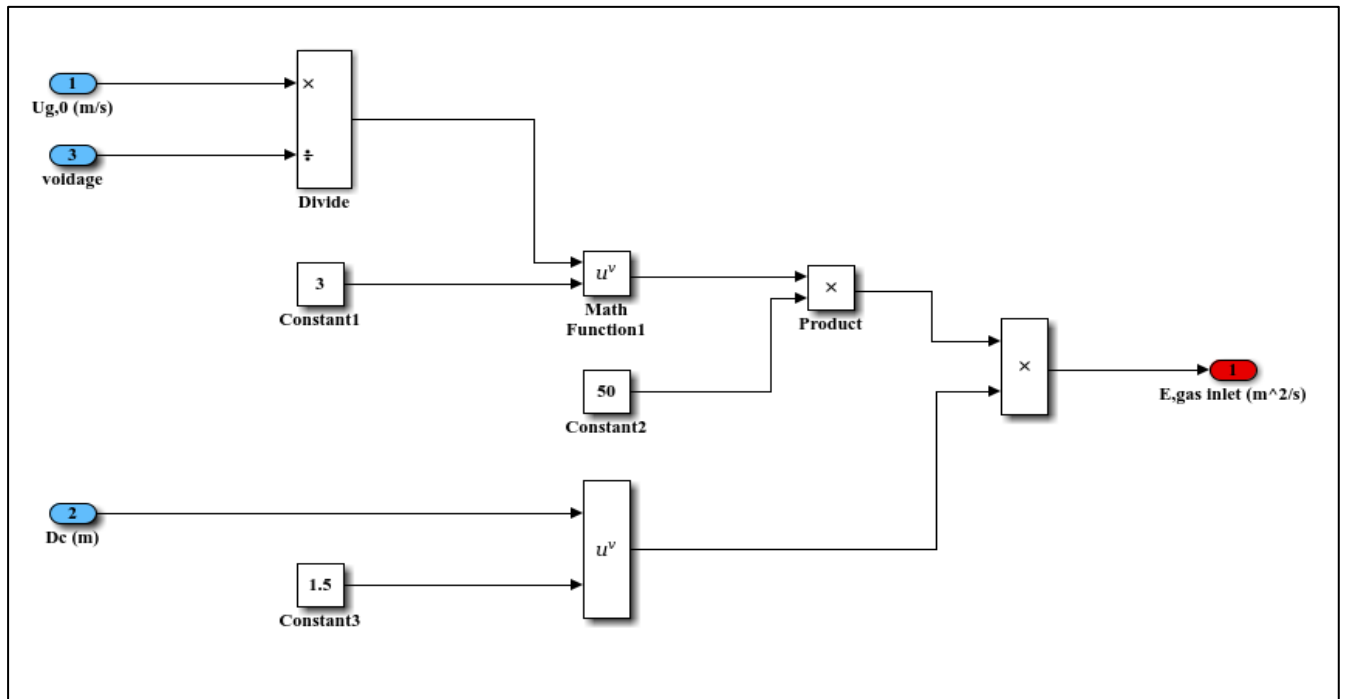


Figure A3: Simulink model for the gas phase axial dispersion coefficient at the reactor inlet

Small bubble phase

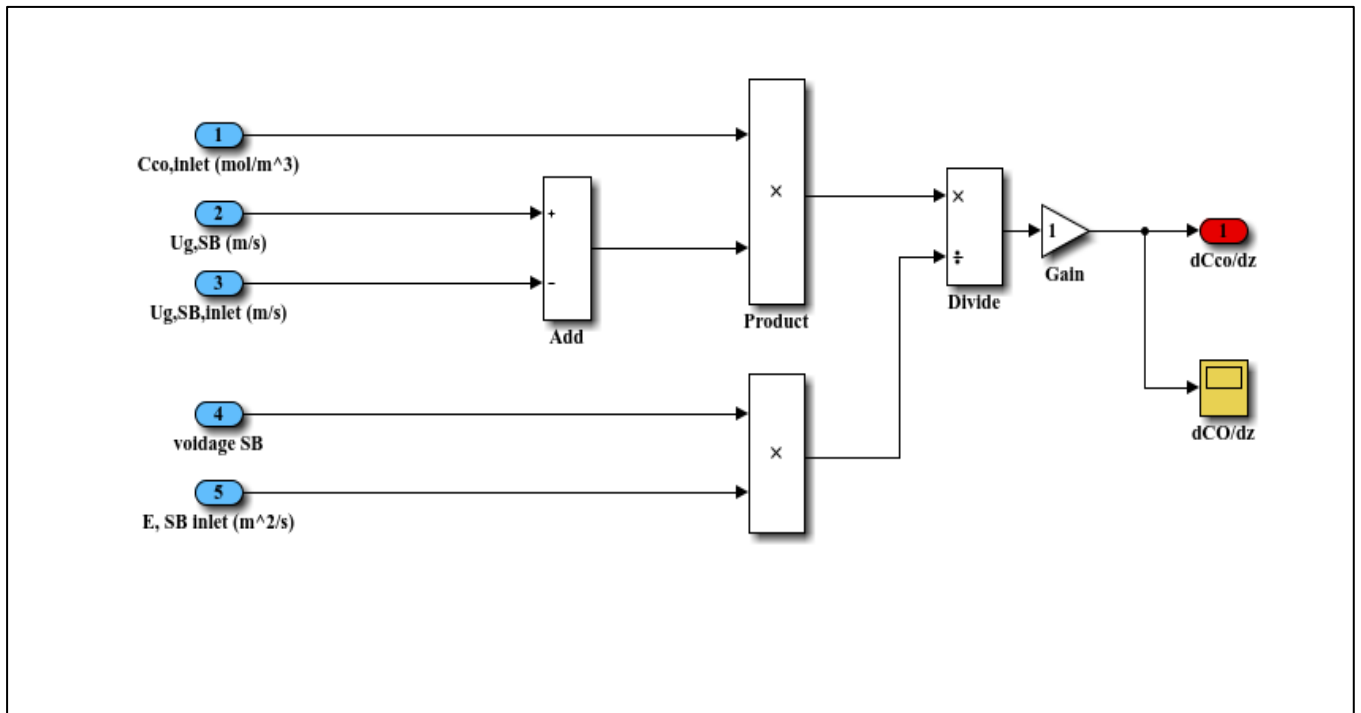


Figure A4: Small bubble CO inlet boundary condition Simulink model

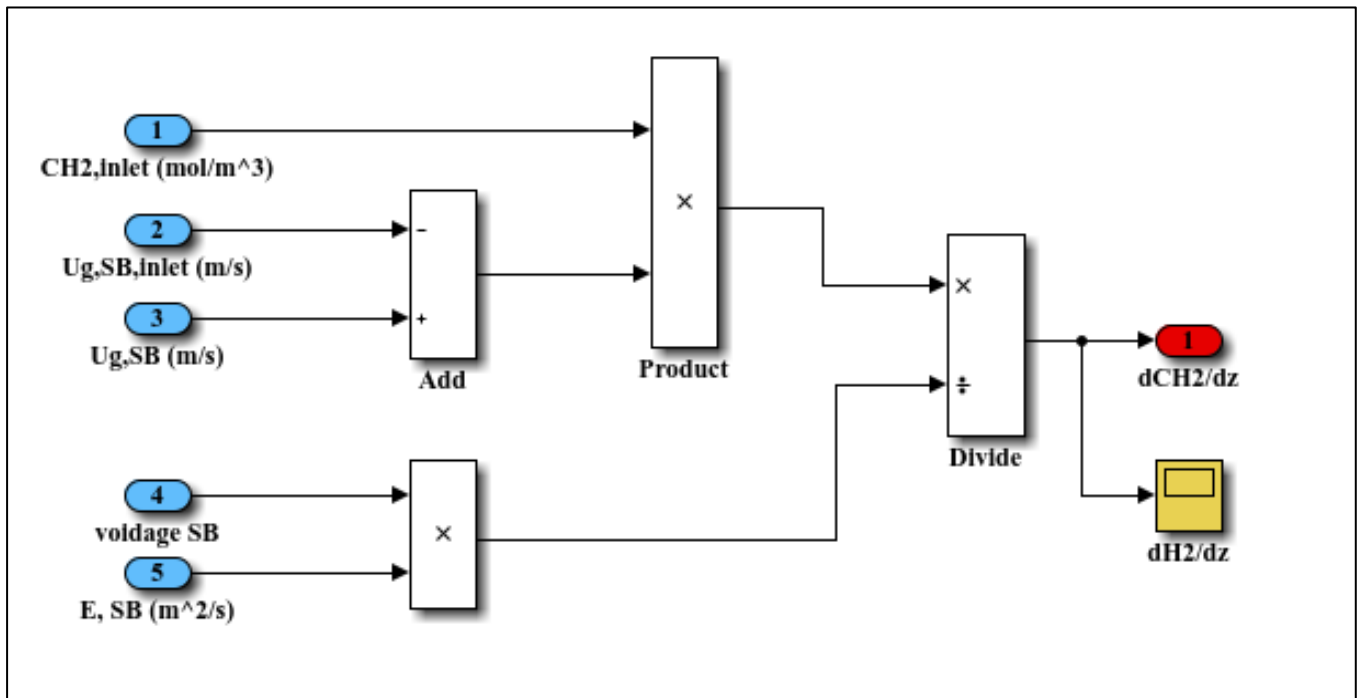


Figure A5: Small bubble H₂ inlet boundary condition Simulink model

As was the case in the large bubble phase, the small bubble inlet dispersion coefficient for both CO and H₂ was determined from the inlet superficial gas velocity using the correlation by Baird and Rice (1975) in Equation 78 and the Simulink model is shown in Figure 106.

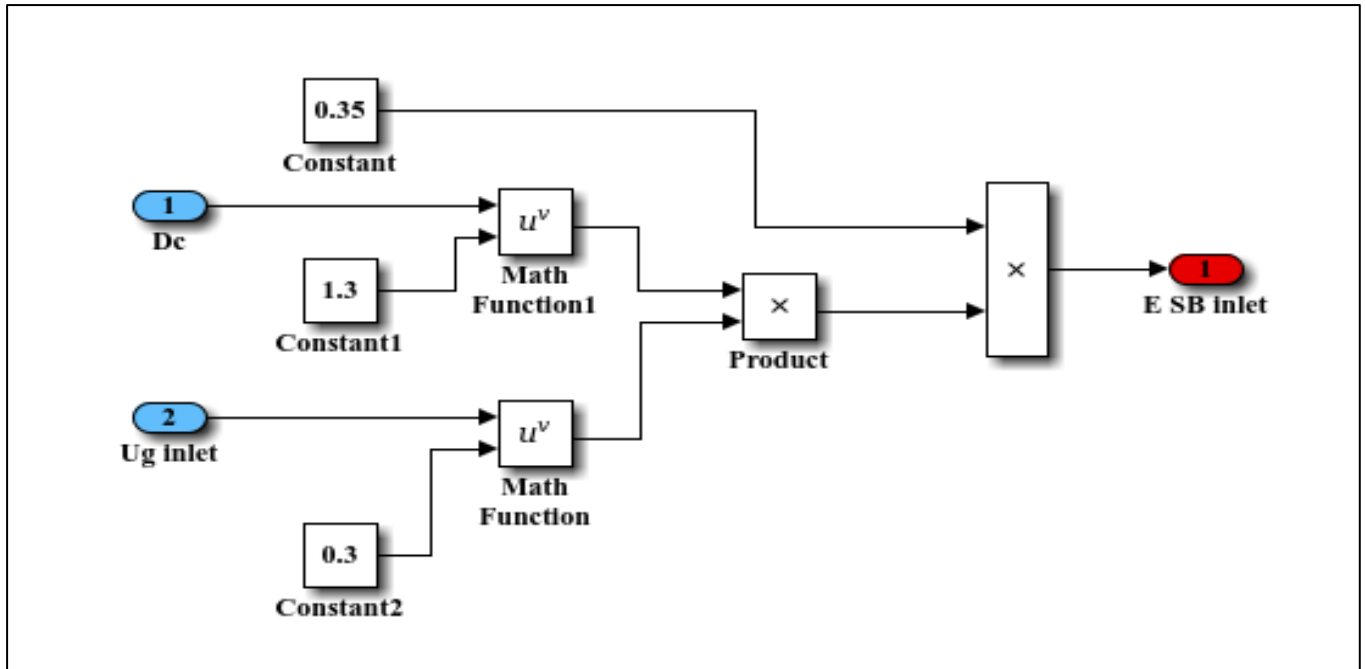


Figure A6: Simulink model for the small bubble phase axial dispersion coefficient at the reactor inlet

Liquid phase

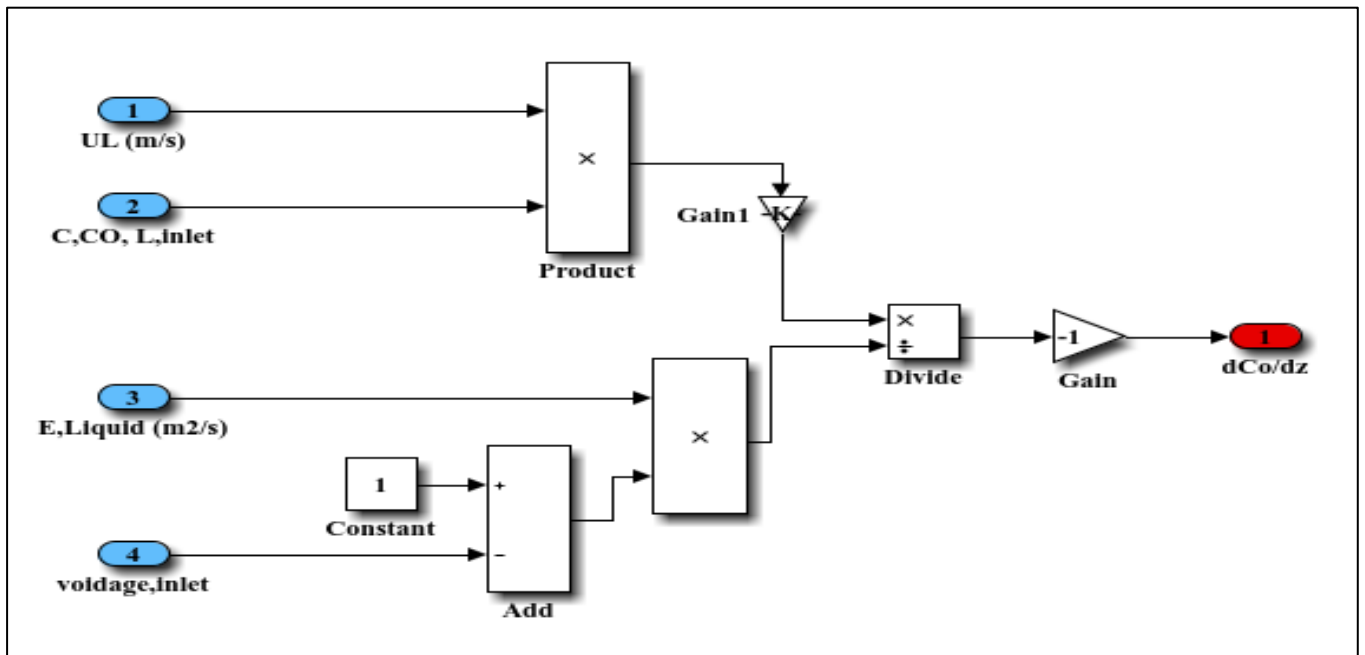


Figure A7: Liquid phase CO inlet boundary condition Simulink model

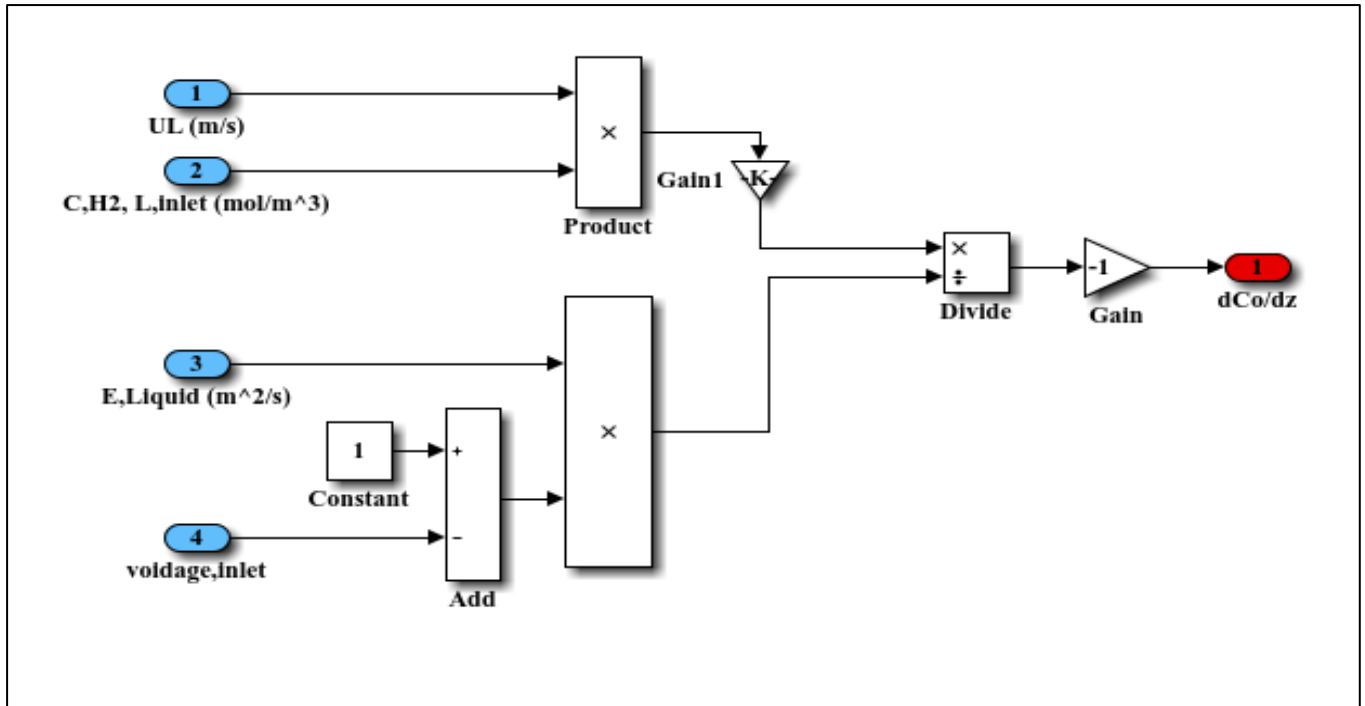


Figure A8: Liquid phase H₂ inlet boundary condition Simulink model

The inlet liquid phase dispersion coefficient was derived from the small bubble dispersion coefficient as the two are, as mentioned in the report, the same.